

**A SYSTEMATIC PERSPECTIVE ON CONDUCTIVE POLYMER BLENDS USING AN
INTEGRATED MICROFLUIDIC-ASSISTED MICROPRINTING SYSTEM FOR
COMBINATORIAL THIN FILM LIBRARY PREPARATION**

by

ANINDYA LAL ROY

A DISSERTATION SUBMITTED IN PARTIAL FULFILLMENT OF
THE REQUIREMENTS FOR THE DEGREE OF

DOCTOR OF PHILOSOPHY

in

THE FACULTY OF GRADUATE AND POSTDOCTORAL STUDIES

(Electrical and Computer Engineering)

THE UNIVERSITY OF BRITISH COLUMBIA

(Vancouver)

February 2023

© Anindya Lal Roy, 2023

The following individuals certify that they have read, and recommend to the Faculty of Graduate and Postdoctoral Studies for acceptance, the dissertation entitled:

A systematic perspective on conductive polymer blends using an integrated microfluidic-assisted microprinting system for combinatorial thin film library preparation

submitted by Anindya Lal Roy in partial fulfillment of the requirements for

the degree of Doctor of Philosophy

in Electrical and Computer Engineering

Examining Committee:

Konrad Walus, Professor, Electrical and Computer Engineering, UBC
Supervisor

Boris Stoeber, Professor, Electrical and Computer Engineering, UBC
Supervisory Committee Member

Mu Chiao, Professor, Mechanical Engineering, UBC
University Examiner

John M. Frostad, Associate Professor, Chemical and Biological Engineering, UBC
University Examiner

Additional Supervisory Committee Members:

John D. W. Madden, Professor, Electrical and Computer Engineering, UBC
Supervisory Committee Member

Abstract

This dissertation demonstrates the development of a novel printing platform with integrated mixing and dispensing capabilities for patterning compositionally graded thin film sample libraries of fluid material blends. The modular nature of the combinatorial print head enables the reusability of the mixing and dispensing modules while the elastomeric base structure may be replaced as desired due to its ease of handling and integration. Such a combinatorial print head is shown to consume smaller functional material volumes along with faster fabrication of thin films using such materials. The key advantage of these print heads is their ability to rapidly homogenize multiple fluid inputs which results in highly efficient multi-material thin film prototyping.

An economical fabrication process for the disposable elastomeric base structure through a simple casting process using 3D printed molds is utilized. The requisite combinatorial functions of fluid proportioning and mixing are validated through extensive direct and indirect characterization. A sample preparation methodology is proposed and the combinatorial printing platform is assembled to validate operational performance electronic solution processable polymers that are typically used for fabricating sensor components. The intrinsically conductive electronic polymers are also tested for their microfluidic processability and inkjet printability.

A statistical hypothesis testing framework is established for analyzing the characterization data which is then used for inferencing and validation. Case studies on multiple hypotheses involving the two types of intrinsically conductive polymers are performed which illustrates the utility of the combinatorial printing platform as a rapid thin film sample patterning tool with minimal material wastage. Analyses of the characterization data of such sample ensembles demonstrate the importance of the availability of a large number of functionally graded samples in the context of high throughput material screening. In addition, these tests are also used as an indirect performance evaluation of the combinatorial printing system when compared with benchmark processing of material blends. Conclusions regarding application-specific advantages and disadvantages of the two polymers are inferred in the context of standalone and temperature-dependent electrical conductivity performance as sensor materials and blending tests are used to determine the ideal operational niche of each material.

Lay Summary

This dissertation presents a novel printing method that can create blends of electronically active polymer materials in fluid dispersions at different proportions and dispense them for testing. The method can enable rapid preparation of electronically active thin films for testing and optimization. As a platform methodology, it can be customized for application in any domain that requires material development and evaluation. The work presented in this dissertation has three primary contributions: (i) development of custom print heads capable of additional preprocessing prior to printing, (ii) definition of an evaluation framework for the printed samples and (iii) using the custom print head and the evaluation framework to determine both the utility of the printing method and the performance of the test materials being printed. Such an approach is expected to be beneficial for the rapidly developing field of additive manufacturing, especially in the field of printed electronics.

Preface

The research presented in this dissertation was carried out at the University of British Columbia (UBC) at the Department of Electrical and Computer Engineering. All contributions presented in this dissertation have been published or accepted in journal articles and conference proceedings with one journal article almost ready to be submitted [1]–[4]. [1] was an inception to the work done in this dissertation as it laid the groundwork for subsequent experimental design and testing. C. Bois conceived the idea of the work and was actively supported by A. A. Gupta in the overall preparation of the printed testing platform as well as writing the manuscript. A. L. Roy contributed to the electrode designs which formed the basis of the testing platform and the work was supervised by K. Walus. [2] and [3] comprise the printing platform development presented in this dissertation for which, A. L. Roy developed the overall framework, performed all the experiments and prepared the manuscripts for publication under the supervision of K. Walus. The co-author in [2] and [3], H. N. Chiu actively worked with A. L. Roy to develop the Python user interface based on the proposed operational flowchart for controlling the operation of the printing platform. [4] is an accepted journal manuscript that describes the different sources of variability that can affect the printing platform using the polymers tested in the dissertation. A. L. Roy conceptualized the theme of the manuscript, performed all the experiments and data analysis and prepared the manuscript for publication under the supervision of K. Walus. C. Beaumont prepared the novel conductive polymer which was one of the two conductive polymers used for the case studies and was supervised by M. Leclerc in this work. In summary, [1] deals with the aspects presented in Chapter 3 while [2], [3] and [4] deal with aspects presented in Chapters 2, 3 and 4. All chapters of this dissertation were written by me and reviewed by the supervisory committee and the examination committee.

Publications from the dissertation

[1] C. Bois, A. A. Gupta, **A. L. Roy** and K. Walus, “Collaborative conception of a R2R printed testing platform for printed electronics standardization,” *IEEE International Flexible Electronics Technology Conference (IFETC)*, 2019.

[2] **A. L. Roy**, H. N. Chiu and K. Walus, “Microfluidic drop-on-demand inkjet print heads for multi-resolution multi-material thin film library preparation” *International Conference on Miniaturized Systems for Chemistry and Life Sciences (μ TAS)*, 2021.

[3] **A. L. Roy**, H. N. Chiu and K. Walus, “A microfluidic-enabled combinatorial formulation and integrated inkjet printing platform for evaluating functionally graded material blends,” *RSC Lab On A Chip*, vol. 21, no. 22, pp. 4427–4436, 2021.

[4] **A. L. Roy**, C. Beaumont, M. Leclerc and K. Walus, “Using integrated combinatorial blending and inkjet printing to study performance of printed polythiophene conductors,” (accepted in *IOP Flexible and Printed Electronics*).

Table of Contents

Abstract.....	iii
Lay Summary.....	iv
Preface.....	v
Table of Contents.....	vii
List of Tables.....	x
List of Figures.....	xi
List of Abbreviations.....	xvii
Acknowledgements.....	xviii
Dedication.....	xix
Chapter 1: Introduction.....	1
1.1 Motivation: Towards combinatorial evaluation of thin films.....	1
1.1.1 Evolution of thin films.....	1
1.1.2 Combinatorial screening as a thin film evaluation methodology.....	2
1.1.3 Utility of thin film solution processing.....	10
1.1.4 Inkjet printing for specialized applications.....	11
1.1.5 Microfluidic compatibility with inkjet printing.....	13
1.2 Electroactive organic polymer thin films.....	14
1.2.1 Polymers and electrical conductivity.....	14
1.2.2 The need for polymer electronics.....	15
1.2.3 High conductivity ICPs.....	16
1.3 Scope and outline of the work.....	18
1.3.1 Contributions of the work.....	18
1.3.2 Organization of the dissertation.....	19

Chapter 2: Combinatorial thin film processing: Materials and Methods.....	20
Chapter overview.....	20
2.1 Combinatorial print heads (CPHs).....	20
2.1.1 The need for integrated microfluidic inkjet processing.....	20
2.1.2 Design and fabrication of the combinatorial print head.....	22
2.1.3 Microfluidic mixing and prior mixer implementations.....	26
2.2 Integrated processing platform.....	28
2.2.1 Platform implementation.....	28
2.2.2 Analytical and empirical considerations for the CPH.....	33
2.2.3 Operational verification.....	37
2.3 Combinatorial thin film library preparation.....	41
Summary.....	44
Chapter 3: Experimental evaluation protocols.....	45
Chapter overview.....	45
3.1 Factor and response variables.....	45
3.2 Design and analysis of experiments.....	46
3.2.1 General analysis using summary statistics.....	46
3.2.2 Single-factor experimental design (one-way ANOVA).....	47
3.2.3 Multi-factor experimental design (two-way ANOVA).....	53
3.2.4 ANOVA assumptions, effect size and statistical power.....	56
3.2.5 ANOVA post-hoc validation.....	58
3.3 Materials and methods.....	60
3.3.1 Library types: Thin films and printable inks.....	60
3.3.2 Characterization methods.....	60

Summary	64
Chapter 4: Investigating Conductive Polymer Blends.....	65
Chapter overview.....	65
4.1 Intrinsically conductive polymers.....	65
4.1.1 Emergence of PEDOT:PSS.....	65
4.1.2 Drawbacks and the need for novel ICPs.....	67
4.2 Material characterization.....	69
4.2.1 Aggregate sizing in ICP dispersions.....	69
4.2.2 Viscosity and surface tension of ICP dispersions.....	70
4.2.3 Crystallinity.....	71
4.3 Case studies.....	72
4.3.1 Case 1: Electrical conductivity dependence on printed layer count.....	72
4.3.2 Case 2: Electrical conductivity dependence on cosolvent additive.....	76
4.3.3 Case 3: Electrical conductivity dependence on temperature.....	92
4.3.4 Case 4: Electrical conductivity dependence on cosolvent additive and temperature.....	93
Summary.....	98
Chapter 5: Conclusions and Future Work	99
5.1 Summarized conclusions.....	99
5.2 Future Work.....	104
Bibliography.....	106
Appendix A.....	123
Appendix B.....	163

List of Tables

Table 1.1: Some standard strategies used for combinatorial screening of materials.....	8
Table 1.2: Typical applications of the commercial-grade ICP poly(3,4-ethylenedioxythiophene) poly(styrene sulfonate) (PEDOT:PSS).....	16
Table 3.1: Data representation for a typical single-factor experiment.....	47
Table 3.2: General structure of a one-way ANOVA table.....	52
Table 3.3: Data representation for a typical multi-factor experiment.....	53
Table 3.4: General structure of a two-way ANOVA table.....	55
Table 4.1: ANOVA evaluation of the different processing types using the different compositions in iteration 1 considering (w/ OL) and excluding (w/o OL) extreme outliers at $\alpha = 0.05$	82
Table 4.2: ANOVA evaluation of the different processing types using the different compositions in iteration 2 considering (w/ OL) and excluding (w/o OL) extreme outliers at $\alpha = 0.05$	82
Table 4.3: ANOVA evaluation of the different compositions for iteration 1 using the different processing types considering (w/ OL) and excluding (w/o OL) extreme outliers.....	84
Table 4.4: ANOVA evaluation of the different compositions for iteration 2 using the different processing types considering (w/ OL) and excluding (w/o) extreme outliers.....	84
Table 4.5: ANOVA evaluation of pristine P1 and P2 electrical conductivity response as a function of temperature including (w/) and excluding (w/o) extreme outliers.....	91
Table 4.6: ANOVA evaluation of temperature-dependent electrical conductivity behavior P1-D blends for PM, UM and OM processing.....	96
Table 4.7: ANOVA evaluation of composition-dependent and temperature-dependent electrical conductivity behavior of P2-P1 and P2-P1-D blends.....	97

List of Figures

Figure 1.1: Applications of thin films in diverse fields of commercial and academic research and development.....	2
Figure 1.2: The cycle of combinatorially evaluating and screening multimaterial systems on the basis of the specific properties being investigated for deployment in targeted applications through iterative processing.....	3
Figure. 1.3: Some examples of conjugated polymers that are also conducting in nature include (clockwise from top left) (i) polyacetylene (homoatomic) (ii) polyphenylene vinylene (homoatomic) (iii) polypyrrole (X = NH) and polythiophene (X = S) (heteroatomic) and (iv) polyaniline (X = NH) and polyphenylene sulfide (X = S) (heteroatomic).....	14
Figure 2.1: Top view of a generalized combinatorial print head (CPH) structure comprising fluid inlets ($F_1, F_2, \dots, F_{N-1}, F_N$) which supply the fluids to the on-chip preprocessing module W from which, the processed blend is fed to the on-chip dispensing module V. for deposition and patterning. The dotted arrows indicate the channels defining the fluid flow path and the general fluid flow direction.....	22
Figure 2.2: (a) Bottom half of the two-part interlocking 3D printed mold for casting elastomeric layer 1 comprising structural definitions for the fluid inlets and the microfluidic channels. (b) Top half of the two-part interlocking 3D printed mold for casting elastomeric layer 1 comprising structural definitions for the check valves and the mixer module insert. (c) 3D printed mold for casting elastomeric layer 2 comprising structural definition for the inkjet module insert (inkjet module shown in the inset). (d) Plasma bonded casts of elastomeric layers 1 and 2 forming the bilayer combinatorial print head (CPH).....	24
Figure 2.3: (<i>left</i>) Fully integrated and mounted combinatorial print head (CPH) in operation. (<i>right</i>) Optical micrograph of the cross-section of the CPH showing the mixer module insertion cavity (blue dashed outline), the plasma bonded elastomeric bilayer interface, the coupling membrane between the mixing actuator and the fluid in the mixing channel (blue solid box).....	25
Figure 2.4: Schematic configuration of (a) a staggered herringbone mixer, (b) a peristaltic mixer and (c) a vibratory mixer. Magnified view of the mixing channel illustrating the expected interdigitation due to chaotic advection by passive or active mechanisms is shown below the three implementations.....	27
Figure 2.5: Color-coded schematic block diagram of the combinatorial ink formulation and thin film patterning platform showing the combinatorial print head (CPH) block (<i>green</i>), the fluid control block (<i>blue</i>), the substrate and CPH positioning block (red) and the software control block (<i>yellow</i>).....	29
Figure 2.6: (<i>top left</i>) Schematic representation of the modular CPH setup showing the configuration of the mixing channel and the structure of the enclosed ERM motor whose casing is tightly coupled with the elastomer structure, (<i>top right</i>) general operation of the mixing module including its advective effect on the binary fluid system within the mixing channel due to wall	

vibration and (*bottom*) motion of motor casing (blue) with respect to insert hole (black dashed outline) for 1 cycle of ERM rotation (t_{PERIOD}) between starting (t_{ON}) and stopping (t_{OFF}) of the haptic motor where the mixing channel is shown in purple as a consequence of mixing red and blue fluids as in the schematic above.....31

Figure 2.7: (*top left to right*) Fluid inputs 1 and 2 being fed (1:1 proportioning) into the mixing channel of the combinatorial print head (CPH) followed by mixing and printing of the proportioned fluid blend. (*bottom left to right*) Rapid mixing effect of the haptic mixer (eccentric rotating mass or ERM motor) module on the unmixed 1:1 proportioned fluid in the mixing channel. The elastomer-coupled haptic mixer module is seen in the background (blue package surface painted white to provide colour contrast).....32

Figure 2.8: Effect of haptic ERM motor vibrations on the speed of homogenization of ICP-additive fluid inputs as a function of driving current from time $t = 0.0$ s to $t = 2.0$ s in time steps of 400 ms and current steps of 25 mA. The background is the whitened motor face seen through the elastomeric coupling membrane with the brown feature being part of a circular depression in the motor packaging.....35

Figure 2.9: High speed imaging (25 frames/s from $t = 0$ s to $t = 1.28$ s) of the CPH mixing channel showing the ICP-additive pair of PEDOT:PSS (dark) and DMSO (light) being agitated by the haptic motor. The curved contour enclosing a dark surface in each frame is the outline of the haptic motor embedded within the CPH body and the length of the mixing channel segment imaged is ~ 1.5 mm.....36

Figure 2.10: Diffusive mixing as observed for 240 s at intervals of 30 s for the ICP-additive (PEDOT:PSS-DMSO) pair to illustrate the mixing time scale estimates obtained from Pe calculations. Also observed in the ICP-additive images is the outline of a stray bubble in the mixing channel near the periphery of the haptic motor which remains static throughout.....36

Figure 2.11: (a) Printed array of droplets comprising on-chip proportioned and mixed red (x) and blue (y) dyed aqueous dispersions showing corresponding compositions of rows. (b) Channel contribution from 3 sample positions (green shape) to obtain the average for a printed dot (yellow shape).....38

Figure 2.12: Row-by-row printed array of droplets comprising on-chip proportioned and mixed red (x) and blue (y) dyed aqueous solutions showing corresponding compositions of rows.....39

Figure 2.13: Comparison of pump output as a function of input flow rate proportion for each syringe pump over (a) larger flow rate range at 10 vol.% steps and (b) smaller flow rate range at 2 vol.% steps.....40

Figure 2.14: Variation of absolute (a) and relative (b) proportioning error in either pump as a function of fluid input proportioning.....40

Fig. 2.15: Proportioning error of (*left*) higher extreme of pump 1 and lower extreme of pump 2 and (*right*) lower extreme of pump 1 and higher extreme of pump 2 estimated from the position of

the blue-red interface of the bar graphs with respect to the targeted proportion. Pump 1 is represented in blue and pump 2 is represented in red.....	41
Figure 2.16: An iterative screening strategy using CPH processing of a binary fluid blend (A/B) at increasingly smaller compositional ranges and increasingly finer compositional resolution until targeted observations are made or hardware limits are reached. The outcome of each iterative step is illustrated graphically by the corresponding behavioral response quantified by Q as a function of composition.....	42
Figure 3.1: Schematic representation of the ANOVA method of using sampling distributions as estimators of the population distribution in order to accept or reject the null hypothesis. The population mean μ_{pop} and sample means μ_1 , μ_2 and μ_3 are denoted by the orange and the yellow dashed lines respectively.....	49
Figure 3.2: Sampling data distribution of two processes (“control” process shown in blue and “test” process shown in red) illustrating large (<i>top left</i>) and small (<i>top right</i>) effect sizes at identical distribution variance or small (<i>bottom left</i>) and large (<i>bottom right</i>) variance within individual data sets at identical effect sizes respectively.....	58
Figure 3.3: Sample probing (<i>left</i>) for printed channel resistance measurement with Keithley 2410 unit (<i>top right</i>) followed by stylus-based cross-sectional profile measurement using Bruker Dektak XT (<i>bottom right</i>) for evaluating electrical conductivity.....	61
Figure 3.4: (<i>left</i>) Bruker Dimension Icon atomic force microscope and its key components and (<i>right</i>) tapping mode measurement schematic methodology for topography and phase imaging...61	
Figure 3.5: (<i>from left to right</i>) Malvern Zetasizer Nano ZS for dynamic light scattering measurements, Bruker D8 Advance x-ray diffractometer, Anton-Paar Physica MCR 301 rheometer and Biolin Scientific Attension Theta tensiometer.....	62
Figure 4.1: (<i>left</i>) Structural formula of the individual 3,4-ethylenedioxythiophene (EDOT) and styrenesulfonate (SS) monomers which form the PEDOT:PSS polyelectrolyte complex, (<i>middle</i>) schematic representation of a PEDOT:PSS gel particle in dilute aqueous dispersions where the inner PEDOT-rich polycationic core (<i>orange</i>) is countered by the PSS polyanions (<i>green</i>) with the non-stoichiometric excess forming a highly solvated shell with water molecules (<i>blue</i>) distributed both within and around it, and (<i>right</i>) schematic morphological representation of dried PEDOT:PSS thin films deposited using solution processing methods and showing how the PEDOT-rich domains (<i>orange</i>) are shrouded by the excess PSS (<i>green</i>) which reduces the electrical conductivity of the film.....	66
Figure 4.2: Structural formula of the regiorandom alkoxy sulfonic acid side chain-doped monomer unit of the PSEDOT macromolecule.....	68
Figure 4.3: Ball-and-stick representation of the P2 monomer structure with the part on the left of the solid blue line representing the P1 (conductive component) monomer.....	69

Figure 4.4: Aggregate sizing of (<i>left</i>) <i>P1</i> and (<i>right</i>) <i>P2</i> 0.65 wt.% aqueous dispersions showing a primary peak ($t = 0$ s) at $\sim 1.2 \mu\text{m}$ and a secondary peak ($t = 120$ s) at $\sim 5.6 \mu\text{m}$ for both ICPs using dynamic light scattering (DLS) measurements.....	71
Figure 4.5: Shear stress (<i>left</i>) and dynamic viscosity (<i>right</i>) of <i>P1</i> and <i>P2</i> measured as a function of the shear strain rate.....	71
Figure 4.6: Measured x-ray diffraction intensities of <i>P1</i> (<i>blue</i>) and <i>P2</i> (<i>red</i>) illustrating limited crystallinity.....	71
Figure 4.7: Examples of printed thin film features comprising 20 layers showing the cross-sectional profile measurements (along the dashed yellow lines) leading to feature approximation (by dotted red lines).....	72
Figure 4.8: Electrical conductivity variation of printed channels with printed layer count for (<i>left</i>) <i>P1</i> and (<i>right</i>) <i>P2</i> while accounting for the effect of outliers.....	73
Fig. 4.9: (a) Schematic representation of contact angle differences on silver and glass surfaces along with the problem areas highlighted (<i>red dashed boxes</i>). (b) Comparative thickness mapping of electrodes and printed channels showing the large height change at the glass-electrode junction. (c) Variation of printed channel thicknesses of <i>P1</i> and <i>P2</i> as a function of layer count.....	75
Figure 4.10: AFM tapping mode phase imaging of (a, b, c, d) <i>P1</i> at 5, 10, 15 and 20 layers and (e, f, g, h) <i>P2</i> at 5, 10, 15 and 20 layers showing differences in polymer grains sizes, homogeneity of distribution and aggregate formation tendencies.....	75
Figure 4.11: Printed thin film sample library comprising multiple blend compositions (rows) with multiple replicates (columns) for each. A magnified view of a set of 3 replicates is shown enclosed by the red dashed box.....	76
Figure 4.12: Electrical resistance heat maps of resistive thin film channels printed using <i>P1-D</i> binary blends in (a, c, e) iteration 1 (10 vol.% resolution) and (b, d, f) iteration 2 (2 vol.% resolution) respectively. Scale bar in Ω	78
Figure 4.13: Cross-sectional area heat maps of resistive thin film channels printed using <i>P1-D</i> binary blends in (a, c, e) iteration 1 (10 vol.% resolution) and (b, d, f) iteration 2 (2 vol.% resolution) respectively. Scale bar in m.....	79
Figure 4.14: Electrical conductivity heat maps of resistive thin film channels printed using <i>P1-D</i> binary blends in (a, c, e) iteration 1 (10 vol.% resolution) and (b, d, f) iteration 2 (2 vol.% resolution) respectively. Scale bar in S/cm.....	80
Figure 4.15: Electrical conductivity and its coefficient of variation with blend composition for (a, c) iteration 1 and (b, d) iteration 2 for PM, UM and OM processing types.....	82
Figure 4.16: ANOVA post-hoc analyses for iteration 1 processing types (<i>P1</i> vol.% fraction denoted by the first cell in each matrix) with the upper row denoting comparisons including extreme outliers and the lower row denoting comparisons excluding extreme outliers. First row and column entries (except the first cell entry) indicate processing types.....	83

Figure 4.17: ANOVA post-hoc analyses for iteration 2 processing types (<i>P1</i> vol.% fraction denoted by the first cell in each matrix) with the upper row denoting comparisons including extreme outliers and the lower row denoting comparisons excluding extreme outliers. First row and column entries (except the first cell entry) indicate processing types.....	84
Figure 4.18: ANOVA post-hoc analyses for iteration 1 compositions (processing type denoted by the first entry in each matrix) with the upper row denoting comparisons including extreme outliers and the lower row denoting comparisons excluding extreme outliers. First row and column entries (except the first cell entry) indicate <i>P1</i> vol.% fraction in blend.....	85
Figure 4.19: ANOVA post-hoc analyses for iteration 2 compositions (processing type denoted by the first entry in each matrix) with the upper row denoting comparisons including extreme outliers and the lower row denoting comparisons excluding extreme outliers. First row and column entries (except the first cell entry) indicate <i>P1</i> vol.% fraction in blend.....	86
Figure 4.20: AFM tapping mode phase imaging of PM processed <i>P1-D</i> at (a) 90/10, (b) 70/30 and (c) 50/50 compositions and at (d) 98/02 and (e) 92/08 compositions showing the morphological evolution of the printed channels with varying volume fraction of <i>D</i>	87
Figure 4.21: AFM tapping mode phase imaging of UM processed <i>P1-D</i> (<i>top, left to right</i>) at 90/10, 70/30 and 50/50 compositions and (<i>bottom, left to right</i>) at 98/02 and 92/08 compositions showing the morphological evolution of the printed channels with varying volume fraction of <i>D</i>	88
Figure 4.22: AFM tapping mode phase imaging of OM processed <i>P1-D</i> (<i>top, left to right</i>) at 90/10, 70/30 and 50/50 compositions and (<i>bottom, left to right</i>) at 98/02 and 92/08 compositions showing the morphological evolution of the printed channels with varying volume fraction of <i>D</i>	89
Figure 4.23: Tunneling current imaging of channels printed using (<i>left</i>) pristine <i>P1</i> and (<i>right</i>) the 90/10 composition of the <i>P1-D</i> blend showing decrease in the spatial separation <i>S</i> between conductive states on the probed channel surface.....	90
Figure 4.24: Temperature dependence of electrical conductivity in pristine <i>P1</i> and <i>P2</i> over the range of 20°C to 60°C.....	91
Figure 4.25: ANOVA post-hoc analyses of the pristine ICPs (ICP type denoted by the first entry in each matrix) with (<i>upper row</i>) and without (<i>lower row</i>) extreme outliers. First row and column entries (except the first cell entry) indicate temperature in °C.....	92
Figure 4.26: Temperature dependence of electrical conductivity in <i>P1-D</i> blends for processing types PM (<i>top left</i>), UM (<i>top right</i>) and OM (<i>bottom</i>).....	94
Figure 4.27: Electrical conductivity behavior of (<i>left</i>) pristine <i>P2</i> and <i>P1</i> blends and (<i>right</i>) pristine <i>P2</i> and secondary doped <i>P1-D</i> (90/10) blends as a function of ambient temperature.....	95
Figure 4.28: AFM tapping mode phase imaging of (<i>top left and right</i>) <i>P2-P1</i> blends at 90/10 and 50/50 and (<i>bottom left and right</i>) <i>P2-P1-D</i> blends at 90/10 and 50/50.....	97

Figure 4.29: Interpolated electrical conductivity response of (*left*) P2-P1 blends and (*right*) P2-P1-D blends across 90/10 to 50/50 compositions and 20°C to 60°C temperatures. Scale bar in S/cm.....98

List of Abbreviations

AFM	Atomic force microscope
ANOVA	Analysis of variance
APCVD	Atmospheric pressure chemical vapor deposition
CPH	Combinatorial print head
DMSO	Dimethyl sulfoxide
HfO ₂	Hafnium dioxide
ICP	Intrinsically conductive polymer
LPCVD	Low pressure chemical vapor deposition
OL	Outlier(s)
OM	On-chip mixed
PCBM(70)	Phenyl-C70-butyric acid methyl ester
PCDTBT	Poly[N-9'-heptadecanyl-2,7-carbazole-alt-5,5-(4',7'-di-2-thienyl-2',1',3'-benzothiadiazole)
PEC	Polyelectrolyte complex
PEDOT:PSS	Poly(3,4-ethylenedioxythiophene) polystyrene sulfonate
PffBT4T-2OD	Poly[(5,6-difluoro-2,1,3-benzothiadiazol-4,7-diyl)- <i>alt</i> -(3,3'''-di(2-octyldodecyl)-2,2',5',2'',5'',2'''-quaterthiophen-5,5'''-diyl)]
PLD	Pulsed laser deposition
PM	Premixed
PSEDOT	Poly(self doped-ethylenedioxythiophene)
PTB7-Th	Poly([2,6'-4,8-di(5-ethylhexylthienyl)benzo[1,2-b;3,3-b]dithiophene]{3-fluoro-2[(2-ethylhexyl)carbonyl]thieno[3,4-b]thiophenediyl})
SnO ₂	Stannic oxide
TCR	Temperature coefficient of resistance
TiO ₂	Titanium dioxide
UM	Unmixed
W	Wolfram

Acknowledgements

I would like to express my heartfelt gratitude to my supervisor Dr. Konrad Walus for providing me with the opportunity to carry out this research in his laboratory and for his steadfast academic, moral and financial support. I would also like to sincerely thank my doctoral committee members Dr. Boris Stoeber and Dr. John Madden for their invaluable guidance and continued encouragement. I would like to thank Dr. Matthew Yedlin, Dr. Mu Chiao, Dr. John Frostad and Dr. Dana Grecov for accommodating the different milestone examinations during this period. I would also like to thank Dr. Yuning Li for his suggestions as the external reviewer which helped to improve certain aspects of the dissertation. I will always be indebted to Dr. Kenichi Takahata who enabled me to begin my journey here and also helped me transition between different research domains. I am grateful to Dr. Mario Leclerc, Dr. Gregory Welch, Dr. Chloé Bois, Dr. Ngoc Duc Trinh and Dr. Michael Wang for their advice and support at various stages of this work.

I've been privileged to have the friendship of Amitava, Sreya, Shirsa, Sonakshi, Raghavendra, Divya and Sneha in uncertain times and I'm sure these relationships will only grow richer. Sincere gratitude is owed to Nathan and Catherine, without whose software development and material synthesis skills, a lot of this work would not have been possible. The time spent working in the lab would not have been as fulfilling without friends like Justin, Sajana, Lakshmi and Nina around with their ever helpful and positive demeanor. This space is not enough to detail my appreciation for all who have been part of this but I would like to earnestly acknowledge Gourav, Anwit, Anirban, Gaurab, Anujit, Madhumanti, Rajarshi, Soham, Sudipta, Manabendra, Pradeep, Reeshav, Oindrila, Avik, Ankita, Snahungshu, Manisa, Debojit, Arpita, Sudipta, Anand, Sadhvi, Soumali, Soutomi, Alivia, Arin, Moumita, Debashish, Ananya, Shantanu, Anuradha, Amit, Chris, Simon, Christoph, Ezequiel, Anas, Padma, Sheng, Suresha, Ajay, Simon, Maziyar, Farzad, Madesh, Babak, Lotfi, Ahmed, Ying, Jiaxu, Xiaotong, Sam, Chang, Carlos, Jorge, Yunhuan, Nicholas, Claire, Adam, Saquib, Yuta and Emad for their intangible contributions towards this work.

I would like to thank my parents and my late grandparents without whose sacrifices, love and nurturing, I would not be the person I am today. I hope to be able to honor the life lessons that you have taught me in different aspects of life. Finally, I would like to thank Amrita who has been my rock during stressful times and my inspiration during times of despair, without whose support this journey would have remained quite incomplete.

To my parents, grandparents and teachers.

Chapter 1: Introduction

1.1 Motivation: Towards combinatorial evaluation of thin films

1.1.1. The evolution of thin films

“Thin films” can be defined as single or multiple layers of any material ranging in thickness between a few angstroms ($\sim 10^{-10}$ m) to a few tens of micrometers ($\sim 10^{-5}$ m) [1]. Milton Ohring describes thin film technology as “one of the oldest arts and one of the newest sciences” [5] given that the ancient crafts of gold beating and gilding dates back millennia, often achieving sub-micrometer leaf/film thicknesses. Besides mechanical modification of malleable materials such as metals into thin sheets and films, there was another method of significant importance in the field of coatings which used completely different starting materials and was even older than the aforementioned method. Dry and wet pigments have existed as part of human society for many millennia and although their mode of application differed, they could both be rendered into thin films and coatings. Since then, thin film preparation has come a long way with new materials and methods being identified and implemented in various coating applications as the centuries passed. Over the 19th century and especially after the turn of the 20th century, thin films no longer remained an art form to be only admired in sculptures and architecture. Scientific advancements such as the refinement of vacuum processing technology [6] [7] [8] and a deeper understanding of matter at the atomic level unlocked the immense potential of thin films and accelerated research and development for industrial and commercial applications.

Besides functional coatings [9] [10], the semiconductor processing industry has been one of the major drivers of growth in thin film research, especially since the invention of the solid-state transistor [11] [12] [13] by William B. Shockley Jr. along with his colleagues John Bardeen and Walter H. Brattain in 1947. As a consequence of such high levels of regular requirement, thin film deposition methods have been and are still being consistently refined to deliver high performance while simultaneously being resource economical. With rapid increase in demand, the variety of thin film processable materials has exploded over the past few decades. In addition to conventional solid-state electronic materials used in the microelectronics, many unconventional materials such as polymers, biomaterials, carbon allotropes, quantum dots and other such exotic material systems have come to the fore. These materials have found applications in chemical and biological sensors [14] [15] [16] [17] [18], actuators [19] [20] [21] [22], photovoltaics [23] [24]

[25], thermoelectrics [26] [27], ferroelectrics [28] [29] [30] and printable electronics [31] [32] to name a few. Fig. 1.1 illustrates the gamut of applications of thin films that are typically in use today. In each of these applications, achieving optimal performance of pristine [33] and/or composite [34] material layers in the final structure is essential. While the physical combination of individual components in multi-material systems may be conceptually simple, possible complexities in intra/inter-layer interactions and unpredictability of hidden factors can make the process of evaluating cause-effect relationships analytically very challenging [35]. Consequently, new techniques as well as modifications to existing methods for addressing the above problem are being continually developed.

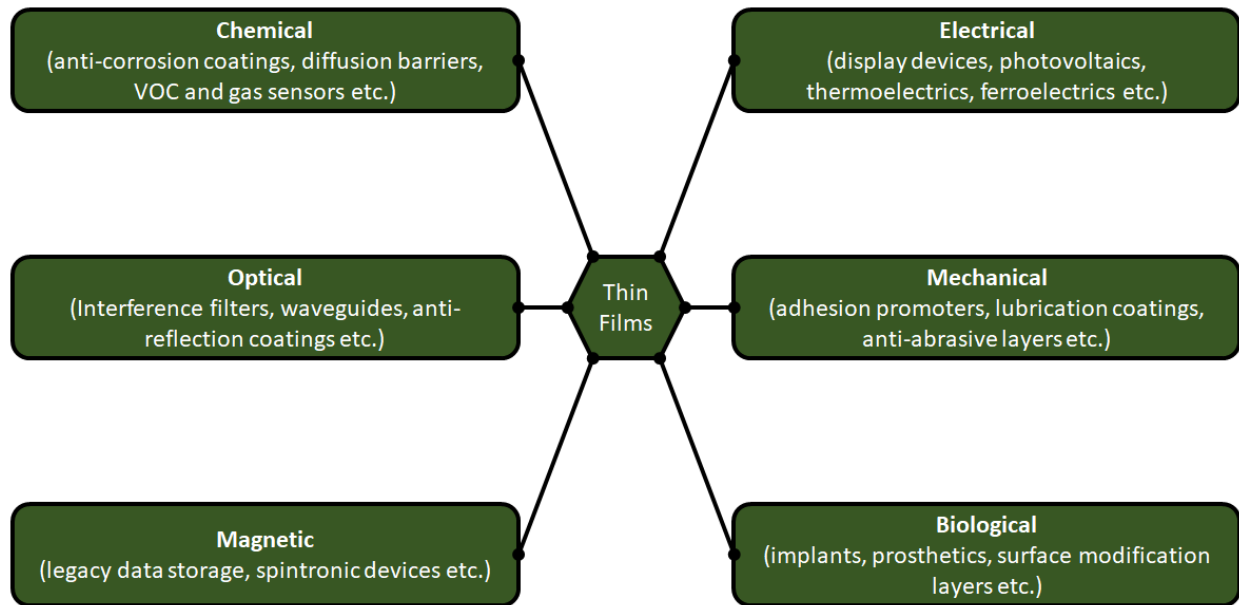


Fig. 1.1: Applications of thin films in diverse fields of commercial and academic research and development.

1.1.2. Combinatorial screening as a thin film evaluation methodology

One of the most widely used empirical solutions to the problem of property investigation of multi-material systems is the method of combinatorial evaluation and/or screening [36] [37] [38] [39]. Combinatorial evaluation can usually be thought of as the interrogation of multi-material systems comprising varying proportions of individual components in order to understand the effect of composition on the specific property being studied. This method may be iterative which involves examining progressively finer resolution coverage of increasingly narrower composition ranges of interest as the property optimum is approached [40]. However, non-iterative methods may be used when the scope of investigation is limited to available predefined options which then

effectively becomes a selection problem [41]. While the latter method may be applicable to many screening problems, the former method is explored in this work to test the limitations of sample preparation. Fig. 1.2 schematically illustrates the overall flow of logic for a typical iterative combinatorial evaluation cycle. As a methodology, it involves multiple steps starting from the design of the experimental evaluation protocol for the system (Step 1) based on the behavior of appropriate response variables across a set of samples referenced against prior literature. Response variables are generally chosen to be explicitly measurable or computable quantities which can be used to characterize the property under test. The response variable is often a function of multiple factors that may be classified in accordance with the stage at which they affect the system, as we shall see subsequently.

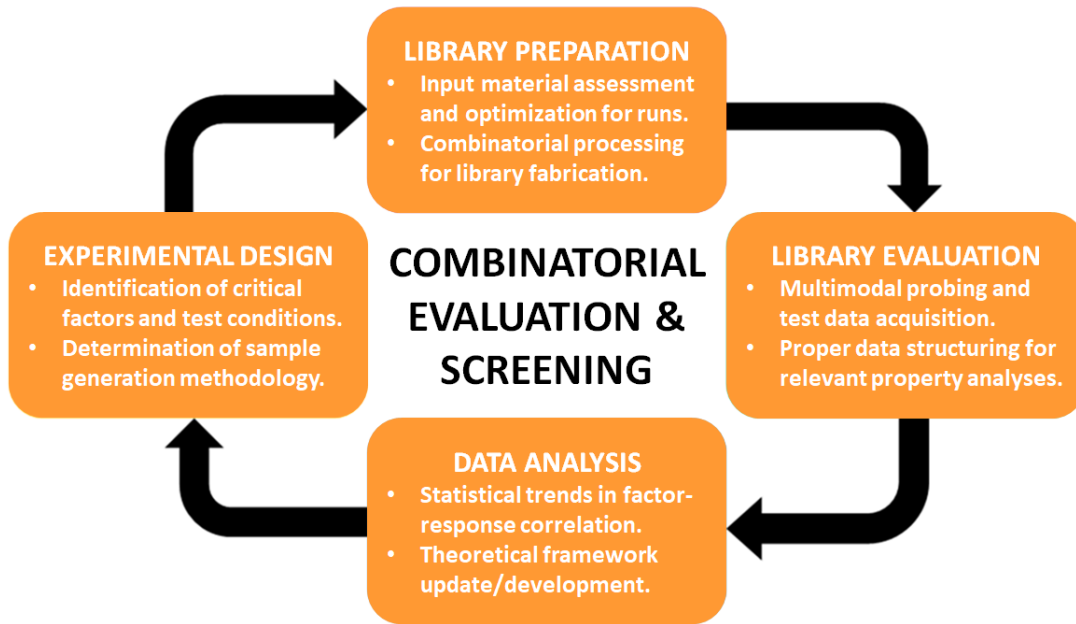


Fig. 1.2: The cycle of combinatorially evaluating and screening multimaterial systems on the basis of the specific properties being investigated for deployment in targeted applications through iterative processing.

The experimental design step is followed by the rendering of the multi-material system into test samples for property characterization (Step 2). This step may involve different manufacturing techniques where factors such as the manufacturing conditions and sample composition determine the nominal behaviour of the response variable when tested under standard conditions. The experimental protocol laid out in Step 1 paves the way for combinatorial sample library preparation based on the premise of rapidly generating multiple replicates of multiple compositions for statistically significant conclusions to be obtained from the testing step. By its very definition, any

combinatorial sample library seeks to increase its sample count, often by leveraging the advantages of process automation and library size minimization up to the hardware limit in order to improve the accuracy of inferred information in Step 3 where the prepared sample library is tested. This increase in sample count can be achieved in a two-fold manner: (i) through an increase in sample resolution and (ii) through an increase in sample replicates. Here, sample resolution refers to the difference in processing conditions used to generate a set of samples with different operational performance within the overall sample library. Sample replicates, on the other hand, are simply copies of a library component generated under identical processing conditions. It can be intuitively understood that the former tracks the average behaviour of the response variable across the entire compositional range being investigated while the latter probes the variability of the response at each individual processing condition within that spectrum. During Step 3, these sample library components are characterized using different methods (electrical, optical, morphological etc.) and are used to obtain a clearer idea of the expected behaviour of the property being interrogated. Step 4 is the final step in the cycle where the inferences drawn from the data generated in Step 3 are coherently reconciled with the existing general framework of similar material classes to validate new hypotheses or update existing ones, both theoretical and empirical.

Research on combinatorial evaluation of multi-material systems expanded rapidly during the 1990s as a sample formulation protocol for the preparation of peptide libraries [42] with the method being later used extensively for pharmaceutical exploration [43] [44] [45]. With advances in material formulation and synthesis techniques over the years, the method has branched out into other fields [46] [47] [48] [49] [50] involving some form of material development. The scale and scope of the implementation of combinatorial evaluation methodologies has varied widely [51] [52] [53] depending upon specific applications with different process variants used. Their favourable impact on materials research and development can be attributed to the ability of the process to reveal underlying interaction mechanisms due to complex dependence of multi-material system performance on component proportions which requires evaluating the different subsets of the overall composition range at different resolutions. Fabricated combinatorial libraries are subjected to various characterization methods demanded by the particulars of the application, allowing optimal material compositions to be selected for further development. One such application of the technique in recent years has been in the domain of thin film processing [54] [55], which has seen widespread usage for a diverse range of research applications. Among some

of the most commonly implemented combinatorial methods, the contribution of automation and miniaturization to the success of the overall process deserves specific mention. Custom modifications in the implementation of these strategies have been at the forefront of combinatorial material evaluation with different groups focusing their research efforts on either library formulation or library testing process or both. For convergence with the scope of this work, the relevant background on combinatorial thin film formulation and fabrication is discussed in the paragraphs below which illustrates the advantages and limitations of the different methods used and where the current work fits in.

Physical [56] [57] [58] and chemical [59] [60] [61] [62] vapor deposition of thin films have been the mainstay of the general process of fabricating micro/nanoscale devices. Physical methods involve no chemical interactions among the species in the vapor while chemical methods utilize the reaction of precursor materials in the vapor phase, both under specific processing conditions to deposit compositionally tailored thin films on substrates. Fukumura *et. al.* [63] demonstrated the utility of modifying one such physical vapor deposition method by using automated moving shutters in a pulsed laser deposition (PLD) system to realize continually graded thin film sample libraries for the evaluation of Mott insulators. While functionally similar to laser-assisted material vaporization methods, sputtering is another physical vapor deposition technique where energetic ions are used to bombard some material target(s), resulting in material ejection and deposition on appropriately placed substrates. This technique was employed by Siol *et. al.* [64] to fabricate indium sulphide ($\text{In}_x\text{S}_{1-x}$) libraries with variable stoichiometry achieved by controlling the partial pressure of sulphur in the process chamber. Apart from deposition processes, vacuum-enabled thin film growth methods are also equivalent techniques for fabricating combinatorial sample libraries as demonstrated by Mao [65]. In this case, a pulsed laser-assisted epitaxial growth process was used in conjunction with sequential masking to obtain 256-sample libraries on single substrate. Smith *et. al.* [61] modified an LPCVD reactor by controlling its precursor flow dynamics and deposition kinetics to create compositional spread in metal dioxide (TiO_2 , SnO_2 and HfO_2) thin films, a technique that was later adapted for an APCVD reactor by Kafizas *et. al.* [62] through specific spatial distributions of reagents to combinatorially dope anatase TiO_2 with W. While vacuum-based physical and chemical vapor deposition and growth processes are capable of accurately controlling film composition and thickness, they mostly deal with traditional inorganic materials and always must be patterned to their final geometry in an additional processing step. In

addition, their operational regimes often require extremes of temperature and thus, are unsuitable for most organic polymer materials that are being increasingly adopted for economical and massively scalable applications such as flexible and wearable electronics, sensors and textiles. Consequently, as combinatorial formulation involving automated sub-systems within conventional thin film growth and deposition tools was being explored, solution-based processing of thin films was making inroads due to key advantages such as reduced processing costs, higher versatility in handling organic polymer materials and processability over different substrate areas and material volumes to name a few methods. To this end, Sanchez-Diaz *et. al.* [66] demonstrated an automated blade coating technique for fabricating polymer thin films using PCDTBT, PTB7-Th and PffBT4T-2OD with PCBM(70) to evaluate their photovoltaic potential while Teichler *et. al.* [67] illustrated the benefits of robotics in thin film printing, making use of a pipetting arm to rapidly formulate large sets of PCPDTBT and PCBM polymer blend samples at different compositions which were then fed to inkjet cartridges for dispensing. These methods were improved upon significantly by Macleod *et. al.* [68] by expanding the utility of an automated robotic arm from a simple pipetting tool to one used for sample manipulation at various stages of their spin coating-based material discovery process. Despite these techniques being highly effective for organic thin film material screening by virtue of being amenable to room temperature processing under atmospheric pressure conditions, their material volume requirements can limit their utility in processing low-yield novel materials that are often expensive to synthesize. Therefore, there is scope for further contribution in organic sample formulation and patterning systems towards improving their economy of volume requirements while enabling processing under standard ambient conditions.

Besides automation, which broadly aims for time efficiency, process precision and repeatability, miniaturization has also been used as a strategy to material economy besides the obvious reduction in spatial dimensions. It is to be noted that automated systems may use miniaturization techniques as well to incorporate the benefits of spatial compactness and material economy along with their aforementioned qualities. Miniaturization can be achieved by the reduction in sample dimensions, inter-sample spacings as well as individual sample volumes. Sample library miniaturization along these lines was shown to be time effective during the evaluation of electrocatalysts by Reddington *et. al.* [69] based on processed materials printed as 16-sample array units (1 cm² per array unit) to create quaternary performance maps. In a

comparable manner, Woodhouse *et. al.* [70] printed spatially dense ternary oxide droplet arrays to identify new oxide blends for the photoelectrolysis of water. Process automation and sample miniaturization have significant impact on the statistical analysis of response variables for data inferencing and performance quantification. Greater degrees of precision and repeatability afforded by process automation may be useful in discerning sensitive phenomena that may otherwise remain shrouded by sample-to-sample fabrication variability. The increased sample replicate count due to sample miniaturization can complement this by reducing metrics like the standard error which may further lower the probability of missing critical effects quantified by the response variable(s).

Typical statistical inferencing of combinatorial test data on organic polymers and polymer blends is performed using *t*-tests [71] [72], chi-square tests [73] [74] and ANOVA [75] [76], both of which rely heavily on sample replication as they seek to detect significant differences among combinatorially prepared samples. Irrespective of the method used, Malo *et. al.* [77] argue that replication is central to improving inferencing reliability through increased sensitivity of the statistical analyses. It is evident that characterization schemes need to be chosen based on the sample preparation approach adopted and what works for a point sample may not necessarily work for an extended sample. Conversely, not all characterization techniques have similar sample size requirements and while this may seem thematically akin to the previous statement, it actually brings out the fact that the choice of both the formulation and testing method play vital roles in the seamless development of any combinatorial evaluation protocol. These examples, while by no means exhaustive, do help to illustrate the advantages of implementing process automation [78] and sample miniaturization [79] in the field of materials research. Most combinatorial screening methods, be they targeted towards sample library formulation or sample library testing, utilize some variation or combination of the above in order to achieve resource efficiency. The aim of this work has been to incorporate both aspects of automation and miniaturization, to a certain degree, in order to reap the benefits of an overall resource economical process which is general enough to have potential avenues of modular feature modification and performance enhancement in the future. The sample preparation approach adopted in this work does not require any extremes of ambient conditions which makes the method compatible with a vast array of thin film materials that cannot be processed using the conventional vacuum-assisted thin film growth and deposition methods covered earlier. Additionally, its economical material volume requirement helps

circumvent the material wastage issues faced by the solution processing methods. Finally, this method has the ability to formulate homogenized material blends using minimal material volumes, something achievable neither by the vapor-phase or by the solution-phase processes developed in prior literature.

Table 1.1: Some standard strategies used for combinatorial screening of materials.

Classification	Typical strategies	Remarks
Array strategies	Gradient arrays [80]	Rapid sample generation for sample performance evaluation
	Masked arrays [81]	
	High-speed conventional arrays [82]	
Parallel strategies	Representational approach [83]	Selective evaluation of subsets from very large sample pools
	Indexed library approach [84]	
	n-way combinations approach [85]	
Data-driven strategies	Randomized runs [86]	Unknown sample chemistry and/or process parameters
	Metaheuristic approaches [87]	
	Software/ML methods [88]	

Combinatorial methods in the field of material development are generally used to search for optimal materials and/or material systems from an extensive sample set based on a relatively limited understanding of such material systems and their interactions. Any standard combinatorial screening strategy employs rapid formulation or rapid testing or a combination of both. This work primarily deals with the rapid sample library preparation aspect of the screening process. As with any process, there are certain trade-offs that are introduced with the combinatorial evaluation of materials, namely the iterative nature of the process and the need for integrated sample fabrication and testing. The former is useful in obtaining first impressions of the materials being interrogated but intensive characterization of the material is not really viable due to the time economy which is a key motivator for combinatorial methods in the first place. With increase in the understanding of variably formulated multi-material systems using hierarchically iterative testing, the number of potentially relevant factors and their ranges decrease based on the research problem at hand. This allows more involved experiments to be conducted on smaller sample sizes to obtain deeper

insights into the relevant factors and their direct and indirect effects. The latter addresses the time economy by integrating the fabrication and testing processes on a single platform. While this enables rapid sample preparation and characterization, integrated platforms have their fair share of limitations regarding the type of fabrication method and the diversity and fidelity of the characterization methods that can be synergistically combined to facilitate the level of intensive evaluation possible using stand-alone fabrication and testing systems.

Table 1 lists some of the different methodologies used for combinatorially evaluating novel multi-material systems. Proper sample formulation plays a central role in the development and optimization process of any material or multi-material blends and all of these listed strategies generally begin with the preparation of a large sample set as determined by the relevant process parameters and the required granularity of observation. For example, array-based strategies [80] [81] [82] typically deal with functionally graded samples that are designed to represent the grading granularity or compositional resolution in the form of a matrix which can then be directly probed for optima. These methods are generally used to study material systems whose functional response is often not simply a proportional sum of its components but also involves complex interactions between them. Parallel strategies are employed in situations where the functional response of the material system is usually a proportional sum of its components [83] [84] [85]. However, the sheer number of combinations of material components and factor variables results in extremely large sample sets if considered exhaustively. Despite the fact that these methods make meticulous use of prior experimental data on similar material systems to optimize the output of the response variable, it is not possible to know exactly how a new material or a multi-material blend will respond when probed with different characterization tools at different levels of factor variable resolution. Consequently, the compositional variation between any two samples has to be minimal to begin with in order to cover the relevant spectrum of compositions without missing key aspects of the response variable and such high factor variable resolution makes the size of the sample set unavoidably large. In case of entirely new material systems, however, data-driven combinatorial strategies are applied with certain bounds that are usually set at the outset of such a developmental initiative. This is because novel material systems that apparently have no predecessors can run into a compounded problem where the requisite granularity of resolution of a factor variable is high and the functional response is not linearly proportional to the factor variable. As a result, the sample sets can quickly become almost unmanageable at larger processing scales. Thus, some

commonly established bounds on combinatorial experimental design include, and are not limited to, minimization of the number of experimental runs within a randomized test framework [86], capping of component fractions in mixtures, constraints related to process equipment and others. Implementation of these bounds involve methods like nuisance factor blocking, machine learning (ML) tools for enhanced designs [87] and software-assisted generation of sample compositions, process parameters and sample sizes and replicates necessary to draw meaningful conclusions [88]. In essence, these bounds are imposed to limit the total sample pool from exploding which is impractical in terms of resource investment and in that sense, are quite similar to some of the more conventionally parallel strategies. While the typical strategies listed for each classification type can be thought of as a general template to go about a particular evaluation and screening process, it would indeed be erroneous to limit ourselves by the assumption that individual aspects of the different strategies cannot be combined to construct optimized protocols with improved outcomes.

1.1.3. Utility of thin film solution processing

The manufacturing of low-cost organic electroactive devices has seen major advancements with the assimilation of solution processing methods [89] [90] [91] within the diverse spectrum of thin film deposition techniques. These methods, while not very new themselves [92], were confined exclusively to certain fields and were not used very extensively for thin film deposition due to limitations in the choice of solution-processable materials. However, with the emergence of interdisciplinary research and accelerated development of novel materials, the accessibility and acceptance of a wide range of solution processable materials have increased manifold within a few decades. This was especially true for those materials which were incompatible with traditional thin film deposition processes which often required extreme conditions such as very low pressures and high temperatures. Hence, thin film deposition of such sensitive materials is performed with relative ease using solution processing techniques. Solution processing techniques are thin and thick film fabrication methods where the materials are deposited from a solution on to the fabrication surface. This is achieved by distributing the solution (or dispersion) on to the substrate in a specific manner and drying the solvent or the dispersing liquid phase, often through exposure to elevated temperatures [93] or by curing the deposited pattern with electromagnetic radiation such as UV light [94]. Standard solution processing comprises methods such as spin coating, slot-die coating and doctor blading. Each of these techniques require the solution phase of the material to have specific physical properties such as viscosity, surface tension and fluid inertia. Generally,

a number of different standard solution processing methods are required to fabricate a multi-material multi-layer device, and this not only incorporates different solutions, but also different equipment to fabricate different layers of the device. Therefore, while the methods themselves may be cost-effective, the process complexity of integrating different approaches are quite high.

Specialized techniques implementing the holistic definition of solution processing are also included within the methodological framework without any loss of generality. These consist of printing techniques where the solution volume is tailored prior to deposition on to the fabrication surface resulting in greater control of the quantity of material being deposited. Perhaps the most popular of these printing techniques is inkjet printing which can create pre-programmed patterns comprising small droplets of ink. Due to its additive nature and the ability to dispense almost any material provided it meets certain physical criteria such as bounds on viscosity and surface tension; it can be a valuable tool for fabricating multi-material multi-layered electroactive devices. This method bypasses the need for integrating different solution processing methods, thereby reducing process complexity and enhancing time efficiency. It is precisely this niche that can be addressed by customized implementations of inkjet printing [95] [96]. As a highly versatile method, inkjet printing holds immense potential for the synergistic integration of microscopic and macroscopic domains. This is because of its ability to handle materials at the droplet level while printing large-area structures comprising these droplets as their building blocks. Scalability of such a process is critical and multi-dispenser inkjet printing systems have been central to the realization of multi-material deposition systems [97]. The customizability of inkjet printing is subject to the specific application being explored and factors of interest such as range of inks, ink composition, print throughput etc. determine which aspect needs to be prioritized. Standard and customizable facets of inkjet printing along with some of its applications relevant to this work is discussed in the following subsections.

1.1.4. Inkjet printing for specialized applications

The most widespread use of inkjet printing technology is in the field of textual and/or graphical document printing. Economical inkjet printing of fluids is accomplished by using either thermally or piezoelectrically actuated dispensers capable of ejecting droplets on demand unlike continuous inkjet printing. Thermal dispensers incorporate electrically heated elements that are coupled with the inks to create expanding vapor bubbles which act as pressure pulses to form ink

droplets. Piezoelectric dispensers utilize the deformation of piezoelectric elements to generate the pressure pulses for ink droplet formation similar to thermal inkjet but without the added temperature effects on the inks. Therefore, piezoelectric dispensing is compatible with a wider range of materials and is slowly replacing thermal dispensing in inkjet systems. Many unique features of inkjet printing technology make it attractive for other applications too, such as scientific and industrial research and development. Its capacity to generate picoliter-sized droplets on demand at high dispensing rates with micro/nanoliter-level dead volumes along with its ability to print on diverse substrates in a contactless manner are the key features which have sparked interest in its applicability to experimental research problems. Upon integration with motorized stages, it can be used to generate programmable patterns of functional materials which complements the field of conventional solution processing of thin and thick films and coatings. The inherent volume efficiency of inkjet printing has advantages in domains requiring manipulation of minimal volumes of low-yield and expensive materials with minimal waste. High droplet dispensing rates facilitate the enhancement of printing resolution while non-contact patterning reduces the risk of dispenser contamination besides preserving the integrity of the printed features during operation.

Consequently, inkjet dispensers have been used to print a variety of materials to enable and improve applications ranging from functional coatings to integrated sensors and actuators. In direct pertinence to the theme of the work presented here, inkjet printing has played a major role in the advancement of electroactive thin film solution processing. Sirringhaus *et. al.* demonstrated the first implementation of inkjet printed polymer thin film transistors (TFTs) and functional materials in general [98] [99] which laid the groundwork for the development of printed electroactive displays. Photovoltaic applications were soon illustrated by Hoth *et. al.* [100] who used inkjet printed polymer-fullerene blends comprising regioregular poly(3-hexylthiophene) (P3HT) mixed with fullerene [6,6]-phenyl C61 butyric acid methyl ester (PCBM) to develop solar cells with appreciable efficiencies. Torrisi *et. al.* [101] followed up soon after by demonstrating the inkjet printability of graphene-based inks for TFTs and proposed its use on other electroactive materials such as transition metal compounds. Beyer *et al.* [102] controlled the alignment and orientation of carbon nanotubes (CNTs) facilitated by inkjet printing of CNT dispersions which was shown to result in high performance electroactive channels. A promising customization of inkjet printing is reactive inkjet (RIJ) printing where droplets are deposited at predefined sites on the substrate for chemical reactions to occur. This method is primarily used as a chemical synthesis tool which

allows functional materials to be synthesized *in situ* at the same time as their final device geometries are patterned. Lemmo *et. al.* [103] pioneered the use of inkjet dispensed droplets as individual chemical reactors for synthesizing combinatorial libraries on substrates. Since then, droplet mixing has been studied extensively and utilized for RIJ printing of functional 2D and 3D structures. Often, the substrate too plays a part in the chemical process other than simply providing a surface for the reaction to occur within the droplet. As examples of this method, Grimaldi *et. al.* [104] used the technique to etch polyimide and polystyrene thin films to create microlens arrays while Yoshioka *et. al.* [105] printed H₂O₂ on to a poly(3,4-ethylenedioxythiophene) poly(styrene sulfonate) (PEDOT:PSS)-modified substrate to control the PEDOT:PSS oxidation state thus allowing digital patterns to be converted into electroluminescent patterns. Thus, the inkjet printing process by itself may also be used in different modes of operation to achieve combinatorial functionality.

1.1.5. Microfluidic compatibility with inkjet printing

While RIJ printing is an elegant concept for tuning droplet compositions on substrates, it is heavily dependent on the droplet evaporation rate as well as intra-droplet mixing dynamics. This intuitively implies that the time scale of the mixing process should be greater than the time scale of the evaporation process for any degree of homogenization to occur. Additionally, such a method of homogenizing droplet components is viable only on substrates which are impervious to fluids which immediately restricts its application to a certain class of substrates only. It is therefore preferable of the mixing process to happen before or within (upstream) the print head rather than beyond it (downstream) where there are competing factors which can often impede proper homogenization.

Most of the work done on on-chip microfluidic mixing has been stand-alone applications such as generating mixed samples for static deposition on to substrates for point-by-point analyses. Various passive and active mixing methods have been employed but most of these have been targeted towards lab-on-chip systems and consequently, there had been no requirement of integration with dynamic patterned dispensing capabilities. Mohebi *et. al.* [106] implemented an active mixing module upstream to an inkjet dispenser module for printing ceramic dispersions using off-the-shelf components and a mixing chamber volume of ~250 μ l which empirically demonstrates the economy of material usage afforded by such integration. However, the volume

waste was at least an order of magnitude greater than what microfluidic processing can achieve. Later, Bsoul *et al.* [107] demonstrated an inkjet dispenser capable of being integrated with upstream microfluidic mixing for printing biochemical materials but it was a passive mixer implementation whose inputs lacked quantitative proportioning and was incapable of rapid processing. The successes and limitations of these studies reinforce the motivation for this work to develop a microfluidic-enabled inkjet printing platform which is capable of rapid mixing of accurately proportioned multi-material fluid inputs upstream that is followed by patterned inkjet dispensing downstream. As a result, the serial operation of microfluidic preprocessing and inkjet printing forms the core of this work as will be seen in subsequent chapters.

1.2 Electroactive organic polymer thin films

1.2.1 Polymers and electrical conductivity

Polymers are a class of large molecules that are often termed as “macromolecules” due to their relatively large sizes in terms of the number of constituent atoms. The key feature of such macromolecules is that from a structural perspective, they are composed of smaller repeating units called “monomers”, chemically bonded to form long chains. If the entire molecule comprises a single type of repeating unit or monomer, the polymer is classified as a “homopolymer” while the presence of more than a single monomeric unit results in the polymer being classified as a “copolymer”. Generally, the term “polymer” encompasses both polymers and oligomers. While the structural idea of both stems from the fundamental concept of multiple repeat units (monomers) covalently bonded to each other, oligomers differ from polymers in the degree of polymerization which is on the lower side for the former and on the higher side for the latter. Henceforth, the term “polymer” will be used as an umbrella term to denote both types of macromolecules.

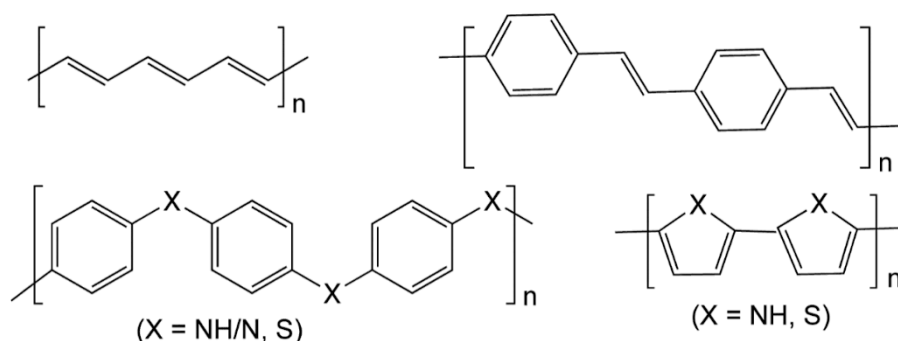


Fig. 1.3: Examples of conjugated conductive polymers include (clockwise from top left) (i) polyacetylene (ii) polyphenylene vinylene (iii) polypyrrole and polythiophene and (iv) polyaniline/polyphenylene sulfide.

Conjugated polymers are a subclass of homo/hetero-atomic organic compounds that are typically identified by their alternating single bond-double bond structure and can range from simple linear chains like polyacetylene to heterocyclic rings like polythiophenes [108] [109]. The occurrence of this conjugation along the macromolecular backbone serves to make the chemical structure rigid towards rotation about double bonds while also giving rise to π -bands which enable charge transport that can lead to electrical conductivity. Intrinsic or neutral conjugated polymers are typically insulating or at most, semiconducting in nature. Some common conjugated polymer structures including polyacetylene and polythiophenes are shown in Fig. 1.3. The idea of “doping” in conductive polymers, while considered an analogue to the doping process of semiconductors, is simply a well-intentioned misnomer for an oxidative or a reductive chemical reaction. The use of an oxidizing agent corresponds to *p*-type doping and the use of a reducing agent corresponds to *n*-type doping [110]. It is this charge generated on the conjugated backbone due to the chemical reaction process that is transported through delocalization of π -electrons when the polymer is subjected to an externally applied electric field.

1.2.2 The need for polymer electronics

With rapid adoption of the technology known as the internet of things (IoT), a dense distribution of sensors and circuits networked among themselves for seamless flow of information is becoming increasingly imperative [111]. This means a significant fraction of these devices have to be simple, low-cost sensor-circuit assemblies built on lightweight, flexible insulating polymer substrates by printing electroactive inks. Given that large-scale deployment of these devices is targeted towards improving the quality of life, it is expected that such printed sensor assemblies will transform traditional consumer products such into “smart” products that are “aware” of their surroundings through tracking and monitoring of the ambient status (temperature, humidity, orientation etc.). An example of this is smart packaging which, by its very nature, is an extremely pervasive entity literally enveloping almost all consumer products. By its very definition, it should be capable of detecting effects such as temperature [112] and humidity [113] variations and mechanical shocks [114] and indicate when corrective action is needed to prevent irreparable damage to the packaged product. Low-cost manufacturing is essential to this vision of the IoT to enable the fabrication of devices inexpensive enough to be disposable, particularly for consumer packaging.

Scalable printing technologies are therefore ideal for the cost-effective fabrication of such smart components. However, the sheer number of connected devices forecast [115] for the IoT also makes it essential that both the fabrication processes and end-of-life disposal of devices leave minimally adverse environmental footprint. Electroactive components that are currently made from inorganic conductors and semiconductors are both expensive and poorly recyclable. As potential alternatives, solution processable electroactive polymers are particularly promising because they combine material processability and mechanical compliance with conducting and semiconducting properties that can be integrated into robust components during their lifetime and readily degradable for their end-of-life processing. The use of these organic materials to replace components of electronic devices such as electrodes and insulating layers or utilize them for their sensing and actuation capabilities would allow for the production of greener low-cost devices. Most research on printable electronics, academic or industrial, is driven almost exclusively by device performance with limited regard for the critical factors of sustainability and environmental impact. To become a viable manufacturing technology, a general shift needs to be made towards environmentally benign materials and processing methods and organic electronics can play a key role in that regard.

1.2.3 High conductivity ICPs

Table 1.2: Typical applications of the commercial-grade ICP poly(3,4-ethylenedioxythiophene) poly(styrene sulfonate) (PEDOT:PSS).

Application	Functionality	Processing	Material forms
Solid electrolyte capacitors, OSCs, OLEDs and other printed displays.	Cathodes, transparent electrodes, hole injection/transport layers.	Chemical polymerization, printing.	PEDOT:PSS, PEDOT:polymer.
Photographic films, packaging films and touchscreens.	Anti-static layers.	Coating, printing.	PEDOT:PSS
Thin film sensors and actuators.	Multifunctional responsive layers (temperature, light, stress, moisture etc.).	Coating, printing.	PEDOT:PSS
Smart windows and glasses.	Electrochromic layer.	Coating, printing.	PEDOT:PSS

Part of the above niche can be addressed many solution processable and intrinsically conductive polymers (ICPs). ICPs are conjugated polymers which have an inherent electrical conductivity within the range of 10^{-8} to 10^3 S/cm. These are different from extrinsically conductive polymers (ECPs) because ECPs can be more accurately defined as conductive polymer composites where highly conductive fillers like carbon allotropes (graphite, CNTs, carbon black etc.) and metallic nanostructures (silver nanowires, gold nanoparticles etc.) are dispersed within a matrix of an insulating polymer. Since their discovery in the 1970s, ICPs have been the subject of much in research in many domains of science and technology owing to their multifunctional nature. ICPs are a fascinating class of macromolecules holding much promise for solution processable applications such as organic solar cells (OSCs), organic light emitting diodes (OLEDs), printed electronic circuits, electroactive chemical/biological sensors and others [116]. Environmentally friendly ICPs need to be processable using non-toxic or at least the very least, low toxicity solvents and the ICPs themselves should be either easily degradable or at the very least, recyclable.

Conductors are an integral component of all printed electronic devices allowing the transport of electrical charge from source to sink to complete the circuit. Printable metallic conductors such as silver inks have been widely studied [117] [118] and are commercially available [119] [120], but high costs and the need to be recycled set a demand for creating new conductors that can be mass produced and is environmentally benign. In this regard, the domain of commercial-grade organic conductors [121] [122] [123] is almost completely dominated by the popular polythiophene poly(3,4-ethylenedioxythiophene) poly(styrene sulfonate) (PEDOT:PSS) and its variants. Table 1.2 outlines the general applications of PEDOT:PSS and it can be seen that this organic polymer conductor is primarily used in both academia and industry as a “metallic” replacement due to its high achievable conductivity ($\sim 10^{-3}$ to $\sim 10^3$ S/cm). In addition, properties such as transparency of its thin films, electrochromism and sensitivity to physical quantities such as heat, moisture etc. make it an attractive option for multifunctional usage. While not immediately apparent from Table 1.2, PEDOT:PSS can only be inkjet printed in certain applications while in the remaining ones, it is either screen printed or coated using methods such as spraying. Inkjet printable applications of PEDOT:PSS include fabrication of conductive layers, electrodes and traces in thin film sensors and actuators. It is therefore a perfect fit for replacing toxic inorganic conductor materials such as silver inks which are expensive and indium tin oxide (ITO) [124] which has been the primary conductive material for the fabrication of thin film transparent

electrodes but is brittle. Besides PEDOT:PSS, there have been reports of a few self-doped PEDOT variants which have reported up to ~1000 S/cm conductivity [125] and are not hindered by the loss of original conductivity like in PEDOT:PSS due to the insulating PSS counterions shielding conductive domains. These are often self-doped and have good solution processability. However, only having solution processability does not guarantee inkjet processability and much work is being conducted to develop newer polythiophene derivatives on the lines of PEDOT. The objective is to develop stable dispersions like PEDOT:PSS but with higher conductivities and greater diversity in the ease of processing.

1.3 Scope and outline of the work

1.3.1 Contributions of the work

The objective of this dissertation is *to demonstrate thin film library preparation capability of a combinatorial printing platform integrating microfluidic mixing and inkjet dispensing which is then used to evaluate electrical properties of pristine and blended conductive polymers*. In this context, the contributions of this dissertation can therefore be outlined as follows:

- (i) Proposed hypothesis of integrating microfluidic processing and inkjet dispensing for the reduction of material volume and fabrication time requirements during thin film sample library preparation.
- (ii) Assembly and functional validation of combinatorial print head (CPH) prototypes comprising microfluidic mixing and inkjet dispensing capabilities.
- (iii) Development of a general multi-material multi-resolution thin film library preparation protocol using the combinatorial formulation and patterning platform.
- (iv) Development of an experimental outcome evaluation protocol for the data sets generated by characterizing the libraries in (ii) based on the principles of statistical inferencing.
- (v) Preparation and evaluation of multi-resolution thin film libraries with binary blends of commercial and novel ICPs with additives and among themselves using the protocols developed in (ii) and (iii) respectively.
- (vi) Preparation and evaluation of multi-resolution conductive thin film libraries with binary blends of two research-grade ICPs using the protocols developed in (ii) and (iii) respectively.

1.3.2 Organization of the dissertation

The underlying theme of this work is the study of inkjet printable and high conductivity intrinsically conductive polymers (ICPs) using combinatorial library formulation methods. To this end, the organization of the dissertation chapters are as follows:

- (i) Chapter 1 introduces the general domain of thin films with a focus on their combinatorial evaluation using electroactive polymers as the thin film materials. The rationale behind the combinatorial evaluation of such thin films is presented based on their solution processability. Invoking solution processability enables the discussion of the broad goals of an integrated inkjet patterning platform capable of combinatorially formulating functionally graded multi-material inks through microfluidic manipulation of the ink components.
- (ii) Chapter 2 describes the combinatorial printing platform in terms of its different components and functionality. Each functional block and its role in the system is described for clarity. In addition, qualitative and quantitative validation of some of the key processes such as fluid proportioning and fluid mixing and combinatorial printing is also included to cover overall system operation.
- (iii) Chapter 3 deals mainly with the statistical evaluation methodology adopted and its implications in the analysis of the primary characterization data sets covered in Chapter 4. The premise of these methods is established with discussions on the assumptions and expected outcomes and how they can be used for experimental inferencing. Besides data analysis protocols, sample characterization techniques are also introduced for future reference.
- (iv) Chapter 4 focuses on quantitative validation of the combinatorial printing platform using commercial-grade and laboratory-grade ICPs and additives using blending experiments. Experimental methods and rationale for sample library preparation are described and all characterization data is analyzed using the statistical framework described in Chapter 3.
- (v) Chapter 5 provides the conclusion to the topics presented in Chapter 2, Chapter 3 and Chapter 4 while also briefly discussing possible improvements and potential avenues of future research based on the work presented in this dissertation.

Chapter 2: Combinatorial thin film processing: Materials and Methods

Chapter overview

This chapter introduces the concept of combinatorial print heads and argues its necessity in the context of functional material printing. A prototype of the overall printing platform into which these print heads can be integrated in general is described along with the fabrication process of such print heads. Initial qualitative and quantitative validation of key functionalities of these print heads is performed for materials with fluid properties similar to those used in this work while also introducing the sample preparation methodology targeted towards combinatorial evaluation based on characterization data.

2.1 Combinatorial print heads (CPHs)

2.1.1 The need for integrated microfluidic inkjet processing

Besides the general reduction in the spatial footprint and energy requirements of typical devices, functionality integration has been the cornerstone of massive strides made in the field of microsystems and nanotechnology. The ease of integration is a subjective concept and is governed by factors pertaining to the qualitative and quantitative nature of the differences between the systems being integrated. For two systems $S1$ and $S2$, it can be intuitively inferred that the lower the difference between the range of possible outputs of $S1$ (or $S2$) being fed to $S2$ (or $S1$) and the range of possible inputs for $S2$ (or $S1$), the higher the probability of facile integration. This is due to reduced signal (mechanical, electrical, optical etc.) conditioning requirements at the physical interface between $S1$ and $S2$ and has been extensively demonstrated for sensor-actuator platforms such as MEMS-CMOS [126] [127] and microfluidic lab-on-a-chip systems [128] [129] [130].

Microfluidics encompasses the study of fluid behaviour and fluid control at sub-millimeter length scales of geometric confinement where the effect of surface forces dominates those of volume forces. Depending upon the application, microfluidic devices can handle fluid volumes ranging from microliters ($\sim 10^{-6}$ l, long microchannels) to picoliters ($\sim 10^{-12}$ l, individual droplets). Due to their ability to manipulate small fluid volumes, microfluidic devices can be deployed in applications requiring economical consumption and wastage of materials. This feature of

microfluidics is exploited in this work as a supply system for the dispenser. Drop-on-demand (DoD) inkjet printing dispenses droplets in the range of picoliters ($\sim 10^{-12}$ l, larger droplets) to femtoliters ($\sim 10^{-15}$ l, smaller droplets) but their supply systems are generally constrained to large, fixed-volume passive cartridges of only a certain material type. This prevents any pre-processing of the printable materials such as mixing which can be used to dynamically manipulate multiple materials in a controlled manner. By integrating the two fluid handling methodologies within a single modular device, it is expected that the advantages of microfluidic processing of minimal volumes of accurately proportioned fluid inputs can be actively conducted on the inkjet print head resulting in the ability of such a platform to be capable of directly patterning compositionally programmed multi-material thin film samples. Facile integration of complementary functionalities does impose some bounds on the range of processable materials in terms of ink flow properties. However, they are not functionally crippling, and the benefits accorded to the range of processable materials are numerous. Through different customizable implementations of the broader functional combination of techniques, facilitated by the modular nature of the integrating platform, high-throughput multi-material patterning can be achieved.

Unlike color printing, which is the predominant use of inkjet printing today, the additive printing of multi-layered multi-material thin film devices has quite a few fundamental phenomenological bounds. For example, colors are blended in inkjet-printed graphics and text through halftoning [131] rather than physical mixing of pigments. Halftoning uses dots of different sizes (equivalent to pulse-width modulation) and different spacings (equivalent to frequency modulation) to create gradients and blends of subtractive colors. However, that technique exploits the inability of the human eye to resolve individual objects closer than a minimum separating distance and is therefore phenomenologically incompatible with functional inks which require additive homogenization of their blend constituents to be able to print structures with tailored properties. This requires an active mixer capable of rapidly homogenizing the accurately proportioned constituents with a compact modular structure that is easily integrable within a customizable inkjet print head.

Another significant difference between the inkjet printing of color pigmented inks and functional multi-phase blends is that of ink composition. For printing multi-material thin functional films consistently, there need to be stable proportioning and efficient processing of the different constituents of the inks prior to droplet deposition. This can be achieved through flow-controlled

fluid driving through a microfluidic platform integrated with the mixing and dispensing modules. Such a processing platform can be used as a combinatorial print head to pattern multi-resolution multi-material thin film libraries for the combinatorial evaluation and optimization of material blends. System development aspects, along with the fabrication and validation of the integrated microfluidic drop-on-demand inkjet print head, are discussed in the next section.

2.1.2 Design and fabrication of the combinatorial print head

The combinatorial printhead (CPH) is at the heart of the combinatorial ink formulation and thin film patterning platform developed and tested in this work. It consists of an integrated microfluidic mixer and inkjet dispenser capable of combining and printing controlled proportions of multiple input fluids. The dispensing platform is capable of printing user-defined patterns and compositions of droplets and/or extended thin films of a range of functional and solution-processable materials. As discussed later in this section, 3D printing of casting molds can be an economical and reusable option to fabricate relatively high-resolution features on elastomeric microfluidic printing platforms due to their mechanical durability and thermal stability. Multi-material thin film library preparation is achieved using these CPHs through the coherent operation of different blocks in the system as will be discussed in a later section. The block-level schematic top view of a generalized elastomeric CPH structure is shown in Fig. 2.1 below.

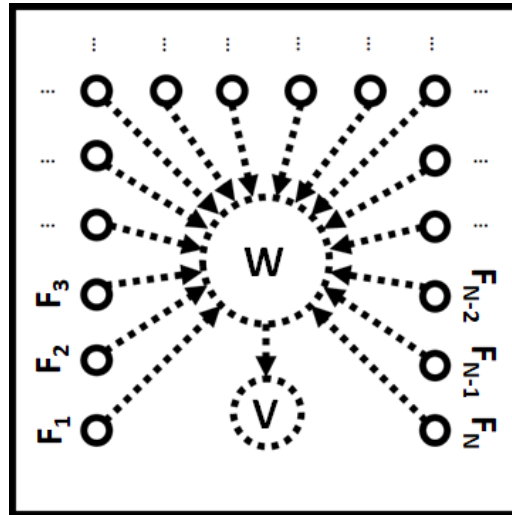


Fig. 2.1: Top view of a generalized combinatorial print head (CPH) structure comprising fluid inlets (F_i) which supply the fluids to the on-chip preprocessing module W from which, the processed blend is fed to the on-chip dispensing module V . for deposition and patterning. The dotted arrows indicate the channels defining the fluid flow path and the general fluid flow direction.

The fluid inlets are denoted by F_i and these inputs are fed to the on-chip preprocessing (mixing in this case) module W from where it is driven to the on-chip dispensing (inkjet in this case) module V . Dotted arrows define the general direction of fluid flow from one processing node to the other. Naturally, the compactness of this platform structure will vary widely and thereby impose bounds on the number of fluid inlets and individual module footprints based on processing feasibility and application-specific requirements. Material selection for the fabrication of such platforms is also very subjective and will depend upon the compatibility with the fluids being handled as well as the ease of synergistically incorporating multiple fluid processing modules. Microfluidic device fabrication has traditionally involved materials such as glass, silicon, SU-8 [132] [133] [134] being used as casting molds or “masters”. These have been used to create fluid flow paths of varying pattern complexity depending upon requirements using different cross-linkable elastomers that are cast using these molds. The advantage of elastomer-based microfluidic devices is their ability to incorporate flexible structures which provides an added benefit of friction-fitted seals capable of withstanding typical operational pressures without fluid leakage. Besides structural compliance, elastomers also exhibit a certain degree of chemical inertness, especially for fluids and solvents used in biocompatible applications which provides them with operational durability over multiple operational cycles.

The most commonly used elastomers for microfluidic applications are a class of materials called silicones. These are generally available commercially as two-part liquids: one part comprising the elastomer and the other part being the cross-linker. Prevalence of such elastomers is due to the factors mentioned above as well as the tunable nature of their mechanical compliance which can be controlled by the weight ratio of the elastomer to the cross-linker. Poly(dimethyl siloxane) (PDMS) is probably the most extensively used silicone for microfluidics [135] [136] and there are quite a few variants with differently tailored physical and chemical properties. However, one of the biggest problems with using materials like glass, SU-8 and silicon as casting molds and stamps for elastomer-based microfluidics is their fragile nature, especially when casting high aspect ratio structures. The other problem is the intrinsic process cost and complexity associated with multi-step patterning of these materials using methods such as photolithography, waterjet and laser cutting. So while the principles of photolithography enable the creation of precise microchannels of dimensions as low as a few tens of microns, these materials have relatively short lifespans due to the cyclic process of casting/de-casting which exerts significant thermal and

mechanical stresses. Moreover, there is a progressive increase in the build-up of difficult-to-clean elastomer debris on the finer features at high production volumes over time. These drawbacks further underline the need for other alternate cost-effective and time-efficient techniques for fabrication of structurally robust and extensively reusable casting molds for microfluidic devices.

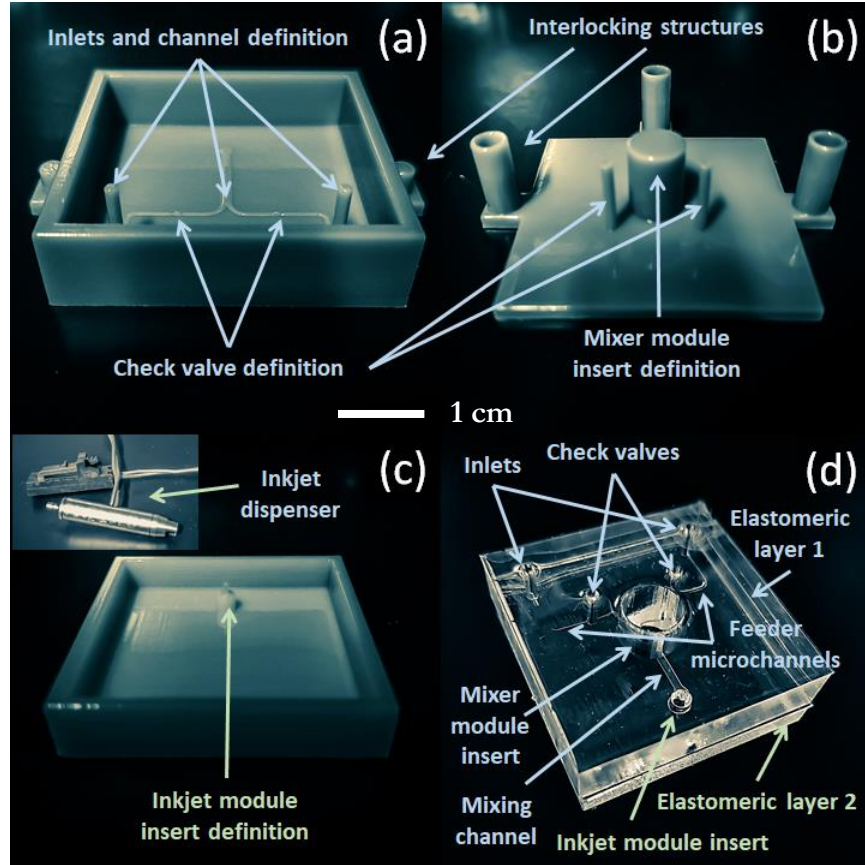


Fig. 2.2: (a) Bottom half of the two-part interlocking 3D printed mold for casting elastomeric layer 1 comprising structural definitions for the fluid inlets and the microfluidic channels. (b) Top half of the two-part interlocking 3D printed mold for casting elastomeric layer 1 comprising structural definitions for the check valves and the mixer module insert. (c) 3D printed mold for casting elastomeric layer 2 comprising structural definition for the inkjet module insert (inkjet module shown in the inset). (d) Plasma bonded casts of elastomeric layers 1 and 2 forming the bilayer combinatorial print head (CPH).

With the advent of additive manufacturing and the advancements made to enhance the structural durability of 3D printed materials, an economically viable method for fabricating robust and reusable casting molds for elastomer-based microfluidics has rapidly come to the fore. While not yet capable of fabricating features that are only a few microns in their characteristic physical dimensions unlike photolithographically processed silicon or SU-8, the additive nature of the 3D printing process enables single-step mold fabrication with feature size and feature resolution currently in the high tens to hundreds of microns range. Other factors such as casting compatibility

with common elastomers, surface finish of the cast, accurate reproducibility of feature sizes and resolution, sharpness of feature edges and dimensional tolerance in general are being continually improved upon and are also seen to vary greatly depending upon the 3D printing technique employed. Nevertheless, 3D printed molds provide the requisite flexibility in terms of feature sizes, feature resolution and material durability to be a practicable solution for implementing integrated microfluidic platforms.

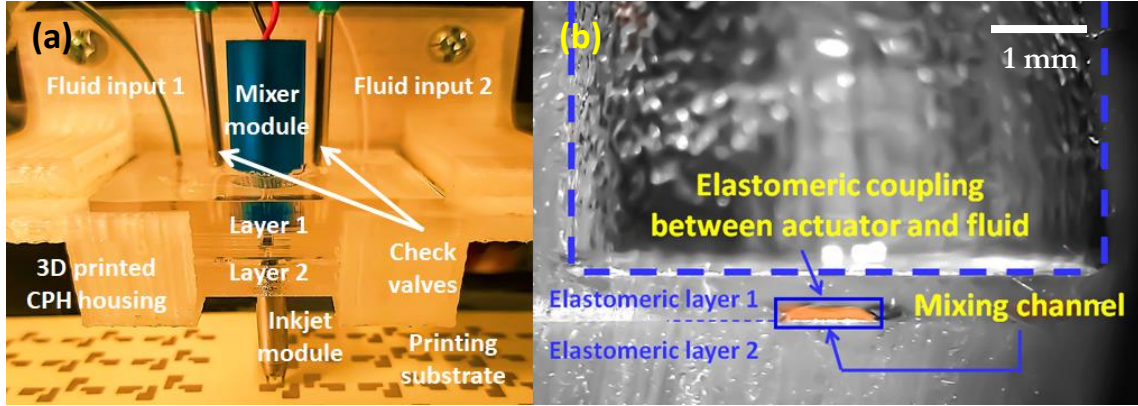


Fig. 2.3: (a) Fully integrated and mounted combinatorial print head (CPH) in operation. (b) Optical micrograph of the cross-section of the CPH showing the mixer module insertion cavity (*blue dashed outline*), the plasma bonded elastomeric bilayer interface, the coupling membrane between the mixing actuator and the fluid in the mixing channel (*blue solid box*).

Fig. 2.2 shows the 3D printed molds used in this work for casting the bilayer base structure of the CPH which contains structural components on both layers and also the bonded elastomeric CPH. In this work, an O₂-plasma bonded (Harrick Plasma PDC-001) elastomer (RTV-615, Momentive Performance Materials) base structure is used which is cast in reusable 3D printed (Stratasys Objet 30 Prime) molds [107] to house the different CPH parts. For the system being demonstrated, two fluid inputs are housed in elastomeric layer 1 with these inputs feeding microchannels of $\sim 500\ \mu\text{m}$ width and $\sim 200\ \mu\text{m}$ height which converge at the mixing channel coupled to the mixer module (encapsulated eccentric rotating mass motor, Digi-Key #1670-1023-ND) shown in Fig. 2.4. The mode of mixing actuation is chosen to be vibratory based on its efficacy as seen in prior literature where both low [137] and high [138] frequency vibrations are used. In this work, low frequency actuation using a commonly available ERM haptic motor was chosen to simplify the fabrication process without the need for multi-step microfabrication. In addition to being capable of producing strong vibrations, its also allows for easy integration without directly contacting the fluid components unlike other active mechanical components like

impellers. This mixing module, also housed in elastomeric layer 1, provides vibratory agitation to the material inputs through elastomeric coupling with the mixing channel of ~ 1 mm width. Coupling membrane thickness is ~ 500 μm with thinner membrane thicknesses possible but with the disadvantage of fragility, especially during the de-molding and mixer module insertion processes. The mixing channel width is kept twice that of the feeder microchannels to keep the total flow rate theoretically constant during the filling and mixing process. Another reason for keeping the mixing channel wider than standard microfluidic channels is to allow the active mixer module enough time to influence the continuously passing fluid volume elements since at constant flow rates, narrower channels will cause the fluid to move faster.

This particular aspect has not been optimized in this work due the broader aim of developing a technology demonstrator for the process of combinatorial ink formulation and patterning of solution-processable thin films. Consequently, there is much scope for the structural modification of such CPH platforms tailored towards similar goals. Elastomeric layer 2 houses a drop-on-demand piezoelectric inkjet dispenser (MicroFab MJ-ABP-01-080) with ~ 80 μm orifice diameter which is fed by the mixing channel directly. It will be seen later that the inkjet dispenser serves as a storage unit for the mixed ink but also constrains the amount of mixed ink volume as a consequence. This is not an issue for the printed ink volumes used in this work due to library size miniaturization but needs to be optimized (either through simultaneous mixing and printing or incorporating a larger ink storage chamber) for future work pertaining to large area printing where mixed volume requirements are proportionally larger. The mixing and dispensing modules are implemented as readily modifiable components that can be friction-fitted on to the elastomeric CPH platform and driven according to requirements.

2.1.3 Microfluidic mixing and prior mixer implementations

Before delving into the integration of the CPH with other components for realizing the printing platform, it may be useful to understand why active mixing methods are superior to passive mixing methods. Mixing of multiple fluids is generally done to enhance the homogeneity of components so that gradients in composition and consequent fluid mixture properties are minimized. In an application like combinatorial printing, the goal is to homogenize multiple fluids on-demand while minimizing the fluid volumes consumed. Microfluidic processing can directly achieve the latter but mixing within microchannels is limited by low flow rate resulting in a strictly

laminar flow regime. The reduction in length scales afforded by microfluidics also introduces challenges like the one above as surface forces on such small fluid quantities begin to dominate volume forces acting on them. The differences in time scales and force magnitudes of the different processes within a microchannel are captured using dimensionless numbers which are basically the ratio of these time scales. The three dimensionless numbers of importance in this work are: (i) Reynolds number (Re) which relates inertial and viscous forces, (ii) Péclet number (Pe) which relates diffusive and advective time scales and (iii) Ohnesorge number (Oh) which relates viscous and inertial and cohesive forces.

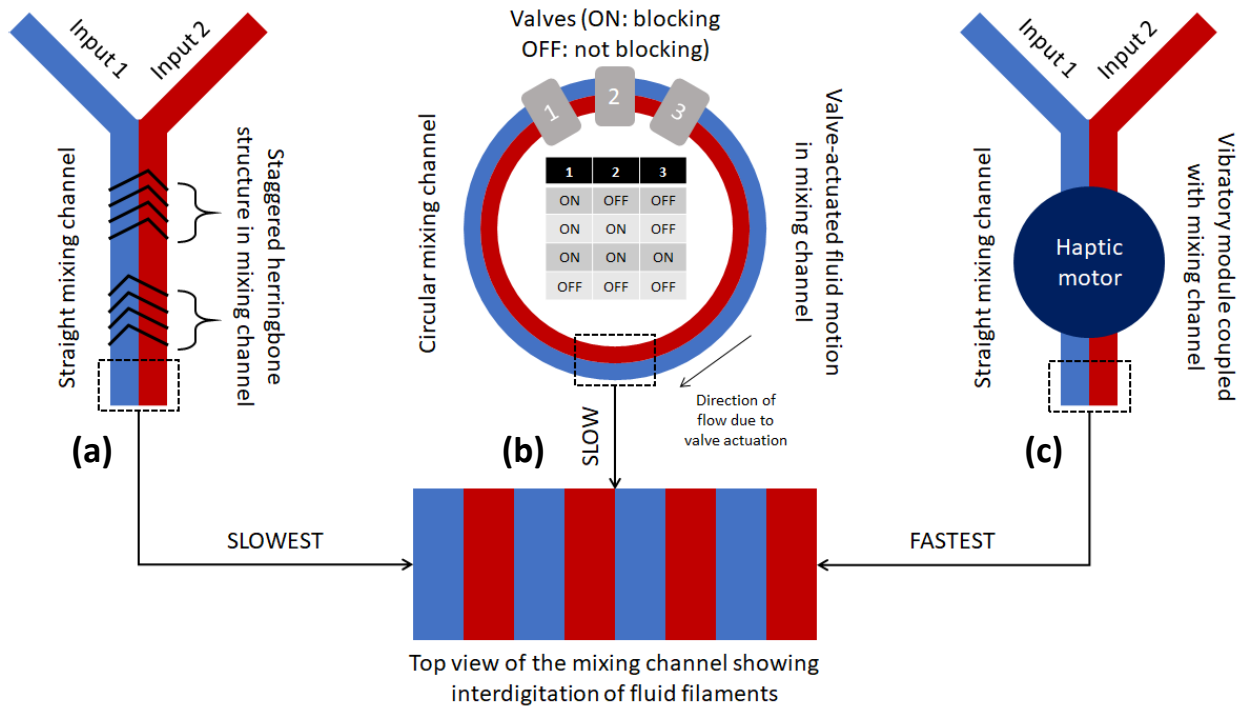


Fig. 2.4: Schematic configuration of (a) a staggered herringbone mixer, (b) a peristaltic mixer and (c) a vibratory mixer. Magnified view of the mixing channel illustrating the expected interdigitation due to chaotic advection by passive or active mechanisms is shown below the three implementations.

While the typical dimensionless numbers applicable for this work are discussed more specifically in a later section, having an intuitive appreciation of how they are invoked in the problem at hand is an important part of any microfluidic mixer implementation. Re and Pe are the most important quantities as far as mixing is concerned as they respectively define the fluid flow regime and how diffusive and advective effects compete in a particular regime. In microchannels, Re is typically less than 1 which means viscous forces dominate inertial forces and in such laminar flow regimes, homogenization of different fluids is a very slow process. Passive mixers of different

types have been implemented in literature [139] [140] although not all of them were attempted during the process of finalizing the mixing methodology in this work. The first mixer iteration was a passive implementation with a staggered herringbone design chosen for its structural simplicity. Such a structure can split the input fluids at each section with the staggered orientation helping to create interdigitation. However, the minimum achievable feature size of the 3D printer used for making the molds was insufficient for realizing the grooved structure that was required for such an implementation. In addition, despite the onset of chaotic advection, the length of the mixing channel required for even reasonably good mixing was estimated to be $\sim 10^1$ m which would have resulted in excessively large mixed, and consequently, waste volumes. Large values of Pe are characteristic of such scenarios. Given the significant speed of mixing advantage of active mixing methods [141] [142] [143] over passive ones, subsequent iterations were focused on active methods instead. Hence, the second mixer iteration was an active implementation with a peristaltic design chosen, once again for its simplicity. In this case, the three valves on the circular mixing channel act as fluid actuation structures by serially blocking and unblocking the flow. In this case however, the minimum valve-to-valve spacing defined by the feature resolution of the 3D printer was the primary limitation. This resulted in weak flows generated by serially activating the valves which resulted in slow interdigitation although it was faster than the first attempt. The third and final mixer iteration was also an active implementation using a haptic motor whose vibrations were coupled to the mixing channel through the elastomeric top wall of the structure. This iteration proved to be the fastest among all three while having the least design complexity and its operation is described in further detail in a later section. All three mixer attempts are shown in Fig. 2.4 which schematically illustrates how the input fluid streams become interdigitated, thereby reducing diffusion length which is ultimately the main driver of homogenization. The impact of Oh is more relevant for the droplet generation aspect of the print head and is discussed in a later section.

2.2 Integrated processing platform

2.2.1 Platform implementation

The overall block diagram of the combinatorial ink formulation and thin film patterning platform is shown in Fig. 2.5. The schematic is color-coded to categorize the different blocks according to their broad functionality. The peripheral components color-coded in blue comprise the fluid processing block, those color-coded in red form the substrate and combinatorial print

head (CPH) positioning block and finally, those color-coded in yellow comprise the software control block. The green color-coded block is the CPH block which has already been touched upon in the previous section and more details of the CPH block and each of the other blocks will be outlined. The fluid flow control block (blue) comprises two sub-blocks which, although shown to be spatially separate in the schematic, belong to the same functional block. One has a flow control unit (Chemyx Fusion 4000 syringe pump) for driving the input fluids in the reservoirs with programmable proportion into the CPH block. The other has a programmed microcontroller board (Arduino MEGA) which actuates the vibratory mixer module and triggers the waveform generator (Agilent 33120A) and signal amplifier (Trek 2200) for actuating the inkjet dispenser module.

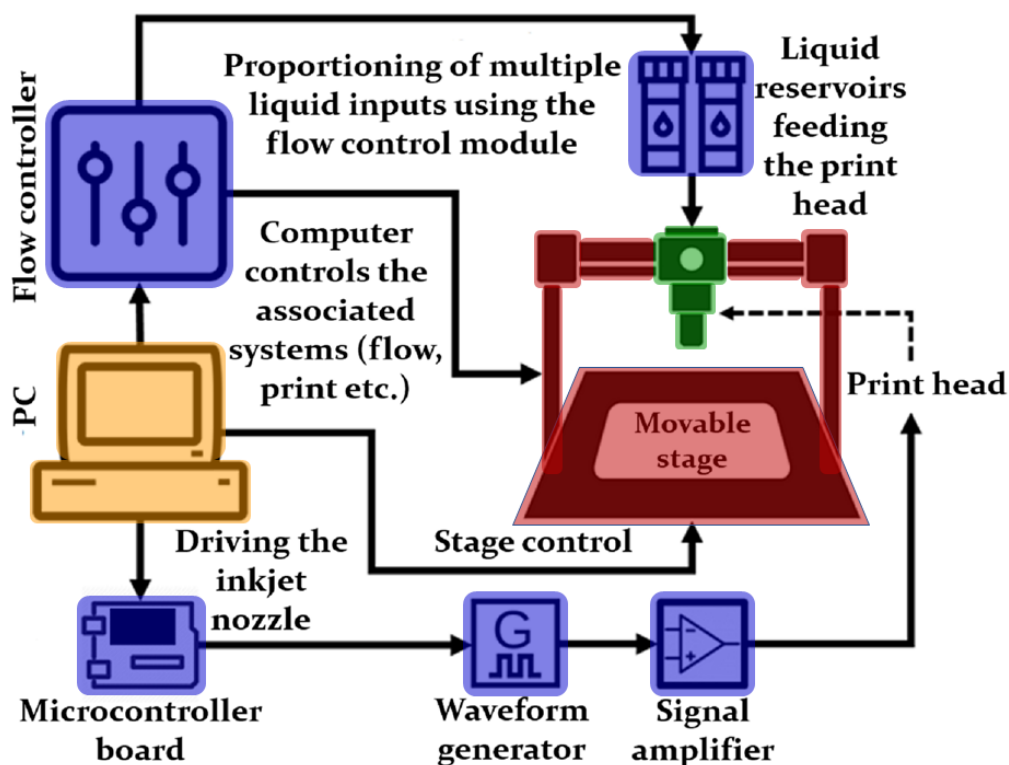


Fig. 2.5: Color-coded schematic block diagram [3] of the combinatorial ink formulation and thin film patterning platform showing the combinatorial print head (CPH) block (*green*), the fluid control block (*blue*), the substrate and CPH positioning block (*red*) and the software control block (*yellow*).

The substrate and print head positioning block (red) is primarily a 3-axis translational stage with the combinatorial print head (CPH) mounted using a 3D printed housing on the z -axis movable arm and the substrate mounted on an xy -movable plexiglass stage. This allows for variation in the speed of stage translation to enable different printing rates as well as print gap between the CPH and the substrate. Used in conjunction with the CPH and fluid control blocks,

the positioning and spacing of droplets becomes highly controllable. Motorized linear actuators (Misumi LX45) are used to move (minimum stepping distance = $0.5\ \mu\text{m}$) both the sample mounting stage as well as the CPH mount. This block is programmed to pattern linear structures along the *X*-axis (left-right) which can be combined with motion along the *Y*-axis (forward-backward) to create user-defined patterns. The software control block (yellow) logically envelopes the hardware blocks described above and comprises a custom-coded Python user interface (UI) for communication control among and operation control of the individual hardware blocks. The UI also provides independent control of multiple process parameters such as 3-axis stage motion control, fluid blend component flow proportion control and mixing module activation time to enable combinatorial printing of thin films features. As described in the previous section, the CPH platform consists of a bilayer elastomer with different components friction-fitted in a modular manner. The mode of CPH operation is explained using binary fluid systems used as case studies in this work but the theory can be easily extended to more than two fluid blend systems. Being structurally symmetric, the fluid inputs 1 and 2 can be used interchangeably. Immediately after the plasma bonding of the elastomer bilayer, the CPH is treated with 1% aqueous polyvinyl alcohol (PVA) solution to enhance the wetting properties of the elastomer. This is done by feeding PVA into the microchannels through the fluid inputs using a regular syringe and letting it adsorb on the surfaces for 10 min at 20°C . The channels are evacuated by blowing air through them using another syringe and dried in an oven at 60°C for 30 min to remove any traces of moisture. After mounting, the appropriate fluid inputs are connected and fed into the feeder microchannels at equal flow rates. Once the fluids are at the entrance of the mixing channel, they are supplied to the mixing channel proportionally using the fluid flow control block. At this point, the active mixer module is activated to agitate the proportioned but unmixed liquids as they traverse the length of the mixing channel ($\sim 1.5\ \text{cm}$) and arrive at the inkjet dispenser orifice in a fully mixed state. This ensures that the entire column of liquid from the entrance of the mixing channel to the exit of the inkjet orifice has been mixed thoroughly.

A schematic representation of the CPH operation is shown in Fig. 2.6 starting with the fluid filling of the mixing channel, agitation of the fluids leading to mixing followed by the inception of inkjet dispensing droplets of the mixed fluid blends. The mixing module has a compact eccentric rotating mass (ERM) mounted on a shaft which induce complex vibrations in the body of the CPH and it was expected that this would translate into a compact but powerful mixing tool when coupled

with elastomeric microfluidic chips. ERM motors, mounted on the CPH as shown in Fig 2.6, induce vibrations on the motor casing due to the rotary motion which are transmitted to the fluid in the mixing channel through the top wall. It is this wall motion that causes the fluid in the mixing channel to be homogenized by inducing chaotic motion through mechanisms hypothesized to be similar to a variation of Stokes' 2nd problem.

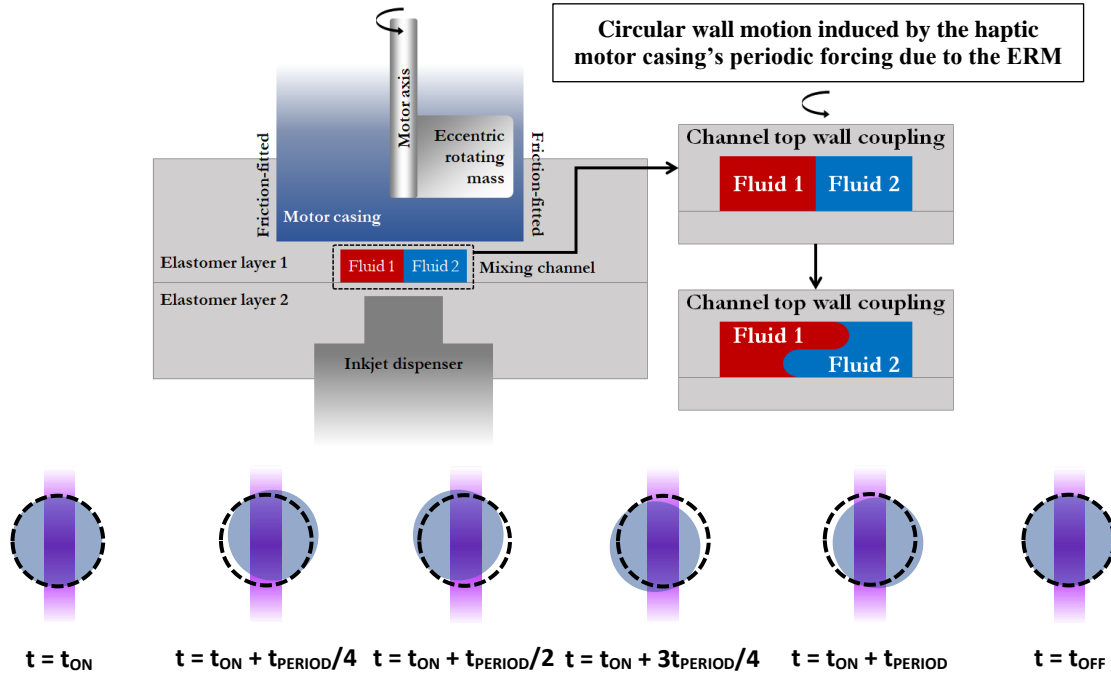


Fig. 2.6: (top left) Schematic representation of the modular CPH setup showing the configuration of the mixing channel and the structure of the enclosed ERM motor whose casing is tightly coupled with the elastomer structure, (top right) general operation of the mixing module including its advective effect on the binary fluid system within the mixing channel due to wall vibration and (bottom) motion of motor casing (blue) with respect to insert hole (black dashed outline) for 1 cycle of ERM rotation (t_{PERIOD}) between starting (t_{ON}) and stopping (t_{OFF}) of the haptic motor where the mixing channel is shown in purple as a consequence of mixing red and blue fluids as in the schematic above.

The rapid nature of this vibratory fluid mixing can be observed in snapshots of the mixing process using red and blue dyed aqueous solutions with a high-speed camera (Phantom VEO-E 310L) as seen in Fig. 2.7. The mixer is turned on at $t = 0.0$ s and homogenizes the color of the dyed solution by $t = 1.0$ s. The total volume of mixed fluid after the mixing module is energized is ~ 23 μ l (~ 20 μ l inkjet dispenser volume + ~ 3 μ l mixing channel volume) which can be used to print patterned replicates from a given fluid blend proportion that has been mixed on-chip. In contrast, for premixed fluid blends, a minimum of a few milliliters of fluid needs to be processed for feeding into any standardized inkjet dispensing unit. Therefore, while the actual amount used for printing the thin film patterns may be equal for both conventional inkjet printing and inkjet printing using

a CPH-based platform, the unused waste volumes are at least an order of magnitude smaller for CPH-based processing. Additionally, for conventional inkjet printing of functional materials, the loading step of these prepared fluid blends becomes a time limiting step which is bypassed in the CPH-based platform due to the mixing step and the loading step occurring serially in an uninterrupted manner. As an estimate of efficiency, the time required to generate a typical printed thin film library comprising 5 different blend compositions with 15 replicates (total 75 samples) for each is ~15 min (~12 s per sample) while the material volume requirement per sample is ~250 nl which is about an order of magnitude smaller than what has been typically reported in literature [66] [67] [68]. It is perhaps not reasonable to assume the per sample volume used by the CPH to be absolute for different characterization methods but it does estimate the lower end of volume consumption efficiency. Automated processes involving robotic handling of specialized tools may be time-efficient and volume-efficient but not both simultaneously, especially during the mixing of fluids at small volume scales.

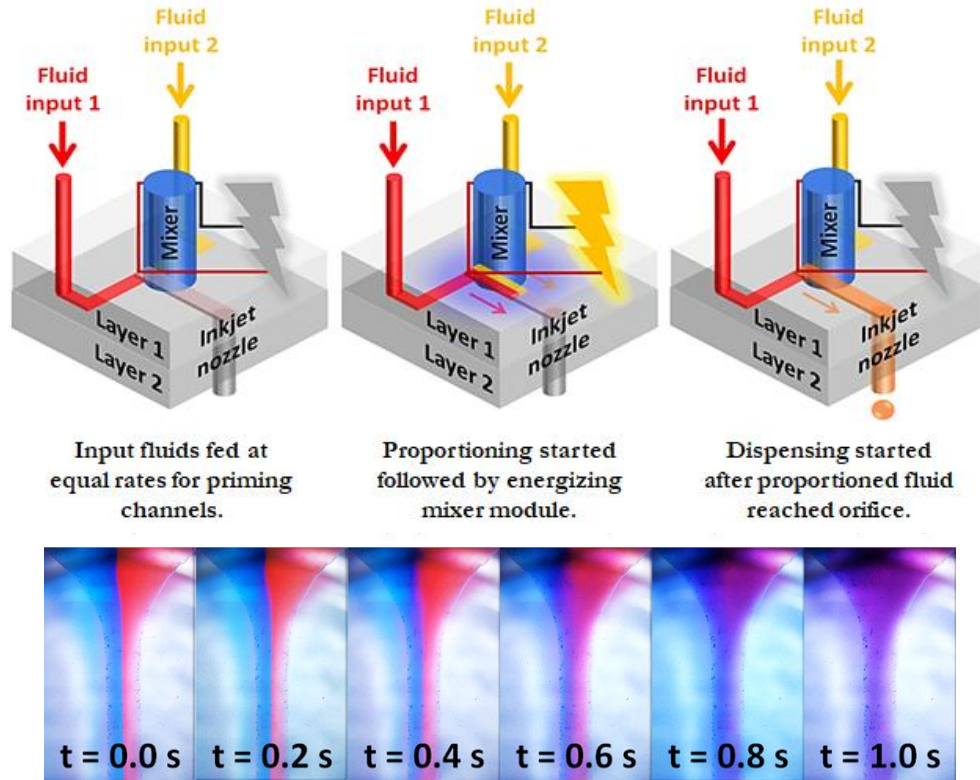


Fig. 2.7: (top left to right) Fluid inputs 1 and 2 being fed (1:1 proportioning) into the mixing channel of the combinatorial print head (CPH) followed by mixing and printing of the proportioned fluid blend. (bottom left to right) Rapid mixing effect of the haptic mixer (eccentric rotating mass or ERM motor) module on the unmixed 1:1 proportioned fluid in the mixing channel. The elastomer-coupled haptic mixer module is seen in the background (blue package surface painted white to provide colour contrast).

2.2.2 Analytical and empirical considerations for the CPH

Dimensionless numbers are ubiquitous in the study of fluid mechanics at different size scales and serve as valuable behavioural indicators of practical fluidic systems. The critical regions of the CPH that need to be considered include the input channels, the mixing channel and the jetting orifice. Driving flow rates are typically around ~ 0.01 ml/min during the on-chip mixing phase from which the flow velocity can be calculated for evaluating the characteristic dimensionless numbers for each of these regions. In general, the flow regime is strictly laminar in both the input channels as well as the mixing channel of the CPH with flow velocities of the order of ~ 1 mm/s and the corresponding Reynolds number (Re) ($\rho U \delta / \mu$) in the range of ~ 15 to ~ 0.75 based on the specified allowable dynamic fluid viscosity range for the MicroFab® inkjet dispenser (< 20 mPa.s) downstream. The fluid density is ρ , U is the flow velocity (~ 1 mm/s), δ is the hydraulic diameter of the mixing channel ($\sim 333 \mu\text{m}$) and μ is the dynamic viscosity where ρ is estimated to be $\sim 1000 \text{ kg/m}^3$ for the blends owing to the dilute nature of the aqueous ICP dispersions and the additive being around $\sim 1100 \text{ kg/m}^3$. Based on these values, laminar flow regime is assumed up to the inkjet orifice which has a diameter of $80 \mu\text{m}$ given that Re is the ratio of inertial forces to viscous forces acting on the fluid being investigated. Fluid inputs into the CPH exhibit approximately Newtonian behaviour despite some of them being polymer dispersions and this can be attributed to their relatively high degree of dilution. In addition, surface tension values of these fluids are measured to be within the specified allowable range (~ 20 to 70 mN/m).

For jettability of fluids as individual droplets, it is common to use the Ohnesorge number (Oh) ($\mu / \sqrt{\rho \sigma d}$) as a reference where σ is the surface tension and d is the orifice diameter. It describes the tendency for a drop to either stay together or fly apart by comparing viscous forces with inertia and surface tension forces. Typical values of the quantities used in Oh that are pertinent to this work result in its value being within 0.1 and 0.3 while the condition for jettability is given by $(\sim 0.05 \text{ to } 0.1) < Oh < 0.5$ which implies that the fluid blends used in this work are printable. For $Oh < (\sim 0.05 \text{ to } 0.1)$, the formation of satellite droplets dominates while for $Oh > (\sim 0.5 \text{ to } 1)$, the viscous forces are too great for droplet ejection. Often, the reciprocal of the Oh is also used as a reference and is called the “Z number”, denoted by Z whose range then varies from $(1 \text{ to } 2) < Z < (\sim 10 \text{ to } 20)$ and is sometimes more convenient to remember. Traditionally, the higher (lower) numerical bounds were used for the Oh (Z) numbers but recent research [144] has shown that the

lower (higher) numerical bounds for the respective dimensionless quantities capture the operation of droplet-on-demand inkjet dispensers more accurately.

The condition for efficient mixing is where the ratio of the length l and hydraulic diameter d of the mixing channel is greater than the Péclet number (Pe) where Pe is the ratio of advective and diffusive mass transport ($U\delta/D$) where D is the diffusion coefficient of the diffusing species. The diffusion coefficient D is approximated using the Stokes-Einstein equation to be of the order of $\sim 10^{-12}$ to 10^{-14} m²/s using measured aggregate sizes of the ICPs from dynamic light scattering (DLS) experiments and discussed in Chapter 4. Differences in measured size from the ICP particle size observed in printed films is simply due to the fact that in aqueous dispersion, multiple ICP particles are agglomerated. This implies that the residence time of a fluid element in the mixing channel must exceed the time required for the diffusing species to diffuse across the mixing length which is the characteristic length dimension defining the mixing channel. In this work, $l/\delta \sim 36$ ($l \sim 3.5$ cm including the dispenser length) while the Péclet number is in the order of $\sim 10^6$ which implies that diffusive transport rate is about three orders of magnitude smaller than advective transport rate which shows the need of active mixing methods to reduce the mixing length. It was shown in Fig. 2.5 that the haptic motor being used as the mixer module can mix the input fluids very rapidly with the qualitative end point being the spatial homogeneity of the purple color when red and blue dyed aqueous dispersions are subjected to the motor vibrations.

To qualitatively investigate the mechanism behind this rapid mixing process, high speed imaging was performed using similar dyed aqueous solutions as well as an ICP-additive (PEDOT:PSS-DMSO) pair and the dynamics of the fluids in mixing channel was observed both with and without the haptic motor being activated. When flowing, the streams interact at their boundaries to form a weak interface diffusion layer which does not visibly broaden significantly with time within the imaging window at the flow rate used during typical CPH operation in the mixing mode. The width of this interface diffusion layer is inversely proportional to the flow rate within the mixing channel and therefore the need for active mixing in short channels. Fig. 2.6 compares the vibratory action of the haptic motor at different driving currents to locate the regime where the homogenization effect of the agitation is almost instantaneous without exceeding rated current limits of the motor, leading to a driving current of ~ 150 mA being used. Fig. 2.7 shows the fluid behavior observed when haptic motor is turned on and a region of the mixing channel further downstream is imaged. Rapid stretching and folding of fluid filaments are observed when the

motor is activated which seem to indicate the formation of eddies. These eddies are seen to form closer to the motor periphery but the alignment along the length of the channel of the stretching and folding filaments exerts vibrational influence extending beyond the region of the mixing channel directly covered by the motor as seen in Fig. 2.7. This results in rapid thinning of the filaments of both fluids leading to reduced mixing lengths which assists diffusion which is ultimately how the chaotically agitated species are mixed.

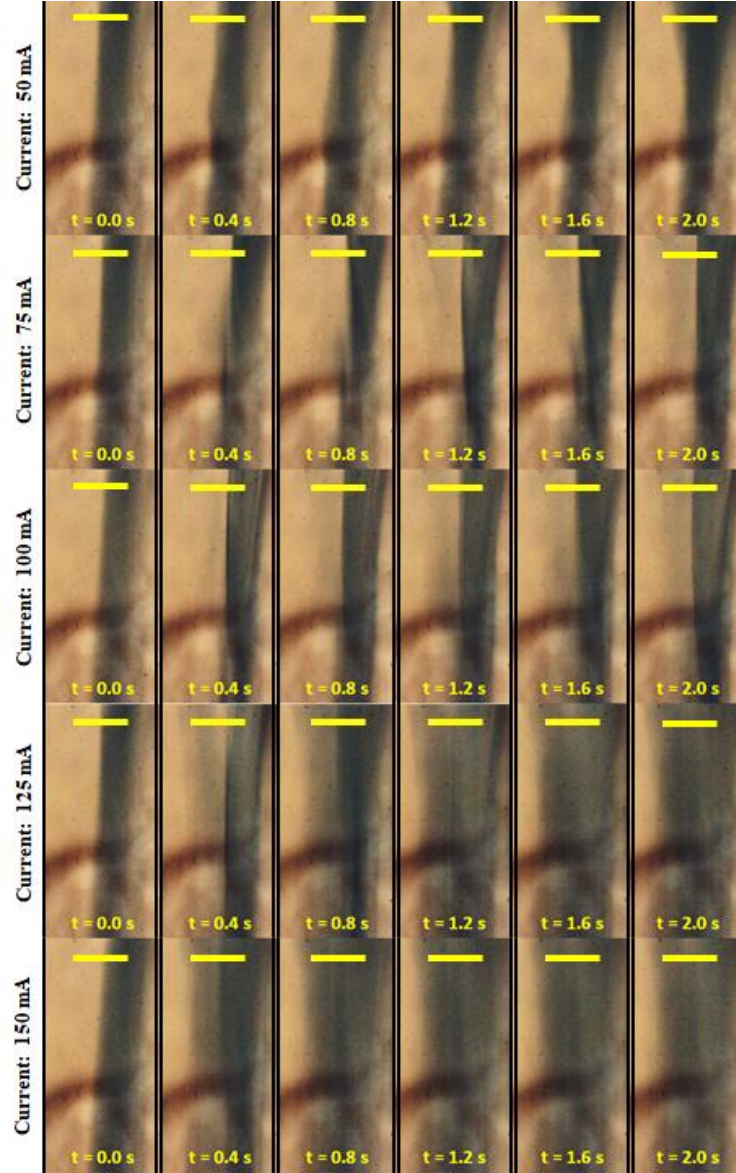


Fig. 2.8: Effect of haptic ERM motor vibrations on the speed of homogenization of ICP-additive fluid inputs as a function of driving current from time $t = 0.0$ s to $t = 2.0$ s in time steps of 400 ms and current steps of 25 mA. The background is the whitened motor face seen through the elastomeric coupling membrane with the brown feature being part of a circular depression in the motor packaging. Black vertical lines indicate channel bounds and yellow scale bars represent 0.5 mm.

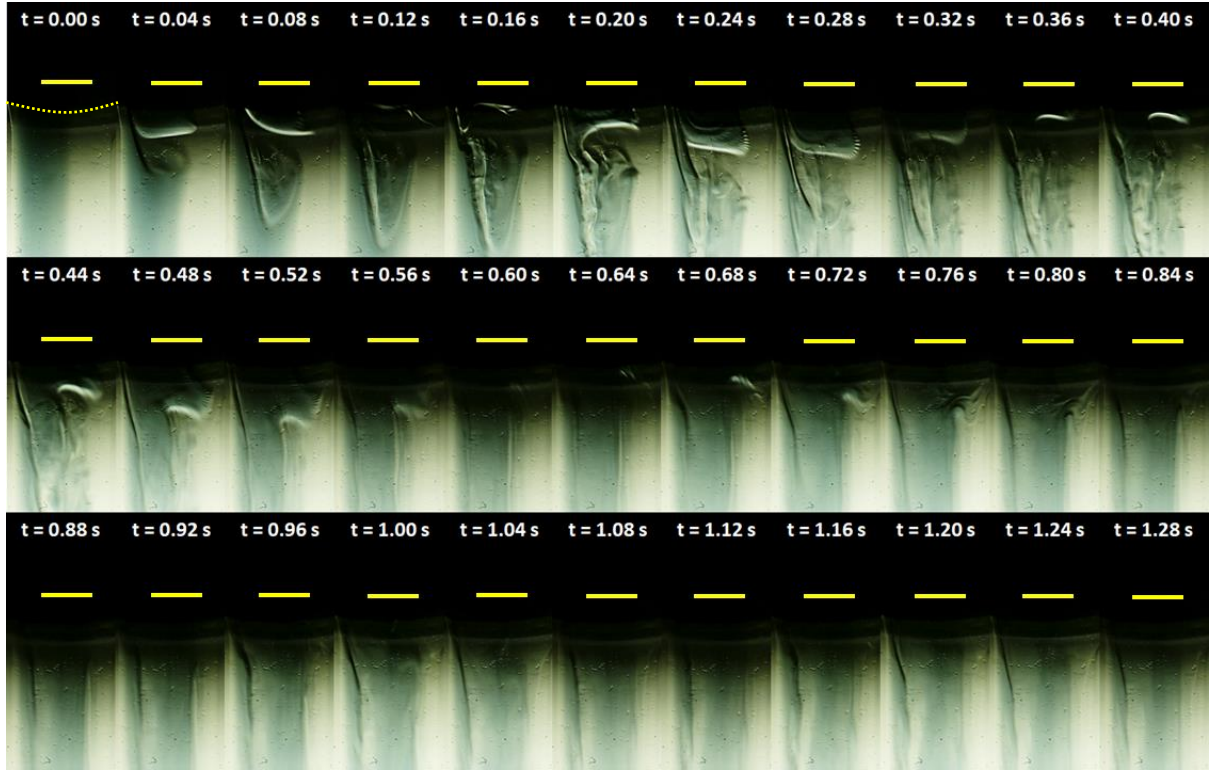


Fig. 2.9: High speed imaging (25 frames/s from $t = 0$ s to $t = 1.28$ s) of the CPH mixing channel showing the ICP-additive pair of PEDOT:PSS (*dark*) and DMSO (*light*) being agitated by the haptic motor. The curved contour enclosing a dark surface in each frame is the outline of the haptic motor (dotted yellow line on first panel at $t = 0.00$ s) embedded within the CPH body and the length of the mixing channel segment imaged is ~ 1.5 mm. Scale bars in yellow represent 0.5 mm.

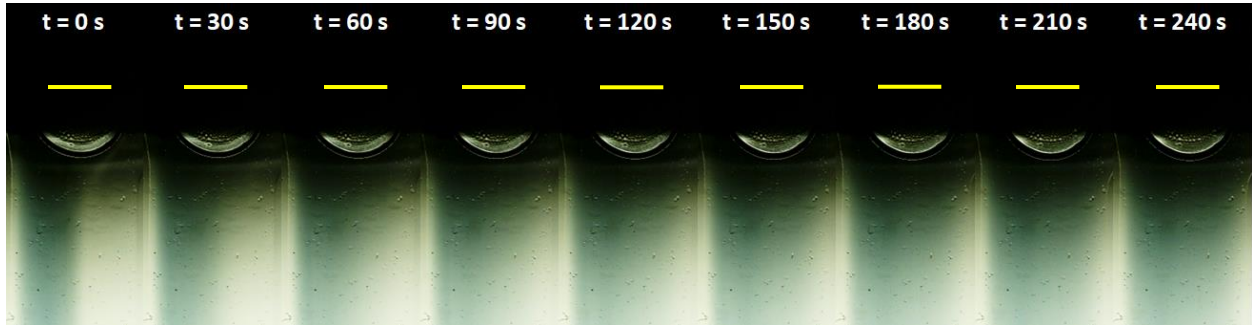


Fig. 2.10: Diffusive mixing as observed for 240 s at intervals of 30 s for the ICP-additive (PEDOT:PSS-DMSO) pair to illustrate the mixing time scale estimates obtained from Pe calculations. Also observed in the ICP-additive images is the outline of a stray bubble in the mixing channel near the periphery of the haptic motor which remains static throughout. Scale bars in yellow represent 0.5 mm.

The generation and stretching of the eddies along the length of the mixing channel happens within ~ 1 s with the ICP color being homogenized across the width of the channel within 10 s when the motor is stopped. As mentioned previously, the haptic motor is run for the entire time starting from the input fluids being proportioned into the mixing channel until the binary fluid

blend is at the dispenser orifice to ensure that the fluids are not undermixed but it is not unreasonable to assume that homogeneity may be achieved earlier. Fig. 2.9 shows the diffusion of the ICP-additive fluid pair when the flow is stopped which results in the broadening of the interface diffusion layer until the color gradient visually disappears. However, this may not be an ideal indicator of the homogenization endpoint and often needs to be corroborated by imaging the cross-section of the mixing channel.

As seen, the time scale for diffusive mixing is much longer in comparison to the chaotic mixing and is one of the primary reasons to opt for active mixing. It is intuitive that longer diffusive mixing time will also require longer mixing channel lengths for a given fluid flow rate and will result in larger processed volumes, thereby simultaneously increasing wasted volumes. For context, actively mixed fluid volume is ~40 μl considering priming and overmixing while passively mixed volume, based on Fig. 2.8, is at least double of that. Assuming identical volume requirement per sample replicate, the wastage would be double or more. Given that there is no specific method for directly estimating the degree of mixing other than what can be gathered from the imaging experiments and calculations performed using the dimensionless quantities like Re and Pe , further quantification is done indirectly by comparing the variability of printed thin film performance between pre-mixed, on-chip mixed and unmixed fluids. Despite diffusion playing a role in homogenizing the input fluids as it traverses the length of the mixing channel and the inkjet dispenser in all cases, the added effect of the haptic motor vibrations is expected to result in lower sample-to-sample variability. It needs to be mentioned here that while there are factors other than the degree of mixing which may introduce performance variability, the printing process can be thought of as a black box with fluid blends as inputs and printed features as outputs and in general, it may be sufficient to recognize such multi-factor dependence and draw inferences on a case-by-case basis.

2.2.3 Operational verification

Functional validation of CPH processing using commercial-grade and laboratory-grade ICP fluid blends is discussed in greater detail in Chapter 4 where thin film electrical conductivity tuning is studied as a function of ink composition using CPH-processed fluid blends and comparing them with premixed and unmixed fluid blends. Qualitative verification of the platform operation is done using a colorimetric test method whereby arrays of red and blue dots are printed

on a white paper (216 gsm) substrate. Binary blends of red (x) and blue (y) aqueous dyed dispersions are mixed at different proportions x/y using the on-chip mixing module and multiple replicates of each blend composition are dispensed as dots in a row-by-row manner. Each row consists of five replicates of the same blend composition with each replicated drop comprising ~100 individually dispensed droplets to ensure color uniformity of each drop. A resolution step size of 25% is used such that 100x0y means all red and no blue while 75x25y implies 75% red and 25% blue in the blend. The drops are oven dried at 60°C for 1 min and the process repeated for all compositions.

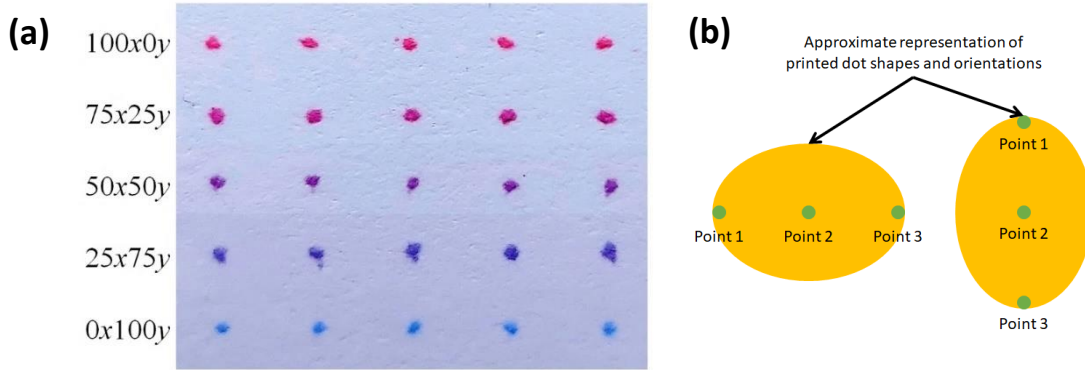


Fig. 2.11: (a) Printed array of droplets comprising on-chip proportioned and mixed red (x) and blue (y) dyed aqueous dispersions showing corresponding compositions of rows. (b) Channel contribution from 3 sample positions (*green shape*) to obtain the average for a printed dot (*yellow shape*).

The row-by-row printed array is illustrated in Fig. 2.10 along with how red and blue channel intensity is averaged over a printed dot. It is to be noted that the printed dots are not exactly circular due to the randomness of the in-plane wicking and therefore, 3 points were chosen by visual estimation as shown in Fig. 2.9 and averaged for the red and the blue channels. The longer dimension of the roughly elliptical was chosen to be the direction along which the 3 points were chosen as the spread in intensity was expected to be maximum along that direction. Variation in the values of the red (R) and blue (B) channels of the RGB color scheme as a function of $R(x)/B(y)$ color proportion is shown in Fig. 2.11. This was done by analyzing a JPEG-formatted image of the individual printed dots for their red and blue channel contents using MATLAB. These channels have a color intensity range varying from 0 to 255 which is mapped by the color bar adjacent to both heat maps. While the range of values seen in the scale bar are not fitted to a percentage scale, their complementarity is clearly observed in the heat maps as expected from changing proportions of each color. This is due to the fact that for the eye or any imaging device to perceive a certain

color in a binary pigment blend, the constituent pigment particles need to be very homogeneously distributed and in physical proximity to each other such that it is impossible to spatially resolve the two different pigment particles and thus, an average of the two colors is perceived. The difference in scale bar limits for the *R*-channel and the *B*-channel can be attributed to the imperfection of the pigment colors on the 0 to 255 scale as well as the inherent tinting of the image captured by the camera. The latter can be attributed to the dual effect of the image sensor as well as the encoding of a particular color used by the corresponding file type. However, qualitative confirmation of the physical mixing process can be obtained from the information illustrated by the row-wise variation of the pristine color components shown in Fig. 2.10.

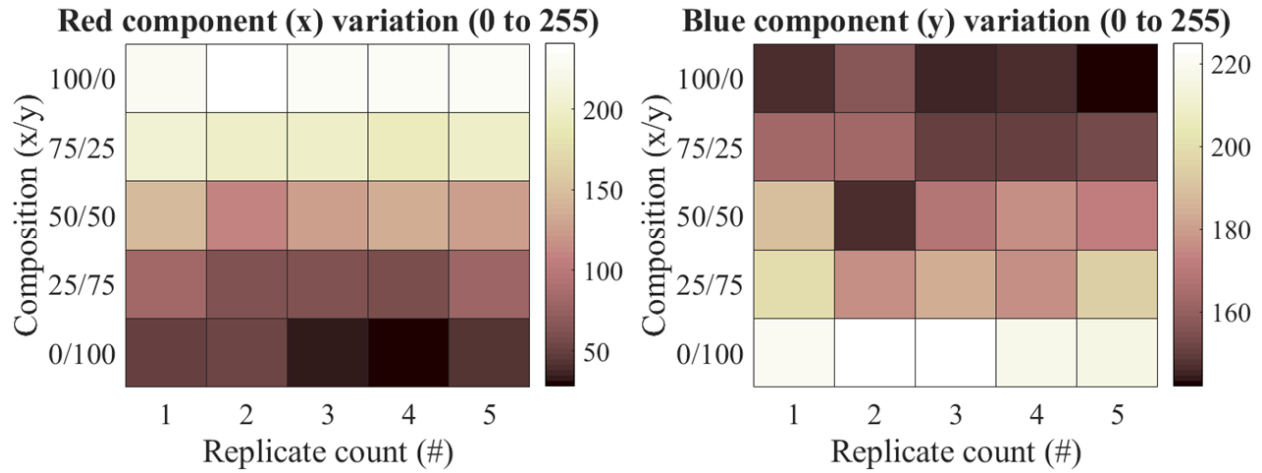


Fig. 2.12: Row-by-row printed array of droplets comprising on-chip proportioned and mixed red (*x*) and blue (*y*) dyed aqueous solutions showing corresponding compositions of rows.

Quantitative comparisons between specified input volume flow rates and output material weight were made to evaluate the proportioning accuracy. The materials used in this experiment were the red dyed aqueous dispersion from the previous qualitative study ($\eta = \sim 1$ mPa.s), the commercial-grade ICP PEDOT:PSS ($\eta = \sim 5$ mPa.s) and ethylene glycol ($\eta = \sim 16$ mPa.s) whose viscosity is near the upper limit of the inkjet dispenser. Each syringe pump was driven for 10 min at different flow rates and step sizes corresponding to those used later in order to cover the entire range of each input. The fluid driven by each pump was collected in a glass vial and weighed individually for all the different flow rate fractions used, thus mapping the specified input fraction to its corresponding output fraction. Fig. 2.12 illustrates these comparisons when conducted at specified input flow rate steps of 10 vol.% and 2 vol.% flow rate ranges used subsequently in this work. For the 10 vol.% step size comparison, flow rates were varied from 0.01 ml/min (100 vol.%)

to 0.001 ml/min (10 vol.%) while for the 2 vol.% step size, flow rates were varied from 0.001 ml/min (10 vol.%) to 0.0002 ml/min (2 vol.%). While the variation in the output fluid weight when compared to the input flow rate proportion does not appear to be very significant, assessing the absolute and relative proportioning errors is important to understand the resolution limits of the pumping system. To be noted here is that the elastomer RTV-615 is typically used for moisture shielding applications and does not undergo large volume changes due to solvent absorption [145].

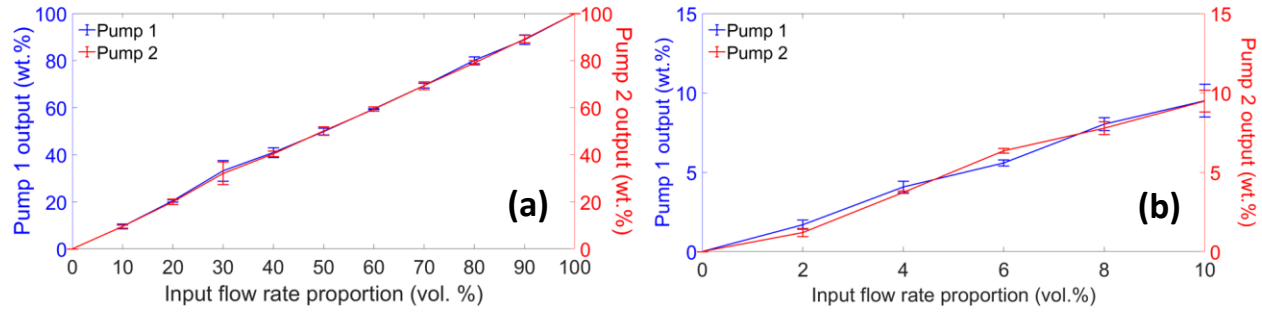


Fig. 2.13: Comparison of pump output as a function of input flow rate proportion for each syringe pump over (a) larger flow rate range at 10 vol.% steps and (b) smaller flow rate range at 2 vol.% steps.

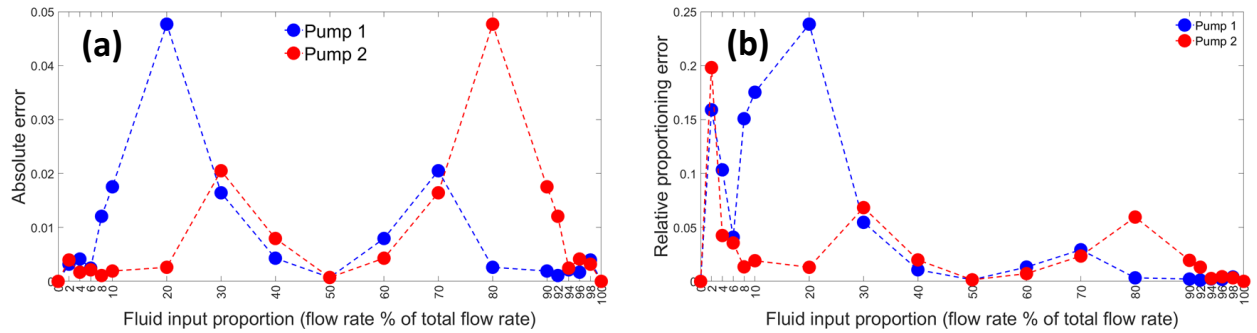


Fig. 2.14: Variation of absolute (a) and relative (b) proportioning error in either pump as a function of fluid input proportioning.

The absolute and relative error in proportion is given by (2.1a and 2.1b) and (2.2a and 2.2b) and capture the uncertainty in proportioning step size for the individual pumps. The ε 's denotes the error and the M 's denotes the output mass for each pump labeled as “pump 1” and “pump 2”. From Fig. 2.13, it can be stated that the maximum error for 10 vol.% and 2 vol.% step sizes are less than half of the respective step sizes. This implies that a change in the input (syringe pump settings) proportion by that such a step size can be expected to show up at the output (inkjet dispenser orifice) assuming equal uncertainty on either side of the specified proportion. It is also observed that the relative proportioning error for pump 1 is somewhat higher than pump 2 in the 10 vol.% to 20 vol.% range and is therefore used accordingly. Thus, however small it may be, the proportioning error will definitely play a role in the operational performance of the CPH platform

and needs to be considered when drawing inferences from the characterization data of printed sample libraries. The proportioning error, expected to influence binary blends at their extreme proportions, is plotted in Fig 2.15. Considering the argument of an acceptable error being less than half the step size from the context of Fig. 2.13, it is clear that the two independent syringe pumps fall well within that range.

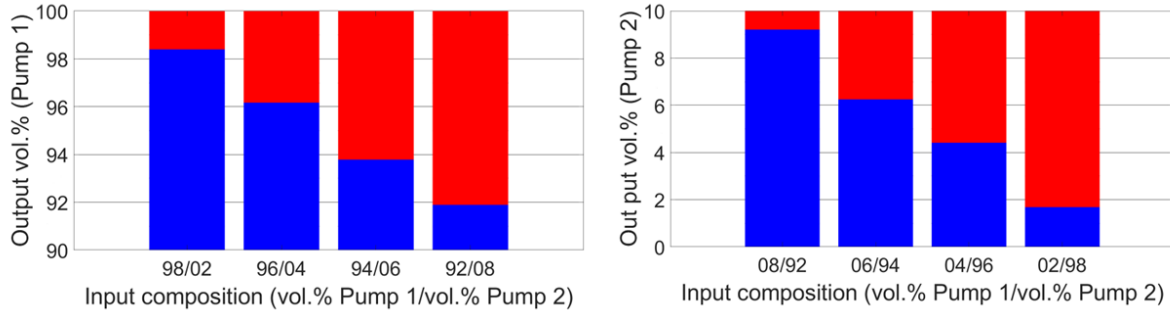


Fig. 2.15: Proportioning error of (left) higher extreme of pump 1 and lower extreme of pump 2 and (right) lower extreme of pump 1 and higher extreme of pump 2 estimated from the position of the blue-red interface of the bar graphs with respect to the targeted proportion. Pump 1 is represented in blue and pump 2 is represented in red.

$$\varepsilon_{Absolute-pump\ 1} = \left| \left(\frac{M_{Actual-pump\ 1}}{M_{Actual-pump\ 1} + M_{Actual-pump\ 2}} \right) - \left(\frac{M_{Ideal-pump\ 1}}{M_{Ideal-pump\ 1} + M_{Ideal-pump\ 2}} \right) \right|. \quad (2.1a)$$

$$\varepsilon_{Absolute-pump\ 2} = \left| \left(\frac{M_{Actual-pump\ 2}}{M_{Actual-pump\ 1} + M_{Actual-pump\ 2}} \right) - \left(\frac{M_{Ideal-pump\ 2}}{M_{Ideal-pump\ 1} + M_{Ideal-pump\ 2}} \right) \right|. \quad (2.1b)$$

$$\varepsilon_{Relative-pump\ 1} = \left| \frac{\left(\frac{M_{Actual-pump\ 1}}{M_{Actual-pump\ 1} + M_{Actual-pump\ 2}} \right) - \left(\frac{M_{Ideal-pump\ 1}}{M_{Ideal-pump\ 1} + M_{Ideal-pump\ 2}} \right)}{\left(\frac{M_{Actual-pump\ 1}}{M_{Actual-pump\ 1} + M_{Actual-pump\ 2}} \right)} \right|. \quad (2.2a)$$

$$\varepsilon_{Relative-pump\ 2} = \left| \frac{\left(\frac{M_{Actual-pump\ 2}}{M_{Actual-pump\ 1} + M_{Actual-pump\ 2}} \right) - \left(\frac{M_{Ideal-pump\ 2}}{M_{Ideal-pump\ 1} + M_{Ideal-pump\ 2}} \right)}{\left(\frac{M_{Actual-pump\ 2}}{M_{Actual-pump\ 1} + M_{Actual-pump\ 2}} \right)} \right|. \quad (2.2b)$$

2.3 Combinatorial thin film library preparation

When considering a certain material *A* that is under development for a thin film application, its characteristic performance indicator can be assigned the quantity *Q*. This quantity *Q* can be anything ranging from viscosity to UV absorbance to a film roughness, among many others. It is also given that material *A* is solution (water or otherwise) processable and can be easily rendered into thin functional films but the ideal formulation and its consequences on *Q* are unknown *a priori*. In typical commercial materials, solution processable or otherwise, the pristine material is

rarely used and there is always at least one additive B which is used to tune Q through a chemical or a physical transformation of A . Examples include surfactants that improve thin film adhesion on certain classes of substrates by regulating interfacial tension [146], additive-induced tuning of the thin film morphology through increased material solubility [147] or additive-induced electrical conductivity tuning of thin films [148]. Based on the specific requirements from the material under development, it may be necessary to explore its properties at different resolutions depending upon the location (along the factor variable axis) of feature in the response variable that is being studied. The experimental endpoint in such cases is typically identified from literature concerning materials that have been developed for similar applications or from relevant simulation studies, both of which may provide a known extremum or optimum in the response.

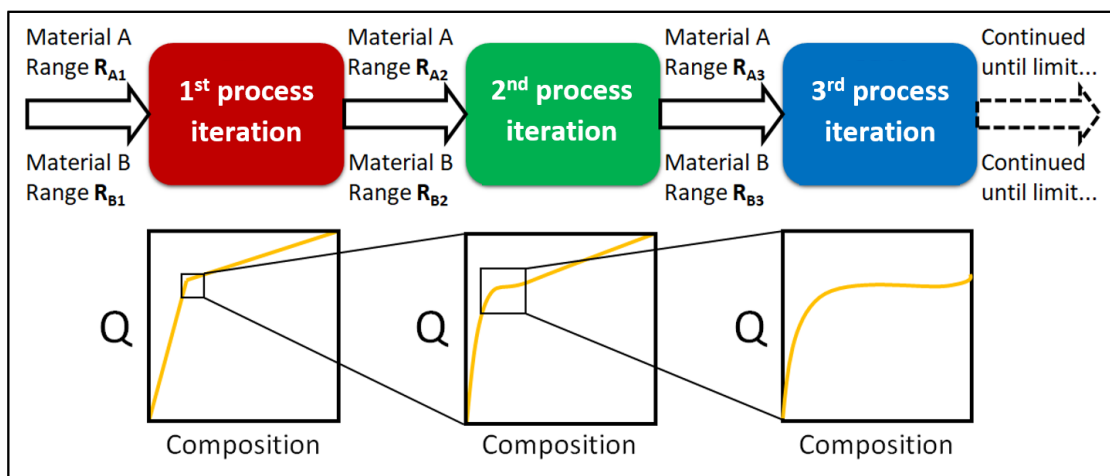


Fig. 2.16: An iterative screening strategy using CPH processing of a binary fluid blend (A/B) at increasingly smaller compositional ranges and increasingly finer compositional resolution until targeted observations are made or hardware limits are reached. The outcome of each iterative step is illustrated graphically by the corresponding behavioral response quantified by Q as a function of composition.

As seen in Fig. 2.14, an iteratively “magnifiable” approach to evaluating the A/B blend response behavior of Q is adopted by directly fabricating patterned thin films using the combinatorial print head (CPH) that integrates microfluidic mixing and inkjet dispensing on-chip as a compact printing device. Using this system, it is possible to explore the effects of composition variations on Q in a multi-resolution manner using variable composition steps. The type of thin film libraries printable using the CPH can be thought of as a variant of the family of array-based strategies outlined in Table 1 in Chapter 1. These libraries take the form of a discretized-gradient array accommodating multiple replicates for each blend composition level. This allows for the possibility of statistically significant observations leading to inferencing clarity of thin film

performance across the array. Fig. 2.13 illustrates the adopted approach for an N -component (primary material A , secondary material B etc.) system where $N = 2$ (primary material A and secondary material B) and can be logically expanded for $N > 2$ up to the physical limit of CPH processability.

The screening protocol begins with the preparation of pristine formulations of material A and material B and the two are CPH-processed (1st iteration) over a broad compositional range of interest to generate coarsely resolved but identically patterned thin film samples. Upon characterizing Q for the compositional range (R_{A1} for A and R_{B1} for B), a sharp transition between two distinct behavioral regimes can be observed. This initial choice of the range of proportions for the materials may be informed by typical ranges used for such materials in similar applications. It is noteworthy that the independent variable shown in Fig. 2.7 need not be only composition for the CPH-based platform but can also be geometric parameters such as the chosen print pattern, the film thickness, as well as combinations of various factors. It is purely a matter of the scope of this work that the focus is on the aspect of material composition. Additionally, this brings to the fore a key advantage of being able to fabricate functionally graded end-use patterns as this also allows for the simultaneous investigation of geometric parameters if required. Thus, the screening of such multi-material thin films can be performed directly at the next level of device hierarchy. The general rule of thumb is to consider standard observable features, their multiplicity and their average statistical spread in similar systems. In the end, however, what really matters is the importance of a particular feature to the application at hand. Refining the ranges to R_{A2} and R_{B2} , another set of CPH-processed (2nd iteration) thin films are generated, this time with a finer compositional resolution. It is seen that the transition which was assumed to be very sharp after the 1st iteration is actually much smoother but slightly kinked. A 3rd iteration of CPH-processing over the ranges R_{A3} and R_{B3} and subsequent analysis of Q at a higher resolution yields a much clearer picture of the transition which can be probed further to reach a well-informed conclusion.

The magnifiable nature of the proposed screening methodology enables the usage of the ink formulation and patterning platform as a "combinatorial microscope", implying that any interesting behavioral artifact observed for Q can be analyzed further by redefining a narrower composition range over the next iteration. This methodology needs to be qualified by asserting that not all solution processable thin film material development roadmaps may require multiple hierarchical levels and often, one or two levels are sufficient to evaluate and/or optimize the

corresponding Q under investigation. While the general methodology adopted for sample fabrication using the CPH platform in this work is described in the last section, overall experimental protocols including statistical analyses of data is covered in greater detail in the next chapter. The framework presented there is used in conjunction with the system described in this chapter to prepare and characterize ICP thin film samples from which, inferences are drawn regarding the tested materials. Additionally, referencing against prior literature on such materials also enables the functional validation of the CPH platform. Statistical inferencing and system and material validation is described in Chapter 4.

Summary

The principles of combinatorial sample formulation introduced in the previous chapter is explored here in greater detail. A general introduction to the concept of a combinatorial print head (CPH) is provided, following which, thin film sample formulation and fabrication is presented. The CPH operation is discussed in the context of proportioning and mixing with the performance of its corresponding elements validated using gravimetric and flow imaging methods. It is found that the proportioning functionality of the CPH is purely limited by hardware capabilities with the current configuration introducing errors within acceptable limits. The mixing functionality of the CPH is achieved by inducing chaotic advection in the fluid through the elastomeric coupling wall of the mixing channel and is corroborated by high-speed imaging. Finally, a hierarchical method for the combinatorial screening of binary fluid blends is proposed for use in experiments described in Chapter 4.

Chapter 3: Experimental evaluation protocols

Chapter overview

The motivation behind this chapter is to provide a detailed outline of the general design of the experiments covered in Chapter 4 concerning case studies using commercial-grade and laboratory-grade intrinsically conductive polymers. A discussion on the usage and limitations of summary statistics leads to the requirement for invoking inferential statistical methods. A particular method of statistical inferencing is chosen and described based on its applicability to the current work. The outcomes and limitations of the method are considered and further analyses introduced to ensure completeness of the protocol. Lastly, the different methods of sample preparation and subsequent characterization are listed in preparation for the analyses in the following chapter.

3.1 Factor and response variables

Before delving into the mathematical framework, it is essential to consider the different constituents of the experiments which are going to be quantified as factors and responses. Given that the combinatorial printing platform is the central tool for creating the thin film libraries used in this work, processing type, blend composition and operating temperature are the independent variables or factors being studied in relation to their corresponding thin film response, which can take multiple forms in multiple domains. Of these different forms, the key dependent or response variable considered is the electrical conductivity of the printed polymer thin films. The choice of this response variable was based on the growing attractiveness of intrinsically conductive polymers (ICPs) for IoT-oriented applications such as multi-functional sensors and actuators for purposes such as healthcare monitoring, body sensor networks and conformable electronics to name a few. In general, the degree of temperature dependence of the measured or response variable is often the determining factor for the utility of any material towards sensor applications. For example, temperature-dependence of electrical conductivity behavior of interconnect materials plays a limiting role with respect to sensor noise and output drift while the requirement for the same temperature-dependent electrical conductivity behavior of sensing materials is quite the opposite.

To this end, printing experiments are performed using the CPH-based platform to fabricate multi-material and sometimes, multi-resolution thin film libraries. These libraries are used not only for the evaluation of the electrical conductivity response of different polymer-additive and

polymer-polymer blend compositions at different temperatures but also to assess the efficacy of the CPH-based platform itself in formulating blends using premixed and unmixed fluids as reference. The latter is an indirect but practically useful method of functional assessment which was initially explored in Chapter 2 for operational validation of the system. The materials used as inks for functional validation include dilute aqueous dispersions of commercial-grade (PEDOT:PSS) and laboratory-grade (PSEDOT) polythiophene-based ICPs and their respective blends. In addition to functional validation, the CPH-based platform is also used to evaluate the electrical conductivity performance of the PSEDOT synthesized by collaborators at Université Laval to replace and/or complement PEDOT:PSS which is currently the most extensively used solution-processable commercial-grade ICP. The need for replacing and/or complementing PEDOT:PSS arises from: (i) its poor water processability without additives; (ii) its poor intrinsic electrical conductivity and (iii) its weak intrinsic temperature-dependent electrical conductivity. As a sensing material, PEDOT:PSS typically needs to always be blended with other non-polymer materials in order to exhibit appreciable change in electrical conductivity and newer ICPs like PSEDOT can potentially be useful in filling this critical niche. Investigation of these aspects, along with the need for assessing platform performance, are what drive the protocols adopted and described here.

3.2 Design and analysis of experiments

3.2.1 General analysis using summary statistics

Most experimental data can be adequately analyzed using observed mean (μ) and standard deviation (σ) values which are measures of central tendency and dispersion respectively. For any response variable being studied as a function of a factor variable, these quantities are reasonably good indicators of variability in the system being investigated with the variability arising from either the position of the mean value or from the variability about the mean value which is indicated by the standard deviation. These measures are typically used to graphically plot response variable trends as functions of the factor variable and provide visual insights into system behavior [149]. In cases where the absolute positions of the mean values are not critical (e.g., means are close to each other for different data sets being compared), a standardized measure of dispersion such as the coefficient of variation (CV), also known as the “relative standard deviation”) is used [150]. CV is the ratio between the standard deviation and the mean of a sample data set and is a

dimensionless number which serves as a useful indicator of repeatability of system response when subjected to the same treatment or factor level. Dispersion in data sets with similar or different means can also be analyzed using *CV* but the drawback of this metric becomes apparent when comparing the mean response at different levels of the factor variables. For significantly different mean responses, the standard deviation about those means may be quite similar. In such cases, the *CV* varies significantly even though the absolute dispersion about a particular mean may not be significant and this gives rise to misleading inferences from the data sets. Besides its underestimation or overestimation of dispersion, *CV* is also invariant [151] to the number of samples in a data set (n) while the deviation of the sample mean from the population mean is dependent on the sample size. In such cases, standard error or the ratio of the standard deviation σ and the square root of the number of samples in the data set (\sqrt{n}), becomes a more reliable measure of dispersion. These scenarios are precisely where inferential statistics, discussed in the next subsection, provides tools to resolve such confusion and is often used in conjunction with the visualizing power of the summary statistics discussed above to draw conclusions about the system being studied.

3.2.2 Single-factor experimental design (one-way ANOVA)

Table 3.1: Data representation for a typical single-factor experiment

Factor levels	Observations						Totals	Means
Level 1	y_{11}	y_{12}	y_{1n}	Y_1	Y'_1
Level 2	y_{21}	y_{22}	y_{2n}	Y_2	Y'_2
...
...
Level m	y_{m1}	y_{m2}	y_{mn}	Y_m	Y'_m
Overall totals							Y	Y'

For a single factor experiment involving a particular material, there can be multiple factor levels that are studied for their corresponding response. Levels of an input factor or independent variable correspond to its different magnitudes or gradations which in turn affect the output response or the dependent variable. Each of these factor levels are generally replicated to

understand statistical variability in the response for that particular factor level. This information can be represented in a tabular manner as shown above. Considering m different factor levels and n replicates for a single factor experiment, it is useful to empirically model the response variable y as a function of the factor variable. It may be trivial but also useful to mention here that the factor variable need not always be numerical as even categorical variables can have levels too.

One way of doing this is by defining the response variable y as:

$$y_{ij} = \mu + \tau_i + \varepsilon_{ij} \begin{cases} i \in 1, 2, \dots, m \\ j \in 1, 2, \dots, n \end{cases} \quad (3.1)$$

This is often referred to as the “effects model” [152] where μ is the overall mean of the data values shown in Table 2.1, τ_i is the i^{th} factor level effect and ε_{ij} is the random error. The indices i and j represent the factor level and the replicate number. The random error component encompasses contributions from the measurement variability arising from uncontrolled and/or insurmountable factors which form the general background noise of the experimental process. This model is intuitively appealing due to the fact that μ is a constant and the τ_i can therefore be thought of as deviations from μ as the different factor levels are implemented. In this context, ε_{ij} can then be thought of as the deviations from each τ_i for each factor level i and replicate j . The y_{ij} represent the different responses (electrical conductivity in this work) to the different factor levels (processing type, blend composition and temperature in this work) with the Y_i and \bar{Y}_i (equivalent to μ_i) representing the total and mean of the measurements made for the i^{th} factor level. Y and \bar{Y} (equivalent to μ) are the overall total and the overall mean of all the measurements and the total number of measurements is $N = mn$.

As is apparent from (3.1), the effects model is a linear statistical model and is used in one of the most powerful analysis techniques for studying the process of experimentation. This technique is called the analysis of variance, more commonly known as ANOVA (ANalysis Of VAriance) [153]. Fig. 3.1 visually summarizes the principle behind the ANOVA method described above for a more intuitive illustration of its workings. A key requirement for the ANOVA method to be valid is that the experiments be performed in random order to ensure uniformity in the experimental environment and adherence to the principles of what is called a “completely randomized design”. The objective of any ANOVA study is to test certain hypotheses about the experiments being undertaken and conclude if they are valid or invalid. Since the m factor levels

are chosen by the experimenter in this work, the broad goal of a corresponding ANOVA study is to test hypotheses about the factor level means. For testing of hypotheses, it is generally assumed that the errors are normally and independently (NID) distributed with zero mean and non-zero variance. Typical hypothesis testing considers two options: (i) a null hypothesis H_0 and (ii) an alternative hypothesis H_1 . Validation of the null hypothesis H_0 implies that the quantities being compared are equal to each other while the alternative hypothesis H_1 is representative of the fact that at least one of the quantities being compared is not equal to the others.

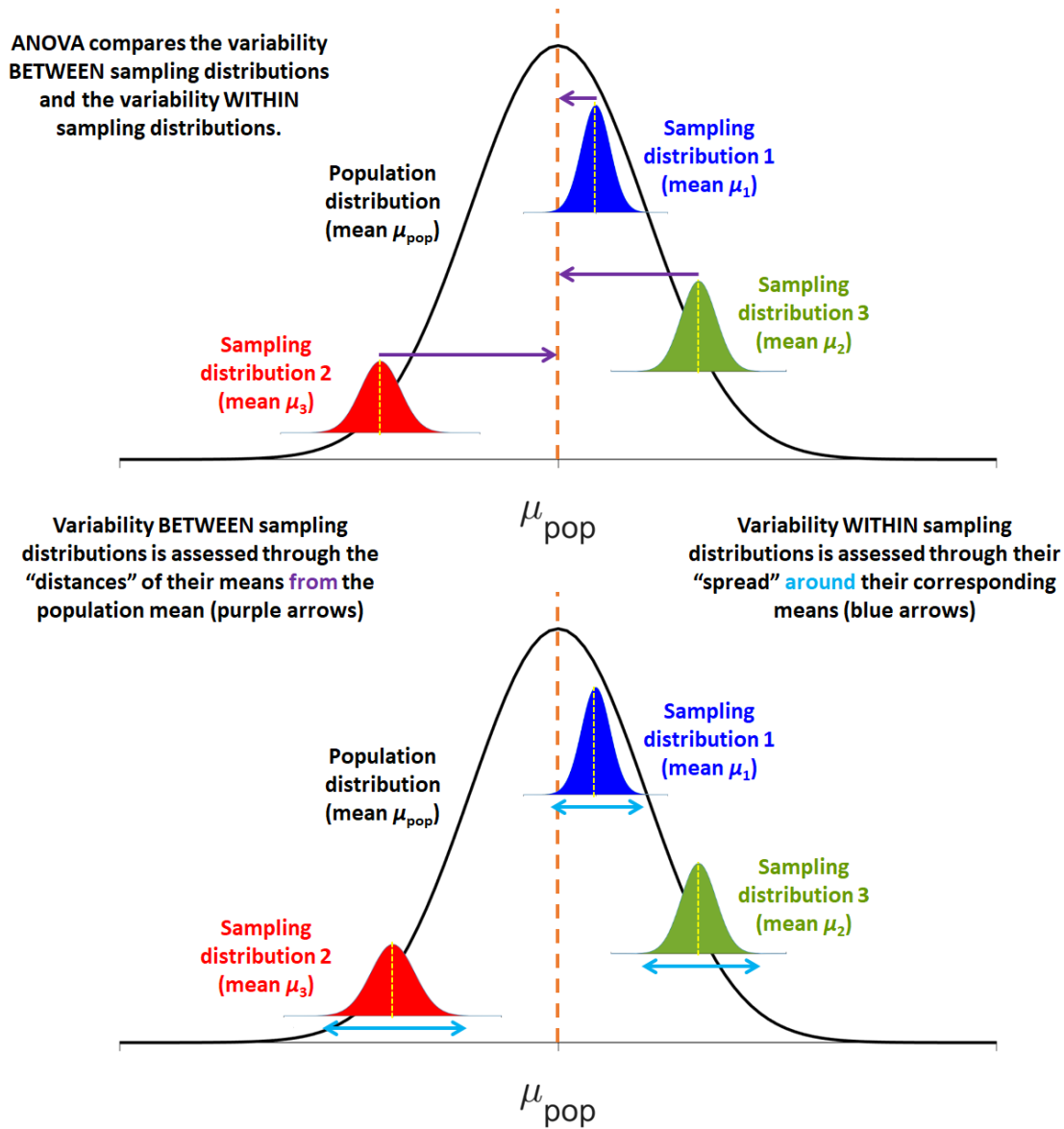


Fig. 3.1: Schematic representation of the ANOVA method of using sampling distributions as estimators of the population distribution in order to accept or reject the null hypothesis. The population mean μ_{pop} and sample means μ_1 , μ_2 and μ_3 are denoted by the orange and the yellow dashed lines respectively.

This can be written for m factor levels in terms of their corresponding factor level means μ_i as:

$$H_0: \mu_1 = \mu_2 = \mu_3 = \dots = \mu_m, \quad (3.2a)$$

$$H_1: \mu_i \neq \mu_j \text{ for at least one pair of } i \text{ and } j. \quad (3.2b)$$

Given that in the effects model, the i^{th} factor level mean μ_i (equivalent to Y_i') can be expanded as $\mu + \tau_i$ with μ (equivalent to Y') being the overall mean shown in (3.1) and τ_i being the effect for the i^{th} factor level, the two hypotheses in (3.2a) and (3.2b) can be reformulated as:

$$H_0: \tau_1 = \tau_2 = \tau_3 = \dots = \tau_m = 0, \quad (3.3a)$$

$$H_1: \tau_i \neq 0 \text{ for at least one } i. \quad (3.3b)$$

It can therefore be stated that ANOVA tests for either the equality of m factor level means for the corresponding factor levels or that the m factor level effects for the corresponding factor levels are zero. The ANOVA method attempts to study the above by partitioning the total variability of the $N = mn$ measurements about Y' into its component parts attributable to the factor levels and the errors. The measure of overall data variability can be defined by the total sum of squares which can be partitioned into two components:

$$SS_{Total} = \sum_{i=1}^m \sum_{j=1}^n (y_{ij} - Y')^2 = n \sum_{i=1}^m (Y'_i - Y')^2 + \sum_{i=1}^m \sum_{j=1}^n (y_{ij} - Y'_i)^2. \quad (3.4)$$

The first term on the right-hand side is an estimate of the mean variability of response between each factor level from the mean overall response. The second term is an estimate of the effect of variability across all replicates within each factor level. These terms are called $SS_{Factor\ Levels}$ (sum of squares of the response at different factor levels) and SS_{Errors} (corrected sum of squares of the response at different factor levels for all replicates) and are central to the principle of the ANOVA method as will become apparent shortly. In a more qualitative manner as shown in Fig. 3.1, it can be said that both terms on the right-hand side are estimates of the response variance; one ($SS_{Factor\ Levels}$) based on the inherent response variability between factor levels and the other (SS_{Errors}) based on the response variability within each factor level. $SS_{Factor\ Levels}$ has a caveat associated with it which is that the null hypothesis of (3.2a) or (3.3a) is valid. If so, then the estimates of sample response variance provided by either of the two sums of squares is expected to be experimentally similar and theoretically identical. If not, then the observed difference can be attributed to the differences in mean response between factor levels. Building on this intuitive

concept, it can be stated that SS_{Total} has $N-1$ degrees of freedom which means that for m factor levels, $SS_{Factor Levels}$ has $m - 1$ degrees of freedom and SS_{Errors} has $N - m$ degrees of freedom. Consequently, $MS_{Total} = SS_{Total} / N - 1$ is called the total mean square of the response and represents the mean sample response variance which can again be partitioned into $MS_{Factor Levels}$ and MS_{Errors} components. $MS_{Factor Levels} = SS_{Factor Levels} / m - 1$ is called the mean square of the mean response variable magnitude at different factor levels and $MS_{Errors} = SS_{Errors} / N - m$ is called the mean square of the random errors within each factor level comprising multiple replicates. Quantitatively, the expectation values of these two quantities [148] shown in (3.5a) and (3.5b) makes it quite apparent that these are estimates of the sample response variance based on the mean response differences between factor levels and the mean response differences within each factor level.

$$E(MS_{Factor Levels}) = E\left(\frac{SS_{Factor Levels}}{m - 1}\right) = \sigma^2 + \frac{n \sum_{i=1}^m \tau_i^2}{m - 1}, \quad (3.5a)$$

$$E(MS_{Errors}) = E\left(\frac{SS_{Errors}}{N - m}\right) = \sigma^2. \quad (3.5b)$$

It is clear from the above that if there are significant mean sample response differences between factor levels, the quantity in (3.5a) will always be greater than the variance of random error σ^2 , assumed to be normally and independently distributed. Otherwise, the sample response variance for each factor level is expected to be exactly equivalent to the random error variance σ^2 with the variation in factor levels having no effect on the mean sample response, the premise of the null hypothesis. This fundamental observation in measurement data, collected and tabulated in the form of Table 3.1, is exploited by the ANOVA method and forms the basis of the test statistic used for evaluating the effect of a factor on the mean sample response at different factor levels. By definition, a test statistic is the summary of a data set which reduces the data set to a single numerical quantity for the purposes of testing hypotheses. In general, any test statistic is defined in a manner such that it is capable of quantifying data behaviour so as to distinguish between the null and the alternative hypotheses.

In (3.1), it has been assumed that the random errors ε_{ij} are normally and independently distributed with zero mean and some non-zero variance. Therefore, it can be inductively stated that the individual sample responses y_{ij} are also normally and independently distributed with mean $\mu + \tau_i$ and variance σ^2 . The implication of this statement is that (SS_{Total} / σ^2) follows a chi-squared

distribution with $N - 1$ degrees of freedom since SS_{Total} is a sum of squares of normally distributed random variables [153]. Under the premise ($H_0: \tau_i = 0$) of the null hypothesis, it can be shown that $(SS_{Factor Levels} / \sigma^2)$ and (SS_{Errors} / σ^2) follow chi-squared distributions too with $m - 1$ and $N - m$ degrees of freedom respectively. Using a modification of Cochran's theorem, it can be inferred that $(SS_{Factor Levels} / \sigma^2)$ and (SS_{Errors} / σ^2) are both independent of each other despite the fact that $SS_{Total} = SS_{Factor Levels} + SS_{Errors}$. It is this independence of the two constituent sums of squares that enables the usage of the ratio of $MS_{Factor Levels}$ and MS_{Errors} as a test statistic for the ANOVA method. Otherwise, it would not be possible to separate the two quantities because of their interdependence which would result in a biased ratio. From the definition of chi-squared [153] distributions, it can also be shown that both $MS_{Factor Levels}$ and MS_{Errors} follow chi-squared distributions too (scaled by the inverse of their respective degrees of freedom) and their ratio follows an F -distribution (named after R. A. Fisher) with $m - 1$ and $N - m$ degrees of freedom.

This test statistic is called the Fisher statistic and is denoted by F_0 . Based on this conjecture, it can be inferred that for a factor to have any significant effect on the response in comparison to the random error, the value of the test statistic F_0 must be at least greater than one. The significance of the value of F_0 where $F_0 > 1$ is generally inferred from estimating the associated p -value. This p -value is defined as the probability of obtaining a test statistic value (F_0 in this case) which is at least as extreme as the observed value of the same statistic given that the null hypothesis is valid and it quantifies whether the specified significance level of the test is met [154]. Significance level [155], also known as Type 1 error probability and usually denoted by α , is the probability of rejecting the null hypothesis given that it is true and is an indicator of “false positive” responses.

Table 3.2: General structure of a one-way ANOVA table.

Sources of variation	Sum of squares	DOF	Mean squares	F_0
Factor	$SS_{Factor Levels}$	$m - 1$	$MS_{Factor Levels}$	$\frac{MS_{Factor Levels}}{MS_{Errors}}$
Error	SS_{Errors}	$N - m$	MS_{Errors}	
Total	SS_{Total}	$N - 1$		

While these calculations are theoretically simple enough to perform by hand, they are also tedious and notoriously susceptible to errors as the data sets become larger. As a result, all of these

calculations pertaining to the ANOVA method are generally performed using software after the fabricated sample library has been characterized and all the relevant data collected. In this work, IBM SPSS Statistics® has been used to perform the ANOVA and post-hoc studies on data acquired from the multi-material thin film sample libraries that were prepared using the combinatorial printing platform. A typical ANOVA response table generated either through manual calculations or software is illustrated in Table 3.2 along with the p -values corresponding to F_0 . All the relevant quantities discussed up to this point are tabulated for ease of inferencing. The key takeaways from such a table include the sum of squares between factor levels and the value of F_0 and its corresponding p -value. The former essentially proposes a model fit while the latter validates its significance. In this work, the corresponding p -value calculated by the software will be included as an added column along with the F_0 statistic column to establish the statistical significance or insignificance of the analysis results, thus paving the way for further evaluation. In addition to the F_0 value and its corresponding p -value, a couple of other metrics called the effect size (denoted by η^2_{partial}) and statistical power (denoted by $1 - \beta$) will be discussed later and included in the ANOVA tables of Appendix A.

3.2.3 Multi-factor experimental design (two-way ANOVA)

Table 3.3: Data representation for a typical multi-factor experiment.

Factors	Factor B				
	Levels	1	2	...	b
Factor A	1	$y_{111}, y_{112}, \dots, y_{11n}$	$y_{121}, y_{122}, \dots, y_{12n}$...	$y_{1b1}, y_{1b2}, \dots, y_{1bn}$
	2	$y_{211}, y_{212}, \dots, y_{21n}$	$y_{221}, y_{222}, \dots, y_{22n}$...	

	a	$y_{a11}, y_{a12}, \dots, y_{a1n}$	$y_{a21}, y_{a22}, \dots, y_{a2n}$...	$y_{ab1}, y_{ab2}, \dots, y_{abn}$

In experiments with multiple factors or treatments, the data representation is similar to single-factor experiments in that each factor has multiple levels and there are multiple replicates for each

factor level as shown in Table 3.3. Multi-factor experiments are also referred to as factorial experiments among which, the two-factor variant is the fundamental design. In such a design, there are two factors A and B with a and b factor levels respectively with n replicates overall. Similar to the one-way ANOVA effects model defined previously, the two-way ANOVA effects model [153] is defined as:

$$y_{ij} = \mu + \tau_i + \omega_j + \tau\omega_{ij} + \varepsilon_{ijk} \begin{cases} i \in 1, 2, \dots, a \\ j \in 1, 2, \dots, b \\ k \in 1, 2, \dots, n \end{cases}, \quad (3.6)$$

where μ is the overall mean, τ_i is the i^{th} level effect of the row factor A , ω_j is the j^{th} level effect of the column factor B , $\tau\omega_{ij}$ is the interaction effect of τ_i and ω_j and ε_{ijk} is the random error. In case of two-way ANOVA, hypothesis testing can be independently done for either the row factor, the column factor or both depending upon the evaluation criteria. In addition, one can also perform hypothesis testing for the interaction between the row and the column factor. The following are the null and alternative hypotheses for each of the above.

Row factor A :

$$H_0: \tau_1 = \tau_2 = \tau_3 = \dots = \tau_a = 0, \quad (3.7a)$$

$$H_1: \tau_i \neq 0 \text{ for at least one } i. \quad (3.7b)$$

Column factor B :

$$H_0: \omega_1 = \omega_2 = \omega_3 = \dots = \omega_b = 0, \quad (3.8a)$$

$$H_1: \omega_j \neq 0 \text{ for at least one } j. \quad (3.8b)$$

Interaction factor AB :

$$H_0: \tau\omega_1 = \tau\omega_2 = \tau\omega_3 = \dots = \tau\omega_{ab} = 0, \quad (3.9a)$$

$$H_1: \tau\omega_{ij} \neq 0 \text{ for at least one } ij. \quad (3.9b)$$

If Y_{i00} denotes the total of all observations at the i^{th} level of the row factor A , Y_{0j0} denotes the total of all observations at the j^{th} level of the column factor B , Y_{ij0} denotes the total of all observations in the ij^{th} cell, and Y_{000} denotes the grand total of all, we have

$$Y'_{i00} = \frac{Y_{i00}}{bn}; Y'_{0j0} = \frac{Y_{0j0}}{an}; Y'_{ij0} = \frac{Y_{ij0}}{n}; Y'_{000} = \frac{Y_{000}}{abn} \quad (3.10)$$

where Y'_{i00} , Y'_{0j0} , Y'_{ij0} and Y'_{000} are the corresponding means and i and j vary from 1 to a and 1 to b respectively. Thus, the total sum of squares for the two-factor experiment described above can then be written as:

$$SS_{Total} = bn \sum_{i=1}^a (Y'_{i00} - Y'_{000})^2 + an \sum_{j=1}^b (Y'_{0j0} - Y'_{000})^2 + n \sum_{i=1}^a \sum_{j=1}^b (Y'_{ij0} - Y'_{i00} - Y'_{0j0} + Y'_{000})^2 + \sum_{i=1}^a \sum_{j=1}^b \sum_{k=1}^n (y_{ijk} - Y'_{ij0})^2. \quad (3.11)$$

Table 3.4: General structure of a two-way ANOVA table.

Sources of variation	Sum of squares	DOF	Mean squares	F_0
Factor A	SS_A	$a - 1$	MS_A	$\frac{MS_{Factor Levels}}{MS_{Errors}}$ for each factor
Factor B	SS_B	$b - 1$	MS_B	
Factor AB	SS_{AB}	$(a - 1)(b - 1)$	MS_{AB}	
Within factor levels	SS_{Errors}	$ab(n - 1)$	MS_{Errors}	
Total	SS_{Total}	$abn - 1$		

The first three summation terms on the right-hand side of (3.11) denote the estimates of response variability between each factor level of factors A , B and AB from the mean overall response while the fourth term is an estimate of the effect of variability across all replicates within each factor level such that the total number of data points is abn . Therefore, the total sum of squares SS_{Total} can be partitioned into sum of squares due to factor A (SS_A), sum of squares due to factor B (SS_B), sum of squares due to the interaction factor AB (SS_{AB}) and the sum of squares due to random error (SS_{Error}) where, as before, the sum of squares represents the dispersion of the mean values of the respective factor levels around the overall mean value of the data set under consideration. As before with one-way ANOVA, the sum of squares of each factor divided by its corresponding degree of freedom results in the corresponding mean square (MS_A , MS_B , MS_{AB} , MS_{Error}) which, under the null hypotheses, results in the familiar statistic F_0 being defined as MS_A/MS_{Error} , MS_B/MS_{Error} and MS_{AB}/MS_{Error} for all three factors. For the null hypothesis to be violated, the numerator of F_0 must be greater than the denominator and its statistical significance is once again established by the corresponding p -value evaluating to a value lower than the Type 1 error rate or significance level α (generally 0.05 or 5%) of the experiment. Table 3.4 illustrates a typical two-way ANOVA table which looks quite similar to a one-way ANOVA table except for the added

rows representing the multiplicity of factors involved. In this work, one-way ANOVA is performed on pristine and blended ICPs as a function of blend composition at different composition ranges while two-way ANOVA is performed for electrical conductivity response of pristine and blended ICPs as a function of blend composition and ambient temperature. Also, α has been chosen to be 0.05 (or 5%) throughout in keeping with its generally accepted value [148] with a higher value implying that a higher false positive rate is acceptable. Choice of α is dependent on the overall aim of the experiment being conducted and the associated practical tolerance thresholds for hypothesis errors.

3.2.4 ANOVA assumptions, effect size and statistical power

Hypothesis testing using methods like ANOVA is useful in commenting on the likelihood of the observed results given certain assumptions such as independence of observations, normality of experimental errors (or residuals) and equality of variances of data sets being compared [148]. Before further discussion, it is essential to establish that the above assumptions hold true for the data sets used in this work. The independence of observations is perhaps the easiest to establish given that each data point in each data set is obtained from an individually printed polymer channel with no dependencies on other channels. The Shapiro-Wilk test [156] is generally the test used for confirming normality of errors (or residuals). This test is similar to an ANOVA test where the null hypothesis H_0 is that the errors (or residuals) are distributed normally with an associated significance level similar to that described for ANOVA. The normality assumption can also be assessed graphically using normal quantile-quantile ($Q-Q$) plots of the observations which can be fitted to straight lines when plotted against the corresponding quantiles from a standard normal distribution if the assumption is true. A quick method of establishing normality of data sets is to compare the standard error for skewness and kurtosis with their respective estimates ($\sim\sqrt{6/n}$ for skewness and $\sim\sqrt{24/n}$ for kurtosis where n is the sample size) and rejecting the normality hypothesis if either or both are greater than twice those estimates. Homoscedasticity or equality of variances of the data sets used is most commonly evaluated using Levene's test [157] which is another test that is similar to ANOVA where the null hypothesis H_0 is that the variances are equal and this too has an associated significance level similar to ANOVA.

It is important to remember that these assumptions may not always hold perfectly true given the existence of outlier data points owing to uncontrollable intrinsic effects which may

introduce skewness in the sampling data distribution. The ANOVA methodology is quite robust against some deviations from the normality and homoscedasticity, especially when the sampling data sets are of equal size. In this work, two levels of statistical analyses are performed: (i) equal sample size and (ii) marginally unequal sample size for different factor level data sets where outliers are not included in level (ii). Criteria for exclusion of outliers is subjective but also stringent and are laid out explicitly for the different case studies covered in the next chapter. Also noteworthy is the fact that there are some deviations from the normality and homoscedasticity assumption in certain data sets and are accounted for by appropriate selection of post-hoc tests as discussed in the next section.

While hypothesis tests do provide valuable information regarding the statistical significance of experimental observations, they cannot comment on the effect size if the null hypothesis H_0 is rejected. This essentially means that the results of an experiment could be significant but the effect itself might be inconsequentially small. Therefore, the conclusions drawn from hypothesis testing remain incomplete unless supplemented by the evaluation of effect sizes [158]. In this work, partial eta squared ($\eta^2_{partial}$) is the metric used to measure the effect size of the factor variables in ANOVA models and is defined as the ratio between the quantities $SS_{Factor Levels}$ and $(SS_{Factor Levels} + SS_{Error})$ as illustrated in (3.11).

$$\eta^2_{partial} = \frac{SS_{Factor Levels}}{SS_{Factor Levels} + SS_{Error}}. \quad (3.12)$$

Despite hypothesis testing primarily concerning itself with significance levels or Type 1 error probabilities (α), the Type 2 error probability (β) also needs to be accounted for [159]. The quantity β is defined as the probability of failing to reject the null hypothesis when it is actually false or simply put, a “false negative”. Statistical power is quantified as $(1 - \beta)$ and represents the probability that the test correctly rejects the null hypothesis H_0 when it is false. This quantity thus becomes important when the ANOVA rejects the null hypothesis and is related to the effect size and the variation within data sets, whereby changing one of these quantities results in a change in the statistical power of an experiment.

Fig. 3.2 illustrates this graphically for two processes corresponding to a control process data set (blue) and a test process data set (red). It becomes intuitively apparent that greater overlap between the sampling data distributions due to either the proximity of means (small effect size) or

greater scatter within data sets (large variance) result in loss of statistical power or the ability to distinguish between the effect of the two processes under investigation. This can generally be remedied by taking larger sample sizes based on power calculations performed on initial data sets using software (like IBM SPSS Statistics®). However, it is also important to remember that in order to detect extremely small effects in an experimental paradigm where inherent sample-to-sample variability is high, sometimes a prohibitively large number of samples may be required based on the estimates provided by power analyses. Hence, it is at these junctures that practicality of such an endeavor needs to be examined from a cost-benefit perspective. With this consideration in mind, the next subsection discusses post-hoc tests for evaluating key contributors to statistically significant ANOVA results where the concept of statistical power is touched upon again.

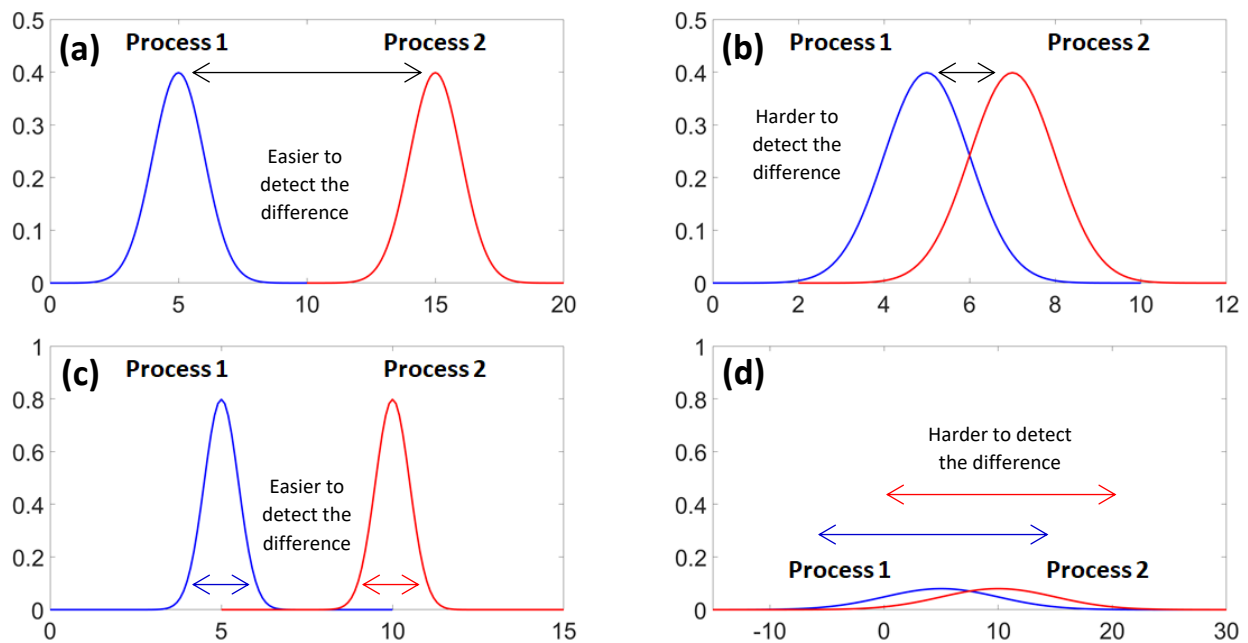


Fig. 3.2: Sampling data distribution of two processes (“control” process shown in blue and “test” process shown in red) illustrating large (a) and small (b) effect sizes at identical distribution variance or small (c) and large (d) variance within individual data sets at identical effect sizes respectively.

3.2.5 ANOVA post-hoc validation

In general, ANOVA F -tests are used to search for significant differences within means of a group of data sets. Such tests provide overall results for the data sets being analyzed as a collective based on the F -value and corresponding p -value of the test in comparison to the chosen Type 1 error probability or the α value. As described earlier, a p -value less than the α -value implies that at least one (if not more) of the mean values being compared in the ANOVA F -test are

different from the others and therefore, the null hypothesis H_0 can be rejected. However, the ANOVA F -test does not provide any explicit information regarding which data sets are significantly different from the others and often, this information is critical for drawing any conclusive inference. This is where the utility of post-hoc validation becomes apparent in the context of evaluating pairs of data sets through multiple comparisons.

For example, analyzing a group of 3 data sets will imply 3 post-hoc pairwise comparisons to be made while a group of 4 data sets will require 6 post-hoc pairwise comparisons and so on. Typically, for an ANOVA F -test, post-hoc validation is required only when H_0 is rejected and not otherwise as in that case, the F -test sufficiently establishes the lack of any statistically significant overall differences among the group of data sets being analyzed. Post-hoc tests need to control the overall Type 1 error probability or the α -value as with increasing number of pairwise comparisons beyond 2 data sets, the overall α value increases drastically and can result in doubtful inferencing. This control is usually achieved by specifying the overall α -value and adjusting the significance level of the pairwise comparisons to ultimately match the specified α value. These procedures are trivially managed by the statistical software being used (IBM SPSS Statistics®) and the results are presented using either the adjusted p -value method or the simultaneous confidence interval method.

There are multiple different post-hoc validation methods available with each method having its own advantages and trade-offs. One of the major trade-offs involves choosing a post-hoc test which is conservative in its significance level estimates versus one which is not. This, in turn, affects statistical power which decreases as the number of pairwise comparisons increases. To compare the effect of control of the significance level on conclusions from pairwise comparisons, the post-hoc validation methods chosen for this work are (i) the Tukey-Kramer test [160] and (ii) the Games-Howell test [161]. Both are conservative in the preservation of Type 1 error rates with the Games-Howell test being preferred over the Tukey-Kramer test for heteroscedastic data sets (unequal variances). In the experiments conducted in this work, the occurrence of Type 1 errors (rejection of the H_0 when it is true) needs greater control compared to Type 2 errors (failure to reject H_0 when it is false) due to variability issues as will be illustrated in the following chapter. However, Type 2 errors are not completely inconsequential as they have a direct effect on statistical power. Statistical software can be used for power analysis of

experimental data sets which can also be used as a tool to estimate the sample size required to detect an effect through an experiment and can provide validation for chosen sample sizes.

3.3 Materials and methods

3.3.1 Library types: Thin films and printable inks

Pristine and blended ICPs are the key materials used for testing different hypotheses regarding platform performance as well as material behavior. These include both a commercial-grade and a laboratory grade ICP. PEDOT:PSS (commercial-grade) and PSEDOT (laboratory-grade) are the two ICPs, distilled water is used as the primary ICP dispersing and diluting solvent while DMSO is used as an additive. The ICPs are discussed in further detail in Chapter 4 along with the roles played by the solvent and the additive.

Hypothesis testing based on the methods outlined in previous sections are carried out on CPH-processed thin film libraries of polymer/additive and polymer/polymer blends of the metallic ICPs using different characterization methods. Based on the characterization method used, different combinatorial library types are prepared using the platform. These are generally in the form of replicated arrays with only the geometric nature of the array element varying. Fluid mixing was demonstrated using imaging tests to compare diffusive and advective. Other characterization methods such as electrical probing and contact profiling require the printed thin film channel arrays to have a more definite geometric shape to assist with post-measurement calculations. In such cases, it is a necessity to have printed features of specific dimensions on a substrate of choice. Printable inks comprise another class of libraries that are used only in a few cases in this work. For such libraries, CPH processing is bypassed as the output volume and volume flow rate requirements are much larger than that of printed thin films. Proportioning using syringe pump as well as manual syringe extraction is used for the pristine ink precursors which are then mixed using magnetic stirring as well as in an ultrasonic bath respectively for homogenization.

3.3.2 Characterization methods

Multiple testing methods are employed to characterize the ICP dispersions in liquid ink phase and as thin solid films. Analysis of the response variables electrical conductivity and temperature coefficient of resistance is carried out as a function of the factor variable blend composition. In addition, the electrical conductivity of the printed channels is also analyzed as a

function of temperature for different blend compositions to determine temperature sensitivity and stability. Quantitative and qualitative characterization methods used and the corresponding information generated by them to provide the framework for drawing inferences about the combinatorially formulated ICP blends are discussed below.

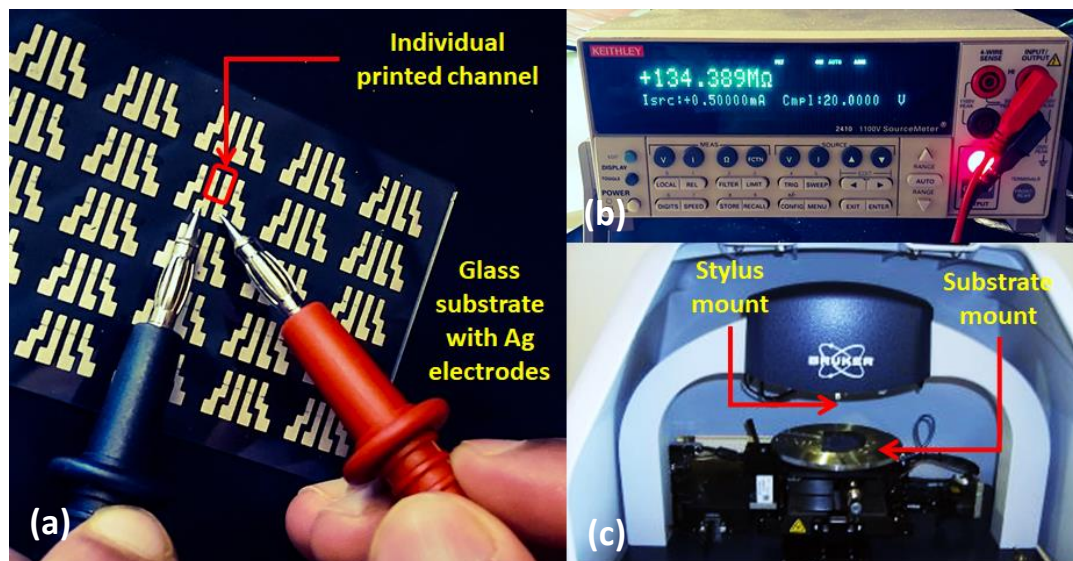


Fig. 3.3: Sample probing (a) for printed channel resistance measurement with Keithley 2410 unit (b) followed by stylus-based cross-sectional profile measurement using Bruker Dektak XT (c) for evaluating electrical conductivity.

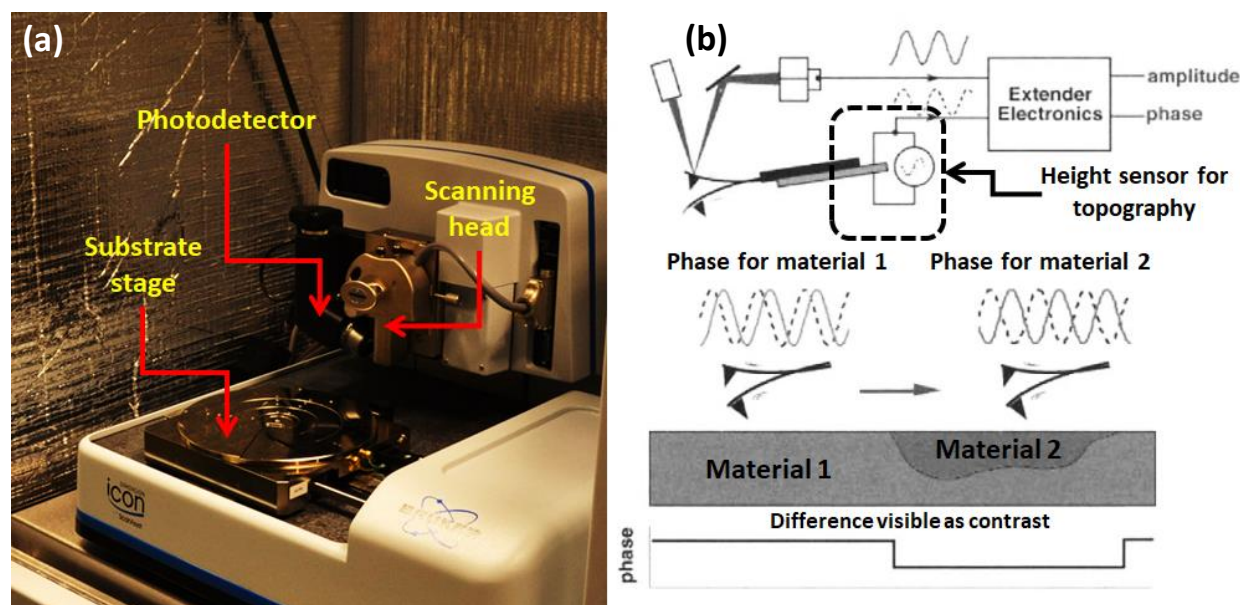


Fig. 3.4: (a) Bruker Dimension Icon atomic force microscope and its key components and (b) tapping mode measurement schematic methodology for topography and phase imaging [158].

(a) *Electrical characterization:* This was the primary mode of testing employed given that the materials of interest are conductive polymers. The combinatorial thin film libraries were subjected

to resistance measurements by probing the individual library components and measuring the cross-sectional profile to obtain the conductivity. Resistance measurements were also performed across a range of temperatures relevant for wearable sensors, point-of-care diagnostics etc. within the IoT framework. Temperature dependence of conductivity of the printed thin films (channels) as a function of ink composition is a key requirement for conductive polymers to be useful in such applications. Resistance measurements were done using a Keithley 2410 source-measurement unit and printed thin film channel cross-sectional profiles [162] were measured using a Bruker Dektak XT stylus profilometer in order to evaluate the electrical conductivity ($= l_{channel}/RA_{channel}$) of the printed channels where R is the measured resistance, $l_{channel}$ is the length of the printed channel and $A_{channel}$ is the cross-sectional area of the channel averaged over three sections as shown in Chapter 4. Temperature variation was achieved using a hot plate (Fisher Scientific Isotemp) whose surface temperature was calibrated using a k -type kapton-encapsulated thermocouple wire probe (Extech Instruments). Fig. 3.3 shows the characterization equipment discussed here.



Fig. 3.5: (from left to right) Malvern Zetasizer Nano ZS for dynamic light scattering measurements, Bruker D8 Advance x-ray diffractometer, Anton-Paar Physica MCR 301 rheometer and Biolin Scientific Attension Theta tensiometer.

(b) *Morphological characterization:* It is well established that charge transport properties of inherently disordered systems such as conductive polymer thin films are strongly dependent on film morphology [163]. Enhanced connectivity between conductive domains within polymer thin films and improved alignment of these regions can lead to the formation of a larger conducting network through which charge transport is maximized. Atomic force microscopy (AFM) is an extensively used tool for imaging thin films for correlation of morphological observations with other characterization results. Over time, many advancements have been made to the basic AFM

platform to add specialized functionalities targeted towards specific sample types in what is known today as the field of scanning probe microscopy (SPM). Printed thin film surface imaging has been primarily conducted using the AFM in different tapping mode variations. Bruker Dimension Icon has been the used for the AFM imaging of the printed thin film libraries. The morphology and phase imaging have been done using the standard tapping mode with aluminum (Al)-coated silicon (Si) probes with non-conductive tips. The force constant and resonance frequency of the probes are ~ 40 N/m (20 N/m to 75 N/m typical range) and ~ 300 kHz (200 kHz to 400 kHz typical range) respectively with a tip radius ~ 10 nm. Tunneling current imaging has been done using the peak force tapping mode with platinum (Pt)/iridium (Ir)-coated silicon nitride (Si_3N_4) probes with conductive tips. The force constant and resonance frequency of the probes are ~ 0.4 N/m (0.2 N/m to 0.8 N/m typical range) and ~ 70 kHz (45 kHz to 95 kHz typical range) respectively with a tip radius ~ 25 nm. For both the imaging modes, a $1\text{ }\mu\text{m} \times 1\text{ }\mu\text{m}$ surface area of the sample has been chosen to maintain consistency of features across images. Fig. 3.4 shows the characterization equipment discussed here.

(c) *Miscellaneous characterization:* Apart from electrical and morphological characterization of printed thin films, other modes of evaluation used range from optical microscopy of printed features to highly sensitive spectroscopic methods that were used to understand the molecular structure of these polymers. Multiple techniques have been used to study the ICPs in their liquid (printable inks) and solid (thin films) states. Dynamic light scattering (DLS) [164] is a liquid phase technique and is useful for determining particle size distribution in suspensions and dispersions. DLS measurements have been conducted using a Malvern Zetasizer Nano to obtain aggregate size estimates in the ICP dispersions used as inks for the printing. This also enables the approximation of their corresponding diffusion coefficients which play an important role during the process of mixing the precursors for homogenization of the fluid blends.

Conjugated polymers are generally disordered by nature although there are various methods to improve ordering and connectivity which also results in conductivity enhancement. Studies on the effect of additives and blending on thin film crystallinity are conducted with x-ray diffraction (XRD) [165] of printed thin films using a Bruker D8-Advance x-ray diffractometer. These studies are meant to provide qualitative insights into the material itself rather than CPH processing. In addition, viscosity [166] and surface tension measurements [167] were performed on the ICP dispersions using an Anton-Paar Physica MCR 301 rheometer and a Biolin Scientific

Attension Theta tensiometer respectively. The above is a general overview of the typical methods used to study ICP dispersions and printed thin films based on the approach adopted and outlined throughout this chapter. Fig. 3.5 shows the characterization equipment discussed here. In addition, optical microscopy of the CPH mixing channel is performed using a Nikon Eclipse Ti-2 inverted microscope with high-speed flow imaging carried out using a Phantom Ametek VEO-E 310L camera. Case-specific details of the experimental processes including sample fabrication will be discussed in the following chapter.

Summary

Besides introducing the different factor variables and the response variable of interest in this work, this chapter provides the framework for the statistical analyses conducted on the data sets from the case studies in the following chapter. Specifically, the pros and cons of summary statistics and their usage in graphical plotting is briefly discussed which leads to the need for using inferential statistical methods of analysis. The workings of the ANOVA method are presented in detail to justify its usage in the case studies conducted in Chapter 4. In addition, the fallacies of using the method by itself are considered and subsequent analyses methods suitable for completion of the inferencing process are explored. These primary and secondary analyses on the case studies' data sets are defined for different scenarios to enable accurate inferencing from measurement data. Finally, a brief overview of the sample library characterization methods is provided.

Chapter 4: Investigating Conductive Polymer Blends

Chapter overview

This chapter discusses the combinatorial printing experiments conducted using the printing and characterization methods described in Chapter 2 and summarizes the statistical analyses done on those data sets based on the protocols described in Chapter 3. A commercial-grade and a laboratory research-grade intrinsically conductive polymers of similar chemical type are used to perform these experiments. The generally established electrical conductivity behavior of the commercial-grade polymer when treated with a certain additive over a certain composition range is used to assess the performance of the combinatorial printing platform against two reference methods. Subsequently, the platform is used to assess the electrical conductivity behavior of the commercial-grade polymer-additive blends over different composition ranges. Lastly, blends of the laboratory-grade polymer and the commercial-grade polymer are explored under different paradigms to assess the viability of their usage as components in temperature sensing applications.

4.1 Intrinsically conductive polymers

4.1.1 Emergence of PEDOT:PSS

Polymerized 3,4-ethylenedioxythiophene (EDOT), abbreviated as PEDOT, has been the subject of extensive research ever since it was first successfully synthesized [116] at Bayer AG's Central Research Department in the late 1980s. After nearly a decade of experimenting with different monomeric thiophene structures which resulted in quite a few promising but mostly unsuccessful trial runs, the breakthrough came by transforming the fundamental thiophene structure into a bi-cyclic system through ring closure of its alkoxy substituents. A few patents and collaborations later, the application of PEDOT as an antistatic agent on photographic films was being investigated by Agfa-Gevaert AG which was also a Bayer subsidiary at the time. The need for a new antistatic agent stemmed from the deficiencies of the existing antistatic agents as vanadium pentoxide (V_2O_5 , used by Kodak) suffered from toxicological hazards and associated environmental issues while the conductivity of sodium poly(styrenesulfonate) (PSS-Na, used by Agfa) was heavily influenced by humidity. In the quest to formulate a humidity-independent environmentally friendly antistatic agent, it was found that the ionic forms of PEDOT and PSS could combine non-stoichiometrically into a stable aqueous polyelectrolyte complex (PEC)

PEDOT:PSS, where the PSS polyanion serves as the counterion for the doped PEDOT polycation. However, PSS is not an oxidizing agent to PEDOT but is simply used as a counterion and a solubility enhancing agent while the oxidation is carried out in the presence of metallic persulfates. Owing to the non-stoichiometric excess PSS in aqueous PEDOT dispersions, the resulting PEC is distributed as gel particles [116] with the PSS acting as the host polyelectrolyte (HPE) and PEDOT as the guest polyelectrolyte (GPE). These gel particles vary in hydrophobicity across their volume with the interior regions being more hydrophobic due to more HPE-GPE charge neutralization in comparison to the exterior regions which have a higher proportion of the HPE forming a charged shell-like structure which becomes the bounding surface of the gel particles. The existence of excess HPE (PSS) thus enables the electrostatic stabilization of the dispersion. But while PSS improves the aqueous dispersion stability of the PEC (PEDOT:PSS), it does so at the expense of its electrical conductivity by forming the cross-linked solvent-rich gel network with and around the insoluble but conductive PEDOT as described above. This leads to greater spatial and energetic separation of conductive PEDOT-rich domains in the gel particles when thin films are formed from such dispersions due to the lowering of charge carrier hopping probability which is the primary charge transport mechanism in disordered systems like polymers. Fig. 4.1 illustrates the chemical structure of PEDOT:PSS and its morphology in dilute dispersions and thin films.

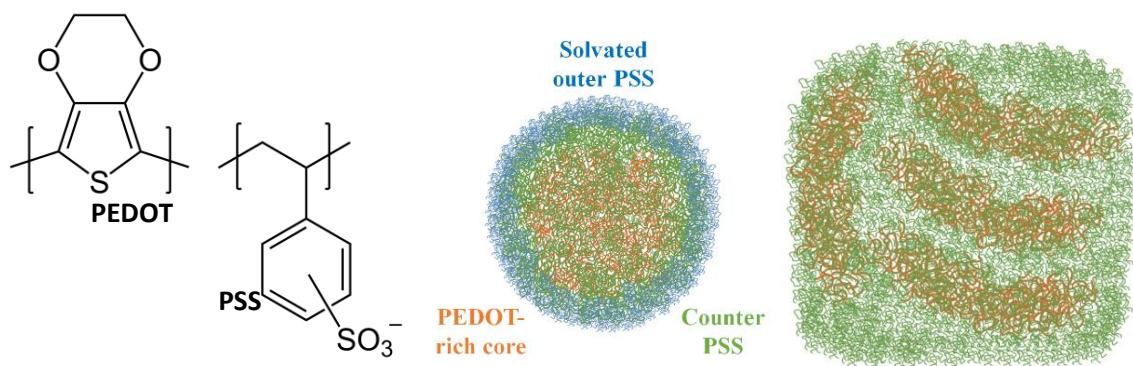


Fig. 4.1: (left) Structural formula of individual 3,4-ethylenedioxythiophene (EDOT) and styrenesulfonate (SS) monomers which form the PEDOT:PSS polyelectrolyte complex, (middle) schematic representation of a PEDOT:PSS gel particle in dilute aqueous dispersions where the inner PEDOT-rich polycationic core (orange) is countered by the PSS polyanions (green) with the non-stoichiometric excess forming a highly solvated shell with water molecules (blue) distributed both within and around it, and (right) schematic morphological representation of dried PEDOT:PSS thin films deposited using solution processing methods and showing how the PEDOT-rich domains (orange) are shrouded by the excess PSS (green) which reduces the electrical conductivity of the film.

Since its emergence as a material of commercial value, poly(3,4-ethylenedioxythiophene) polystyrene sulfonate, commonly known as PEDOT:PSS, has been the intrinsically conductive polymer of choice for solution processable applications in multiple domains of thin film research. It has seen extensive usage in different forms of processing such as aqueous dispersions for spin/slot-die/dip coating and droplet-based dispensing/printing (thinner sub-micrometer layers), paste-like viscous compositions for doctor blading and screen/3D printability (thicker sub-millimeter layers) as well as in the form of hydrogels and free-standing films.

4.1.2 Drawbacks and the need for novel ICPs

While PEDOT:PSS has enjoyed commercial success over the past decades as the ICP of choice for a wide array of applications ranging from self-healing electrode layers in solid electrolytic capacitors to hole-injection layers in organic light emitting devices (OLEDs) to printed “smart” electronics, there are a few drawbacks associated with the material with its patterned deposition as well as its stoichiometric composition. Patterned additive deposition methods typically rely on droplet dispensing techniques such as inkjet and aerosol jet printing among others which requires the dispensing orifices to remain consistently unobstructed throughout the deposition process which often includes time gaps where the dispersion remains idle at the orifice without droplet jetting such as during substrate positioning or in between consecutive printing runs. One of the primary difficulties associated with printing PEDOT:PSS dispersions is its tendency to form agglomerates within the dispensers and solute deposits at dispenser orifices, progressively choking it off until fully clogged. While the use of filtering, dilution and surfactants can alleviate this to a certain degree, it is never completely resolved. In addition, the process of filtering or dilution reduces the solute fraction in the dispersion significantly, leading to the requirement of greater dispersion quantity to achieve the same electrical conductivity response as that of unfiltered or undiluted dispersions. The use of surfactant additives does ensure lower levels of agglomeration within the dispersion inside the dispenser but it does not do much to prevent the growth of solute deposits at the dispenser orifice. Clogging is driven by solvent evaporation at the meniscus but is particularly problematic for PEDOT:PSS due to the inherent aqueous insolubility of PEDOT. The addition of PSS to the dispersion counters this to a certain degree but at the dispenser orifice, the tendency to form agglomerates is greater due to volume confinement which leads to increased interaction of PEDOT:PSS gel particles shown in Fig. 4.1 and is worsened by solvent evaporation. The other key deficiency of PEDOT:PSS is the presence of the solubility

enhancer but electrical insulator PSS which drastically reduces the electrical conductivity of the deposited feature when used in its pristine form. Certain additives help to overcome this but at the cost of compromising on some other performance metric as will be seen later in this chapter.

The above issues have led to research on novel ICPs which do not require solubility enhancement components like PSS which also suppresses the electrical conductivity of ICPs like PEDOT. Functionalizing polymers with branched and unbranched side chains are known to increase their water solubility. Indeed, this solubility enhancement extends not only to water but also other polar solvents and solvent blends such as poly(ethylene glycol), dimethyl sulfoxide and water-alcohol mixtures. As a result, increased processability using environmentally friendly and relatively low toxicity solvents is possible. This principle gave rise to the idea that it may also be possible to create highly processable aqueous dispersions of ICPs with branched side chains without the need for additives. The answer to the problem of charge balance, as in the case of positive PEDOT being balanced using negative PSS as the counterion, was found by a process called “self-doping” where branched side chains were terminated using sulfonic acid ($-\text{SO}_3\text{H}$) such that the counterions were provided within the ICP molecule. The key structural difference between a polyelectrolyte complex (PEC) like PEDOT:PSS and a self-doped version of PEDOT is seen in Fig. 4.2. It is important to remember that the concept of “self-doping” using sulfonic acid-terminated branched side chains is concerned more with charge stabilization rather than doping in the true chemical or electrochemical sense. True or primary doping is brought about by the processes of oxidation or reduction depending upon the macromolecule in question and is governed by the synthesis process which determines its HOMO-LUMO levels. Having a HOMO value higher than a threshold value causes the self-doped ICP to have a partially oxidized state even in its pristine form due to spontaneous reaction with atmospheric oxygen.

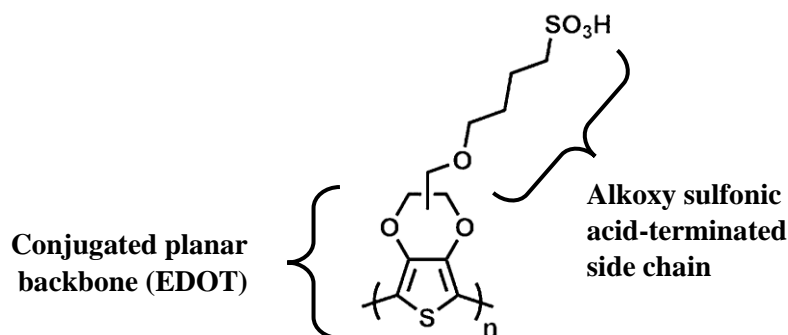


Fig. 4.2: Structural formula of the regiorandom alkoxy sulfonic acid side chain-doped monomer unit of the PSEDOT macromolecule.

The self-doped regiorandom poly(3,4-alkylenedioxythiophene) (PSEDOT) variant evaluated in this chapter was synthesized by the Leclerc group [168] who are our research collaborators at the Université Laval. For the ease of nomenclature correlation with the literature reported from the Leclerc group, the PSEDOT variant will be called *P2* while PEDOT:PSS is referred to as *P1* in all text, figures and tables henceforth. The chemical structure of the *P2* monomer unit is illustrated in Fig. 4.3 with ball-and-stick representation relaxed using the DFT-based molecular structure visualization software CrystalMaker 10.6. The difference with *P1* is shown through the solid blue line as *P1* contains the polymer PSS as its counterion rather than the sulfonic acid-terminated alkoxy side chain while the remaining planar thiophene structure is identical for both ICPs.

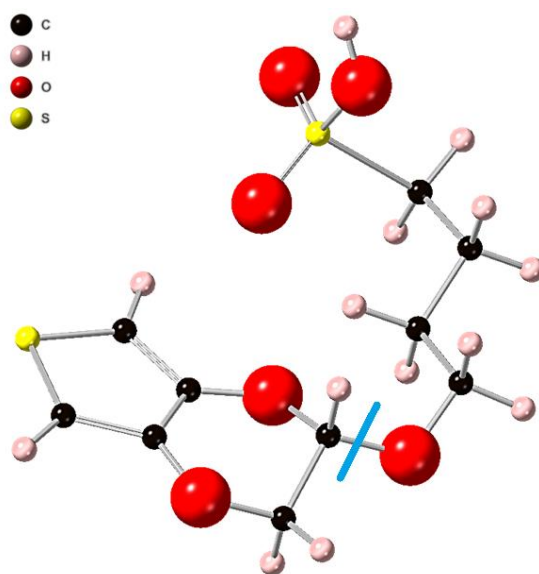


Fig. 4.3: Ball-and-stick representation of the *P2* monomer structure with the part on the left of the solid blue line representing the *P1* (conductive component) monomer.

4.2 Material characterization

4.2.1 Aggregate sizing in ICP dispersions

ICP nanoparticles (or any other nanoparticles for that matter) are rarely unaggregated when dispersed in a suitable solvent due to their high surface energy resulting from high surface area to volume ratios. A certain degree of agglomeration occurs in pristine dispersions to reduce this high surface energy through physical adhesion of multiple nanoparticles by weak forces like van der Waals and hydrogen bonding which results in the reduction of the surface area to volume ratio of the aggregate. It is these aggregates and not the individual nanoparticles themselves that diffuse over reduced length scales after being subjected to vibratory actuation within the mixing channel

of the CPH. Dynamic light scattering (DLS) measurements of the aqueous *P1* and *P2* dispersions at 0.65 wt.% yield the aggregate sizes (diameters) and under the spherical aggregate approximation, the Stokes-Einstein relation can be used to estimate the diffusion constant in each case. Fig. 4.4 illustrates the aggregate size distribution in *P1* and *P2* dispersions which also reveals a tendency of these dispersions to form progressively larger aggregates with time. The time gap $t = 120$ s is chosen in accordance with the approximate time required for a fluid element to move from the entrance of the mixing channel to the inkjet dispenser orifice as mentioned in Chapter 2. *P1* shows a bimodal aggregate size distribution even at the initial measurement which conforms with its observed tendency to form aggregates. The coincidence of the aggregate size peaks (~ 1.2 μm and ~ 5.6 μm) is definitely interesting and may be due to the identical polythiophene backbone and solubility enhancing sulfonic acid group (on the polystyrene matrix in *P1* and on the alkoxy side chains in *P2*) which can lead to similar polymer chain coiling effects in their respective dispersions. These aggregate size estimates are on the higher side of those reported in literature [163] and reflect the characteristics of the as-received dispersion. Unfiltered dispersions are known to have larger aggregates that are unsuitable for consistent inkjet dispensing due to nozzle clogging issues. Individual aggregates are much smaller as evidenced later in morphological studies of thin films printed using filtered ink (0.45 μm syringe filter) which correlate well with the lower end of those reported in literature. From the above estimates, the diffusion coefficients for either aggregate size in either case can be approximated to be around $\sim 10^{-12}$ to $\sim 10^{-14}$ m^2/s respectively. This further corroborates the assertion made in Chapter 2 about the purely diffusive mixing time and the consequent mixing channel length being greater in comparison to the vibration-assisted diffusive mixing time which reduces the effective mixing channel length due to chaotic advection.

4.2.2 Viscosity and surface tension of ICP dispersions

The inkjet dispenser used in this work is capable of printing fluids of viscosities ranging from that of water ($\eta = \sim 0.89$ $\text{mPa}\cdot\text{s}$ at 25°C) up to a specified upper limit of ~ 20 $\text{mPa}\cdot\text{s}$. For surface tension, the upper limit of the dispenser is quite similar to that of water ($\gamma = \sim 72$ mN/m at 25°C) with a specified value of ~ 70 mN/m . The measured dynamic viscosity ($\eta_{P1} = \sim 5$ $\text{mPa}\cdot\text{s}$ and $\eta_{P2} = \sim 2$ $\text{mPa}\cdot\text{s}$) and surface tension ($\gamma_{P1} = \sim 68$ mN/m and $\gamma_{P2} = \sim 59$ mN/m at 25°C) for *P1* and *P2* are well within the specified range of jettability as also evidenced by their printability. The shear stress and dynamic viscosity behavior of *P1* and *P2* is shown in Fig. 4.5 as a function of shear strain rates whose nature has led to the assumption of approximately Newtonian behavior in this work.

4.2.3 Crystallinity

X-ray diffraction analysis of printed films of both *P1* and *P2* were conducted to evaluate structural crystallinity in printed thin films. Both appear to have very similar structures as seen in Fig. 4.6. The broad peak centered around $\sim 25^\circ$ is representative of the π - π stacking of the thiophene rings with the broadening attributable to the lack of long-range π -stacking (~ 3.4 Å for *P1* and ~ 3.6 Å for *P2*) order due to the random coiling of either polymer.

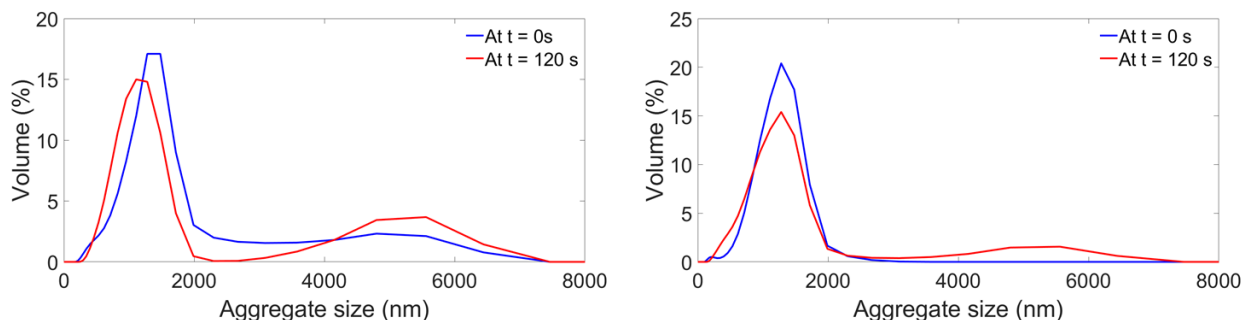


Fig. 4.4: Aggregate sizing of (left) *P1* and (right) *P2* 0.65 wt.% aqueous dispersions showing a primary peak ($t = 0$ s) at ~ 1.2 μm and a secondary peak ($t = 120$ s) at ~ 5.6 μm for both ICPs using dynamic light scattering (DLS) measurements.

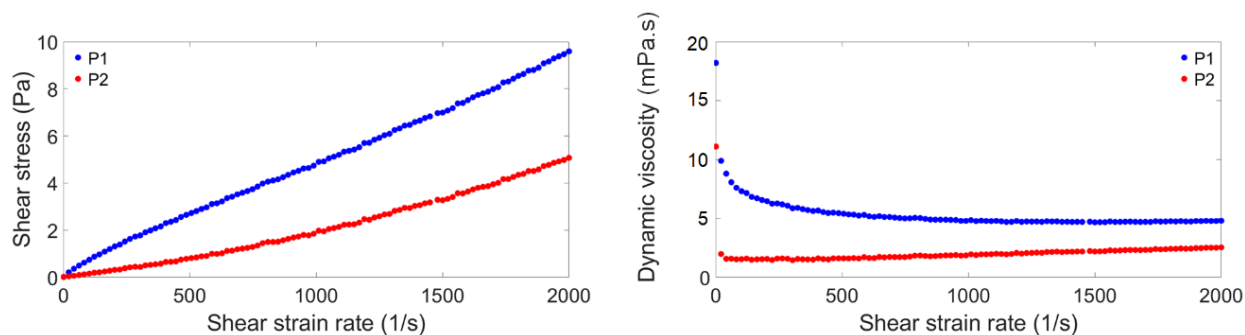


Fig. 4.5: Shear stress (left) and dynamic viscosity (right) of *P1* and *P2* measured as a function of the shear strain rate.

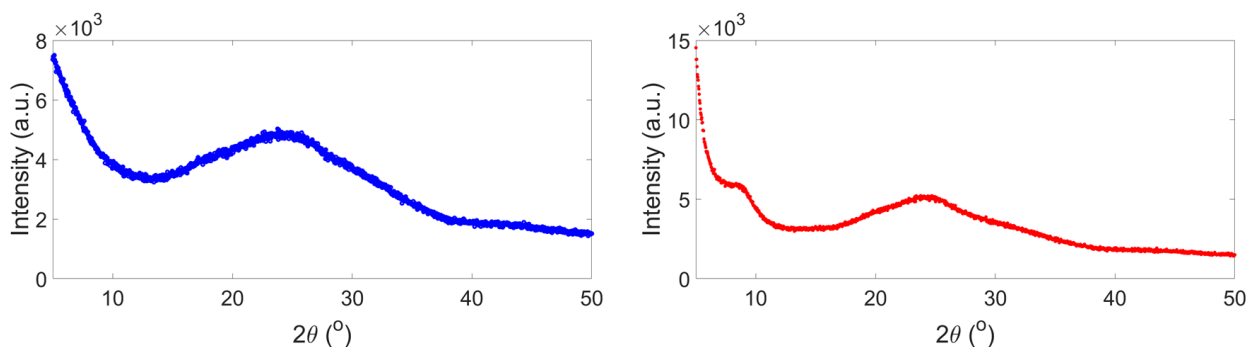


Fig. 4.6: Measured x-ray diffraction intensities of *P1* (blue) and *P2* (red) illustrating limited crystallinity.

This corresponds to the (020) plane of the orthorhombic unit cell. While *P2* exhibits a peak at $\sim 10^\circ$ corresponding to a plane separation of $\sim 9 \text{ \AA}$, it is absent in *P1* and is likely due to suppression from PSS. This corresponds to the (200) plane of the orthorhombic unit cell. The peak at $\sim 5^\circ$ similarly corresponds to the (100) plane of the orthorhombic unit cell with a plane separation of $\sim 17 \text{ \AA}$. While these observations agree with reported literature [169], no significant degree of long range crystallinity has been found in either pristine or secondary doped PEDOT:PSS (*P1*) or self-doped PEDOT (*P2*) macromolecules thus far. However, there is formation of typically orthorhombic crystallites with crystal planes corresponding directly to the intensity peaks seen in both polymers.

4.3 Case studies

4.3.1 Case 1: Electrical conductivity dependence on printed layer count

Pristine PEDOT:PSS (Sigma-Aldrich, #483095, 1.3 wt.% dispersion in H_2O) (*P1*) and PSEDOT (Université Laval, 0.65 wt.% dispersion in H_2O) (*P2*) were used as the test materials and the purpose was to investigate the existence of any electrical conductivity dependence on the printed material quantity. Subsequent printing runs are to be conducted based on the conclusions from this case study. Clean $2'' \times 3''$ glass slides (Ted Pella Inc., #26005) with screen printed silver (Ag) electrodes were used as substrates for this and all other case studies. In this and all other case studies, a 1:1 aqueous (distilled water) dilution of *P1* was used as the pristine reference (0.65 wt.% dispersion) to reduce the probability of *P1* clog formation at the dispenser orifice and an identical concentration of *P2* was used for comparison equivalence. Parameters governing material printability are its dynamic viscosity (η) and surface tension (γ). Pristine dispersions were used in both cases to print channels with layer count varying from 5 layers to 20 layers of ~ 70 to $\sim 80 \text{ }\mu\text{m}$ diameter droplets in steps of 5 layers at 250 Hz ejection frequency and 20 mm/s substrate stage speed resulting in $\sim 40 \text{ }\mu\text{m}$ droplet spacing (center-to-center). Each layer count comprises 15 replicates to ensure the sufficiency in the capture of any statistically significant effects.

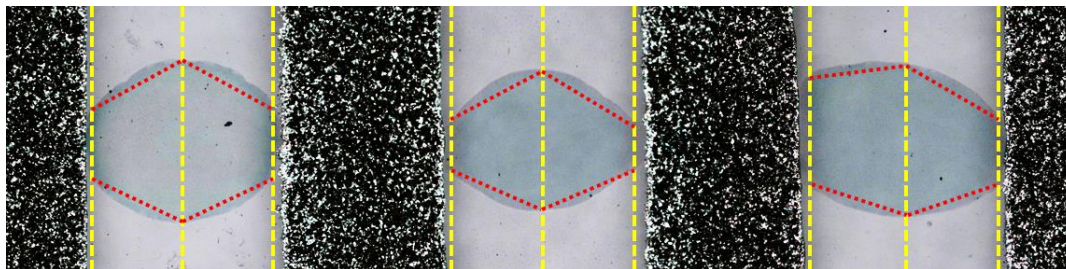


Fig. 4.7: Examples of printed thin film features comprising 20 layers showing the cross-sectional profile measurements (along the dashed yellow lines) leading to feature approximation (by dotted red lines).

All layers were printed at the same time to reduce the probability of dispenser orifice clogging, resulting in bulging instabilities in the printed lines as shown in Fig. 4.7 which were accounted for geometrically prior to calculating the electrical conductivity. This was done by taking stylus-based cross-sectional profile measurements along the sections denoted by the dashed yellow lines, making linearized approximations of the feature boundaries as denoted by the dotted red lines and using these measurements to approximate the cross-sectional area for electrical conductivity calculations. The separation between the probing Ag electrodes is ~ 1 mm with an error of ± 0.1 mm.

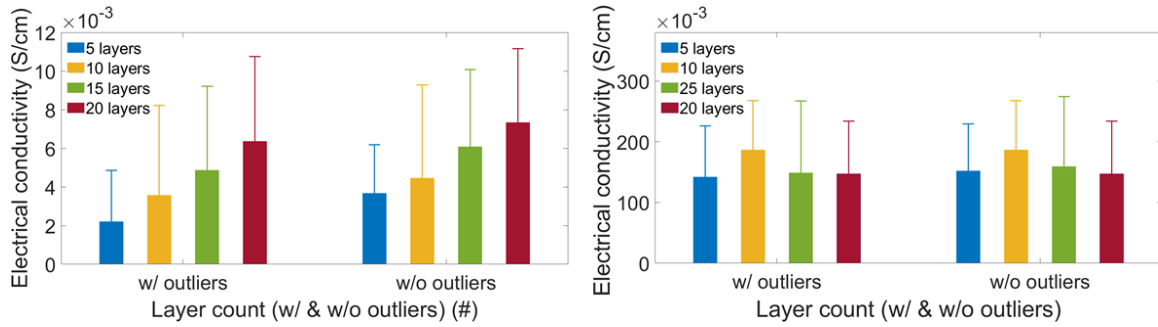


Fig. 4.8: Electrical conductivity variation of printed channels with printed layer count for (left) *P1* and (right) *P2* while accounting for the effect of outliers.

Fig. 4.8 shows the variation of electrical conductivities of *P1* and *P2* as a function of layer count for cases including (w/) and excluding (w/o) extreme outliers. A data point is considered to be an extreme outlier when the measured resistance indicates poor or no connection with the electrodes and are referenced against measurements on electrode pairs with no printed channel between them. Such data points are designated as outliers because they do not contribute meaningfully to the actual effect of layer count variability but rather, are artifacts originating from the interaction of the printed material with the substrate and the electrode.

There is a visible dependence of layer count on the electrical conductivity of *P1* but there also seems to be significant measurement scatter around the plotted mean values. In contrast, the electrical conductivity of *P2* does not appear to vary too much with layer count and has lower measurement scatter as well, in comparison to *P1*. One-way ANOVA was performed for both *P1* and *P2* data sets (tables in Appendix A) to see if the graphical observations were at all significant. $F_0@α$ values of $2.849@0.046$ (w/ outliers) and $1.943@0.137$ (w/o outliers) are calculated for a Type 1 error probability of 5% ($α = 0.05$). Interestingly, significant evidence against the null hypothesis for *P1* is observed only when outliers are included while no such significance is seen

when outliers are excluded. Tukey-Kramer analysis on the *P1* data set with outliers suggests significant difference in electrical conductivity between 5 layers and 20 layers which indicates that the extreme outliers for 5 layers can inflate the electrical conductivity difference. The effect size of the different layer counts as estimated by the $\eta^2_{partial}$ is ~ 0.132 (w/ outliers) and ~ 0.122 (w/o outliers) which are relatively small, thereby requiring a much larger sample size to eliminate the effect of outliers. However, prudence must be exercised given that 6 of the 15 replicates for the 5-layer printing run in comparison to 2 of the 15 replicates for the 20-layer printing run are electrically disconnected. For the 5-layer printing run to achieve the same probability of electrical disconnection as the 20-layer printing run, 45 samples must be printed based on what has been observed. While this may improve the statistical power which is relatively low at 65% (w/ outliers) and 47% (w/o outliers), the ANOVA w/ outliers indicates that the differences observed are only between the 5-layer and the 20-layer printing runs. Thus, trying to isolate such a tiny effect size may not be a worthwhile cost-benefit decision and instead, the conventional wisdom of using higher layer counts to reduce electrical disconnection events for *P1* may suffice.

From the shape of the printed channels shown in Fig. 4.7, it may be postulated that any differences in solvent evaporation rates between droplets at glass-electrode junctions and droplets on glass and electrode surfaces affect the profile of the dry channel. Channel thicknesses are seen to increase with increasing layer count which reduces the pinch-off effect happening at the glass-electrode junction, thereby ensuring better physical connectivity. Increasing channel thickness due to increasing layer counts is not reflected similarly for *P1* and *P2* electrical conductivities, as seen in Fig. 4.8. Analyzing such effects is therefore critical to establish the veracity of the observations. Coupled with the effects of disparity in electrode and printed layer thicknesses, surface energy transition at glass-electrode junctions can sometimes also lead to imperfect (minimal or non-existent) physical contact between the printed channels and electrodes as illustrated schematically in Fig. 4.9. Droplet sparsity at lower layer counts and high surface tension of *P1* is the primary driving cause behind the printed channel-electrode connectivity problems through the multiple mechanisms described above, each playing a role in the overall effect. The typical order of magnitude ($\sim 10^{10} \Omega$) of open-circuit resistance between the pairs of silver electrodes were measured and used as a threshold value for inclusion in the statistical analyses above. Besides the physical connectivity effect on measured channel resistance, *P1* also has an insulating component (PSS) in stoichiometric excess which may reduce electrical contact at lower layer counts.

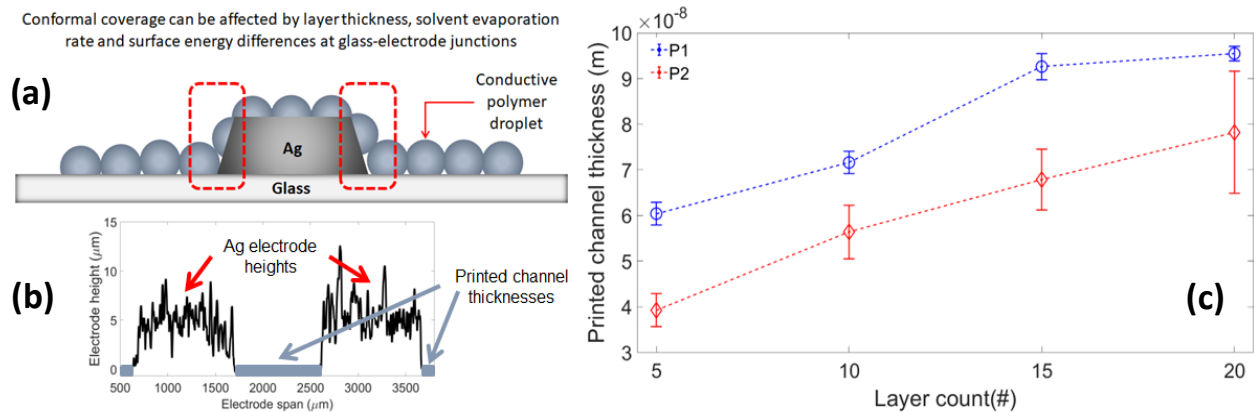


Fig. 4.9: (a) Schematic representation of contact angle differences on silver and glass surfaces along with the problem areas highlighted (red dashed boxes). (b) Comparative thickness mapping of electrodes and printed channels showing the large height change at the glass-electrode junction. (c) Variation of printed channel thicknesses of *P1* and *P2* as a function of layer count.

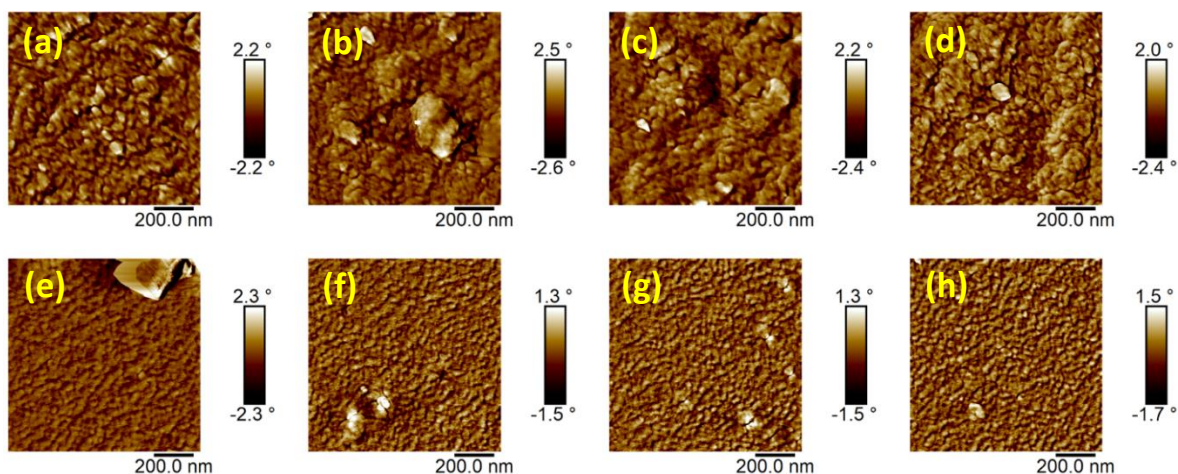


Fig. 4.10: AFM tapping mode phase imaging of (a, b, c, d)pristine *P1* at 5, 10, 15 and 20 layers and (e, f, g, h) pristine *P2* at 5, 10, 15 and 20 layers showing differences in polymer grain sizes, homogeneity of distribution and aggregate formation tendencies.

For the *P2* case, the ANOVA conclusions are comparatively straightforward. For both w/ and w/o outliers, there is no statistically significant difference between electrical conductivities at any of the different layer counts. The low power of 19% (w/ outliers) and 16% (w/o outliers) here merely indicates that the effect size is so small (as seen by the η^2_{partial} values of 0.04 and 0.03 for w/ and w/o outliers respectively) that to discern between different layer counts, an unnecessarily large number of replicates would be required with any observed difference likely being random rather than systematic. This too can be explained physically by the fact that *P2* does not have any insulating component unlike *P1* and any outliers are solely due to local energetic effects of the substrate interacting with the *P2* dispersion, resulting in bad electrical contact with the electrodes.

Overall, it is to be expected that once the percolation threshold has been crossed for printed channels of a heterogeneous (*P1*) or homogeneous material (*P2*) in its pristine form, the electrical conductivity will saturate quite rapidly unless impeded by artifacts such as the aforementioned droplet-substrate interactions and poor contacts with probing electrodes.

AFM phase imaging of pristine *P1* and *P2* sheds some light on these observations by looking at the morphology of the printed films in Fig. 4.10. It is evident that *P1* has larger particle sizes (~35 nm) in comparison to *P2* (~15 nm) but in either case, the film morphology does not change much as layer count increases although *P1* seems to tend to form lumpier films as opposed to the much flatter *P2* films. Given that electrical conductivity in amorphous films like ICPs depends greatly on film morphology, it is expected that they will exhibit similar electrical conductivities if the print has sufficiently connected particles. Here, even 5 layers seems to be populated enough for both *P1* and *P2* at the solute fractions used but as a precaution, 20 layers has been used for subsequent case studies to ensure better connectivity with probing electrodes.

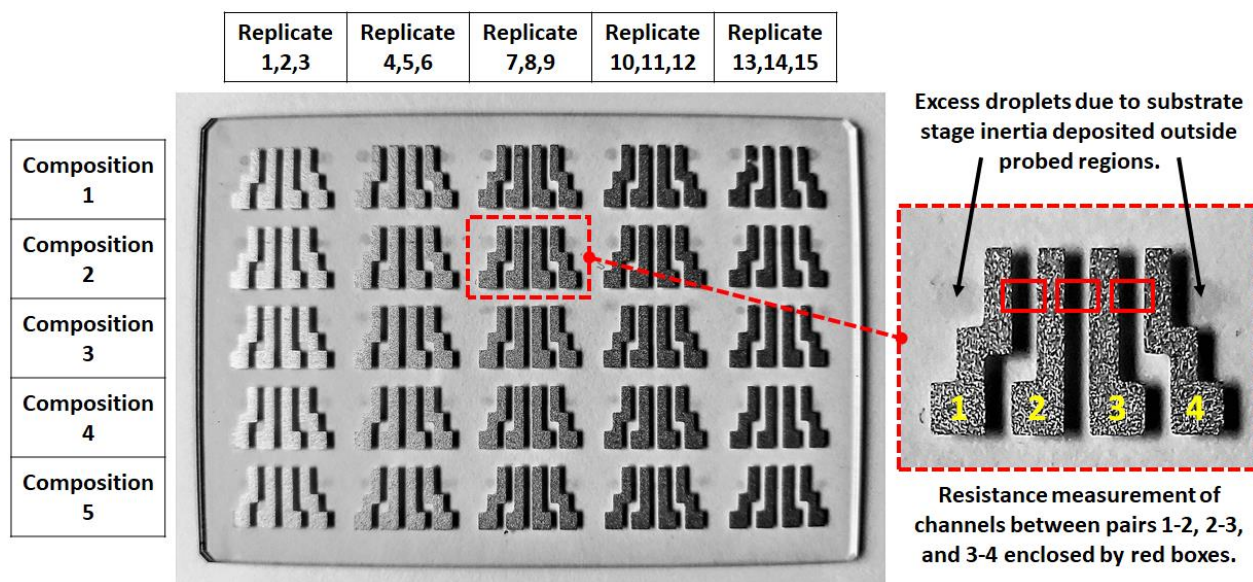


Fig. 4.11: Printed thin film sample library comprising multiple blend compositions (rows) with multiple replicates (columns) for each. Magnified view of set of 3 replicates shown enclosed by the red dashed box.

4.3.2 Case 2: Electrical conductivity dependence on cosolvent additive

Blending experiments are the cornerstone of CPH processing and this case study is critical in terms of its two-fold ramifications: (i) validating the functionality of the CPH and (ii) determining optima in blended material properties. Once again, a 1:1 aqueous dilution of PEDOT:PSS (Sigma-Aldrich, #483095, 1.3 wt.% dispersion in H₂O) was used as the primary ink component (*P1*) while dimethyl sulfoxide (Sigma-Aldrich, #472301, ~99%) was chosen to be the

secondary ink component (*D*) due to its known conductivity enhancing effect on PEDOT:PSS [170]. Thus, *P1-D* blends were chosen for this printing run to evaluate the electrical conductivity behavior of *P1* as a function of *P1-D* blend composition, validating CPH operation in the process.

The blend composition on the CPH is denoted as x/y ($x + y = 100$) where x and y are the percentage volume fractions of the ink components *P1* and *D* for a certain composition. As an example of this notation, a blend composition comprising 60% pristine (0.65 wt.%) *P1* dispersion and 40% pristine (99%) *D* is denoted as 60/40 while another blend composition comprising 80% pristine (0.65 wt.%) *P1* dispersion and 20% pristine (99%) *D* is denoted as 80/20. These tests were performed iteratively to demonstrate the multi-resolution ink formulation capability of the CPH using binary mixtures for combinatorial evaluation of printed multi-material thin films. In the first broader iteration, x decreased from 100% (pristine PEDOT:PSS) to 50% (y was increased from 0% to 50%) in steps of 10% and while in the second narrower iteration, x decreased from 100% (pristine PEDOT:PSS) to 90% (y was increased from 0% to 10%) in steps of 2%. The range was chosen up to the point where *P1* was equal in proportion to the cosolvent *D* thereby ensuring that *P1* was the primary conductive component as is the case with any functional binary blends. The blends were fed to the inkjet dispenser module of the CPH as described in Chapter 2. The programmed print sequence was then activated and multiple thin film channels with identical composition were patterned for 20 layers. The printed channels were then dried in an oven at 60°C for 5 min and then cooled to room temperature (~25°C) before being individually characterized. This protocol was used to print 15 replicate channels for each of the 5 and 4 compositions tested for each binary mixture to account for statistical variation, which gave us 75 and 60 printed channels for each iteration respectively. An example of the printed libraries is shown in Fig. 4.11 with distinct compositions and replicates along individual rows and columns.

For referencing, identical arrays of premixed (components proportioned manually and mixed in an ultrasonic bath for 10 min) and unmixed (components proportioned on the CPH but the mixer module is not activated) *P1* and *D* are printed. Here, PM denotes premixed, UM denotes unmixed and OM denotes on-chip mixed. Iteration 1 of the blending experiments was performed to observe broad trends in the electrical conductivity response of the printed *P1-D* channels while iteration 2 was conducted to further evaluate regions of interest. It is to be noted that the UM process is not strictly “unmixed” as it includes any homogenization that occurs at the nozzle orifice during droplet generation as well as the delay between printing the channels and drying them.

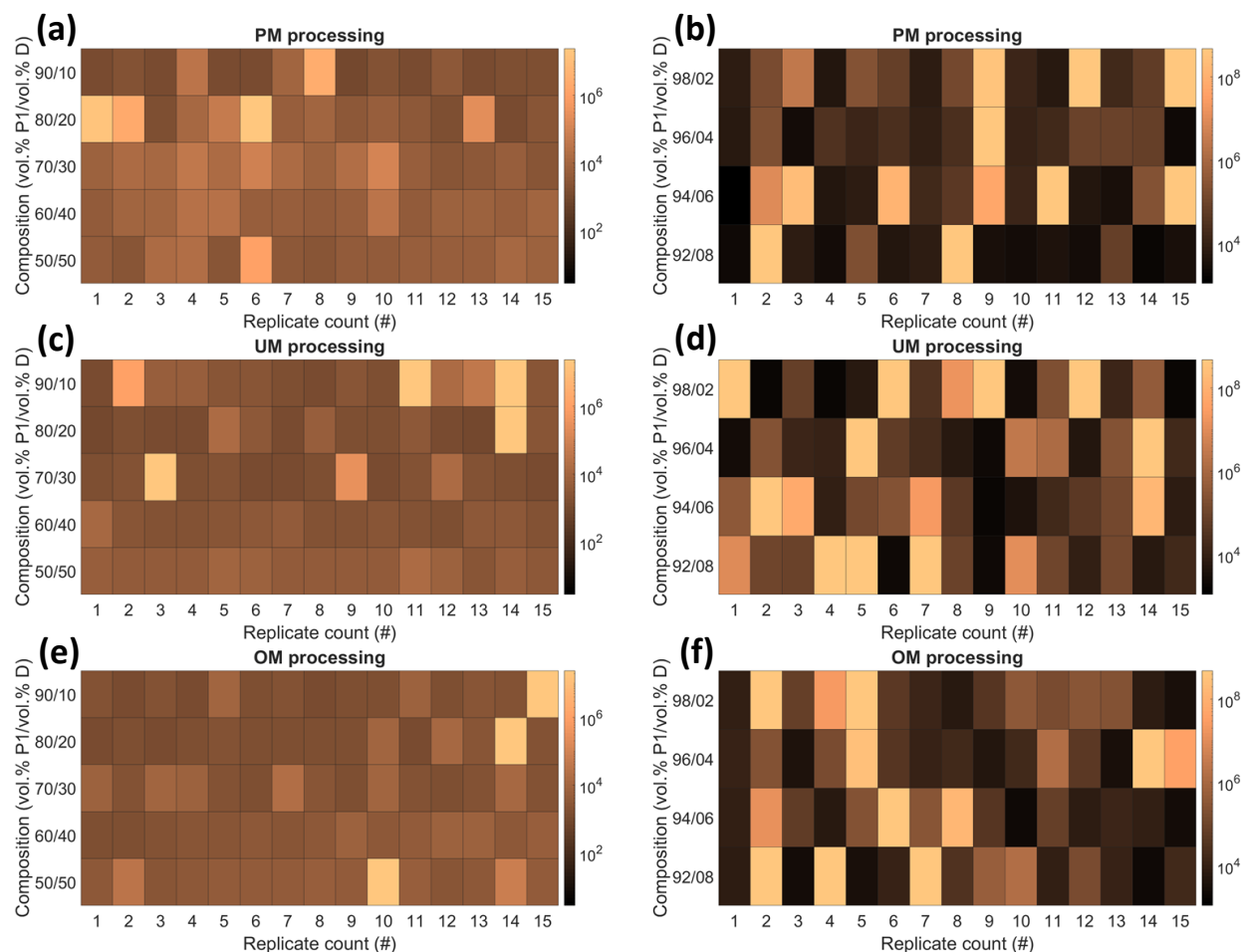


Fig. 4.12: Electrical resistance heat maps of resistive thin film channels printed using *P1-D* binary blends in (a, c, e) iteration 1 (10 vol.% resolution) and (b, d, f) iteration 2 (2 vol.% resolution) respectively. Scale bar in Ω .

Literature suggests a manifold increase in the electrical conductivity of *P1-D* blends when secondary doped with high boiling point cosolvents such as *D*. While there is no specific volume fraction of *D* which seems to be a clear optimum, it can be established from density considerations of the dispersions and additives that the increase occurs within 0% to 10% volume fraction of the cosolvents [171]. Thus, the region of interest studied in iteration 2 is between 0% and 10% of the cosolvent volume fraction. Measured electrical resistances of the printed channels for PM, UM and OM processing are shown as heat maps at both broad (iteration 1) and magnified (iteration 2) resolutions in Fig 4.12. Heat maps of the respective cross-sectional areas of the printed channels and the calculated electrical conductivity for all three processing methods are also shown in Fig. 4.13 and 4.14 for completeness. The color tone of the heat maps has been chosen such that the lightest (iteration 1) and darkest (iteration 2) array elements correspond to the extreme outliers and are readily captured visually.

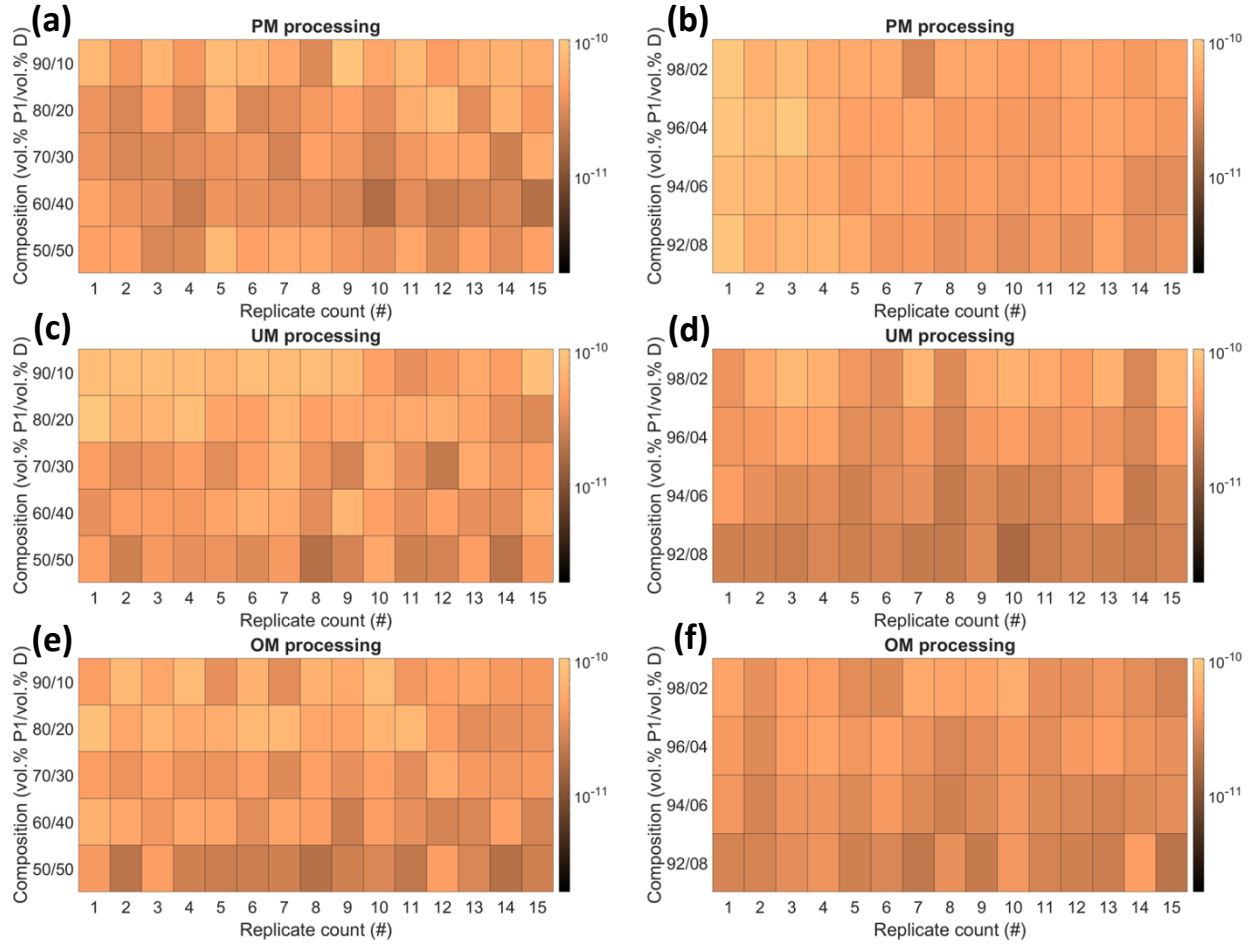


Fig. 4.13: Cross-sectional area heat maps of resistive thin film channels printed using *P1-D* binary blends in (a, c, e) iteration 1 (10 vol.% resolution) and (b, d, f) iteration 2 (2 vol.% resolution) respectively. Scale bar in m^2 .

An immediate observation that can be made from Fig. 4.12 and 4.14 is that there are outliers here too which show up as lighter shades in a darker field (electrical resistance) and darker shades in a lighter field (electrical conductivity) respectively and these will be addressed later during statistical analyses. Comparing these two heat maps for any particular processing type, it is noted that the brighter areas in Fig. 4.12 directly correspond to the darker areas in Fig. 4.14, thus demonstrating the minimal effect any geometric variations in cross-sectional area has on electrical conductivity variations. This is further corroborated by Fig. 4.12 where the cross-sectional area typically falls within the range $\sim 10^{-11} \text{ m}^2$ to $\sim 10^{-10} \text{ m}^2$, indicating relatively consistent material quantity in each printed channel in the library. Fig. 4.15 shows the variation in electrical conductivity across PM, UM and OM processing as a function of blend composition with a 1σ scatter plotted about each composition. In addition, the *CV* values are plotted below the electrical conductivity characteristics to indicate the relative differences among the three methods.

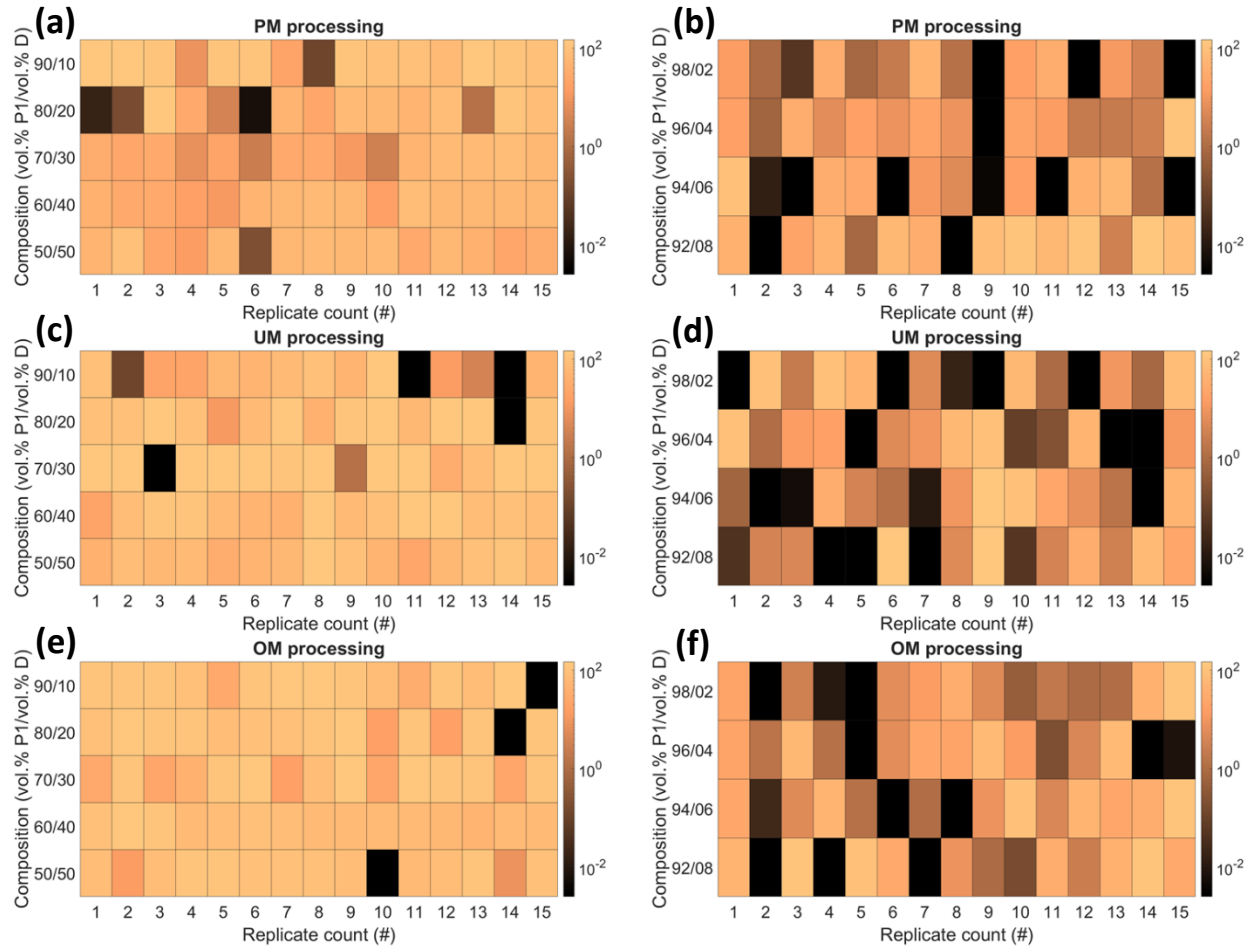


Fig. 4.14: Electrical conductivity heat maps of resistive thin film channels printed using *P1-D* binary blends in (a, c, e) iteration 1 (10 vol.% resolution) and (b, d, f) iteration 2 (2 vol.% resolution) respectively. Scale bar in S/cm.

The CV estimates suggest that OM processing results in marginally lower scatter compared to both PM and UM processing except for the 70/30 composition in iteration 1 and the 98/02 composition in iteration 2. Due to the large data scatter, it is difficult to conclusively comment on the differences and/or similarities among (i) different processing types and (ii) different compositions. Therefore, the ANOVA method is invoked once again to provide a degree of concreteness to these observations. The first part of this case study compares PM, UM and OM processing for each composition in iterations 1 and 2 in order to shed more light on the similarities and differences among these methods. PM processing is taken to be the reference against which OM and UM processing are evaluated. However, as seen in the prior subsection, extreme outliers often tend to artificially inflate or suppress any differences or similarities and therefore, ANOVA is performed for both with (w/) and without (w/o) extreme outliers for fairness of comparison to eliminate non-existent spurious effects. As before, data points designated as extreme outliers had

a measured resistance value equivalent to an open circuit condition and there were none in compositions 60/40 and 50/50. Table 4.1 and 4.2 lists the F_0 statistic and the p -value calculated using the ANOVA method for iterations 1 and 2 respectively. To determine which processing type was significantly different for each composition, the Tukey-Kramer (for homoscedastic data sets) and the Games-Howell (for heteroscedastic data sets) tests were conducted, and the results are shown in color-coded matrix form in Fig. 4.16 and 4.17. Since the matrices are symmetric, the upper halves have been removed to reduce redundancy with green indicating “not significantly different” and red indicating “significantly different”. To quantify the differences between pairs of PM, UM and OM, values of Δ_{Glass} [172] have been used as entries in the matrix in units of σ . For UM-PM and OM-PM pairs, the σ for the corresponding PM data set has been used and for the UM-OM pairs, the σ for the corresponding OM data set has been used and the change in formula has been denoted by underlining. This is done to conform with the assumption that PM is the reference (theoretically best mixing) for UM-PM and OM-PM pairs while OM is the reference (theoretically better mixing) for the UM-OM pair. However, the error due to manual proportioning in PM has not been considered and may be a contributing factor to the variations between PM and OM as well as between PM and UM respectively.

Based on the trends in differences in pairwise observations made in iteration 1 irrespective of extreme outliers being included or excluded as in Fig. 4.16, it appears that UM and OM processing are somewhat similar when compared against PM processing. However, it is also seen that OM processing is consistently better than UM processing except for the 60/40 and 50/50 compositions where the difference with PM processing reverses. This is likely to be more due to chance rather than anything systemic given that the volume fraction of D approaching that of $P1$ results in an inherently greater probability of the D component to synergistically affect the $P1$ component. More importantly, OM processing seems to be able to capture the region of interest (peak conductivity at the 90/10 composition) better than UM processing, especially since the region of interest seems to have an offset of ~ 20 vol.% fraction (peak conductivity at the 70/30 composition). In case of iteration 2, no significant differences are observed among UM, OM and PM processing but here too, OM processing appears to be better than UM processing irrespective of whether extreme outliers are included or excluded as seen in Fig. 4.16. This region is of interest as the $P1$ transitions from a poor conductor in its pristine form to a good conductor in its doped form which is captured later using AFM imaging.

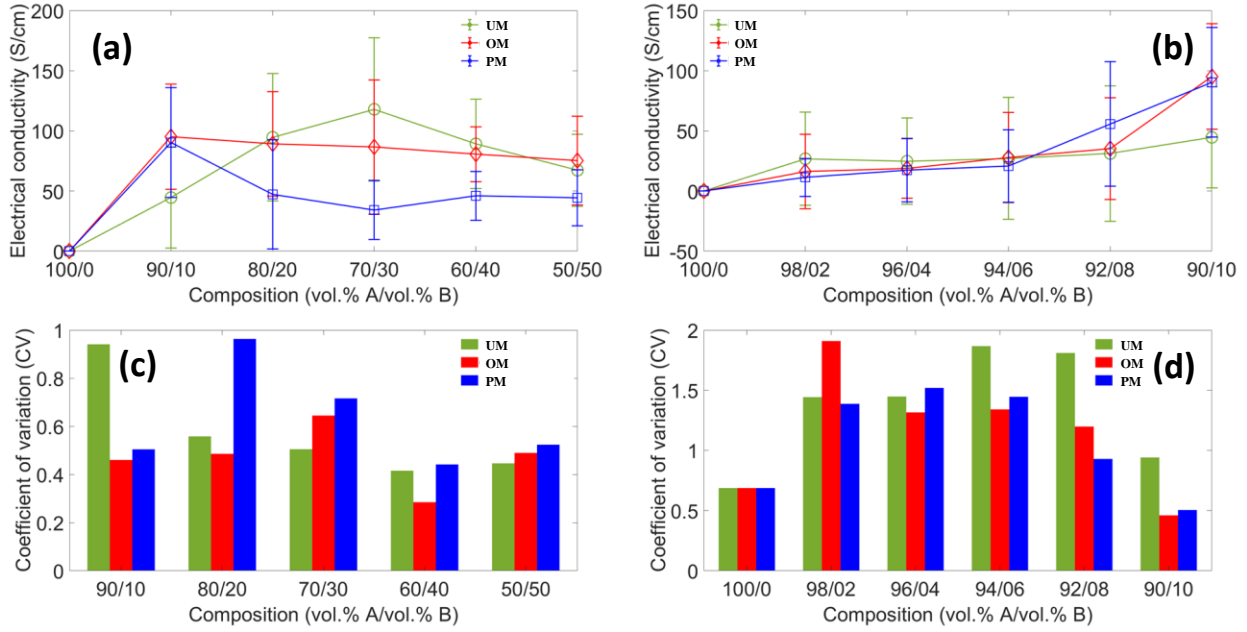


Fig. 4.15: Electrical conductivity and its coefficient of variation with blend composition for (a, c) iteration 1 and (b, d) iteration 2 for PM, UM and OM processing types.

Table 4.1: ANOVA evaluation of the different processing types using the different compositions in iteration 1 considering (w/ OL) and excluding (w/o OL) extreme outliers at $\alpha = 0.05$.

Composition	F_0 (w/ OL)	p -value (w/ OL)	F_0 (w/o OL)	p -value (w/o OL)
90/10	6.104	0.005	5.528	0.008
80/20	4.502	0.017	6.806	0.003
70/30	11.074	< 0.001	14.658	< 0.001
60/40	10.182	< 0.001	10.182	< 0.001
50/50	4.118	0.023	4.118	0.023

Table 4.2: ANOVA evaluation of the different processing types using the different compositions in iteration 2 considering (w/ OL) and excluding (w/o OL) extreme outliers at $\alpha = 0.05$.

Composition	F_0 (w/ OL)	p -value (w/ OL)	F_0 (w/o OL)	p -value (w/o OL)
98/02	1.172	0.320	1.657	0.208
96/04	0.272	0.763	0.579	0.566
94/06	0.143	0.867	0.579	0.566
92/08	1.024	0.368	0.847	0.438

Meanwhile, the lack of any significant distinction among the three processing types seems to suggest that they are roughly equivalent in this transition region. However, effect size and statistical power must be considered in order for these hypothesis tests to be conclusive. For iteration 1, statistical power is always ~ 0.7 and beyond with appreciable effect sizes stemming primarily from UM processing followed by PM processing (also seen from the red values in Fig. 4.16) which implies that those corresponding inferences are accurate within the available bounds

of Type 1 and Type 2 error probabilities. Iteration 2 is not as conclusive due to the fact that statistical power does not exceed ~ 0.3 with correspondingly low effect sizes which once again implies the need for more samples to negate the effect of large measurement scatter as observed in Fig. 4.15. While fabrication of more samples is trivial, manual measurements are the bottleneck for efficient combinatorial evaluation as their number gets compounded.

90	PM	OM	UM	80	PM	OM	UM	70	PM	OM	UM	60	PM	OM	UM	50	PM	OM	UM
PM				PM				PM				PM				PM			
OM			$1 - \beta: \sim 0.9$	OM			$1 - \beta: \sim 0.7$	OM			$1 - \beta: \sim 1.0$	OM			$1 - \beta: \sim 1.0$	OM			$1 - \beta: \sim 0.7$
UM	1.0σ	1.2σ		UM	1.0σ	0.1σ		UM	3.4σ	0.6σ		UM	0.4σ	2.1σ		UM	1.0σ	0.2σ	

90	PM	OM	UM	80	PM	OM	UM	70	PM	OM	UM	60	PM	OM	UM	50	PM	OM	UM
PM				PM				PM				PM				PM			
OM			$1 - \beta: \sim 0.8$	OM			$1 - \beta: \sim 0.9$	OM			$1 - \beta: \sim 1.0$	OM			$1 - \beta: \sim 1.0$	OM			$1 - \beta: \sim 0.7$
UM	0.9σ	1.4σ		UM	1.2σ	0.2σ		UM	3.8σ	0.7σ		UM	0.4σ	2.1σ		UM	1.0σ	0.2σ	

Fig. 4.16: ANOVA post-hoc analyses for iteration 1 processing types ($P1$ vol.% fraction denoted by the first cell in each matrix) with the upper row denoting comparisons including extreme outliers and the lower row denoting comparisons excluding extreme outliers. First row and column entries (except the first cell entry) indicate processing types.

The issue is that the sample size requirements are prohibitively large (41, 926, 927 and 66 samples for 98/02, 96/04, 94/06 and 92/08 compositions respectively, as generated by an ad hoc power analysis comparing iteration 2 OM and PM processing in each case) for conducting manual measurements to obtain adequate statistical power assumed to be ~ 0.7 (or 70%) with the same 5% significance level used for all ANOVA tests in this chapter. The limitation faced here can result in the defeat of the original goal of speeding up the evaluation process using combinatorial methods while simultaneously minimizing material consumption. Small effect sizes and large variations in the data sets being compared highlight the need for greater number of samples as described above. This inevitably points to the requirement of measurement automation for very large sample sizes, which is beyond the scope of the current work. Nevertheless, in this first part of the case study, it can be readily demonstrated that OM is likely to capture the conductivity peak estimated by PM. In addition, the data generated from the combinatorially printed sample libraries are helpful for understanding the type of future challenges that may be encountered and their resolution.

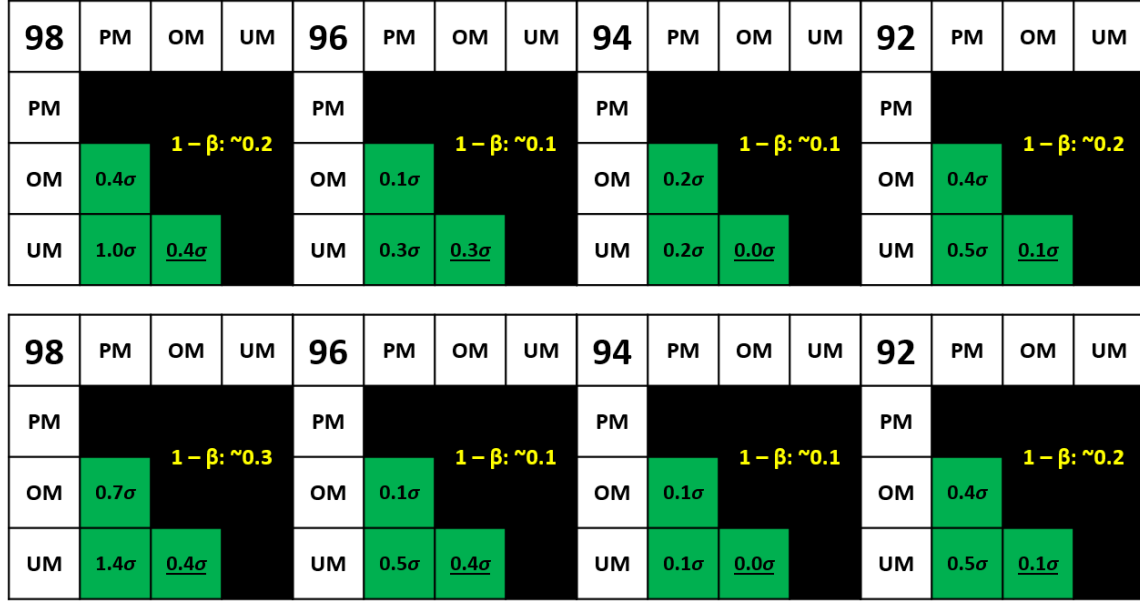


Fig. 4.17: ANOVA post-hoc analyses for iteration 2 processing types (P_1 vol.% fraction denoted by the first cell in each matrix) with the upper row denoting comparisons including extreme outliers and the lower row denoting comparisons excluding extreme outliers. First row and column entries (except the first cell entry) indicate processing types.

Table 4.3: ANOVA evaluation of the different compositions for iteration 1 using the different processing types considering (w/ OL) and excluding (w/o OL) extreme outliers.

Processing type	F_0 (w/ OL)	p -value (w/ OL)	F_0 (w/o OL)	p -value (w/o OL)
PM	6.269	< 0.001	6.269	< 0.001
UM	5.641	< 0.001	6.675	< 0.001
OM	0.506	0.732	1.105	0.361

Table 4.4: ANOVA evaluation of the different compositions for iteration 2 using the different processing types considering (w/ OL) and excluding (w/o) extreme outliers.

Processing type	F_0 (w/ OL)	p -value (w/ OL)	F_0 (w/o OL)	p -value (w/o OL)
PM	5.312	0.003	5.730	0.002
UM	0.049	0.985	0.056	0.982
OM	0.962	0.417	1.209	0.317

The second part of this case study compares the different compositions for each of the processing types PM, UM and OM for both iterations 1 and 2 to assess the behavior of P_1 when doped with different volume fractions of D . Once again, the behavior of PM processed P_1 - D blends are assumed to be the reference against which the behavior of UM and OM processed P_1 - D blends are evaluated. Here too, trends across compositions for particular processing types suggested by Fig. 4.15 remain inconclusive owing to the large measurement scatter which requires further resolution. ANOVA evaluation results are shown in Tables 4.3 and 4.4 for iterations 1 and 2 respectively.

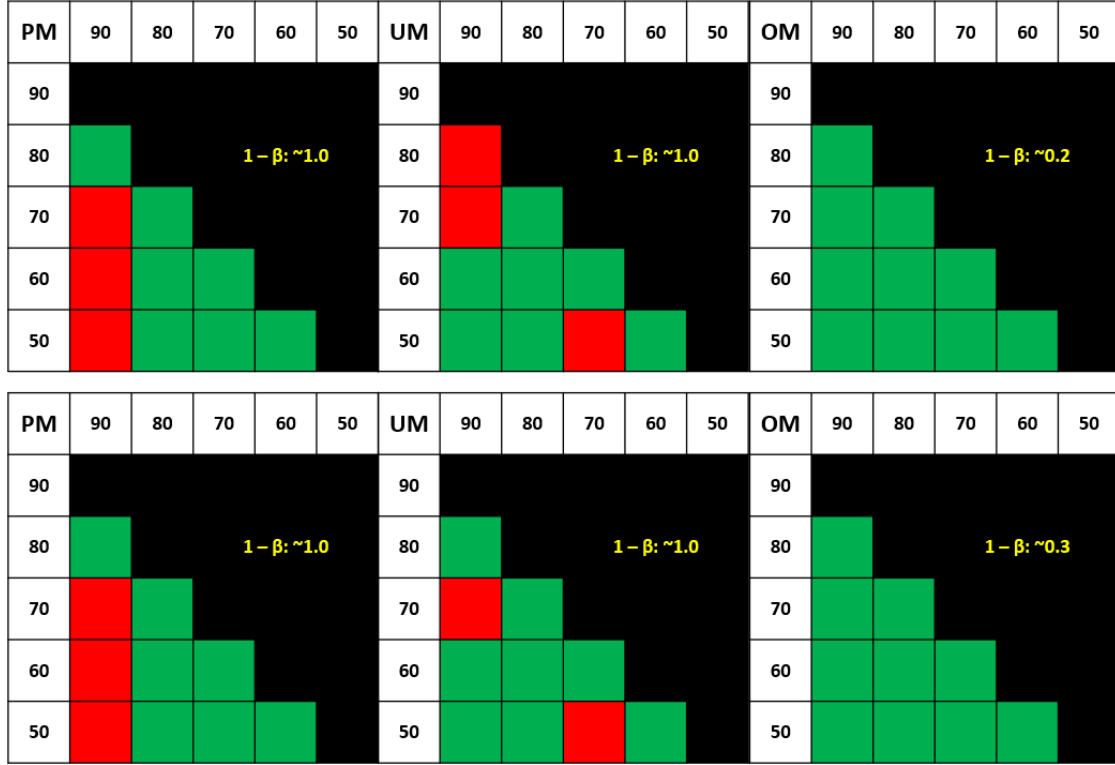


Fig. 4.18: ANOVA post-hoc analyses for iteration 1 compositions (processing type denoted by the first entry in each matrix) with the upper row denoting comparisons including extreme outliers and the lower row denoting comparisons excluding extreme outliers. First row and column entries (except the first cell entry) indicate $P1$ vol.% fraction in blend.

While literature suggests that the electrical conductivity saturates and decreases beyond a certain weight fraction of D [171], not much work has been done to explore the effect of a range of low to high fractions of D on $P1$ and the conclusions on peak electrical conductivity location are not defined in absolute terms. Thus, the peak position for PM processing is used as reference here. Fig. 4.15 suggests coincidence of peaks for PM and OM processing at the 90/10 composition while UM processing yields a peak which is offset to the 70/30 composition for iteration 1. This may be an indicator of lower levels of homogenization in UM processed prints leading to a requirement for a larger fraction of D to fully penetrate the $P1$ network. From the Tukey-Kramer (for homoscedastic data sets) and the Games-Howell (for heteroscedastic data sets) analyses shown schematically in Fig. 4.18 and 4.19, it is clear that PM processing results in significant differences between the 90/10 and the 70/30, 60, 40 and 50/50 compositions while UM processing yields significant differences between the 90/10 and the 80/20, 70/30 as well as between the 70/30 and the 50/50 compositions

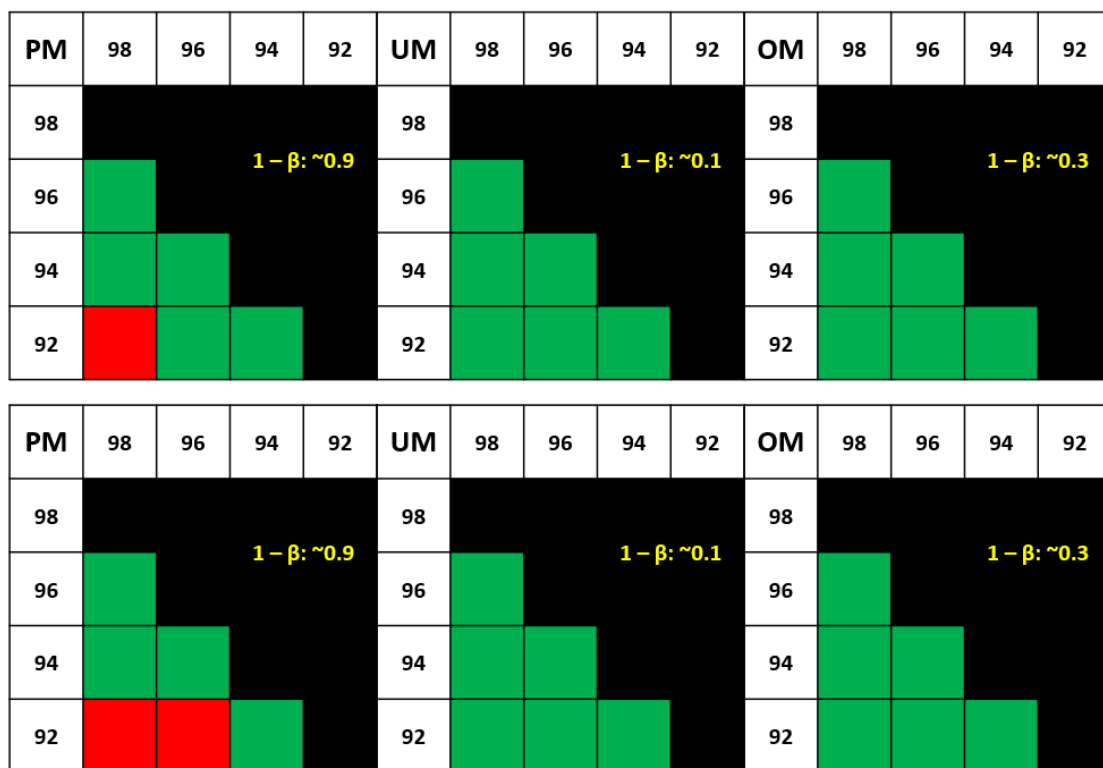


Fig. 4.19: ANOVA post-hoc analyses for iteration 2 compositions (processing type denoted by the first entry in each matrix) with the upper row denoting comparisons including extreme outliers and the lower row denoting comparisons excluding extreme outliers. First row and column entries (except the first cell entry) indicate $P1$ vol.% fraction in blend.

In contrast, OM processed $P1$ - D blends, while showing a decreasing trend in Fig. 4.15 similar to PM processing, do not show any significant differences in Fig. 4.19. Removing extreme outliers leads to a change in only the UM processed compositions where the significant difference between 90/10 and 80/20 compositions disappears, indicating significant differences only between the peak and the extremes of the blend composition. Similarly, for iteration 2, PM processing registers a significant difference between the extremes of the blend composition 98/02 and 92/08 with the removal of extreme outliers resulting in the inclusion of 96/04 as also being different from 92/08. Neither UM nor OM processing exhibits any significant difference between the extremes of the blend composition. Once again, low values of power and effect size indicates that the differences for OM and UM processing are too small to be captured which implies a relative superiority of PM processing at finer resolutions of blend composition. Considering the evidence from literature as well as from AFM phase imaging conducted for this work, it can be stated with confidence that the enhancement in electrical conductivity is due to morphological rearrangement of the $P1$ components where the high polarity and high boiling point character of D keeps it in the

drying film longer and enables the reordering of the polycationic (PEDOT) and polyanionic (PSS) species via a plasticizing effect in order to drastically improve the electrical connectivity among the PEDOT domains. Figs. 4.20, 4.21 and 4.22 show the AFM phase images of PM, UM and OM processed *P1-D* blends at 90/10; 70/30; 50/50 and 98/02; 92/08 compositions for iterations 1 and 2 respectively.

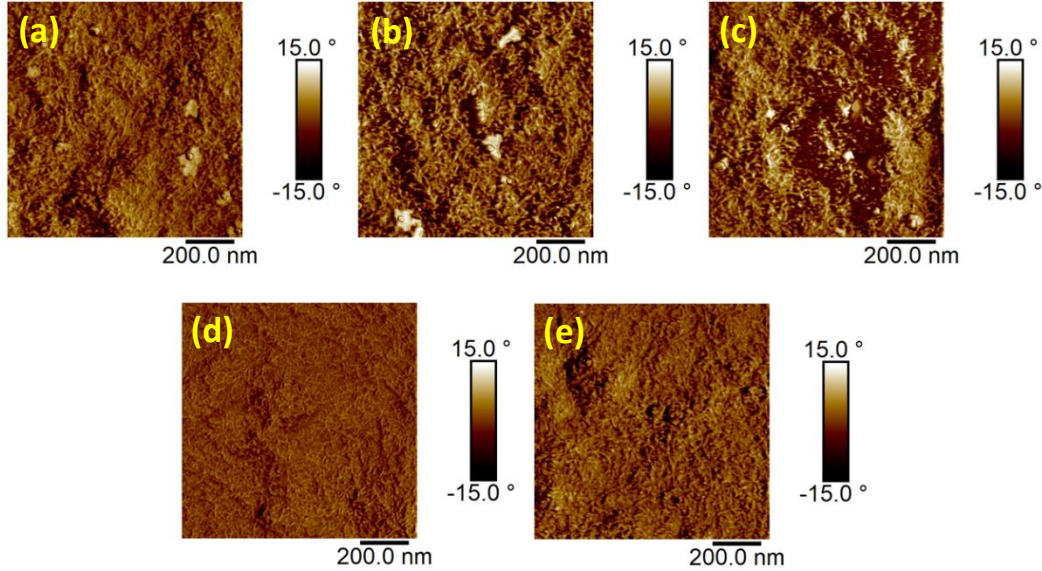


Fig. 4.20: AFM tapping mode phase imaging of PM processed *P1-D* at (a) 90/10, (b) 70/30 and (c) 50/50 compositions and at (d) 98/02 and (e) 92/08 compositions showing the morphological evolution of the printed channels with varying volume fraction of *D*.

Transition from a discrete particle-like structure to a connected chain-like structure is immediately apparent when comparing the pristine *P1* (100/0 composition) in Fig. 4.10 and the 90/10 composition, starting from the 98/02 composition. This is suggestive of the drastic effect on *P1* morphology that *D* has, even in the smallest of volume fractions within the *P1-D* blend. The difference in the phase range between Fig. 4.10 and Figs. 4.20, 4.21 and 4.22 is another indicator of phase rearrangement with the brighter regions denoting the harder PEDOT phase and the darker regions the softer and more hygroscopic PSS phase [173]. The electrical conductivity behavior in iteration 2 tends to follow the morphological character of the printed channels from 98/02 to 92/08 with increasing chain-like PEDOT:PEDOT connectivity being reflected in the generally upward trend in Fig. 4.15. However, the 1σ scatter is much larger in this iteration resulting in low power, making differences harder to detect in a manner similar to the first part of this case study. While the morphological evolution of the printed channels is quite evident irrespective of processing type, not much difference is observable between the 90/10 and 50/50 compositions in iteration 1.

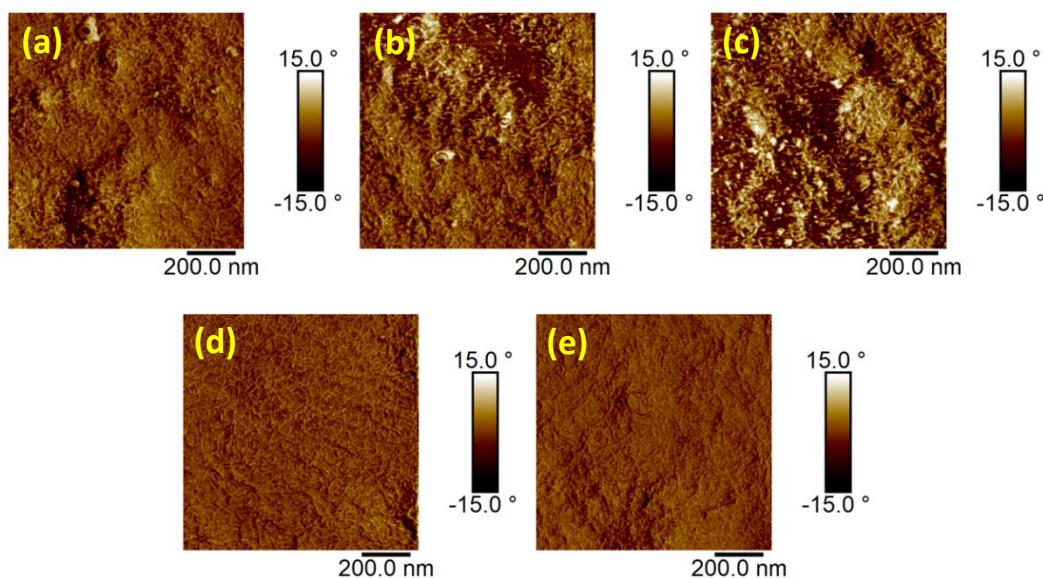


Fig. 4.21: AFM tapping mode phase imaging of UM processed *P1-D* (a) 90/10, (b) 70/30 and (c) 50/50 compositions and at (d) 98/02 and (e) 92/08 compositions showing the morphological evolution of the printed channels with varying volume fraction of *D*.

However, there is a decrease in the solute fraction of *P1* which should ideally lead to a reduction in the electrical conductivity owing to the hopping sites being progressively spaced out. Thus, a downward trend in electrical conductivity is justifiably observed between 90/10 and 50/50 compositions but according to the extended ANOVA analyses, the 1σ scatter overpowers this trend for OM processing as also indicated by the low power. The fact that UM processing shows a difference is primarily because the mean electrical conductivity at 90/10 starts off even lower than that at 50/50 which automatically positions the extremes of the blend composition to be different from the peak (70/30 in this case). PM processing does show significant differences in electrical conductivities between 90/10 and the latter half of the compositions 70/30, 60/40 and 50/50, thereby suggesting a greater effect of electrical conductivity reduction compared to the scatter. However, given the linearity in the PEDOT fraction reduction, the sudden drop at 80/20 followed by a much flatter trend from 70/30 to 50/50 most likely indicates a chance effect. The variability of using PM processing must be considered as the introduction of *D* into the pristine dispersion causes unraveling of *P1* particles which comprise PEDOT cores surrounded by PSS shells. The longer residence time of *D* in the reservoir leads to larger aggregate formation due to the networking of PEDOT domains which may cause variability in connectivity.

The comparatively low conductivity of pristine *P1* films is typically attributed to the lack of connectivity of the conductive PEDOT domains in these disordered films. While the particles

may be physically connected to each other, the connections are primarily between PSS-PSS and PEDOT-PSS which are simply insulator-insulator and conductor-insulator contacts. Electrical conductivity in disordered systems such as polymers is known to follow some approximation of variable range hopping (VRH) [174] where the range parameter is a linear combination of spatial and energetic separation of adjacent sites. In such systems, charge carriers move under the influence of an electric field based on the probability $P \sim \exp[-2\phi S - W/kT]$ of a charge carrier hopping from one state to another with transition to a higher energy state being the rate limiting process and the contact types described above result in an increase in both spatial and energetic separation S and W respectively. Here, ϕ^{-1} is the attenuation length for hydrogen-like localized wavefunctions, k is the Boltzmann constant and T is the temperature.

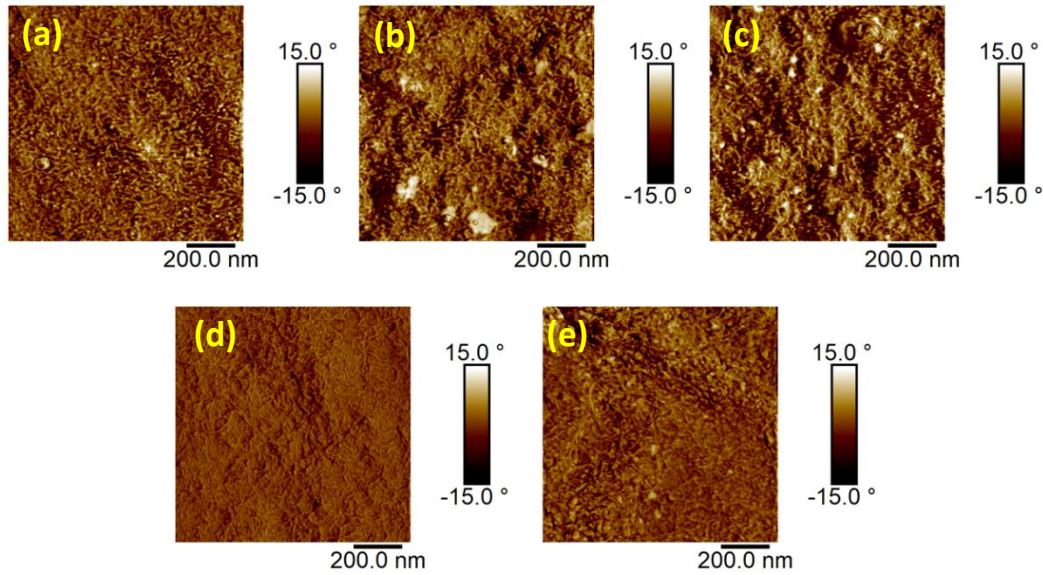


Fig. 4.22: AFM tapping mode phase imaging of OM processed *P1-D* at (a) 90/10, (b) 70/30 and (c) 50/50 compositions and at (d) 98/02 and (e) 92/08 compositions showing the morphological evolution of the printed channels with varying volume fraction of *D*.

While excess PSS enhances the solubility of the PEDOT by forming a polyelectrolyte complex PEDOT:PSS (*P1*), it also results in the domination of the imaged film surface as seen in the low phase range of Fig. 4.10. The RMS roughness of the pristine film is of the order of ~ 1.7 nm and is generally known to depend on the ratio of PEDOT:PSS in the dispersion. The pristine dispersion of PEDOT:PSS has a PEDOT to PSS ratio of about 1:1.6 and the observed roughness is well within expectation. The addition of the high boiling point ($\sim 189^\circ\text{C}$) polar cosolvent *D* (DMSO) for secondary doping induces morphological changes in the printed film as *P1* undergoes structural reorganization as mentioned previously. This enables the PEDOT domains to form a

highly connected chain-like network while the excess PSS domains are redistributed into insulating lamellae within the spanning PEDOT network and is attributed to the change of state of PEDOT from coiled, flexible to planar, rigid [175]. The film roughness increases to ~ 3.5 nm due to the more rigid networked structure of the conjugated PEDOT domains without the smoothing effect of the soft PSS shells which become localized after cosolvent treatment. This results in the enhancement of electrical conductivity in an interesting manner that can be explained using the hopping probability expression introduced previously. Secondary doping leads to the rearrangement of the excess PSS covering the PEDOT domains which results in a reduction in W . As W decreases, viable hopping states hitherto buried under a large energy barrier begin to emerge which also results in a significant reduction in S due to the increased connectivity of PEDOT domains. Tunneling current imaging of OM processed channels printed using 100/0 and 90/10 $P1$ - D blends shown in Fig. 4.23 demonstrates this quite decisively by probing the printed channel surface for the distribution of conducting states. Such an increase in the density of conducting states is not limited only to the surface but throughout the printed structure given that secondary doping is effectively a volume phenomenon. Another aspect of secondary doping will emerge in the following subsections which deals with the effect of temperature on the electrical conductivity of $P1$ and $P2$ and their blends and is expected to have interesting ramifications for sensor applications.

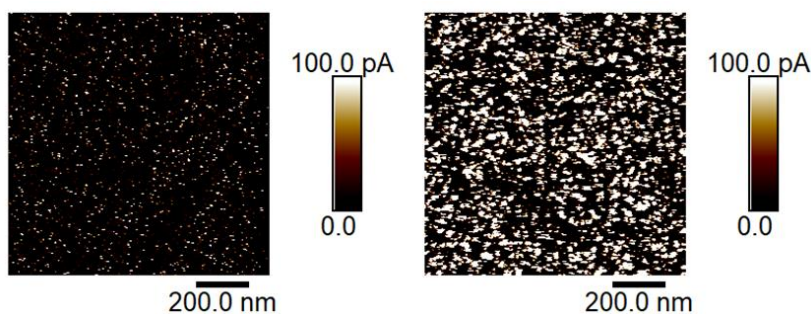


Fig. 4.23: Tunneling current imaging of channels printed using (left) pristine $P1$ and (right) the 90/10 composition of the $P1$ - D blend showing decrease in the spatial separation S between conducting states on the probed channel surface.

For completeness, blending of $P2$ and D was also tested but D was not found to have any noticeable effect on the electrical conductivity of printed $P2$ channels. This is due to the nature of $P2$ which is a self-doped polythiophene with no significantly ionic character as opposed to $P1$ which is a polyelectrolyte complex. Consequently, D does not have the usual charge screening effect on $P2$ unlike $P1$ where its high polarity and high boiling point character keeps it in the drying film longer and enables the reordering of the polycationic (PEDOT) and polyanionic (PSS) species

by acting as a plasticizer in order to dramatically improve the electrical connectivity among the PEDOT domains, thereby enhancing electrical conductivity. Thus, *P2* blends with *D* have qualitatively identical morphological and electrical response respectively, to pristine *P2* after the drying of solvents. Before concluding this case study, it must be mentioned that while PM processing is considered to be the benchmark against which UM and OM processing are compared in the hypothesis tests, it also needs to be acknowledged that the sample libraries printed using PM processing may not be perfect owing to the nature of *P1* itself. The reasons for such scenarios to occur are: (i) local aberrations in print drying leading to electrical contact issues (PSS dominates electrode contact instead of PEDOT) between the channel and the probing electrodes and (ii) inhomogeneities in solute fraction within printing fluids leading to inconsistent solute distribution (chain lengths of PEDOT much smaller than PSS) from print to print. These occurrences are not only valid for PM processing but for both UM and OM processing too. Therefore, non-idealities in the substrate and printing fluids can be difficult to decouple from the actual effects due to the parametric being investigated. This aspect has been discussed in greater detail in Case 1 where the effect of outliers confounded the effect of layer count, resulting in conflicting inferences.

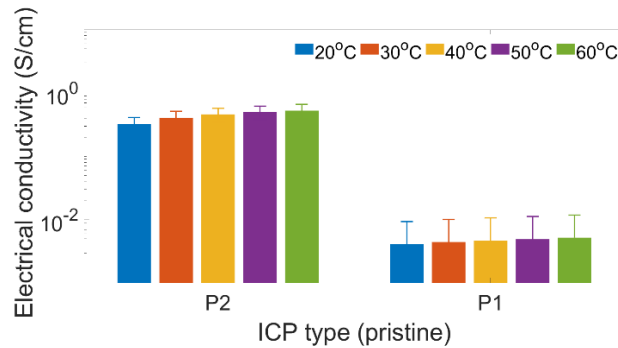


Fig. 4.24: Temperature dependence of electrical conductivity in pristine *P1* and *P2* over the range of 20°C to 60°C.

Table 4.5: ANOVA evaluation of pristine *P1* and *P2* electrical conductivity response as a function of temperature including (w/) and excluding (w/o) extreme outliers.

ICP type	F_0 (w/ OL)	p -value (w/ OL)	F_0 (w/o OL)	p -value (w/o OL)
<i>P1</i>	0.075	0.990	0.088	0.986
<i>P2</i>	7.301	< 0.001	7.302	< 0.001

4.3.3 Case 3: Electrical conductivity dependence on temperature

For deployment in wearable temperature sensor applications, temperature-dependent drift of the electrical conductivity in ICPs (due to temperature sensitivity) needs to be extremely low when used as an interconnect element while significant dependence on temperature is required

when used as temperature sensing elements. In this brief case study, the temperature behavior of pristine *P1* and *P2* are explored with the intent of identifying the best options for the different modes of deployment discussed above. Fig. 4.24 shows the temperature dependence of the electrical conductivities of *P1* and *P2*. Two observations become immediately apparent: (i) pristine *P2* is a better conductor than pristine *P1* and (ii) measurement scatter is noticeably less for *P2* which corroborates the issue of poor electrical contact of the printed channel with the probing electrodes in *P1*. The electrical conductivities of both ICPs seem to increase with temperature. To evaluate if the upward trend is significant, ANOVA is performed with Table 4.5 summarizing its outcomes. TCR or temperature coefficients of resistance of individual printed replicates of pristine *P1* and *P2*, averaged over the temperature range 20°C to 60°C, are illustrated in Appendix B.

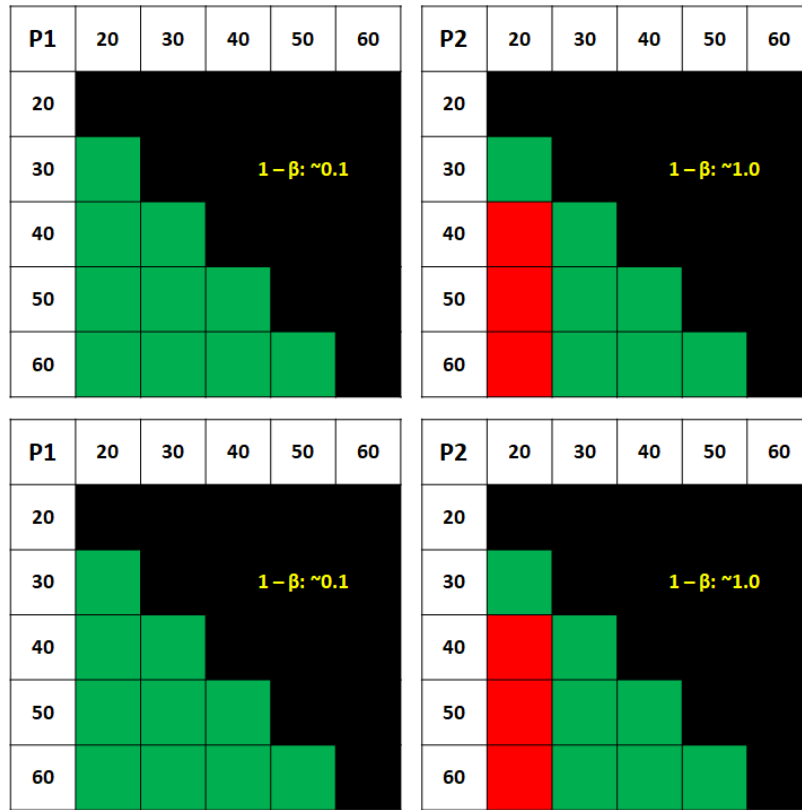


Fig. 4.25: ANOVA post-hoc analyses of the pristine ICPs (ICP type denoted by the first entry in each matrix) with (*upper row*) and without (*lower row*) extreme outliers. First row and column entries (except the first cell entry) indicate temperature in °C.

Tukey-Kramer post-hoc tests for locating the significant differences are conducted and compiled in Fig. 4.25. As expected from a non-significant ANOVA, there are no observable differences (all cells green) for the electrical conductivity of *P1* which also results in an extremely low power since the effect size is extremely small. This suggests that *P1* in its pristine form is

unsuitable for use as temperature sensing elements as the temperature sensitivity is likely to be overpowered by thermal noise but its secondary doped form as a *P1-D* blend may be a more suitable fit. *P2* on the other hand shows significant differences in electrical conductivity when measured between 20°C and 40°C, 20°C and 50°C and 20°C and 60°C as illustrated by the cells in red. A large effect size is therefore corroborated by the high power of this test. Consequently, *P2* is a better candidate for use in sensing elements within the evaluated temperature range. However, significant differences were not observed between adjacent temperatures but only between temperatures further apart. This indicates a vulnerability to thermal noise although not as much as for *P1*. Hence, it may be beneficial to investigate ways in which the thermal noise performance of *P2* may be improved.

4.3.4 Case 4: Electrical conductivity dependence on cosolvent additive and temperature

Based on the conclusions from the above, it can be deduced that *P2* is a better candidate for use as a temperature sensing element compared to *P1* due to the greater temperature sensitivity of its electrical conductivity. As conjectured in the previous subsection, *P1* (in its secondary doped state) may be a good candidate for use in sensing elements given its favorable response to treatment with the cosolvent *D* as seen from the case study on the enhancement of electrical conductivity. Thus, it is of relevance to evaluate the temperature dependence of electrical conductivity of films printed using *P1-D* blends to evaluate their temperature dependence when used in all-polymer sensor applications. Blend compositions from iteration 1 in Case 2 have been used for this study using all three types of processing (PM, UM and OM) as the goal is to look for temperature dependence at the highest electrical conductivity levels of secondary doped *P1*. Fig. 4.26 depicts the electrical conductivity behavior of the channels printed using the aforementioned blend compositions as a function of ambient temperature for all processing types. Interestingly, while the envelope of the electrical conductivity values follows the trends seen in Fig. 4.15 individually across different compositions, the range of temperatures 20°C to 60°C tested seems to have almost no effect on the secondary doped *P1* prints. ANOVA evaluation of temperature dependence remains statistically insignificant as shown in Table 4.6 for all blend compositions irrespective of the presence of outliers. These tests also suggest an effect size too small to be practically meaningful as is indicated by the low power (< 0.1 for all three processing types).

To explain this, the hopping probability is referenced once again where the “range” in VRH is defined by the argument within the exponential function. This range \hat{R} is a sum of terms

comprising the spatial term S and the energy term W which can be used to postulate the loss of temperature dependence. As shown in Fig. 4.23, secondary doping results in a significant reduction in the S term which is due to the drastic increase in the networked PEDOT after the unraveling of $P1$ particles. Enhancement of PEDOT domain connectivity also results in a proportional decrease in W and the only way temperature dependence can become vanishingly small is when the W term in the range \hat{R} approaches zero. This suggests that when \hat{R} approaches zero, temperature dependence of electrical conductivity also disappears.

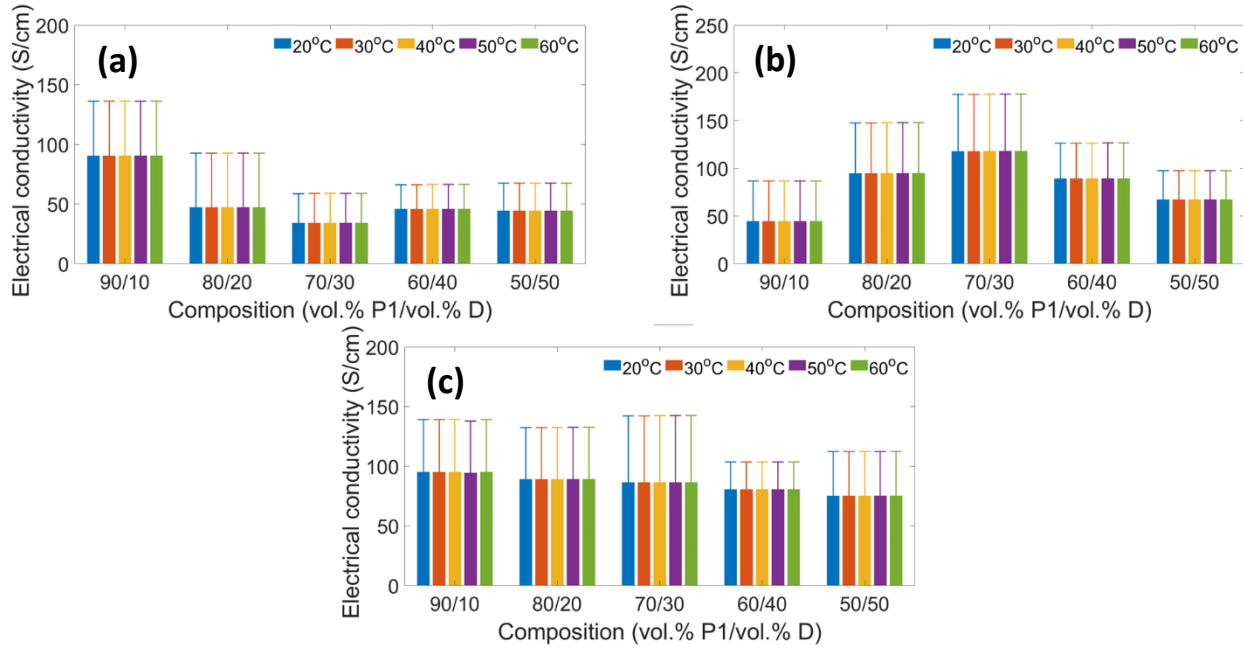


Fig. 4.26: Temperature dependence of electrical conductivity in $P1$ - D blends for processing types (a) PM, (b) UM and (c) OM.

While this suggests that $P1$ is not suitable as a temperature sensing element in any form, pristine or secondary doped, it also demonstrates the temperature inertness of its electrical conductivity in its secondary doped high conductivity form. This implies that a temperature sensor manufactured using $P2$ as the sensing element and secondary doped $P1$ as the interconnect element will not suffer from drift in electrical conductivity when subjected to variability of ambient temperatures. As touched upon previously, another aspect of temperature sensing using ICPs is their thermal noise performance which is a quantity that is proportional to temperature. Specifically, the mean voltage variance in an electrical element facilitating charge carrier transport due to the Johnson-Nyquist (thermal) noise is dependent on the product of its resistance and the ambient temperature [176]. Such dependence implies that while the temperature contribution to

sensor noise may be uncontrollable for temperature sensing applications, the contribution due to the resistance can be minimized by improving electrical conductivity of the element. From the temperature behavior of pristine *P2* and *P1-D* blends, it was hypothesized that blending *P2* with *P1-D* may impart an electrical conductivity enhancement effect to the blend while retaining the temperature sensitivity. For this test, the PM processed *P1-D* composition resulting in the highest electrical conductivity (90/10) was used as the tuning additive with *P2* and the same composition range (90/10 to 50/50) was studied where *P2* was varied from 90 vol.% to 50 vol.%. For reference, blends of pristine *P2* and *P1* were also studied to see if *P1* has any synergistic or antagonistic effect on the temperature behavior of *P2*. TCR of *P2-P1* and *P2-P1-D* blends are shown Appendix B for each composition.

Fig. 4.26 shows the trends observed in the electrical conductivities of the different blend compositions across the same temperature range of 20°C to 60°C used previously. There is a stark contrast in the characteristics both with respect to blend composition as well as the ambient temperature. For pristine *P2* and *P1* blends, while the temperature sensitivity of their electrical conductivity decreases, the dependence of composition appears to pivot towards *P1* between 60/40 and 70/30 and is corroborated by the Games-Howell pairwise tests following a significant ANOVA. The electrical conductivity between 60/40 and 50/50 are statistically similar while both are significantly different from the remaining blend compositions. This suggests linear interaction between the pristine *P2* and *P1* until the 70/30 composition beyond which, the increasing PSS fraction dominates and drag the electrical conductivity towards that of pristine *P1*.

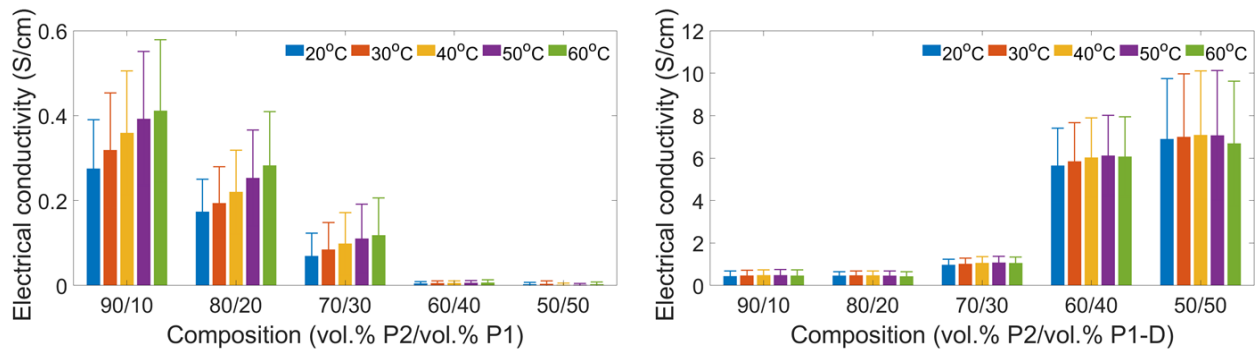


Fig. 4.27: Electrical conductivity behavior of (left) pristine *P2* and *P1* blends and (right) pristine *P2* and secondary doped *P1-D* (90/10) blends as a function of ambient temperature.

The reason for this effect of PSS is due to its hygroscopic nature which traps water owing to ambient humidity, thereby suppressing the electrical conductivity of *P1* under normal laboratory conditions as also evidenced in literature [177]. In contrast, when secondary doped *P1-D* (90/10)

is used as the additive instead of *P1*, the behavior reverses as expected from the hypothesis. However, a pivot point can once again be seen around the 70/30 composition beyond which, the electrical conductivity shoots up drastically. It is to be noted that the fraction of *D* in this blend varies linearly from 1 vol.% at 90/10 to 5 vol.% at 50/50 which suggests that beyond 30 vol.% *P1-D* fraction (comprising 90% *P1* and 10% *D* from the definition of *P1-D* in this case study) in the *P2-P1-D* blend, the *P1-D* component starts dominating the *P2* component. This implies that the highly connected network of PEDOT domains in the *P1-D* additive has started spanning the printed channel. This behavior can be observed as morphological changes in the AFM phase images of the *P2-P1* and *P2-P1-D* blends once again as illustrated in Fig. 4.28. While particle size growth is observed from 90/10 to 50/50 in either case, the *P2-P1-D* blend shows a clear transition from purely particle-like to chain-like connectivity similar to that observed between Fig. 4.10 and Fig. 4.22. Based on the correlation between electrical conductivity enhancement and such morphological changes in printed channels in the prior case study, the observations made here can be similarly explained. However, the temperature dependence of *P2* electrical conductivity suffers as evidenced by the envelope of the corresponding bars in Fig. 4.27 at a particular composition.

Table 4.6: ANOVA evaluation of temperature-dependent electrical conductivity behavior *P1-D* blends for PM, UM and OM processing.

Processing type	F_0 w/ OL	p -value w/ OL	F_0 w/o OL	p -value w/o OL
PM	0.000	1.000	0.000	1.000
UM	0.000	1.000	0.000	1.000
OM	0.000	1.000	0.000	1.000

More importantly, even a 10 vol.% fraction of *P1-D* in the blend seems to be sufficient to overpower the temperature sensitivity of *P2* even when the *P1-D* fraction has not started affecting the electrical conductivity manifold. Assuming linearity of interaction between *P2* and *P1/P1-D* by virtue of linear changes in component proportioning, it may be postulated that this effect is due to *P1-D* starting to play a role in the hopping transport. To elaborate, the highly networked PEDOT domains are uniformly interspersed among the *P2* particles even though it does not span the printed channel. This implies that part of the carrier transport is happening due to *P2* to *P1-D* and *P1-D* to *P1-D* transitions and the fact that *P1-D* is approximately insensitive to temperature results in the lack of temperature dependence. While this may seem like an argument for exploring lower *P1-D* fractions in the blend to minimize the above transitions, it is nullified by the fact that sufficient increase in electrical conductivity will not occur at those fractions (< 1 vol.%) of *D* in the blend.

Thus, the fundamental premise of blending the two ICPs (for imparting the enhanced electrical conductivity of *P1-D* to the *P2-P1-D* blend) in order to reduce the mean Johnson-Nyquist noise voltage variance is defeated by lowering the fraction of highly networked PEDOT domains in the blend.

Table 4.7: ANOVA evaluation of composition-dependent and temperature-dependent electrical conductivity behavior of *P2-P1* and *P2-P1-D* blends.

Factor	F_0 (<i>P2-P1</i>)	p -value (<i>P2-P1</i>)	F_0 (<i>P2-P1-D</i>)	p -value (<i>P2-P1-D</i>)
Composition	231.023	< 0.001	310.539	< 0.001
Temperature	5.576	< 0.001	0.972	0.982
Interaction	1.307	0.190	0.069	1.000

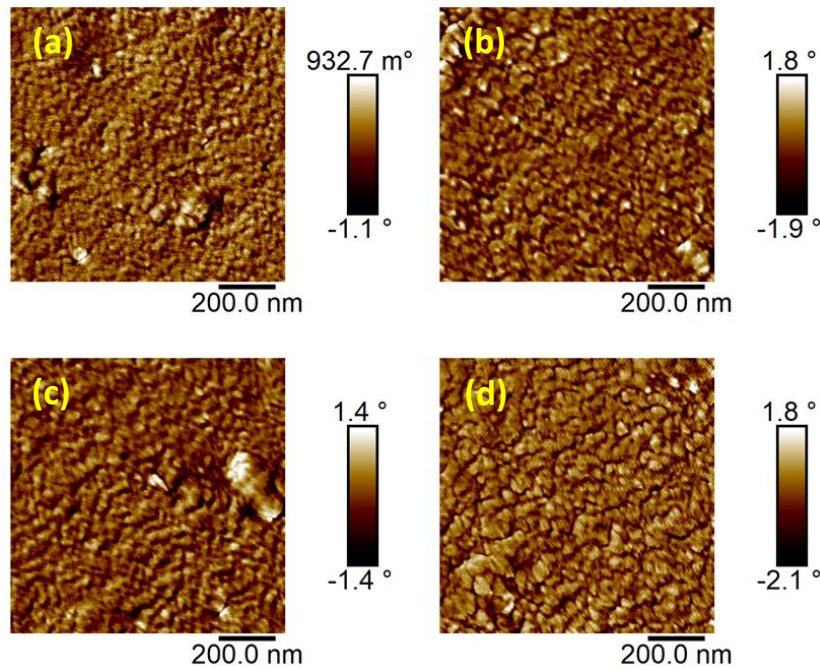


Fig. 4.28: AFM tapping mode phase imaging of *P2-P1* blends at (a) 90/10 and (b) 50/50 and *P2-P1-D* blends at (c) 90/10 and (d) 50/50.

Table 4.7 summarizes the conclusions from the two-way ANOVA evaluation of the *P2-P1* and *P2-P1-D* blending studies. There is definite significance for differences in electrical conductivity of both *P2-P1* and *P2-P1-D* as a function of composition but only significance for differences as a function of temperature in the former and not for the latter as corroborated above. In addition, there is minimal interaction between composition and temperature on the electrical conductivity response in *P2-P1* and none in *P2-P1-D*. Fig. 4.29 shows the electrical conductivity of both blends as a function of both composition and temperature where the lack of any significant interaction effects is manifested through the lack of any significant curvature in the contours. It

needs to be stated here that the temperature studies did not correct for extreme outliers since it was shown in Case 2 that these extreme outliers mostly had a minimal effect when comparing among different compositions and almost no effect when comparing different temperatures in Case 3.

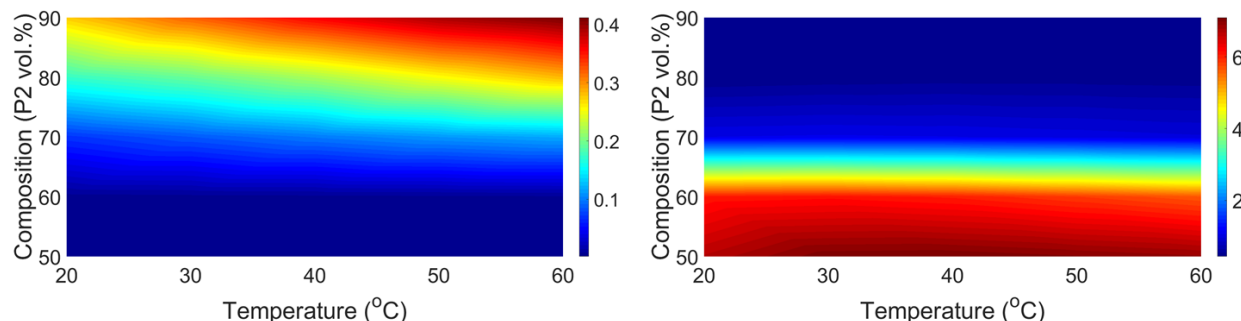


Fig. 4.29: Interpolated electrical conductivity response of (*left*) *P2-P1* blends and (*right*) *P2-P1-D* blends across 90/10 to 50/50 compositions and 20°C to 60°C temperatures. Scale bar in S/cm.

Summary

Libraries of commercial-grade and laboratory-grade ICP thin film features printed using the CPH-based platform are evaluated for their temperature-dependent electrical conductivity performance using electrical and morphological characterization methods coupled with statistical analyses. It is inferred from these experiments that differences between premixed blends are marginally easier to observe in comparison to on-chip mixed blends but the two processes are quite similar. Unmixed blends are technically not totally inhomogeneous due to diffusive effects at the inkjet orifice which reduces the mixing length through droplet formation. However, this is not enough to accurately capture performance extrema and a greater degree of homogenization is required than that offered by diffusive mixing in droplets prior to drying. Additionally, negative validation through blending tests enables the identification of appropriate functional regimes for each of the ICPs for sensor applications.

Chapter 5: Conclusions and Future Work

5.1 Summarized conclusions

Despite extensive use in chemical and biological engineering for sample preparation and testing, microfluidic processing has seen limited use in the field of electronic materials. When coupled with an additive feature patterning technique like inkjet printing, it has the potential to transform multi-material testing as well as the sensor manufacturing and optimization process. This becomes increasingly relevant with the advent of the IoT paradigm discussed previously as it is estimated that the number of devices connected to the IoT framework will more than double to ~29 billion from its current levels at ~13 billion. Such increased levels of device connectivity will logically translate into a requirement for the mass production of economically fabricated optimized sensors which find ubiquitous usage in almost any device that can be designated as “smart”. The examples demonstrated in this dissertation represent a key step in the roadmap towards high throughput screening of sensor materials: the combinatorial fabrication of printed thin and/or thick film sample libraries. The general concept of a combinatorial print head (CPH) can be quite useful for multi-material processing prior to dispensing, thereby enabling the on-CPH integration of multiple preprocessing functionalities such as fluid mixing (investigated in this work) for fluid mixture homogenization, heating for fluid property modification, chemical reaction between fluids to minimize reactivity with the ambient environment etc. In this work, intrinsically conductive polymers (ICPs) have been used as test materials to not only validate the performance of a CPH-based thin film sample manufacturing platform but to also probe the functionality of the ICPs themselves. ICPs are an appropriate choice of materials given their solution processability and good performance leading to their rapid adoption in the field of sensors and actuators.

The primary objective of this dissertation is to enable the integration of microfluidic preprocessing with inkjet printing for combinatorial sample library preparation and validate such an integrated system using solution processable materials. Therefore, the research presented here focuses on (i) the development of a CPH which can be used to process multiple fluid inputs at multiple resolutions, (ii) characterization of CPH proportioning and mixing capabilities, (iii) operational validation of the CPH platform using ICP dispersions and (iv) statistical analyses of characterization data. Some bottlenecks to the integration between microfluidic preprocessing and inkjet printing have been addressed in this dissertation which include circumventing the general

integration incompatibility of microfluidic devices and inkjet dispenser by modular design and demonstrating the durability of such modular CPH devices despite significant mechanical forcing. Both of these can be attributed to the elastomeric implementation of the CPH base structure which not only enables robust friction fitting but also offers structural compliance during handling and operation.

Modular combination of off-the-shelf components has been performed in this work using PDMS as the base housing structure for the CPH to illustrate a plug-and-play approach to assembling such devices. Such a proof-of-concept CPH device has been central to the fabrication of printed sample libraries of different ICPs. With the motivation behind the utility of CPH-based platforms firmly established, the platform deployed in this work is developed by assembling linear actuators as positioning components, syringe pumps as fluid flow regulators and associated electronics (waveform generator, piezoelectric amplifier and a programmable microcontroller board) and user-interface to control the operation of the system. One of the key elements of combinatorial sample formulation is fluid proportioning which is done using syringe pumps whose accuracy needs to be at least better than the step sizes used to formulate different sample compositions. This was validated using gravimetric testing of the pumps' outputs when driven at specified input flow rates to assess the uncertainty being propagated from the inlets to the outlet for dispensing. Once the proportioning error bounds were established to be lower than the step size or compositional resolution being targeted, the next parameter that needed to be addressed was the mixing or homogenization of the blend components. While low frequency vibrations of extended sources like loudspeaker membranes have been shown in literature to be effective in the mixing fluids, the focus of this work was to integrate a homogenization or mixing module that was compact, modular and did not require multi-step microfabrication processing. This was done to keep the CPH fabrication as simple as possible which allowed for more focus to be on the functional validation of the system. The encapsulated ERM motor was an attractive choice as a vibratory mixing and homogenization component given that it met all three requirements for fabrication simplicity along with being extremely economical due to the advent and mass adoption of haptic actuators.

Characterization of the mixing module was performed using flow imaging tests under different driving conditions of the motor in order to identify the operational regime offering fastest mixing while not subjecting the CPH to overly strong vibrations to cause structural damage to

delicate features with time. While the CPH is compliant in general, the structures patterned in it are mostly robust with the only highly compliant structure being the elastomeric membrane which physically separates the mixing channel and the haptic mixing actuator. To prevent damage such as microtears at the membrane edges and motor overheating, the haptic mixing actuator was driven much below its maximum rated driving current of ~ 250 mA. The imaging tests conclusively demonstrated the occurrence of chaotic advection in the mixing channel which rapidly decreased the mixing lengths of the fluid inputs, allowing diffusive homogenization over highly reduced length scales. The effect of homogenization was qualitatively evaluated using a colorimetric test as well as high speed imaging of ICP-additive and fluorescent dye flows. Apart from these, performance comparisons of printed thin film structures were also done later in the work among pre-mixed (PM), unmixed (UM) and on-chip mixed (OM) processes as a quantitative measure of differences in outcomes. Printability of the fluids used in this work was established using dynamic viscosity and surface tension measurements and it was observed that the inkjet dispenser was capable of printing water (highest surface tension of ~ 72 mN/m) and ethylene glycol (highest dynamic viscosity of ~ 16 mPa.s) under room temperature conditions. Among the ICP-additive blends, the dynamic viscosity varied from ~ 2 mPa.s to ~ 7 mPa.s at different blend compositions while the surface tension varied from ~ 47 mN/m to ~ 68 mN/m. Based on the jettability estimates using dimensionless numbers as well as the direct observation of the printing process, printability of all the fluids, pristine and blended, was confirmed.

Given the inferential nature of the experiments for validating CPH performance with the ICPs used in this work and vice versa, ANOVA was chosen to be the statistical testing framework due to its ability to test multiple levels of the factor variables to search for meaningful differences among the corresponding response variable outcomes. While other methods such as *t*-tests and *z*-scores have been used in prior literature, ANOVA is superior to these methods which can only handle pairwise and not multi-level evaluation without increased susceptibility to inferencing errors. With this framework established, case studies involving the pristine and blended ICPs *P1* and *P2* were conducted to study the behavior of the processing as well as the material systems. These case studies were based on different hypotheses pertaining to both the processing and the material systems. Electrical conductivity was used as the response variable while printed layer count, blend composition and ambient temperature were used as the factor variables for these studies. The tested hypotheses were defined such that the null hypothesis represented no change

in response variable outcome due to change in factor variable levels and the alternate hypothesis represented any statistically significant deviation from the null hypothesis. For statistically significant ANOVA outcomes, follow-up post-hoc tests were done to determine which factor levels were the source of the observed differences so that nuanced inferences could be drawn regarding the validity of the conclusions considering the limits of manual measurements.

It was observed that the consistency in the electrical conductivity of pristine *P1* was affected due to its insulating component (PSS) which is present as a counterion for charge balance and also to improve aqueous dispersibility of the conducting component (PEDOT). Artifacts attributable to this binary nature of *P1* were observed where there seemed to be an increase in electrical conductivity with increasing printed layer count but when extreme outliers equivalent to disconnected prints were eliminated, the statistically significant differences disappeared within the sample-to-sample variations. Apart from interference due to PSS, another confounding factor is print connectivity with probing electrodes due to differential wetting of the glass and Ag electrode by the droplets. This can cause inconsistency in the level of electrical contact between Ag and *P1* which can manifest as variability in electrical conductivity. Decoupling the effects of PSS and its role in inconsistent electrical contact with probing electrodes is difficult based on the range of printed layer counts tested given that PSS is always in stoichiometric excess to PEDOT in the pristine dispersion of *P1*. On the other hand, *P2* does not show such behavior due to lack of PSS but it also has lower surface tension, implying greater wettability than *P1* which lends credence to the hypothesis of confounding of the two factors.

To evaluate the CPH performance, blends of *P1* with the additive *D* were formulated at coarse and fine proportioning steps using PM, UM and OM processing to test the statistical significance of electrical conductivity differences at different blend compositions, if any. It was found that OM processing was capable of capturing the general trend in electrical conductivity equally well as PM processing but there were some differences observed for the response at lower fractions of *P1* in the blend which may have been due to differences between manual proportioning and longer homogenization times for PM versus automated proportioning and shorter homogenization times for OM. At the same time, UM processing was not able to capture the established trend in electrical conductivity despite having the advantage of automated proportioning, meaning that OM does have a positive impact on blend homogenization which is reflected in performance outcomes. It was also observed that the differences between PM and OM

appeared in some compositions only for coarser (10 vol.%) changes in blend composition whereas in some cases, PM and UM has no differences while OM and UM did. The nature of these observations suggests that there may be a randomness to the differences between PM and OM rather than anything systematic as none of the processes showed any performance difference for finer (2 vol.%) changes in blend composition. As mentioned earlier, this randomness has multiple sources like proportioning errors, incompleteness of homogenization and when considered as a whole, PM appears to be marginally better than OM while UM completely misses the overall trend.

Using the same tests to evaluate *P1-D* blend behavior, the electrical conductivity peak for PM was coincident with that for OM but the former showed differences with the electrical conductivity for lower *P1* blend fractions while the latter did not. While this appears to indicate that PM is better at distinguishing different blend compositions than OM, at least for coarser changes, thin film morphology does not show significant differences between PM and OM. Given that the electrical conductivity behavior of *P1* is completely dependent on morphology, this suggests inconclusive inferencing differences between PM and OM processing of *P1-D* blends. However, there is a clear distinction between UM and both PM and OM from the 92/08 to the 70/30 composition which indicates that UM requires more blend fraction of *D* to cause similar changes to *P1* compared to PM and OM. This is also reflected in the stark difference in electrical conductivity trends over the coarser variations in blend composition. As before, no significant differences were observed for the finer changes in blend composition except between the extremes for PM. Based on the observations made, it can be deduced that PM is once again somewhat superior to OM while both PM and OM are superior to UM in terms of capturing the behavior of *P1* when blended with *D*.

After establishment of reasonable similarity between the PM and the OM methods, temperature testing of the electrical conductivities of *P1* and *P2* in their pristine as well as blended forms was conducted. The goal here was to identify which ICP was better suited as a temperature sensing element and if *P1-D* could be used as the interconnect element. Electrical conductivity of pristine *P1* was not as highly sensitive to temperature as *P2*, making the latter a clear choice as the sensing element. Interestingly, the electrical conductivity of *P1-D* blends was found to be almost totally independent of temperature which made it the clear choice as an interconnect element in an all-polymer sensor due to lack of temperature-dependent drift in electrical conductivity. This also led to the hypothesis that blending *P2* with minimal quantities of *P1-D* blends might improve the

overall electrical conductivity while still retaining reasonable temperature dependence. This was attempted in order to reduce the thermal noise contribution of pristine *P2* to the temperature sensor. While the overall electrical conductivity did improve, it was also observed that even the slightest amounts of *D* in the blend could cause the temperature independence seen in *P1-D* blends to manifest. As a result, it was concluded that when the morphology of *P1* has been modulated to some degree by *D* such that its conductive component is highly networked, that effect dominates despite the fact that the blend is a composite of *P2* and *P1*.

5.2 Scope of future work

Improved functionality calibration

The nature of commercial-grade *P1* was observed to be responsible for the introduction of significant sample-to-sample variation. This is detrimental to the process of evaluating differences among response data sets using different factor levels or treatments. Using materials which can interact with additives along with having established response thresholds and lower material randomness can improve statistical inferencing about the quantitative differences among the processing methods. Functionality verification without confounding of the response due to material and substrate effects may help with better statistical inferencing of combinatorially printed thin film sample libraries.

Enhanced chemical resistance of the CPH elastomer

Typical elastomers used in microfluidic applications are capable of absorbing small molecules and moisture to a certain degree which may result in concentration variations in handled fluids when the device is operated continuously for extended time periods. Apart from this, they are also not resistant to a lot of conventional solvents used for solution processed electronics which makes for limited processability. This has been one of the reasons that typically non-toxic and biocompatible materials such as water and DMSO have been used in this work. Exploring alternative elastomers such as fluorinated elastomers used as industrial-grade sealants may result in chemical resistance to a wide range of solvents and broaden the scope of material processability.

Optimization of vibratory actuation module for fluid homogenization

Reducing the area footprint of the vibratory actuator may enable clustering of multiple actuator modules. Such a reduction can be achieved through the use of newer actuator designs that

can be fully embedded within the bilayer print head base structure for This can be exploited to create a rapid on-the-fly combinatorial printing process where fluid homogenization can happen continuously during the printing process. Parallelization will result in a time efficient process and enable continuous compositional variation as opposed to the discrete variation demonstrated in the current work. Continuous compositional variation is superior to discrete compositional variation in situations where the composition(s) for optimal material blend performance is unknown. This will facilitate the evaluation of novel material systems which can then be further interrogated using the iterative methodology around the neighborhoods of the optima.

Fully integrated printing system

The combinatorial printing platform used in this work is the first generation compilation of standalone components such as triaxial substrate and print head positioning system, syringe pumps (proportioning), mixing actuator module (homogenizing), dispenser module (printing) controlled by software. There is much scope for the refinement of the integrated assembly of components including updated print head designs for accommodating more fluid inputs, optimizing the mixing actuator module as touched upon before, addition of multiple dispenser modules for faster sample library preparation. Larger printable substrate area can offer greater sample replication leading to better inferencing when investigating smaller effect sizes. Upgrading of the control software is essential for completeness of the automated printing process which should result in greater time efficiency along with the volume efficiency already established here.

Range of applicability of the work

While this work has demonstrated the utility of combinatorial sample preparation by integrating microfluidic processing with inkjet printing and used it as a tool to evaluate ICP performance, the technology platform can be used for a wide array of other domains. These include optimization of material blends for thin and thick films that may find use in device applications related to sensors and actuators, energy generation and highly programmable 3D printing among others. As an enabling technology platform, there can be applications where integration of more functionalities can magnify the impact of the overall system in terms of material volume and time efficiency.

Bibliography

- [1] C. Bois, A. A. Gupta, A. L. Roy and K. Walus, “Collaborative conception of a R2R printed testing platform for printed electronics standardization,” *IEEE International Flexible Electronics Technology Conference (IFETC)*, 2019.
- [2] A. L. Roy, H. N. Chiu and K. Walus, “Microfluidic drop-on-demand inkjet print heads for multi-resolution multi-material thin film library preparation” *International Conference on Miniaturized Systems for Chemistry and Life Sciences (μ TAS)*, 2021.
- [3] A. L. Roy, H. N. Chiu and K. Walus, “A microfluidic-enabled combinatorial formulation and integrated inkjet printing platform for evaluating functionally graded material blends,” *Lab Chip*, vol. 21, no. 22, pp. 4427–4436, 2021.
- [4] A. L. Roy, C. Beaumont, M. Leclerc and K. Walus, “Fabrication and characterization of low-cost standalone polymer-based disposable inkjet dispenser,” (manuscript in preparation).
- [5] M. Ohring, “Materials Science of Thin Films: Deposition and Structure,” 2nd Edition, 2001.
- [6] H. M. Smith and A. F. Turner, “Vacuum Deposited Thin Films Using a Ruby Laser,” *Appl. Opt.*, vol. 4, no. 1, pp. 147–148, 1965.
- [7] S. K. Deb, “Optical and photoelectric properties and colour centres in thin films of tungsten oxide,” *Philos. Mag.*, vol. 27, no. 4, pp. 801–822, 1973.
- [8] J. A. Thornton and D. W. Hoffman, “Stress-related effects in thin films,” *Thin Solid Films*, vol. 171, no. 1, pp. 5–31, 1989.
- [9] F. Keller, M. S. Hunter, and D. L. Robinson, “Structural Features of Oxide Coatings on Aluminum,” *J. Electrochem. Soc.*, vol. 100, no. 9, pp. 411–419, 1953.
- [10] G. Hass and R. Tousey, “Reflecting coatings for the extreme ultraviolet,” *J. Opt. Soc. Am.*, vol. 49, no. 6, pp. 593–602, 1959.
- [11] W. Shockley, “The path to the conception of the junction transistor,” *IEEE Trans. Electron Devices*, vol. 31, no. 11, pp. 1523–1546, 1984.
- [12] K. Jang, K. Sato, K. Igawa, U. Il Chung, and T. Kitamori, “Development of an osteoblast-based 3D continuous-perfusion microfluidic system for drug screening,” *Anal. Bioanal. Chem.*, vol. 390, no. 3, pp. 825–832, 2008.

- [13] J. Bardeen and W. H. Brattain, “Physical Principles Involved in Transistor Action,” *Phys. Rev.*, vol. 75, pp. 1208–1225, 1949.
- [14] P. Lin and F. Yan, “Organic Thin-Film Transistors for Chemical and Biological Sensing,” *Adv. Mater.*, vol. 24, pp. 34–51, 2012.
- [15] J. T. Mabeck and G. G. Malliaras, “Chemical and biological sensors based on organic thin-film transistors,” *Anal. Bioanal. Chem.*, vol. 384, pp. 343–353, 2006.
- [16] L. Wang, D. Fine, D. Sharma, L. Torsi, and A. Dodabalapur, “Nanoscale organic and polymeric field-effect transistors as chemical sensors,” *Anal. Bioanal. Chem.*, vol. 384, pp. 310–321, 2006.
- [17] J. H. L. Ngai, G. Y. Chang, X. Gao, X. Zhou, A. D. Hendsbee, and Y. Li, “Design and synthesis of stable indigo polymer semiconductors for organic field-effect transistors with high fluoride sensitivity and selectivity,” *RSC Adv.*, vol. 9, no. 45, pp. 26230–26237, 2019.
- [18] M. Nilolou and G. G. Malliaras, “Applications of poly(3,4-ethylenedioxythiophene) doped with poly(styrene sulfonic acid) transistors in chemical and biological sensors,” *Chem. Rec.*, vol. 3, no. 1, pp. 13–22, 2008.
- [19] A. W. Feinberg, A. Feigel, S. S. Shevkoplyas, S. Sheehy, G. M. Whitesides, and K. K. Parker, “Muscular Thin Films for Building Actuators and Powering Devices,” *Science*, vol. 317, no. 5843, pp. 1366–1370, 2007.
- [20] D. J. Bell, T. J. Lu, N. A. Fleck, and S. M. Spearing, “MEMS actuators and sensors: Observations on their performance and selection for purpose,” *J. Micromech. Microeng.*, vol. 15, no. 7, pp. S153–S164, 2005.
- [21] C. Wang, Y. Wang, Y. Yao, W. Luo, J. Wan, J. Dai, E. Hitz, K. Fu, and L. Hu, “A solution-processed, high-temperature, flexible, thin film actuator,” *Adv. Mater.*, vol. 28, no. 39, pp. 8618–8624, 2016.
- [22] F. Filhol, E. Defaÿ, C. Divoux, C. Zinck, and M.T. Delaye, “Resonant micro-mirror excited by a thin-film piezoelectric actuator for fast optical beam scanning,” *Sens. Actuators, A*, vol. 123–124, pp. 483–489.

- [23] V. Fthenakis, “Sustainability of photovoltaics: The case for thin-film solar cells,” *Renew. Sustain. Energy Rev.*, vol.13, no. 9, pp. 2746–2750, 2009.
- [24] B. A. Andersson, “Materials availability for large-scale thin-film photovoltaics,” *Prog. Photovoltaics Res. Appl.*, vol. 8, no. 1, pp. 61–76, 2000.
- [25] B. Kippelen and J.L. Brédas, “Organic photovoltaics,” *Energy Environ. Sci.*, vol. 2, no. 3, pp. 251–261, 2009.
- [26] R. Venkatasubramanian, E. Siivola, T. Colpitts, and B. O’Quinn, “Thin-film thermoelectric devices with high room-temperature figures of merit,” *Nature.*, vol. 413, pp. 597–602, 2001.
- [27] C. Cho, B. Stevens, J.-H. Hsu, R. Bureau, D. A. Hagen, O. Regev, C. Yu, and J. C. Grunlan, “Completely organic multilayer thin film with thermoelectric power factor rivaling inorganic tellurides,” *Adv. Mater.*, vol. 27, no. 19, pp. 2996–3001, 2015.
- [28] M. Dawber, K. M. Rabe, and J. F. Scott, “Physics of thin-film ferroelectric oxides,” *Rev. Mod. Phys.*, vol. 77, pp. 1083–1130, 2005.
- [29] S. Horiuchi and Y. Tokura, “Organic ferroelectrics,” *Nat. Mater.*, vol. 7, pp. 357–366, 2008.
- [30] L. W. Martin and A. M. Rappe, “Thin-film ferroelectric materials and their applications,” *Nat. Rev. Mater.*, vol. 2, pp. 588–597, 2017.
- [31] M. Berggren, D. Nilsson, and N. D. Robinson, “Organic materials for printed electronics,” *Nat. Mater.*, vol. 6, pp. 3–5, 2007.
- [32] A. Kamysny and S. Magdassi, “Conductive Nanomaterials for Printed Electronics,” *Small.*, vol. 10, no. 17, 3515–3535, 2014.
- [33] Y. Xu, W. Zheng, X. Liu, L. Zhang, L. Zheng, C. Yang, N. Pinna, and J. Zhang, “Platinum single atoms on tin oxide ultrathin films for extremely sensitive gas detection,” *Mater. Horiz.*, vol. 7, no. 6, pp. 1519–1527, 2020.
- [34] B. Philip, J. K Abraham, A. Chandrasekhar, and V. K Varadan, “Carbon nanotube/PMMA composite thin films for gas-sensing applications,” *Smart Mater. Struct.*, vol. 2, no. 6, pp. 935–939, 2003.
- [35] C. Wöll, *Physical and Chemical Aspects of Organic Electronics*. John Wiley & Sons, 2009.

- [36] B. Jandeleit, D. J. Schaefer, T. S. Powers, H. W. Turner, and W. H. Weinberg, "Combinatorial materials science and catalysis," *Angew. Chem. Int. Ed.*, vol. 38, no. 22, pp. 2494–2532, 1999.
- [37] S. T. Beyer and K. Walus, "Controlled orientation and alignment in films of single-walled carbon nanotubes using inkjet printing," *Langmuir*, vol. 28, no. 23, pp. 8753–8759, 2012.
- [38] R. Potyrailo, K. Rajan, K. Stoewe, I. Takeuchi, B. Chisholm, and H. Lam, "Combinatorial and high-throughput screening of materials libraries: Review of state of the art," *ACS Comb. Sci.*, vol. 13, no. 6, pp. 579–633, 2011.
- [39] X. D. Xiang, X. Sun, G. Briceno, Y. Lou, K. A. Wang, H. Chang, W. G. Wallace-Freedman, S. W. Chen, and P. G. Schultz, "A Combinatorial Approach to Materials Discovery," *Science*, vol. 268, no. 5218, pp. 1738–1740, 1995.
- [40] E. L. First, M. M. Faruque Hasan, and C. A. Floudas, "Discovery of novel zeolites for natural gas purification through combined material screening and process optimization," *AIChE J.*, vol. 60, no. 5, pp. 1767–1785, 2014.
- [41] D. Wolf, O. V. Buyevskaya, and M. Baerns, "An evolutionary approach in the combinatorial selection and optimization of catalytic materials," *Appl. Catal., A*, vol. 200, no. 1–2, pp. 63–77, 2000.
- [42] R. B. Merrifield, "Solid Phase Peptide Synthesis. I. The Synthesis of a Tetrapeptide," *J. Am. Chem. Soc.*, vol. 85, no. 14, pp. 2149–2154, 1963.
- [43] J. E. M. Gordon, R. W. Barrett, W. J. Dower, S. P. A. Fodor, and M. A. Gallop, "Applications of combinatorial technologies to drug discovery. 2. combinatorial organic synthesis, library screening strategies, and future directions," *J. Med. Chem.*, vol. 37, no. 10, pp. 1385–1401, 1994.
- [44] D. J. Ecker and S. T. Crooke, "Combinatorial drug discovery: Which methods will produce the greatest value?" *Nat. Biotechnol.*, vol. 13, pp. 351–360, 1995.
- [45] S. Nelander, W. Wang, B. Nilsson, Q.-B. She, C. Pratilas, N. Rosen, P. Gennemark, and C. Sander, "Models from experiments: combinatorial drug perturbations of cancer cells," *Mol. Syst. Biol.*, vol. 4, pp. 216(1–11), 2008.
- [46] H. Koinuma and I. Takeuchi, "Combinatorial solid-state chemistry of inorganic materials," *Nat. Mater.*, vol. 3, pp. 429–438, 2004.

- [47] R. Hoogenboom, M. A. R. Meier, and U. S. Schubert, “Combinatorial methods, automated Synthesis and high-throughput screening in polymer research: Past and Present,” *Macromol. Rapid Commun.*, vol. 24, no. 1, pp. 15–32, 2003.
- [48] M. Varshney, Y. Li, B. Srinivasan, and S. Tung, “Combinatorial materials synthesis and screening: An integrated materials chip approach to discovery and optimization of functional materials,” *Annu. Rev. Mater. Sci.*, vol. 29, pp. 149–171, 1999.
- [49] F. Drolet and G. H. Fredrickson, “Combinatorial screening of complex block copolymer assembly with self-consistent field theory,” *Phys. Rev. Lett.*, vol. 83, no. 21, pp. 4317–4320, 1999.
- [50] C. G. Simon Jr. and S. Lin-Gibson, “Combinatorial and high-throughput screening of biomaterials,” *Adv. Mater.*, vol. 23, no. 3, pp. 369–387, 2011.
- [51] E. Danielson, J. H. Golden, E. W. McFarland, C. M. Reaves, W. H. Weinberg, and X. D. Wu, “A combinatorial approach to the discovery and optimization of luminescent materials,” *Nature*, vol. 389, no. 3, pp. 944–948, 1997.
- [52] P. Cong, R. D. Doolen, Q. Fan, D. M. Giaquinta, S. Guan, E. W. McFarland, D. M. Poojary, K. Self, H. W. Turner, and W. H. Weinberg, “High-throughput synthesis and screening of combinatorial heterogeneous catalyst libraries,” *Angew. Chem. Int. Ed.*, vol. 38, no. 4, pp. 483–488, 1999.
- [53] O. Ramström, L. Ye, and K. Mosbach, “Screening of a combinatorial steroid library using molecularly imprinted polymers,” *Proc. Natl. Acad. Sci.*, vol. 35, no. 1, pp. 9–11, 1998.
- [54] K. Kawashima, Y. Okamoto, O. Annayev, N. Toyokura, R. Takahashi, M. Lippmaa, K. Itaka, Y. Suzuki, N. Matsuki, and H. Koinuma, “Combinatorial screening of halide perovskite thin films and solar cells by mask-defined IR laser molecular beam epitaxy,” *Sci. Technol. Adv. Mater.*, vol. 18, no. 1, pp. 307–315, 2017.
- [55] Q. Wang, J. Perkins, H. M. Branz, J. Alleman, C. Duncan, and D. Ginley, “Combinatorial synthesis of solid state electronic materials for renewable energy applications,” *Appl. Surf. Sci.*, vol. 189, no. 3–4, pp. 271–276, 2002.
- [56] D. M. Mattox, “Physical vapor deposition (PVD) processes,” *Met. Finish.*, vol. 100, no. 1, pp. 394–408, 2002.

- [57] W. D. Sproul, “Physical vapor deposition tool coatings,” *Surf. Coat. Technol.*, vol. 81, no. 1, pp. 1–7, 1996.
- [58] S. Guerin and B. E. Hayden, “Physical vapor deposition method for the high-throughput synthesis of solid-state material libraries,” *J. Comb. Chem.*, vol. 8, no. 1, 8867(1–8), 2020.
- [59] J M Jasinski, B S Meyerson, and B A Scott, “Mechanistic studies of chemical vapor deposition,” *Annu. Rev. Phys. Chem.*, vol. 38, pp. 109–140, 1987.
- [60] J. O. Carlsson and P. M. Martin, “Chapter 7 - Chemical Vapor Deposition” in *Handbook of Deposition Technologies for Films and Coatings (Third Edition)*, pp. 314–363, 2010.
- [61] M. Kirschbaum, C. Guernth-Marschner, S. Cherré, A. de Pablo Peña, M. Jaeger, R. Kroczeck, T. Schnelle, T. Mueller, and C. Duschl, “Combinatorial chemical vapor deposition. Achieving compositional spreads of titanium, tin, and hafnium oxides by balancing reactor fluid dynamics and deposition kinetics,” *Chem. Mater.*, vol. 15, no. 1, pp. 292–298, 2003.
- [62] A. Kafizas and I. P. Perkin, “Combinatorial atmospheric pressure chemical vapor deposition (cAPCVD): a route to functional property optimization,” *J. Am. Chem. Soc.*, vol. 133, no. 50, pp. 20458–20467, 2011.
- [63] T. Fukumura, M. Ohtani, M. Kawasaki, Y. Okimoto, T. Kageyama, T. Koida, T. Hasegawa, Y. Tokura, and H. Koinuma “Rapid construction of a phase diagram of doped Mott insulators with a composition-spread approach,” *Appl. Phys. Lett.*, vol. 77, no. 21, pp. 3426–3428, 2000.
- [64] S. Siol, T. P. Dhakal, G. S. Gudavalli, P. P. Rajbhandari, C. Dehart, L. L. Baranowski, and A. Zakutayev, “Combinatorial reactive sputtering of In_2S_3 as an alternative contact layer for thin Film solar cells,” *ACS Appl. Mater. Interfaces.*, vol. 8, no. 22, pp. 14004–14011, 2016.
- [65] S. S. Mao, “High throughput growth and characterization of thin film materials,” *J. Cryst. Growth.*, vol. 379, no. 15, pp. 123–130, 2013.
- [66] A. Sánchez-Díaz, X. Rodríguez-Martínez, L. Córcoles-Guija, G. Mora-Martín, and Mariano Campoy-Quiles, “High-throughput multiparametric screening of solution processed bulk heterojunction solar cells,” *Adv. Electron. Mater.*, vol. 4, no. 10, pp. 1700477(1–13), 2018.

- [67] A. Teichler, R. Eckardt, S. Hoepfner, C. Friebe, J. Perelaer, A. Senes, M. Morana, C. J. Brabec, and U. S. Schubert, "Combinatorial Screening of Polymer:Fullerene Blends for Organic Solar Cells by Inkjet Printing," *Adv. Energy Mater.*, vol. 1, no. 1, pp. 105–114, 2011.
- [68] B. P. MacLeod, F. G. L. Parlange, T. D. Morrissey, F. Häse, L. M. Roch, K. E. Dettelbach, R. Moreira, L. P. E. Yunker, M. B. Rooney, J. R. Deeth, V. Lai, G. J. Ng, H. Situ, R. H. Zhang, M. S. Elliott, T. H. Haley, D. J. Dvorak, A. Aspuru-Guzik, J. E. Hein, and C. P. Berlinguette, "Self-driving laboratory for accelerated discovery of thin-film materials," *Sci. Adv.*, vol. 6, no. 20, pp. 231–245, 1997.
- [69] E. Reddington, A. Sapienza, B. Gurau, R. Viswanathan, S. Sarangapani, E. S. Smotkin, and T. E. Mallouk, "Combinatorial electrochemistry: A highly parallel, optical screening method for discovery of better electrocatalysts," *Science*, vol. 280, no. 5370, pp. 1735–1737, 1998.
- [70] M. Woodhouse and B. A. Parkinson, "Combinatorial approaches for the identification and optimization of oxide semiconductors for efficient solar photoelectrolysis," *Chem. Soc. Rev.*, vol. 38, no. 1, pp. 197–210, 2009.
- [71] Y. Yang, D. Bolikal, M. L. Becker, J. Kohn, D. N. Zeiger, and C. G. Simon Jr., "Combinatorial polymer scaffold libraries for screening cell-biomaterial interactions in 3D," *Adv. Mater.*, vol. 20, no. 11, pp. 2037–2043, 2008.
- [72] C. G. Simon Jr., J. S. Stephens, S. M. Dorsey, and M. L. becker., "Fabrication of combinatorial polymer scaffold libraries," *Rev. Sci. Instrum.*, vol. 78, no. 7, pp. 072207(1–8), 2007.
- [73] S. Sarntinoranont, Z. Xiang, K. A. Shedden, H. Markel, G. S. Omenn, B. D. Athey, and Y. He, "Ontology-based combinatorial comparative analysis of adverse events associated with killed and live influenza vaccines," *PLoS One.*, vol. 7, no. 11, pp. 49941(1–19), 2012.
- [74] A. L. Garske, S. S. Oliver, E. K. Wagner, C. A. Musselman, G. LeRoy, B. A. Garcia, T. G. Kutateladze, and J. M. Denu, "Combinatorial profiling of chromatin binding modules reveals multisite discrimination," *Nat. Chem. Biol.*, vol. 6, pp. 283–290, 2010.
- [75] C. G. Simon Jr., N. Eidelman, S. B. Kennedy, A. Sehgal, C. A. Khatia, and N. R. Washburn, "Combinatorial screening of cell proliferation on poly(L-lactic acid)-poly(D, L-lactic acid) blends," *Biomaterials.*, vol. 26, no. 34, pp. 6906–6915, 2005.

- [76] J. J. Green, G. T. Zugates, N. C. Tedford, Y.-H. Huang, L. G. Griffith, D. A. Lauffenburger, J. A. Sawicki, R. Langer, and D. G. Anderson, "Combinatorial Modification of Degradable Polymers Enables Transfection of Human Cells Comparable to Adenovirus," *Adv. Mater.*, vol. 19, no. 19, pp. 2836–2842, 2007.
- [77] N. Malo, J. A. Hanley, S. Cerquozzi, J. Pelletier, and Robert Nadon, "Statistical practice in high-throughput screening data analysis," *Nat. Biotechnol.*, vol. 24, pp. 167–175, 2006.
- [78] M. A. R. Meier, R. Hoogenboom, and U. S. Schubert, "Combinatorial methods, automated synthesis and high-throughput screening in polymer research: The evolution continues," *Macromol. Rapid Commun.*, vol. 25, no. 1, pp. 21–33, 2004.
- [79] J. C. Charpentier, "Process Intensification by Miniaturization," *Chem. Eng. Technol.*, vol. 28, no. 3, pp. 255–258, 2005.
- [80] R. B. van Dover, L. F. Schneemeyer, and R. M. Fleming, "Discovery of a useful thin-film dielectric using a composition-spread approach," *Nature*, vol. 392, pp. 162–164, 1998..
- [81] J. Wang, Y. Yoo, C. Gao, I. Takeuchi, X. Sun, H. Chang, X.-D. Xiang, and P. G. Schultz, "Identification of a blue photoluminescent composite material from a combinatorial library," *Science*, vol. 279, pp. 1712–1714, 1998.
- [82] V. Stadler, T. Felgenhauer, M. Beyer, S. Fernandez, K. Leibe, S. Güttler, M. Gröning, K. König, G. Torralba, M. Hausmann, V. Lindenstruth, A. Nesterov, I. Block, R. Pipkorn, A. Poustka, F. R. Bischoff, and F. Breitling, "Combinatorial Synthesis of Peptide Arrays with a Laser Printer," *Angew. Chemie Int. Ed.*, vol. 47, pp. 7132–7135, 2008.
- [83] M. T. Reetz, "Combinatorial and Evolution-Based Methods in the Creation of Enantioselective Catalysts," *Angew. Chemie Int. Ed.*, vol. 40, pp. 284–310, 2001.
- [84] M. H. Ohlmeyer, R. N. Swanson, L. W. Dillard, J. C. Reader, G. Asouline, R. Kobayashi, M. Wigler, and W. C. Still, "Complex synthetic chemical libraries indexed with molecular tags," *Proc. Natl. Acad. Sci.*, vol. 90, pp. 10922–10926, 1993.
- [85] L. M. Mayr and D. Bojanic, "Novel trends in high-throughput screening," *Curr. Opin. Pharmacol.*, vol. 9, no. 5, pp. 580–588, 2009.

- [86] P. Esling, F. Lejzerowicz, and J. Pawlowski, “Accurate multiplexing and filtering for high-throughput amplicon-sequencing,” *Nucleic Acids Res.*, vol. 43, no. 5, pp. 2513–2524, 2015.
- [87] J.-W. Lee, S. P. Singh, M. Kim, S. U. Hong, W. B. Park, and K.-S. Sohn, Metaheuristics-Assisted Combinatorial Screening of Eu²⁺-Doped Ca–Sr–Ba–Li–Mg–Al–Si–Ge–N Compositional Space in Search of a Narrow-Band Green Emitting Phosphor and Density Functional Theory Calculations. *Inorg. Chem.*, vol. 56, no. 16, pp. 9814–9824, 2017.
- [88] B. Meredig, A. Agrawal, S. Kirklin, J. E. Saal, J. W. Doak, A. Thompson, K. Zhang, A. Choudhary, and C. Wolverton, “Combinatorial screening for new materials in unconstrained composition space with machine learning,” *Phys. Rev. B.*, vol. 89, 94104(1–7), 2014.
- [89] V. C. Tung, M. J. Allen, Y. Yang, and R. B. Kaner, “High-throughput solution processing of large-scale graphene,” *Nat. Nanotechnol.*, vol. 4, pp. 25–29, 2009.
- [90] R. M. Pasquarelli, D. S. Ginley and R. O’Hayre, “Solution processing of transparent conductors: from flask to film,” *Chem. Soc. Rev.*, vol. 40, no. 11, pp. 5406–5441, 2011.
- [91] J. Y. Kim, K. Lee, N.E. Coates, D. Moses, T.Q. Nguyen, M. Dante, and A. J. Heeger, “Efficient tandem polymer solar cells fabricated by all-solution processing,” *Science*, vol. 317, no. 5835, pp. 222–225, 2007.
- [92] L. M. Cook, W. H. Lowdermilk, D. Milam, and J. E. Swain, “Antireflective surfaces for high-energy laser optics formed by neutral-solution processing,” *Appl. Opt.*, vol. 21, no. 8, pp. 1482–1485, 1982.
- [93] V. Kumar, V. Kumar, S. Som, A. Yousif, N. Singh, O. M. Ntwaeaborwa, A. Kapoor, and H. C. Swart, “Effect of annealing on the structural, morphological and photoluminescence properties of ZnO thin films prepared by spin coating,” *J. Colloid Interface Sci.*, vol. 428, no. 15, pp. 8–15, 2014.
- [94] K. Norrman, A. Ghanbari-Siahkalia, and N. B. Larsen, “Studies of spin-coated polymer films,” *Annu. Rep. Prog. Chem., Sect. C: Phys. Chem.*, vol. 101, pp. 174–201, 2005.
- [95] B.-J. de Gans, P. C. Duineveld, and U. S. Schubert, “Inkjet Printing of Polymers: State of the Art and Future Developments,” *Adv. Mater.*, vol. 16, no. 3, pp. 203–213, 2004.

- [96] P. Calvert, “Inkjet printing for materials and devices,” *Chem. Mater.*, vol. 13, no. 10, pp. 3299–3305, 2001.
- [97] P. Sitthi-Amorn, J. E. Ramos, Y. Wangy, J. Kwan, J. Lan, W. Wang, and W. Matusik, “MultiFab: a machine vision assisted platform for multi-material 3D printing,” *ACM Trans. Graphics*, vol. 34, no. 4, pp. 129(1–11), 2015.
- [98] H. Sirringhaus, T. Kawase, R. H. Friend, T. Shimoda, M. Inbasekaran, W. Wu, and E. P. Woo, “High-Resolution Inkjet Printing of All-Polymer Transistor Circuits,” *Science*, vol. 290, no. 5499, pp. 2123–2126, 2000.
- [99] H. Sirringhaus and T. Shimoda, “Inkjet printing of functional materials,” *MRS Bulletin*, pp. 802–806, 2003.
- [100] C. N. Hoth, S. A. Choulis, P. Schilinsky, and C. J. Brabec, “High photovoltaic performance of inkjet printed polymer:Fullerene blends,” *Adv. Mater.*, vol. 19, no. 22, pp. 3973–3978, 2007.
- [101] R. E. Saunders, B. Derby, R. Elizabeth, B. Derby, R. E. Saunders, and B. Derby, “Inkjet printing biomaterials for tissue engineering : bioprinting Inkjet printing biomaterials for tissue engineering : bioprinting,” *Int. Mater. Rev.*, vol. 59, no. September, pp. 430–448, 2017.
- [102] S. T. Beyer and K. Walus, “Controlled orientation and alignment in films of single-walled carbon nanotubes using inkjet printing,” *Langmuir.*, vol. 28, no. 23, pp. 8753–8759, 2012.
- [103] A. V. Lemmo, J. T. Fisher, H. M. Geysen, and D. J. Rose, “Characterization of an inkjet chemical microdispenser for combinatorial library synthesis,” *Anal. Chem.*, vol. 69, no. 4, pp. 543–551, 1997.
- [104] I. A. Grimaldi, A. De Girolamo Del Mauro, F. Loffredo, G. Nenna, F. Villani, and C. Minarini, “Microlens array manufactured by inkjet printing: study of the effects of the solvent and the polymer concentration on the microstructure shape,” *Proc. SPIE 8082, Optical Measurement Systems for Industrial Inspection VII*, 2011.
- [105] Y. Yoshioka and G. E. Jabbour, “Inkjet printing of oxidants for patterning of nanometer-thick conducting polymer electrodes,” *Adv. Mater.*, vol. 18, no. 10, pp. 1307–1312, 2006.
- [106] M. M. Mohebi and J. R. G. Evans, “A drop-on-demand ink-jet printer for combinatorial libraries and functionally graded ceramics,” *J. Comb. Chem.*, vol. 4, no. 4, pp. 267–274, 2002.

- [107] A. Bsoul, S. Pan, E. Cretu, B. Stoeber, and K. Walus, “Design, microfabrication, and characterization of a moulded PDMS/SU-8 inkjet dispenser for a Lab-on-a-Printer platform technology with disposable microfluidic chip,” *Lab Chip.*, vol. 16, no. 17, pp. 3351–3361, 2016.
- [108] C. K. Chiang, C. R. Fincher, Jr., Y. W. Park, A. J. Heeger, H. Shirakawa, E. J. Louis, S. C. Gau, and A. G. MacDiarmid, “Electrical conductivity in doped polyacetylene,” *Phys. Rev. Lett.*, vol. 38, pp. 1098–1101, 1977.
- [109] A. H. Koezuka, A. Tsumura, and T. Ando, “Field-effect transistor with polythiophene thin film,” *Synth. Met.*, vol. 18, no. 1–3, pp. 699–704, 1987.
- [110] G. Tourillon and F. Garnier, “Effect of dopant on the physicochemical and electrical properties of organic conducting polymers,” *J. Phys. Chem.*, vol. 87, pp. 2289–2292, 1983.
- [111] L. D. Shu, W. He, and S. Li, “Internet of Things in Industries: A Survey,” *IEEE Trans. Ind. Inf.*, vol. 10, no. 4, pp. 2233–2243, 2014.
- [112] G. A. Salvatore, J. Sülzle, F. Dalla Valle, G. Cantarella, F. Robotti, P. Jokic, S. Knobelspies, A. Daus, L. Büthe, L. Petti, N. Kirchgessner, R. Hopf, M. Magno, and G. Tröster, “Biodegradable and highly deformable temperature sensors for the internet of things,” *Adv. Funct. Mater.*, vol. 27, no. 35, pp. 976–987, 2006.
- [113] S. Santra, G. Hu, R. C. T. Howe, A. De Luca, S. Z. Ali, F. Udrea, J. W. Gardner, S. K. Ray, P. K. Guha, and T. Hasan, “CMOS integration of inkjet-printed graphene for humidity sensing,” *Sci. Rep.*, vol. 5, pp. 17374(1–12), 2015.
- [114] D. Briand, F. Molina-Lopez, A. V. Quintero, G. Mattana, and Nico F. de Rooij, “Printed sensors on smart RFID labels for logistics,” *IEEE International NEWCAS Conference.*, pp. 449–452, 2012.
- [115] NSERC Green Electronics Network (GreEN) proposal, 2018.
- [116] A. Elschner, S. Kirchmeyer, W. Lövenich, U. Merker, and K. Reuter, “PEDOT: Principles and Applications of an Intrinsically Conductive Polymer,” *CRC Press*, 2010.
- [117] V. K. Rao R., V. A. K., Karthik P. S., and S. P. Singh, “Conductive silver inks and their applications in printed and flexible electronics,” *RSC Adv.*, vol. 5, no. 95, pp. 77760–77790, 2015.

- [118] M. Grouchko, A. Kamyshny, C. F. Mihailescu, D. F. Anghel, and S. Magdassi, “Conductive inks with a “built-in” mechanism that enables sintering at room temperature,” *ACS Nano.*, vol. 5, no. 4, pp. 3354–3359, 2011.
- [119] Creative Materials printable silver inks (<https://www.creativematerials.com/products/silver-inks/>).
- [120] Novacentrix inkjet printable silver inks (<https://www.novacentrix.com/inkjet-conductive-inks/>).
- [121] Sigma-Aldrich PEDOT:PSS [Poly(3,4-ethylenedioxythiophene)-poly(styrenesulfonate)] (<https://www.sigmaaldrich.com/CA/en/product/aldrich/739324>).
- [122] Ossila PEDOT:PSS [Poly(3,4-ethylenedioxythiophene)-poly(styrenesulfonate)] (<https://www.ossila.com/en-ca/products/pedot-pss?variant=30366225268832>).
- [123] Nanoshel PEDOT:PSS [Poly(3,4-ethylenedioxythiophene)-poly(styrenesulfonate)] (<https://www.nanoshel.com/product/pedot-pss>).
- [124] O. N. Mryasov and A. J. Freeman, “Electronic band structure of indium tin oxide and criteria for transparent conducting behavior,” *Phys. Rev. B.*, vol. 64, pp. 238–246, 2005.
- [125] Y. Yoshioka and G. E. Jabbour, “Inkjet printing of oxidants for patterning of nanometer-thick conducting polymer electrodes,” *Adv. Mater.*, vol. 18, no. 10, pp. 2331–2333, 2001.
- [126] H. Baltes, O. Brand, A. Hierlemann, D. Lange, and C. Hagleitner, “CMOS MEMS – Present and Future,” *IEEE International Conference on Micro Electro Mechanical Systems. (MEMS)*, pp. 459–466, 2002.
- [127] R. R. Mansour, “RF MEMS-CMOS Device Integration,” *IEEE Microwave Magazine.*, pp. 39–56, 2013.
- [128] T. Thorsen, S. J. Maerkl and S. R. Quake, “Microfluidic large-scale integration,” *Science*, vol. 298, no. 5593, pp. 1059–1062, 2002.
- [129] P. N. Nge, C. I. Rogers, and A. T. Woolley, “Advances in microfluidic materials, functions, integration, and applications,” *Chem. Rev.*, vol. 113, no. 4, pp. 2550–2583, 2013.

- [130] A. J. Hughes, R. K. C. Lin, D. M. Peele, and A. E. Herr, "Microfluidic integration for automated targeted proteomic assays," *Proc. Natl. Acad. Sci. U.S.A.*, vol. 109, no. 16, pp. 5972–5977, 2012.
- [131] J. H. Lee and J. R. Allebach, "Inkjet printer model-based halftoning," *IEEE International Conference on Image Processing*, pp. 461–464, 2002.
- [132] P. Wägli, B. Y. Guélat, A. Homsy, and N. F. de Rooij, "Microfluidic devices made of UV-curable glue (NOA81) for fluorescence detection based applications," *International Conference on Miniaturized Systems for Chemistry and Life Sciences (μ TAS)*, pp. 1937–1939, 2010.
- [133] O. Kašpar, A. H. Koyuncu, A. Pittermannová, P. Ulbrich, and V. Tokárová, "Governing factors for preparation of silver nanoparticles using droplet-based microfluidic device," *Biomed. Microdevices.*, vol. 21, no.88, pp. 461–464, 2019.
- [134] A. Ayoib, U. Hashim, M. K. Md. Arshad, and V. Thivina, "Soft lithography of microfluidics channels using SU-8 mould on glass substrate for low cost fabrication," *IEEE EMBS Conference on Biomedical Engineering and Sciences (IECBES)*, pp. 226–229, 2016.
- [135] K. Raj. M and S. Chakraborty, "PDMS microfluidics: A mini review," *J. Appl. Polym. Sci.*, vol. 137, no. 27, pp. 48958(1–14), 2020.
- [136] T. Fujii, "PDMS-based microfluidic devices for biomedical applications," *Microelectron. Eng.*, vol. 61–62, pp. 907–914, 2002.
- [137] S. Oberti, A. Neild, and T. W. Ng, "Microfluidic mixing under low frequency vibration," *Lab Chip*, vol. 9, no. 10, pp. 1435–1438, 2009.
- [138] Z. Yang, S. Matsumoto, H. Goto, M. Matsumoto, and R. Maeda, "Ultrasonic micromixer for microfluidic systems," *Sens. Actuators, A.*, vol. 93, no. 3, pp. 266–272, 2001.
- [139] I. Shah, S. W. Kim, K. Kim, Y. H. Doh and K. H. Choi, "Experimental and numerical analysis of Y-shaped split and recombination micro-mixer with different mixing units," *Chem. Eng. J.*, vol. 358, pp. 691–706, 2019.
- [140] L. Capretto, W. Cheng, M. Hill and X. Zhang, "Micromixing in microfluidic devices," *Top. Curr. Chem.*, vol. 304, pp. 27–68, 2011.

- [141] M. Bayareh, M. N. Ashani and A. Usefian, “Active and passive micromixers: A comprehensive review,” *Chem. Eng. Process.*, vol. 147, pp. 107771(1–19), 2020.
- [142] K. Ward and Z. Hugh Fan, “Mixing in microfluidic devices and enhancement methods,” *J Micromech. Microeng.*, vol. 25, pp. 094004(1–17), 2015.
- [143] E. A. Mansur, Y. E. Mingxing, W. Yundong and D. Youyuan, “A state-of-the-art review of mixing in microfluidic mixers,” *Chin. J Chem. Eng.*, vol. 16, pp. 503–516, 2008.
- [144] Y. Liu and B. Derby, “Experimental study of the parameters for stable drop-on-demand inkjet performance,” *Phys. Fluids.*, vol. 31, pp. 032004(1–11), 2019.
- [145] Momentive RTV-615 silicone rubber technical data sheet (<https://www.momentive.com/en-us/products/tds/rtv615?productId=64616a84-08ff-4372-a2a2-a58eb45be627>).
- [146] S. H. Cho, S. R. White, and P. V Braun, “Self-Healing Polymer Coatings,” *Adv. Mater.*, vol. 21, no. 6, pp. 645–649, 2009.
- [147] T. Konno, J. Watanabe, and K. Ishihara, “Enhanced solubility of paclitaxel using water-soluble and biocompatible 2-methacryloyloxyethyl phosphorylcholine polymers,” *J. Biomed. Mater. Res. Part A.*, vol. 65A, no. 2, pp. 209–214, 2003.
- [148] H. Shi, C. Liu, Q. Jiang, and J. Xu, “Effective Approaches to Improve the Electrical Conductivity of PEDOT:PSS: A Review,” *Adv. Electron. Mater.*, vol. 1, no. 4, pp. 1500017(1–16), 2015.
- [149] R. W. Cooksey, “Descriptive Statistics for Summarising Data,” in *Illustrating Statistical Procedures: Finding Meaning in Quantitative Data.*, Springer, 2020.
- [150] G. F. Reed, F. Lynn, and B. D. Meade, “Use of coefficient of variation in assessing variability of quantitative assays,” *Clin. Vaccine Immunol.*, vol. 9, no. 6, pp. 1235–1239, 2002.
- [151] O. Schechtman, “The coefficient of variation as an index of measurement reliability,” in *Methods of Clinical Epidemiology, Springer Series on Epidemiology and Public Health*, 2013.
- [152] Statistics 203: Introduction to Regression and Analysis of Variance [ANOVA: Fixed Effects] (<https://statweb.stanford.edu/~jtaylo/courses/stats203/notes/anova.fixed.pdf>).
- [153] D. C. Montgomery, “Design and Analysis of Experiments,” 10th edition, *Wiley Publishing*, 2017.

- [154] F. N. David and N. L. Johnson, “The effect of non-normality on the power function of the F-test in the analysis of variance,” *Biometrika.*, vol. 38, no. 1–2, pp. 43–57, 1951.
- [155] S. Labovitz, “Criteria for selecting a significance level: A note on the sacredness of. 05,” *Am. Sociol. The.*, vol. 3, no. 3, 220–222, pp. , 1968.
- [156] S. S. Shapiro and M. B. Wilk, “An analysis of variance test for normality (complete samples),” *Biometrika*, vol. 52, no. 3–4, pp. 591–611, 1965.
- [157] G. V. Glass, “Testing homogeneity of variances,” *Am. Educ. Res. J.*, vol. 3, no. 3, pp. 187–190, 1966.
- [158] J. K. Brewer, “Effect size: The most troublesome of the hypothesis testing considerations,” *CEDR Quarterly*, vol. 11, no. 4, pp. 7–10, 1978.
- [159] E. L. Lehmann, “Significance level and power,” *Ann. Math. Statist.*, vol. 29, no. 4, pp. 1167–1176, 1958.
- [160] C. W. Dunnett, “Pairwise multiple comparisons in the homogeneous variance, unequal sample size case,” *J. Am. Stat. Assoc.*, vol. 75, no. 372, pp. 789–795, 1980.
- [161] P. A. Games and J. F. Howell, “Pairwise multiple comparison procedures with unequal n's and/or variances: a Monte Carlo study,” *J. Educ. Behav. Stat.*, vol. 1, no. 2, pp. 113–125, 1976.
- [162] SBQMI Advanced Nanofabrication Facility Bruker DEKTAK XT stylus-based profilometer (<https://www.nanofab.ubc.ca/equipment/analysis/dektak-150-profilometer-with-3d-capability-and-imaging/>).
- [163] K. Jain, A. Y. Mehandzhiysky, I. Zozoulenko and L. Wågberg “PEDOT:PSS nano-particles in aqueous media: A comparative experimental and molecular dynamics study of particle size, morphology and z-potential,” *J. Colloid Interface Sci.*, vol.584, pp. 57–66, 2021.
- [164] J. Stetefeld, S. A. McKenna, and T. R. Patel, “Dynamic light scattering: a practical guide and applications in biomedical sciences,” *Biophys. Rev.*, vol. 8, pp. 409–427, 2016.
- [165] B. E. Warren, “X-ray Diffraction,” *Dover Publications Inc.*, 1990.
- [166] Anton-Paar Wiki: How To Measure Viscosity (<https://wiki.anton-paar.com/ca-en/how-to-measure-viscosity/>).

- [167] Biolin Scientific white paper (<https://www.biolinscientific.com/hubfs/Pdf/Attension/White-papers-case-studies/surface-and-interfacial-tension-what-is-it-and-how-to-measure-it.pdf?hsLang=en>).
- [168] C. Beaumont, J. Turgeon, M. Idir, D. Neusser, R. Lapointe, S. Caron, W. Dupont, D. D'Astous, S. Shamsuddin, S. Hamza, É. Landry, S. Ludwigs and M. Leclerc, "Water-processable self-doped conducting polymers via direct (hetero)arylation polymerization," *Macromolecules*, vol. 54, no. 12, pp. 5464–5472, 2021.
- [169] H. Yano, K. Kudo, K. Marumo, and H. Okuzaki, "Fully soluble self-doped poly(3,4-ethylenedioxythiophene) with an electrical conductivity greater than 1000 S cm^{-1} ," *Sci. Adv.*, vol. 5, no. 4, pp. 9492(1–12), 2019.
- [170] J. Ouyang, Q. Xu, C. W. Chu, Y. Yang, G. Li, and J. Shinar, "On the mechanism of conductivity enhancement in poly(3,4-ethylenedioxythiophene):poly(styrene sulfonate) film through solvent treatment," *Polymer*, vol. 45, no. 25, pp. 8443–8450, 2004.
- [171] I. Cruz-Cruz, M. Reyes-Reyes, M. A. Aguilar-Frutis, A. G. Rodriguez, and R. López-Sandoval, "Study of the effect of DMSO concentration on the thickness of the PSS insulating barrier in PEDOT:PSS thin films," *Synth. Met.*, vol. 160, no. 13–14, pp. 1501–1506, 2010.
- [172] R. Rosenthal and D. B. Rubin, "Meta-analytic procedures for combining studies with multiple effect sizes," *Psychol. Bull.*, vol. 99, pp. 400–406, 1986.
- [173] X. Crispin, F. L. E. Jakobsson, A. Crispin, P. C. M. Grim, P. Andersson, A. Volodin, C. van Haesendonck, M. Van der Auweraer, W. R. Salaneck, and M. Berggren "The origin of the high conductivity of poly(3,4-ethylenedioxythiophene)–poly(styrenesulfonate) (PEDOT–PSS) plastic electrodes," *Chem. Mater.*, vol. 18, no. 18, 4354–4360, 2006.
- [174] N. F. Mott, "Conduction in non-crystalline materials," *Philos. Mag.*, vol. 19, no. 8, pp. 835–852, 1968.
- [175] J. Ouyang, C.-W. Chu, F.-C. Chen, Q. Xu, and Y. Yang, "High-conductivity poly (3, 4-ethylenedioxythiophene): poly (styrene sulfonate) film and its application in polymer optoelectronic devices," *Adv. Funct. Mater.*, vol. 15, no. 2, pp. 203–208, 2005.
- [176] L. B. Kish, "End of Moore's law: thermal (noise) death of integration in micro and nano electronics," *Phys. Lett. A*, vol. 305, no. 3–4, pp. 144–149, 2002.

[177] J. Zhou, D. H. Anjum, L. Chen, X. Xu, I. A. Ventura, L. Jiang, and G. Lubineau, “The temperature-dependent microstructure of PEDOT/PSS films: insights from morphological, mechanical and electrical analyses,” *J. Mater. Chem. C*, vol. 2, no. 46, pp. 9903–9910, 2014.

Appendix A

ANOVA and associated tables from Case Study 1

Table A1: Levene's test for homoscedasticity of $P1$ layer count data including extreme outliers.

Basis	Levene statistic	DOF 1	DOF 2	p -value
Based on Mean	1.441	3	56	0.241
Based on Median	0.959	3	56	0.419

Table A2: ANOVA test for layer count study of $P1$ with including extreme outliers.

Sources of variation	Sum of squares	DOF	Mean squares	F_0 value	p -value	$\eta^2_{partial}$	$1 - \beta$
Layers	1.422	3	0.474	2.849	0.046	0.132	0.652
Error	9.321	56	0.166				
Total	10.743	59					

Table A3: Tukey-Kramer test for layer count study of $P1$ with including extreme outliers.

(I) Layers	(J) Layers	Mean Difference (I-J)	Std. Error	p -value
5	10	-0.1362	0.148967	0.797
	15	-0.26617	0.148967	0.29
	20	-0.415547	0.148967	0.035
10	5	0.1362	0.148967	0.797
	15	-0.12997	0.148967	0.819
	20	-0.279346	0.148967	0.25
15	5	0.26617	0.148967	0.29
	10	0.12997	0.148967	0.819
	20	-0.149376	0.148967	0.748
20	5	0.415547	0.148967	0.035
	10	0.279346	0.148967	0.25
	15	0.149376	0.148967	0.748

Table A4: Levene's test for homoscedasticity of $P1$ layer count data excluding extreme outliers.

Basis	Levene statistic	DOF 1	DOF 2	p-value
Based on Mean	1.020	3	42	0.393
Based on Median	0.637	3	42	0.595

Table A5: ANOVA test for layer count study of $P1$ with excluding extreme outliers.

Sources of variation	Sum of squares	DOF	Mean squares	F_0 value	p-value	$\eta^2_{partial}$	$1 - \beta$
Layers	0.909	3	0.303	1.943	0.137	0.122	0.466
Error	6.548	42	0.156				
Total	7.457	45					

Table A6: Tukey-Kramer test for layer count study of $P1$ with excluding extreme outliers.

(I) Layers	(J) Layers	Mean Difference (I-J)	Std. Error	p-value
5	10	-0.078825	0.174117	0.969
	15	-0.241099	0.174117	0.516
	20	-0.366474	0.1712229	0.157
10	5	0.078825	0.174117	0.969
	15	-0.162274	0.161201	0.746
	20	-0.287649	0.1580706	0.279
15	5	0.241099	0.174117	0.516
	10	0.162274	0.161201	0.746
	20	-0.125375	0.1580706	0.857
20	5	0.366474	0.1712229	0.157
	10	0.287649	0.1580706	0.279
	15	0.125375	0.1580706	0.857

Table A7: Levene's test for homoscedasticity of $P2$ layer count data including extreme outliers.

Basis	Levene statistic	DOF 1	DOF 2	p-value
Based on Mean	0.522	3	56	0.669
Based on Median	0.169	3	56	0.917

Table A8: ANOVA test for layer count study of $P2$ with including extreme outliers.

Sources of variation	Sum of squares	DOF	Mean squares	F_0 value	p-value	$\eta^2_{partial}$	$1 - \beta$
Layers	0.019	3	0.006	0.721	0.544	0.037	0.194
Error	0.49	56	0.009				
Total	0.509	59					

Table A9: Tukey-Kramer test for layer count study of $P2$ with including extreme outliers.

(I) Layers	(J) Layers	Mean Difference (I-J)	Std. Error	p-value
5	10	-0.044592	0.0341703	0.564
	15	-0.006823	0.0341703	0.997
	20	-0.005098	0.0341703	0.999
10	15	0.037769	0.0341703	0.688
	20	0.039495	0.0341703	0.657
	5	0.044592	0.0341703	0.564
15	10	-0.037769	0.0341703	0.688
	20	0.001725	0.0341703	1.000
	5	0.006823	0.0341703	0.997
20	10	-0.039495	0.0341703	0.657
	15	-0.001725	0.0341703	1.000
	5	0.005098	0.0341703	0.999

Table A10: Levene's test for homoscedasticity of $P2$ layer count data excluding extreme outliers.

Basis	Levene statistic	DOF 1	DOF 2	p-value
Based on Mean	0.745	3	54	0.530
Based on Median	0.164	3	54	0.920

Table A11: ANOVA test for layer count study of $P2$ with excluding extreme outliers.

Sources of variation	Sum of squares	DOF	Mean squares	F_0 value	p-value	$\eta^2_{partial}$	$1 - \beta$
Process	0.014	3	.005	0.560	0.644	0.030	0.158
Error	0.446	54	.008				
Total	0.460	58					

Table A12: Tukey-Kramer test for layer count study of $P2$ with excluding extreme outliers.

(I) Process	(J) Process	Mean Difference (I-J)	Std. Error	p-value
5	10	-0.034517	0.0337704	0.737
	15	-0.007242	0.0343477	0.997
	20	0.004978	0.0337704	0.999
10	15	0.027275	0.0337704	0.851
	20	0.039495	0.0331831	0.636
	5	0.034517	0.0337704	0.737
15	10	-0.027275	0.0337704	0.851
	20	0.012220	0.0337704	0.984
	5	0.007242	0.0343477	0.997
20	10	-0.039495	0.0331831	0.636
	15	-0.012220	0.0337704	0.984
	5	-0.004978	0.0337704	0.999

ANOVA and associated tables from Case Study 2

90/10 comparison

Table A13: Levene's test for homoscedasticity of PM, UM, OM data including extreme outliers.

Basis	Levene statistic	DOF 1	DOF 2	<i>p</i> -value
Based on Mean	0.029	2	42	0.972
Based on Median	0.023	2	42	0.977

Table A14: ANOVA test for study of PM, UM, OM data including extreme outliers.

Sources of variation	Sum of squares	DOF	Mean squares	F_0 value	<i>p</i> -value	$\eta^2_{partial}$	$1 - \beta$
Process	23429.047	2	11714.524	6.104	0.005	0.225	0.864
Error	80601.668	42	1919.087				
Total	104030.715	44					

Table A15: Tukey-Kramer test for study of PM, UM, OM data including extreme outliers.

(I) Process	(J) Process	Mean Difference (I-J)	Std. Error	<i>p</i> -value
OM	PM	4.74634051	15.996196745	1.000
	UM	50.60188500	15.996196745	0.009
PM	OM	-4.74634051	15.996196745	1.000
	UM	45.85554449	15.996196745	0.019
UM	OM	-50.60188500	15.996196745	0.009
	PM	-45.85554449	15.996196745	0.019

Table A16: Levene's test for homoscedasticity of PM, UM, OM data excluding extreme outliers.

Basis	Levene statistic	DOF 1	DOF 2	<i>p</i>-value
Based on Mean	0.436	2	39	0.650
Based on Median	0.190	2	39	0.828

Table A17: ANOVA test for study of PM, UM, OM data excluding extreme outliers.

Sources of variation	Sum of squares	DOF	Mean squares	F_0 value	<i>p</i>-value	$\eta^2_{partial}$	$1 - \beta$
Process	18798.097	2	9399.048	5.528	0.008	0.221	0.824
Error	66315.542	39	1700.399				
Total	85113.638	41					

Table A18: Tukey-Kramer test for study of PM, UM, OM data excluding extreme outliers.

(I) Process	(J) Process	Mean Difference (I-J)	Std. Error	<i>p</i>-value
OM	PM	11.5439	15.32374	0.733
	UM	50.5435	15.88260	0.008
PM	OM	-11.5439	15.32374	0.733
	UM	38.9997	15.62561	0.044
UM	OM	-50.5435	15.88260	0.008
	PM	-38.9997	15.62561	0.044

80/20 comparison

Table A19: Levene's test for homoscedasticity of PM, UM, OM data including extreme outliers.

Basis	Levene statistic	DOF 1	DOF 2	<i>p</i> -value
Based on Mean	.336	2	42	0.717
Based on Median	.361	2	42	0.699

Table A20: ANOVA test for study of PM, UM, OM data including extreme outliers.

Sources of variation	Sum of squares	DOF	Mean squares	F_0 value	<i>p</i> -value	$\eta^2_{partial}$	$1 - \beta$
Process	20231.407	2	10115.703	4.502	0.017	0.177	0.739
Error	94363.555	42	2246.751				
Total	114594.962	44					

Table A21: Tukey-Kramer test for study of PM, UM, OM data including extreme outliers.

(I) Process	(J) Process	Mean Difference (I-J)	Std. Error	<i>p</i> -value
OM	PM	41.96875296	17.307999389	0.051
	UM	-5.51295331	17.307999389	0.946
PM	OM	-41.96875296	17.307999389	0.051
	UM	-47.48170627	17.307999389	0.024
UM	OM	5.51295331	17.307999389	0.946
	PM	47.48170627	17.307999389	0.024

Table A22: Levene's test for homoscedasticity of PM, UM, OM data excluding extreme outliers.

Basis	Levene statistic	DOF 1	DOF 2	<i>p</i>-value
Based on Mean	0.601	2	40	.553
Based on Median	0.680	2	40	.513

Table A23: ANOVA test for study of PM, UM, OM data excluding extreme outliers.

Sources of variation	Sum of squares	DOF	Mean squares	F_0 value	<i>p</i>-value	$\eta^2_{partial}$	$1 - \beta$
Process	25942.104	2	12971.052	6.806	0.003	0.254	0.899
Error	76230.174	40	1905.754				
Total	102172.278	42					

Table A24: Tukey-Kramer test for study of PM, UM, OM data excluding extreme outliers.

(I) Process	(J) Process	Mean Difference (I-J)	Std. Error	<i>p</i>-value
OM	PM	48.3398	16.22269	0.013
	UM	-5.9065	16.50002	0.932
PM	OM	-48.3398	16.22269	0.013
	UM	-54.2463	16.22269	0.005
UM	OM	5.9065	16.50002	0.932
	PM	54.2463	16.22269	0.005

70/30 comparison

Table A25: Levene's test for homoscedasticity of PM, UM, OM data including extreme outliers.

Basis	Levene statistic	DOF 1	DOF 2	<i>p</i> -value
Based on Mean	6.617	2	42	0.003
Based on Median	2.402	2	42	0.103

Table A26: ANOVA test for study of PM, UM, OM data including extreme outliers.

Sources of variation	Sum of squares	DOF	Mean squares	F_0 value	<i>p</i> -value	$\eta^2_{partial}$	$1 - \beta$
Process	53614.248	2	26807.124	11.074	0.000	0.345	0.987
Error	101670.503	42	2420.726				
Total	155284.751	44					

Table A27: Games-Howell test for study of PM, UM, OM data including extreme outliers.

(I) Process	(J) Process	Mean Difference (I-J)	Std. Error	<i>p</i> -value
OM	PM	52.27061493	17.965619959	0.017
	UM	-31.41694659	17.965619959	0.263
PM	OM	-52.27061493	17.965619959	0.017
	UM	-83.68756152	17.965619959	0.000
UM	OM	31.41694659	17.965619959	0.263
	PM	83.68756152	17.965619959	0.000

Table A28: Levene's test for homoscedasticity of PM, UM, OM data excluding extreme outliers.

Basis	Levene statistic	DOF 1	DOF 2	<i>p</i>-value
Based on Mean	5.900	2	41	0.006
Based on Median	2.670	2	41	0.081

Table A29: ANOVA test for study of PM, UM, OM data excluding extreme outliers.

Sources of variation	Sum of squares	DOF	Mean squares	F_0 value	<i>p</i>-value	$\eta^2_{partial}$	$1 - \beta$
Process	62042.227	2	31021.113	14.658	0.000	0.417	0.998
Error	86766.670	41	2116.260				
Total	148808.897	43					

Table A30: Games-Howell test for study of PM, UM, OM data excluding extreme outliers.

(I) Process	(J) Process	Mean Difference (I-J)	Std. Error	<i>p</i>-value
OM	PM	52.2706	16.79786	0.009
	UM	-39.8414	17.09519	0.063
PM	OM	-52.2706	16.79786	0.009
	UM	-92.1120	17.09519	0.000
UM	OM	39.8414	17.09519	0.063
	PM	92.1120	17.09519	0.000

60/40 comparison

Table A31: Levene's test for homoscedasticity of PM, UM, OM data.

Basis	Levene statistic	DOF 1	DOF 2	<i>p</i> -value
Based on Mean	2.250	2	42	0.118
Based on Median	2.188	2	42	0.125

Table A32: ANOVA test for study of PM, UM, OM data.

Sources of variation	Sum of squares	DOF	Mean squares	F_0 value	<i>p</i> -value	$\eta^2_{partial}$	$1 - \beta$
Process	15704.115	2	7852.058	10.182	0.000	0.327	0.980
Error	32390.209	42	771.195				
Total	48094.324	44					

Table A33: Tukey-Kramer test for study of PM, UM, OM data.

(I) Process	(J) Process	Mean Difference (I-J)	Std. Error	<i>p</i> -value
OM	PM	-34.59472114	10.140318543	0.004
	UM	-43.23604751	10.140318543	0.000
PM	OM	34.59472114	10.140318543	0.004
	UM	-8.64132636	10.140318543	1.000
UM	OM	43.23604751	10.140318543	0.000
	PM	8.64132636	10.140318543	1.000

50/50 comparison

Table A34: Levene's test for homoscedasticity of PM, UM, OM data.

Basis	Levene statistic	DOF 1	DOF 2	<i>p</i> -value
Based on Mean	0.841	2	42	0.438
Based on Median	0.377	2	42	0.689

Table A35: ANOVA test for study of PM, UM, OM data.

Sources of variation	Sum of squares	DOF	Mean squares	F_0 value	<i>p</i> -value	$\eta^2_{partial}$	$1 - \beta$
Process	7686.119	2	3843.060	4.118	0.023	0.164	0.698
Error	39193.787	42	933.185				
Total	46879.906	44					

Table A36: Tukey-Kramer test for study of PM, UM, OM data.

(I) Process	(J) Process	Mean Difference (I-J)	Std. Error	<i>p</i> -value
OM	PM	30.84617411	11.154582879	0.022
	UM	8.00708553	11.154582879	0.754
PM	OM	-30.84617411	11.154582879	0.022
	UM	-22.83908857	11.154582879	0.113
UM	OM	-8.00708553	11.154582879	0.754
	PM	22.83908857	11.154582879	0.113

98/02 comparison

Table A37: Levene's test for homoscedasticity of PM, UM, OM data including extreme outliers.

Basis	Levene statistic	DOF 1	DOF 2	<i>p</i>-value
Based on Mean	8.766	2	42	0.001
Based on Median	1.392	2	42	0.260

Table A38: ANOVA test for study of PM, UM, OM data including extreme outliers.

Sources of variation	Sum of squares	DOF	Mean squares	F_0 value	<i>p</i>-value	$\eta^2_{partial}$	$1 - \beta$
Process	1847.276	2	923.638	1.172	0.320	0.053	0.243
Error	33088.807	42	787.829				
Total	34936.083	44					

Table A39: Games-Howell test for study of PM, UM, OM data including extreme outliers.

(I) Process	(J) Process	Mean Difference (I-J)	Std. Error	<i>p</i>-value
OM	PM	6.0431	10.24909	1.000
	UM	-9.5219	10.24909	1.000
PM	OM	-6.0431	10.24909	1.000
	UM	-15.5650	10.24909	0.409
UM	OM	9.5219	10.24909	1.000
	PM	15.5650	10.24909	0.409

Table A40: Levene's test for homoscedasticity of PM, UM, OM data excluding extreme outliers.

Basis	Levene statistic	DOF 1	DOF 2	<i>p</i>-value
Based on Mean	10.385	2	30	0.000
Based on Median	2.424	2	30	0.106

Table A41: ANOVA test for study of PM, UM, OM data excluding extreme outliers.

Sources of variation	Sum of squares	DOF	Mean squares	F_0 value	<i>p</i>-value	$\eta^2_{partial}$	$1 - \beta$
Process	2916.950	2	1458.475	1.657	0.208	0.099	0.321
Error	26410.876	30	880.363				
Total	29327.826	32					

Table A42: Games-Howell test for study of PM, UM, OM data excluding extreme outliers.

(I) Process	(J) Process	Mean Difference (I-J)	Std. Error	<i>p</i>-value
OM	PM	11.8923	12.70432	0.622
	UM	-10.6181	12.96415	0.694
PM	OM	-11.8923	12.70432	0.622
	UM	-22.5103	12.38533	0.181
UM	OM	10.6181	12.96415	0.694
	PM	22.5103	12.38533	0.181

96/04 comparison

Table A41: Levene's test for homoscedasticity of PM, UM, OM data including extreme outliers.

Basis	Levene statistic	DOF 1	DOF 2	<i>p</i>-value
Based on Mean	1.855	2	42	0.169
Based on Median	0.522	2	42	0.597

Table A42: ANOVA test for study of PM, UM, OM data including extreme outliers.

Sources of variation	Sum of squares	DOF	Mean squares	F_0 value	<i>p</i>-value	$\eta^2_{partial}$	$1 - \beta$
Process	469.830	2	234.915	0.272	0.763	0.013	0.090
Error	36316.064	42	864.668				
Total	36785.895	44					

Table A43: Tukey-Kramer test for study of PM, UM, OM data including extreme outliers.

(I) Process	(J) Process	Mean Difference (I-J)	Std. Error	<i>p</i>-value
OM	PM	1.3812	10.73728	1.000
	UM	-6.0586	10.73728	1.000
PM	OM	-1.3812	10.73728	1.000
	UM	-7.4398	10.73728	1.000
UM	OM	6.0586	10.73728	1.000
	PM	7.4398	10.73728	1.000

Table A44: Levene's test for homoscedasticity of PM, UM, OM data excluding extreme outliers.

Basis	Levene statistic	DOF 1	DOF 2	<i>p</i>-value
Based on Mean	2.346	2	36	0.110
Based on Median	0.747	2	36	0.481

Table A45: ANOVA test for study of PM, UM, OM data excluding extreme outliers.

Sources of variation	Sum of squares	DOF	Mean squares	F_0 value	<i>p</i>-value	$\eta^2_{partial}$	$1 - \beta$
Process	1056.841	2	528.420	0.579	0.566	0.031	0.139
Error	32873.780	36	913.161				
Total	33930.621	38					

Table A46: Tukey-Kramer test for study of PM, UM, OM data excluding extreme outliers.

(I) Process	(J) Process	Mean Difference (I-J)	Std. Error	<i>p</i>-value
OM	PM	3.0251	11.63911	0.963
	UM	-9.3762	12.09710	0.721
PM	OM	-3.0251	11.63911	0.963
	UM	-12.4013	11.88791	0.555
UM	OM	9.3762	12.09710	0.721
	PM	12.4013	11.88791	0.555

94/06 comparison

Table A47: Levene's test for homoscedasticity of PM, UM, OM data including extreme outliers.

Basis	Levene statistic	DOF 1	DOF 2	<i>p</i>-value
Based on Mean	0.544	2	42	0.584
Based on Median	0.121	2	42	0.886

Table A48: ANOVA test for study of PM, UM, OM data including extreme outliers.

Sources of variation	Sum of squares	DOF	Mean squares	F_0 value	<i>p</i>-value	$\eta^2_{partial}$	$1 - \beta$
Process	463.331	2	231.665	0.143	0.867	0.007	0.071
Error	68148.050	42	1622.573				
Total	68611.381	44					

Table A49: Tukey-Kramer test for study of PM, UM, OM data including extreme outliers.

(I) Process	(J) Process	Mean Difference (I-J)	Std. Error	<i>p</i>-value
OM	PM	7.1755	14.70860	1.000
	UM	0.8098	14.70860	1.000
PM	OM	-7.1755	14.70860	1.000
	UM	-6.3657	14.70860	1.000
UM	OM	-0.8098	14.70860	1.000
	PM	6.3657	14.70860	1.000

Table A50: Levene's test for homoscedasticity of PM, UM, OM data excluding extreme outliers.

Basis	Levene statistic	DOF 1	DOF 2	<i>p</i>-value
Based on Mean	0.449	2	37	0.642
Based on Median	0.070	2	37	0.932

Table A51: ANOVA test for study of PM, UM, OM data excluding extreme outliers.

Sources of variation	Sum of squares	DOF	Mean squares	F_0 value	<i>p</i>-value	$\eta^2_{partial}$	$1 - \beta$
Process	110.954	2	55.477	0.032	0.969	0.002	0.054
Error	64907.292	37	1754.251				
Total	65018.246	39					

Table A52: Tukey-Kramer test for study of PM, UM, OM data excluding extreme outliers.

(I) Process	(J) Process	Mean Difference (I-J)	Std. Error	<i>p</i>-value
OM	PM	3.9808	16.47699	0.968
	UM	0.8676	15.83058	0.998
PM	OM	-3.9808	16.47699	0.968
	UM	-3.1132	16.47699	0.981
UM	OM	-0.8676	15.83058	0.998
	PM	3.1132	16.47699	0.981

92/08 comparison

Table A53: Levene's test for homoscedasticity of PM, UM, OM data including extreme outliers.

Basis	Levene statistic	DOF 1	DOF 2	<i>p</i> -value
Based on Mean	0.235	2	42	0.792
Based on Median	0.213	2	42	0.809

Table A54: ANOVA test for study of PM, UM, OM data including extreme outliers.

Sources of variation	Sum of squares	DOF	Mean squares	F_0 value	<i>p</i> -value	$\eta^2_{partial}$	$1 - \beta$
Process	5213.827	2	2606.913	1.024	0.368	0.046	0.217
Error	106911.944	42	2545.522				
Total	112125.771	44					

Table A55: Tukey-Kramer test for study of PM, UM, OM data including extreme outliers.

(I) Process	(J) Process	Mean Difference (I-J)	Std. Error	<i>p</i> -value
OM	PM	-20.5175	18.42289	0.815
	UM	4.0819	18.42289	1.000
PM	OM	20.5175	18.42289	0.815
	UM	24.5995	18.42289	0.567
UM	OM	-4.0819	18.42289	1.000
	PM	-24.5995	18.42289	0.567

Table A56: Levene's test for homoscedasticity of PM, UM, OM data excluding extreme outliers.

Basis	Levene statistic	DOF 1	DOF 2	<i>p</i>-value
Based on Mean	0.373	2	34	0.692
Based on Median	0.050	2	34	0.951

Table A57: ANOVA test for study of PM, UM, OM data excluding extreme outliers.

Sources of variation	Sum of squares	DOF	Mean squares	F_0 value	<i>p</i>-value	$\eta^2_{partial}$	$1 - \beta$
Process	4554.712	2	2277.356	0.847	0.438	0.047	0.183
Error	91456.507	34	2689.897				
Total	96011.219	36					

Table A58: Tukey-Kramer test for study of PM, UM, OM data excluding extreme outliers.

(I) Process	(J) Process	Mean Difference (I-J)	Std. Error	<i>p</i>-value
OM	PM	-20.2877	20.76230	0.596
	UM	5.1024	21.17348	0.969
PM	OM	20.2877	20.76230	0.596
	UM	25.3902	20.76230	0.448
UM	OM	-5.1024	21.17348	0.969
	PM	-25.3902	20.76230	0.448

PM comparison

Iteration 1

Table A59: Levene's test for homoscedasticity of composition data including extreme outliers.

Basis	Levene statistic	DOF 1	DOF 2	<i>p</i> -value
Based on Mean	3.617	4	70	0.010
Based on Median	2.296	4	70	0.068

Table A60: ANOVA test for study of composition data including extreme outliers.

Sources of variation	Sum of squares	DOF	Mean squares	F_0 value	<i>p</i> -value	$\eta^2_{partial}$	$1 - \beta$
Composition	28588.816	4	7147.204	6.269	0.000	0.264	0.984
Error	79807.563	70	1140.108				
Total	108396.379	74					

Table A61: Tukey-Kramer test for study of composition data including extreme outliers.

(I) Composition	(J) Composition	Mean Difference (I-J)	Std. Error	<i>p</i> -value
50/50	60/40	-1.5665	7.97112	1.000
	70/30	10.1614	8.72842	0.771
	80/20	-2.8554	13.18098	0.999
	90/10	-46.0032	13.22092	0.017
60/40	50/50	1.5665	7.97112	1.000
	70/30	11.7280	8.22059	0.617
	80/20	-1.2888	12.85033	1.000
	90/10	-44.4366	12.89129	0.020
70.00	50/50	-10.1614	8.72842	0.771
	60/40	-11.7280	8.22059	0.617
	80/20	-13.0168	13.33333	0.863
	90/10	-56.1646	13.37281	0.003
80.00	50/50	2.8554	13.18098	0.999
	60/40	1.2888	12.85033	1.000
	70/30	13.0168	13.33333	0.863
	90/10	-43.1478	16.62483	0.099

	50/50	46.0032	13.22092	0.017
	60/40	44.4366	12.89129	0.020
	70/30	56.1646	13.37281	0.003
	80/20	43.1478	16.62483	0.099

Iteration 2

Table A62: Levene's test for homoscedasticity of composition data including extreme outliers.

Basis	Levene statistic	DOF 1	DOF 2	<i>p</i> -value
Based on Mean	4.722	3	56	0.005
Based on Median	3.704	3	56	0.017

Table A63: ANOVA test for study of composition data including extreme outliers.

Sources of variation	Sum of squares	DOF	Mean squares	F_0 value	<i>p</i> -value	$\eta^2_{partial}$	$1 - \beta$
Composition	18024.236	3	6008.079	5.312	0.003	0.222	0.914
Error	63339.539	56	1131.063				
Total	81363.775	59					

Table A64: Games-Howell test for study of composition data including extreme outliers.

(I) Composition	(J) Composition	Mean Difference (I-J)	Std. Error	<i>p</i> -value
92/08	94/06	34.97513629	15.453414434	0.137
	96/04	38.36756150	15.006108614	0.080
	98/02	44.42542939	13.970993956	0.026
94/06	92/08	-34.97513629	15.453414434	0.137
	96/04	3.39242520	10.316403354	0.987
	98/02	9.45029310	8.742628583	0.705
96/04	92/08	-38.36756150	15.006108614	0.080
	94/06	-3.39242520	10.316403354	0.987
	98/02	6.05786789	7.925202370	0.870

98/02	92/08	-44.42542939	13.970993956	0.026
	94/06	-9.45029310	8.742628583	0.705
	96/04	-6.05786789	7.925202370	0.870

Table A65: Levene's test for homoscedasticity of composition data including extreme outliers.

Basis	Levene statistic	DOF 1	DOF 2	<i>p</i> -value
Based on Mean	3.261	3	45	0.030
Based on Median	2.710	3	45	0.056

Table A63: ANOVA test for study of composition data including extreme outliers.

Sources of variation	Sum of squares	DOF	Mean squares	F_0 value	<i>p</i> -value	$\eta^2_{partial}$	$1 - \beta$
Composition	19916.317	3	6638.772	5.730	0.002	0.276	0.930
Error	52135.751	45	1158.572				
Total	72052.067	48					

Table A67: Games-Howell test for study of composition data including extreme outliers.

(I) Composition	(J) Composition	Mean Difference (I-J)	Std. Error	<i>p</i> -value
92/08	94/06	33.17018100	17.287652889	0.251
	96/04	45.70170468	15.699632069	0.042
	98/02	50.17266451	14.737098362	0.019
94/06	92/08	-33.17018100	17.287652889	0.251
	96/04	12.53152367	12.486543630	0.749
	98/02	17.00248351	11.252439417	0.459
96/04	92/08	-45.70170468	15.699632069	0.042
	94/06	-12.53152367	12.486543630	0.749
	98/02	4.47095983	8.615851527	0.954
98/02	92/08	-50.17266451	14.737098362	0.019
	94/06	-17.00248351	11.252439417	0.459
	96/04	-4.47095983	8.615851527	0.954

UM comparison

Iteration 1

Table A68: Levene's test for homoscedasticity of composition data including extreme outliers.

Basis	Levene statistic	DOF 1	DOF 2	<i>p</i> -value
Based on Mean	1.801	4	70	0.138
Based on Median	0.819	4	70	0.517

Table A69: ANOVA test for study of composition data including extreme outliers.

Sources of variation	Sum of squares	DOF	Mean squares	F_0 value	<i>p</i> -value	$\eta^2_{partial}$	$1 - \beta$
Composition	46823.973	4	11705.993	5.641	0.001	0.244	0.972
Error	145261.023	70	2075.157				
Total	192084.997	74					

Table A70: Tukey-Kramer test for study of composition data including extreme outliers.

(I) Composition	(J) Composition	Mean Difference (I-J)	Std. Error	<i>p</i> -value
50/50	60/40	-21.96350513	16.633931082	0.680
	70/30	-50.68706430	16.633931082	0.026
	80/20	-27.45225823	16.633931082	0.471
	90/10	22.69145105	16.633931082	0.652
60/40	50/50	21.96350513	16.633931082	0.680
	70/30	-28.72355917	16.633931082	0.425
	80/20	-5.48875310	16.633931082	0.997
	90/10	44.65495618	16.633931082	0.067
70/30	50/50	50.68706430	16.633931082	0.026
	60/40	28.72355917	16.633931082	0.425
	80/20	23.23480607	16.633931082	0.632
	90/10	73.37851535	16.633931082	0.000

80/20	50/50	27.45225823	16.633931082	0.471
	60/40	5.48875310	16.633931082	0.997
	70/30	-23.23480607	16.633931082	0.632
	90/10	50.14370928	16.633931082	0.029
90/10	50/50	-22.69145105	16.633931082	0.652
	60/40	-44.65495618	16.633931082	0.067
	70/30	-73.37851535	16.633931082	0.000
	80/20	-50.14370928	16.633931082	0.029

Table A71: Levene's test for homoscedasticity of composition data excluding extreme outliers.

Basis	Levene statistic	DOF 1	DOF 2	<i>p</i> -value
Based on Mean	0.708	4	66	0.590
Based on Median	0.373	4	66	0.827

Table A72: ANOVA test for study of composition data excluding extreme outliers.

Sources of variation	Sum of squares	DOF	Mean squares	F_0 value	<i>p</i> -value	$\eta^2_{partial}$	$1 - \beta$
Composition	46996.367	4	11749.092	6.675	0.000	0.288	0.989
Error	116164.834	66	1760.073				
Total	163161.201	70					

Table A73: Tukey-Kramer test for study of composition data excluding extreme outliers.

(I) Composition	(J) Composition	Mean Difference (I-J)	Std. Error	<i>p</i> -value
50/50	60/40	-21.96350513	12.317971267	0.404
	70/30	-59.11147120	15.843043066	0.010
	80/20	-34.21685039	14.907712515	0.185
	90/10	15.83555835	13.729127203	0.777

60/40	50/50	21.96350513	12.317971267	0.404
	70/30	-37.14796607	16.810902774	0.211
	80/20	-12.25334526	15.932492929	0.937
	90/10	37.79906348	14.835544218	0.112
70/30	50/50	59.11147120	15.843043066	0.010
	60/40	37.14796607	16.810902774	0.211
	80/20	24.89462081	18.791325882	0.679
	90/10	74.94702956	17.870729412	0.003
80/20	50/50	34.21685039	14.907712515	0.185
	60/40	12.25334526	15.932492929	0.937
	70/30	-24.89462081	18.791325882	0.679
	90/10	50.05240875	17.047018759	0.050
90/10	50/50	-15.83555835	13.729127203	0.777
	60/40	-37.79906348	14.835544218	0.112
	70/30	-74.94702956	17.870729412	0.003
	80/20	-50.05240875	17.047018759	0.050

Iteration 2

Table A74: Levene's test for homoscedasticity of composition data including extreme outliers.

Basis	Levene statistic	DOF 1	DOF 2	<i>p</i> -value
Based on Mean	0.376	3	56	0.771
Based on Median	0.059	3	56	0.981

Table A75: ANOVA test for study of composition data including extreme outliers.

Sources of variation	Sum of squares	DOF	Mean squares	F_0 value	<i>p</i> -value	$\eta^2_{partial}$	$1 - \beta$
Composition	314.975	3	104.992	0.049	0.985	0.003	0.058
Error	119442.813	56	2132.907				
Total	119757.788	59					

Table A76: Tukey-Kramer test for study of composition data including extreme outliers.

(I) Composition	(J) Composition	Mean Difference (I-J)	Std. Error	<i>p</i> -value
92/08	94/06	4.00994059	16.863797000	0.995
	96/04	6.32825180	16.863797000	0.982
	98/02	4.26096349	16.863797000	0.994
94/06	92/08	-4.00994059	16.863797000	0.995
	96/04	2.31831121	16.863797000	0.999
	98/02	.25102290	16.863797000	1.000
96/04	92/08	-6.32825180	16.863797000	0.982
	94/06	-2.31831121	16.863797000	0.999
	98/02	-2.06728831	16.863797000	0.999
98/02	92/08	-4.26096349	16.863797000	0.994
	94/06	-.25102290	16.863797000	1.000
	96/04	2.06728831	16.863797000	0.999

Table A77: Levene's test for homoscedasticity of composition data including extreme outliers.

Basis	Levene statistic	DOF 1	DOF 2	<i>p</i> -value
Based on Mean	0.435	3	43	0.729
Based on Median	0.110	3	43	0.954

Table A78: ANOVA test for study of composition data including extreme outliers.

Sources of variation	Sum of squares	DOF	Mean squares	F_0 value	<i>p</i> -value	$\eta^2_{partial}$	$1 - \beta$
Composition	419.303	3	139.768	0.056	0.982	0.004	0.059
Error	106800.918	43	2483.742				
Total	107220.222	46					

Table A79: Tukey-Kramer test for study of composition data including extreme outliers.

(I) Composition	(J) Composition	Mean Difference (I-J)	Std. Error	<i>p</i> -value
92/08	94/06	5.01307833	23.669708261	0.997
	96/04	7.91029074	20.699191124	0.980
	98/02	2.27216650	21.555837004	1.000
94/06	92/08	-5.01307833	23.669708261	0.997
	96/04	2.89721241	19.244649073	0.999
	98/02	-2.74091184	20.163187092	0.999
96/04	92/08	-7.91029074	20.699191124	0.980
	94/06	-2.89721241	19.244649073	0.999
	98/02	-5.63812424	16.575751497	0.986
98/02	92/08	-2.27216650	21.555837004	1.000
	94/06	2.74091184	20.163187092	0.999
	96/04	5.63812424	16.575751497	0.986

OM comparison**Iteration 1**

Table A80: Levene's test for homoscedasticity of composition data including extreme outliers.

Basis	Levene statistic	DOF 1	DOF 2	<i>p</i> -value
Based on Mean	3.824	4	70	0.007
Based on Median	2.106	4	70	0.089

Table A81: ANOVA test for study of composition data including extreme outliers.

Sources of variation	Sum of squares	DOF	Mean squares	F_0 value	<i>p</i> -value	$\eta^2_{partial}$	$1 - \beta$
Composition	3555.720	4	888.930	0.506	0.732	0.028	0.164
Error	123086.772	70	1758.382				
Total	126642.492	74					

Table A82: Games-Howell test for study of composition data including extreme outliers.

(I) Composition	(J) Composition	Mean Difference (I-J)	Std. Error	<i>p</i> -value
50/50	60/40	-5.3151	11.20736	0.989
	70/30	-11.2630	17.26508	0.965
	80/20	-13.9322	14.68218	0.875
	90/10	-19.9033	14.77747	0.665
60/40	50/50	5.3151	11.20736	0.989
	70/30	-5.9479	15.57843	0.995
	80/20	-8.6171	12.65588	0.958
	90/10	-14.5883	12.76630	0.782
70/30	50/50	11.2630	17.26508	0.965
	60/40	5.9479	15.57843	0.995
	80/20	-2.6692	18.23867	1.000
	90/10	-8.6403	18.31546	0.989
80/20	50/50	13.9322	14.68218	0.875
	60/40	8.6171	12.65588	0.958
	70/30	2.6692	18.23867	1.000
	90/10	-5.9711	15.90408	0.996
90/10	50/50	19.9033	14.77747	0.665
	60/40	14.5883	12.76630	0.782
	70/30	8.6403	18.31546	0.989
	80/20	5.9711	15.90408	0.996

Table A83: Levene's test for homoscedasticity of composition data excluding extreme outliers.

Basis	Levene statistic	DOF 1	DOF 2	<i>p</i> -value
Based on Mean	4.492	4	68	0.003
Based on Median	2.614	4	68	0.043

Table A84: ANOVA test for study of composition data excluding extreme outliers.

Sources of variation	Sum of squares	DOF	Mean squares	F_0 value	p -value	$\eta^2_{partial}$	$1 - \beta$
Composition	6816.357	4	1704.089	1.105	0.361	0.061	0.330
Error	104859.621	68	1542.053				
Total	111675.978	72					

Table A85: Games-Howell test for study of composition data excluding extreme outliers.

(I) Composition	(J) Composition	Mean Difference (I-J)	Std. Error	p -value
50/50	60/40	-5.3151	11.20736	0.989
	70/30	-11.2630	17.26508	0.965
	80/20	-20.3032	13.71033	0.583
	90/10	-26.7009	13.59160	0.310
60/40	50/50	5.3151	11.20736	0.989
	70/30	-5.9479	15.57843	0.995
	80/20	-14.9881	11.51425	0.693
	90/10	-21.3858	11.37261	0.357
70/30	50/50	11.2630	17.26508	0.965
	60/40	5.9479	15.57843	0.995
	80/20	-9.0402	17.46584	0.985
	90/10	-15.4378	17.37280	0.898
80/20	50/50	20.3032	13.71033	0.583
	60/40	14.9881	11.51425	0.693
	70/30	9.0402	17.46584	0.985
	90/10	-6.3976	13.84574	0.990
90/10	50/50	26.7009	13.59160	0.310
	60/40	21.3858	11.37261	0.357
	70/30	15.4378	17.37280	0.898
	80/20	6.3976	13.84574	0.990

Iteration 2

Table A86: Levene's test for homoscedasticity of composition data including extreme outliers.

Basis	Levene statistic	DOF 1	DOF 2	<i>p</i> -value
Based on Mean	1.317	3	56	0.278
Based on Median	1.060	3	56	0.374

Table A87: ANOVA test for study of composition data including extreme outliers.

Sources of variation	Sum of squares	DOF	Mean squares	F_0 value	<i>p</i> -value	$\eta^2_{partial}$	$1 - \beta$
Composition	3425.596	3	1141.865	0.962	0.417	0.049	0.249
Error	66495.331	56	1187.417				
Total	69920.927	59					

Table A88: Tukey-Kramer test for study of composition data including extreme outliers.

(I) Composition	(J) Composition	Mean Difference (I–J)	Std. Error	<i>p</i> -value
92/08	94/06	7.28208652	12.582615635	0.938
	96/04	16.46879801	12.582615635	0.561
	98/02	19.00195705	12.582615635	0.438
94/06	92/08	-7.28208652	12.582615635	0.938
	96/04	9.18671148	12.582615635	0.885
	98/02	11.71987053	12.582615635	0.788
96/04	92/08	-16.46879801	12.582615635	0.561
	94/06	-9.18671148	12.582615635	0.885
	98/02	2.53315904	12.582615635	0.997
98/02	92/08	-19.00195705	12.582615635	0.438
	94/06	-11.71987053	12.582615635	0.788
	96/04	-2.53315904	12.582615635	0.997

Table A89: Levene's test for homoscedasticity of composition data excluding extreme outliers.

Basis	Levene statistic	DOF 1	DOF 2	<i>p</i>-value
Based on Mean	1.074	3	46	0.369
Based on Median	0.825	3	46	0.487

Table A90: ANOVA test for study of composition data excluding extreme outliers.

Sources of variation	Sum of squares	DOF	Mean squares	F_0 value	<i>p</i>-value	$\eta^2_{partial}$	$1 - \beta$
Composition	4582.352	3	1527.451	1.209	0.317	0.073	0.303
Error	58118.606	46	1263.448				
Total	62700.958	49					

Table A91: Tukey-Kramer test for study of composition data excluding extreme outliers.

(I) Composition	(J) Composition	Mean Difference (I-J)	Std. Error	<i>p</i>-value
92/08	94/06	11.78895813	16.368303070	0.888
	96/04	20.58669432	14.426100942	0.500
	98/02	25.31170905	15.351079775	0.375
94/06	92/08	-11.78895813	16.368303070	0.888
	96/04	8.79773619	12.996799783	0.905
	98/02	13.52275092	14.016421315	0.770
96/04	92/08	-20.58669432	14.426100942	0.500
	94/06	-8.79773619	12.996799783	0.905
	98/02	4.72501473	11.689786546	0.977
98/02	92/08	-25.31170905	15.351079775	0.375
	94/06	-13.52275092	14.016421315	0.770
	96/04	-4.72501473	11.689786546	0.977

ANOVA and associate tables for Case Study 3

P1

Table A92: Levene's test for homoscedasticity of temperature data including extreme outliers.

Basis	Levene statistic	DOF 1	DOF 2	<i>p</i> -value
Based on Mean	0.287	4	70	0.885
Based on Median	0.110	4	70	0.979

Table A93: ANOVA test for study of temperature data including extreme outliers.

Sources of variation	Sum of squares	DOF	Mean squares	F_0 value	<i>p</i> -value	$\eta^2_{partial}$	$1 - \beta$
Temperature	0.108	4	0.027	0.075	0.990	0.004	0.064
Error	25.105	70	0.359				
Total	25.213	74					

Table A94: Tukey-Kramer test for study of temperature data including extreme outliers.

(I) Temperature	(J) Temperature	Mean Difference (I-J)	Std. Error	<i>p</i> -value
20	30	-0.032371	0.1986309	1.000
	40	-0.054847	0.2043779	0.999
	50	-0.082980	0.2121846	0.995
	60	-0.108613	0.2192001	0.987
30	20	0.032371	0.1986309	1.000
	40	-0.022476	0.2114828	1.000
	50	-0.050609	0.2190363	0.999
	60	-0.076242	0.2258391	0.997
40	20	0.054847	0.2043779	0.999
	30	0.022476	0.2114828	1.000
	50	-0.028133	0.2242611	1.000
	60	-0.053766	0.2309100	0.999
50	20	0.082980	0.2121846	0.995
	30	0.050609	0.2190363	0.999
	40	0.028133	0.2242611	1.000
	60	-0.025634	0.2378474	1.000

60	20	0.108613	0.2192001	0.987
	30	0.076242	0.2258391	0.997
	40	0.053766	0.2309100	0.999
	50	0.025634	0.2378474	1.000

Table A95: Levene's test for homoscedasticity of temperature data excluding extreme outliers.

Basis	Levene statistic	DOF 1	DOF 2	<i>p</i> -value
Based on Mean	0.256	4	55	0.905
Based on Median	0.155	4	55	0.960

Table A96: ANOVA test for study of temperature data excluding extreme outliers.

Sources of variation	Sum of squares	DOF	Mean squares	F_0 value	<i>p</i> -value	$\eta^2_{partial}$	$1 - \beta$
Temperature	0.135	4	0.034	0.088	0.986	0.006	0.067
Error	20.974	55	0.381				
Total	21.109	59					

Table A97: Tukey-Kramer test for study of temperature data excluding extreme outliers.

(I) Temperature	(J) Temperature	Mean Difference (I-J)	Std. Error	<i>p</i> -value
20	30	-0.040457	0.2287643	1.000
	40	-0.068553	0.2354483	0.998
	50	-0.103716	0.2446243	0.993
	60	-0.135759	0.2528162	0.982
30	20	0.040457	0.2287643	1.000
	40	-0.028096	0.2436173	1.000
	50	-0.063258	0.2524966	0.999
	60	-0.095301	0.2604410	0.996
40	20	0.068553	0.2354483	0.998
	30	0.028096	0.2436173	1.000
	50	-.035162	.2585678	1.000
	60	-.067205	.2663312	0.999

50	20	0.103716	.2446243	0.993
	30	0.063258	.2524966	0.999
	40	0.035162	.2585678	1.000
	60	-0.032043	.2744767	1.000
60	20	0.135759	.2528162	0.982
	30	0.095301	.2604410	0.996
	40	0.067205	.2663312	.999
	50	0.032043	.2744767	1.000

P2

Table A98: Levene's test for homoscedasticity of temperature data including extreme outliers.

Basis	Levene statistic	DOF 1	DOF 2	<i>p</i> -value
Based on Mean	1.016	4	70	0.405
Based on Median	0.854	4	70	0.496

Table A99: ANOVA test for study of temperature data including extreme outliers.

Sources of variation	Sum of squares	DOF	Mean squares	F_0 value	<i>p</i> -value	$\eta^2_{partial}$	$1 - \beta$
Temperature	3889.113	4	972.278	7.302	0.000	0.294	0.994
Error	9320.963	70	133.157				
Total	13210.076	74					

Table A100: Tukey-Kramer test for study of temperature data including extreme outliers.

(I) Temperature	(J) Temperature	Mean Difference (I-J)	Std. Error	<i>p</i> -value
20	30	-7.969152	3.7128829	0.231
	40	-13.663974	3.6946920	0.008
	50	-17.400157	3.9159127	0.001
	60	-20.198414	4.1480297	0.000
30	20	7.969152	3.7128829	0.231
	40	-5.694822	4.1282070	0.645
	50	-9.431006	4.3273221	0.217
	60	-12.229263	4.5384462	0.081

40	20	13.663974	3.6946920	0.008
	30	5.694822	4.1282070	0.645
	50	-3.736183	4.3117242	0.907
	60	-6.534440	4.5235764	0.605
50	20	17.400157	3.9159127	0.001
	30	9.431006	4.3273221	0.217
	40	3.736183	4.3117242	0.907
	60	-2.798257	4.7059927	0.975
60	20	20.198414	4.1480297	0.000
	30	12.229263	4.5384462	0.081
	40	6.534440	4.5235764	0.605
	50	2.798257	4.7059927	0.975

ANOVA and associate tables for Case Study 4

P2-P1

Table A101: Levene's test for homoscedasticity of temperature and composition data.

Basis	Levene statistic	DOF 1	DOF 2	<i>p</i> -value
Based on Mean	10.230	24	350	0.000
Based on Median	9.053	24	350	0.000

Table A102: ANOVA test for study of temperature and composition data.

Sources of variation	Sum of squares	DOF	Mean squares	F_0 value	<i>p</i> -value	$\eta^2_{partial}$	$1 - \beta$
Temperature	0.169	4	0.042	5.756	0.000	0.062	0.981
Composition	6.797	4	1.699	231.023	0.000	0.725	1.000
Temperature*Composition	0.154	16	0.010	1.307	0.190	0.056	0.822
Error	2.575	350	.007				
Total	9.695	374					

Table A103: Games-Howell test for study of temperature data.

(I) Temperature	(J) Temperature	Mean Difference (I-J)	Std. Error	<i>p</i> -value
20	30	-0.01616538	0.014005557	0.777
	40	-0.03192817	0.014005557	0.154
	50	-0.04762502	0.014005557	0.007
	60	-0.05928242	0.014005557	0.000
30	20	0.01616538	0.014005557	0.777
	40	-0.01576279	0.014005557	0.793
	50	-0.03145964	0.014005557	0.165
	60	-0.04311704	0.014005557	0.019
40	20	0.03192817	0.014005557	0.154
	30	0.01576279	0.014005557	0.793
	50	-0.01569685	0.014005557	0.796
	60	-0.02735424	0.014005557	0.291
50	20	0.04762502	0.014005557	0.007
	30	0.03145964	0.014005557	0.165
	40	0.01569685	0.014005557	0.796
	60	-0.01165740	0.014005557	0.920
60	20	0.05928242	0.014005557	0.000
	30	0.04311704	0.014005557	0.019
	40	0.02735424	0.014005557	0.291
	50	0.01165740	0.014005557	0.920

Table A104: Games-Howell test for study of composition data.

(I) Composition	(J) Composition	Mean Difference (I-J)	Std. Error	<i>p</i> -value
50/50	60/40	-0.00339790	0.014005557	0.999
	70/30	-0.09377648	0.014005557	0.000
	80/20	-0.22229621	0.014005557	0.000
	90/10	-0.34895671	0.014005557	0.000

60/40	50/50	0.00339790	0.014005557	.999
	70/30	-0.09037858	0.014005557	0.000
	80/20	-0.21889831	0.014005557	0.000
	90/10	-0.34555881	0.014005557	0.000
70/30	50/50	0.09377648	0.014005557	0.000
	60/40	0.09037858	0.014005557	0.000
	80/20	-0.12851973	0.014005557	0.000
	90/10	-0.25518023	0.014005557	0.000
80/20	50/50	0.22229621	0.014005557	0.000
	60/40	0.21889831	0.014005557	0.000
	70/30	0.12851973	0.014005557	0.000
	90/10	-0.12666049	0.014005557	0.000
90/10	50/50	0.34895671	0.014005557	0.000
	60/40	0.34555881	0.014005557	0.000
	70/30	0.25518023	0.014005557	0.000
	80/20	0.12666049	0.014005557	0.000

P2-P1-D

Table A105: Levene's test for homoscedasticity of temperature and composition data.

Basis	Levene statistic	DOF 1	DOF 2	<i>p</i> -value
Based on Mean	12.571	24	350	0.000
Based on Median	8.806	24	350	0.000

Table A106: ANOVA test for study of temperature and composition data.

Sources of variation	Sum of squares	DOF	Mean squares	F_0 value	<i>p</i> -value	$\eta^2_{partial}$	$1 - \beta$
Temperature	1.271	4	.318	0.128	0.972	0.001	0.077
Composition	3071.203	4	767.801	310.539	0.000	0.780	1.000
Temperature*Composition	2.737	16	.171	0.069	1.000	0.003	0.076
Error	865.368	350	2.472				
Total	3940.579	374					

Table A107: Games-Howell test for study of temperature data.

(I) Temperature	(J) Temperature	Mean Difference (I-J)	Std. Error	<i>p</i> -value
20	30	-0.077609	0.2567738	0.998
	40	-0.144443	0.2567738	0.980
	50	-0.159217	0.2567738	0.972
	60	-0.059149	0.2567738	0.999
30	20	0.077609	0.2567738	0.998
	40	-0.066834	0.2567738	0.999
	50	-0.081608	0.2567738	0.998
	60	0.018460	0.2567738	1.000
40	20	0.144443	0.2567738	0.980
	30	0.066834	0.2567738	0.999
	50	-0.014774	0.2567738	1.000
	60	0.085294	0.2567738	0.997
50	20	0.159217	0.2567738	0.972
	30	0.081608	0.2567738	0.998
	40	0.014774	0.2567738	1.000
	60	0.100069	0.2567738	0.995
60	20	0.059149	0.2567738	0.999
	30	-0.018460	0.2567738	1.000
	40	-0.085294	0.2567738	0.997
	50	-0.100069	0.2567738	0.995

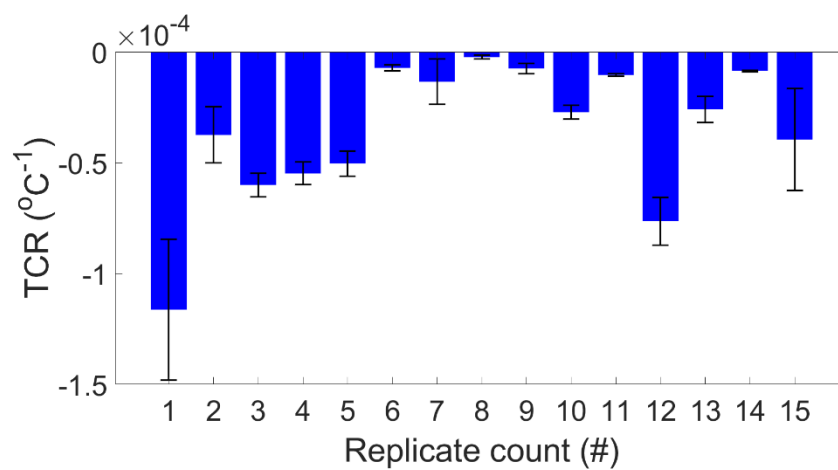
Table A108: Games-Howell test for study of composition data.

(I) Composition	(J) Composition	Mean Difference (I-J)	Std. Error	<i>p</i> -value
50/50	60/40	1.007574	0.2567738	0.001
	70/30	5.911679	0.2567738	0.000
	80/20	6.487252	0.2567738	0.000
	90/10	6.481198	0.2567738	0.000

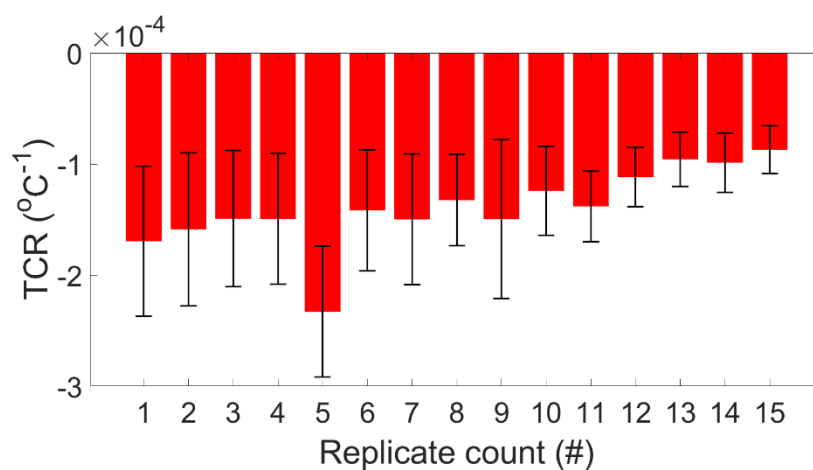
60/40	50/50	-1.007574	0.2567738	0.001
	70/30	4.904105	0.2567738	0.000
	80/20	5.479678	0.2567738	0.000
	90/10	5.473623	0.2567738	0.000
70/30	50/50	-5.911679	0.2567738	0.000
	60/40	-4.904105	0.2567738	0.000
	80/20	.575573	0.2567738	0.167
	90/10	.569518	0.2567738	0.175
80/20	50/50	-6.487252	0.2567738	0.000
	60/40	-5.479678	0.2567738	0.000
	70/30	-.575573	0.2567738	0.167
	90/10	-.006055	0.2567738	1.000
90/10	50/50	-6.481198	0.2567738	0.000
	60/40	-5.473623	0.2567738	0.000
	70/30	-.569518	0.2567738	0.175
	80/20	.006055	0.2567738	1.000

Appendix B

TCR of pristine *P1* replicates

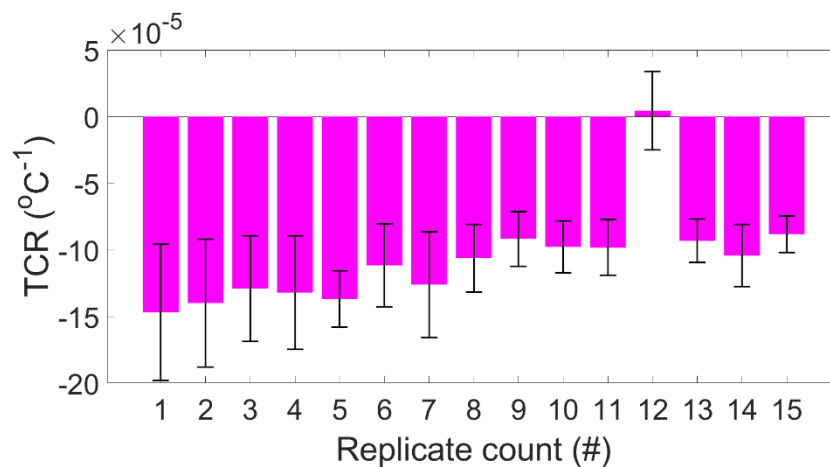


TCR of pristine *P2* replicates

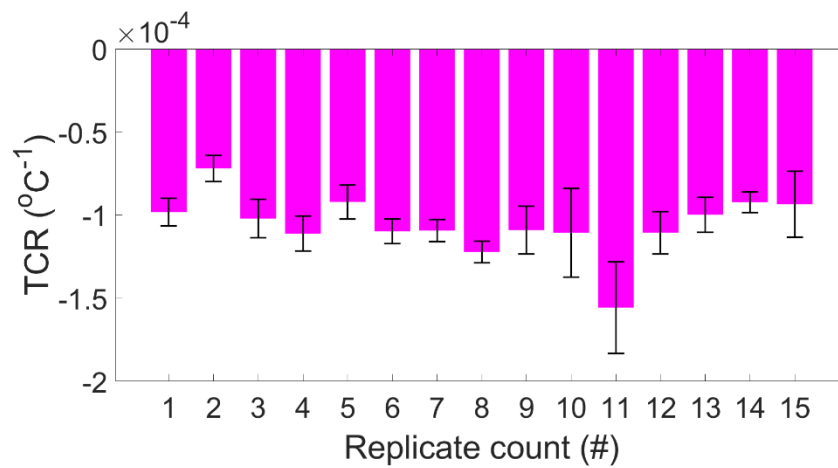


TCR of *P2-P1* blends

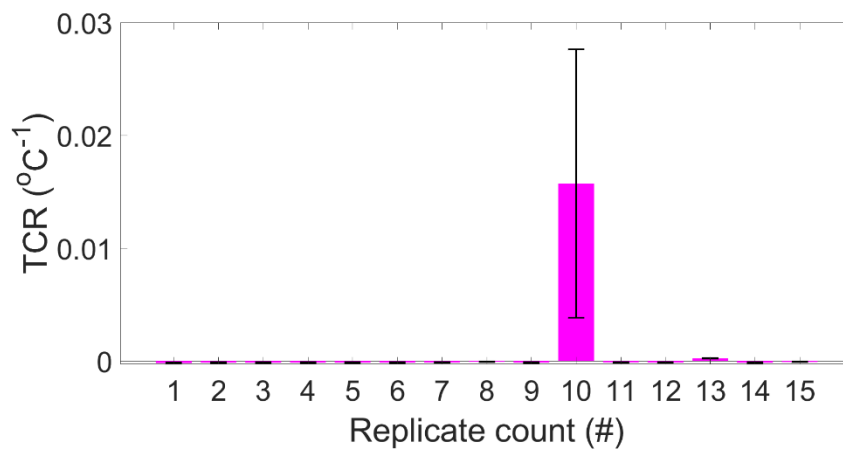
90/10



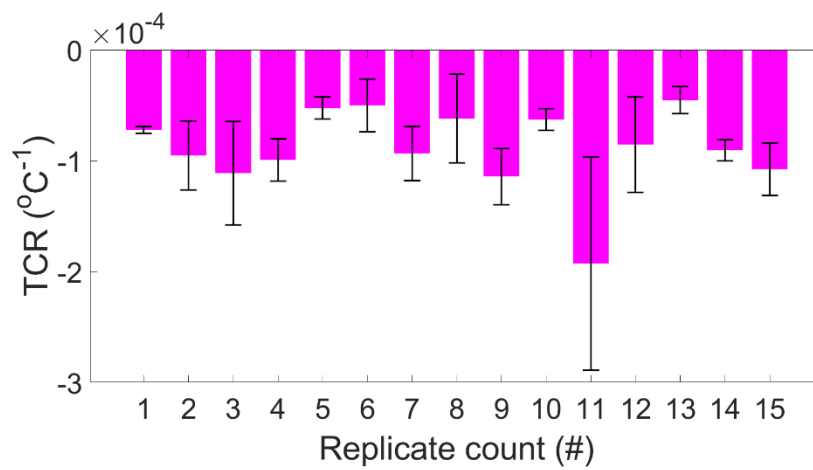
80/20



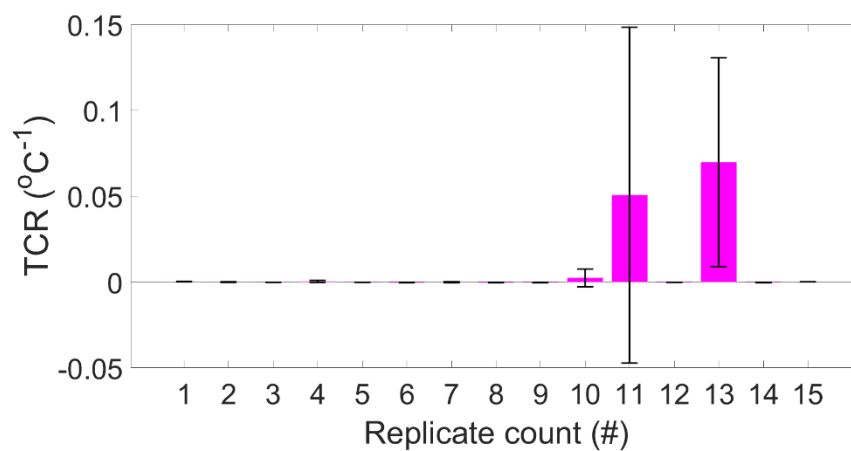
70/30



60/40

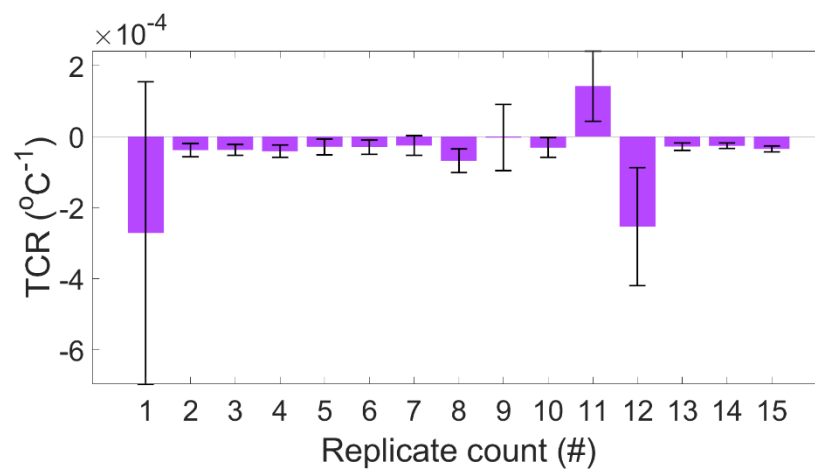


50/50

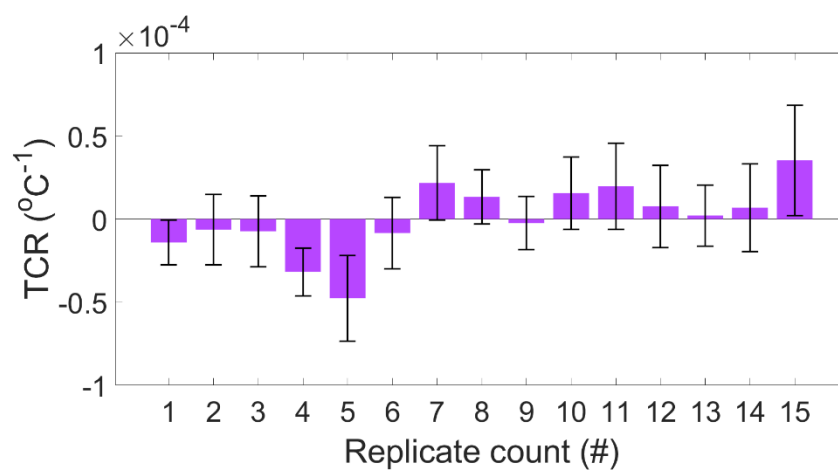


TCR of *P2-P1-D* blends

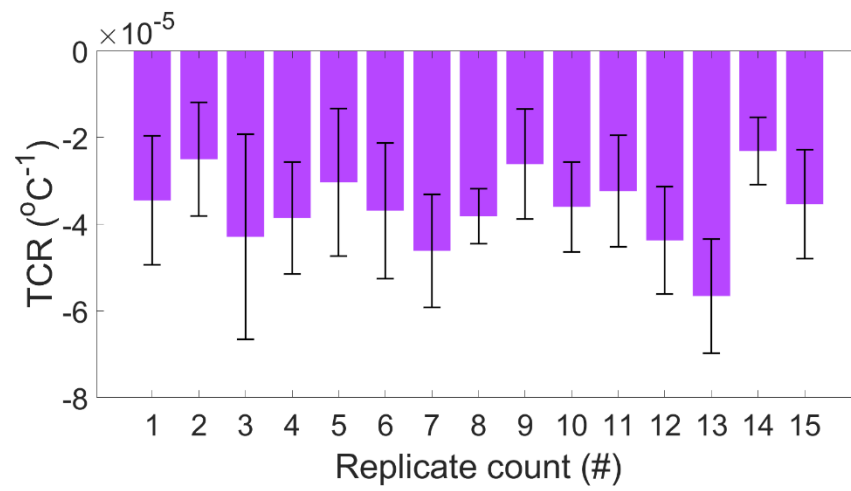
90/10



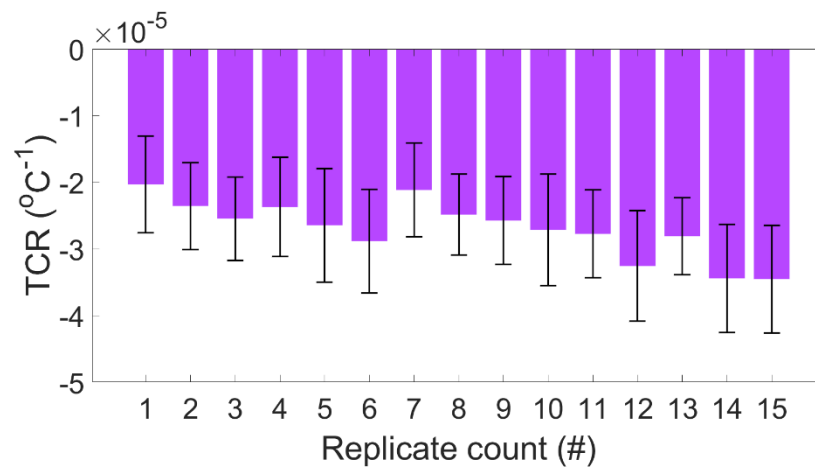
80/20



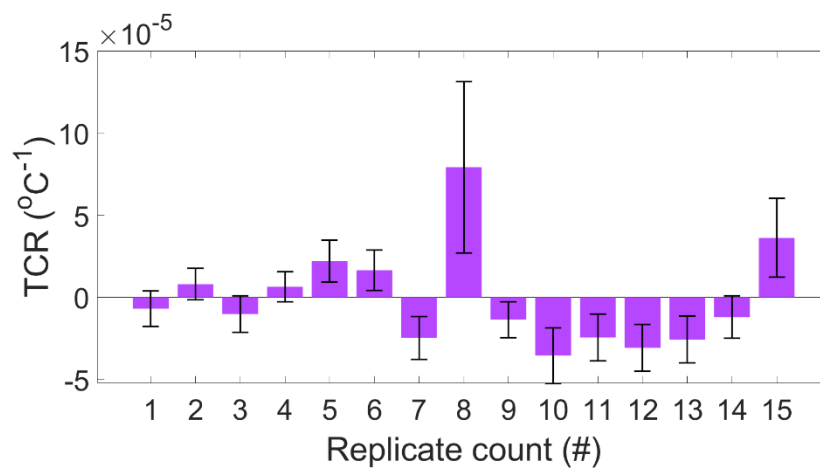
70/30



60/40



50/50



General specifications of the CPH used in this work	
Viscosity	~1 to 20 mPa.s
Surface tension	~20 to 70 mN/m
Solvent compatibility	Water and low molecular weight alcohols
Fluid inputs	2